PHYSICO-CHEMICAL INVESTIGATIONS OF DIFFERENT MATERIALS OF RELEVANCE IN NUCLEAR TECHNOLOGY

By

KOMAL CHANDRA SHRIVASTAVA

Enrolment No: CHEM01201004012

Bhabha Atomic Research Centre, Mumbai, INDIA

A thesis submitted to the

Board of Studies in Chemical Sciences

In partial fulfillment of requirements

For the degree of

DOCTOR OF PHILOSOPHY

of

HOMI BHABHA NATIONAL INSTITUTE

October, 2016

Homi Bhabha National Institute

Recommendations of the Viva Voce Committee

As members of the Viva Voce Committee, we certify that we have read the dissertation prepared by **Komal Chandra Shrivastava** entitled **"Physico-chemical investigations of different materials of relevance in nuclear technology"** and recommend that it may be accepted as fulfilling the thesis requirement for the award of Degree of Doctor of Philosophy.

Chairman – **Prof. V. Venugopal** **Date:** 17/10/16

Guide/Convener – **Prof. K. L. Ramakumar** **Date:** 17/10 2016

External Examiner – **Prof. P. Maiti** Pmaiti **Date:** 17.10.16

Member 1 – **Prof. S. Kannan** **Date:** 17.10.16

Member 2 – **Prof. R. N. Singh** **Date:** 17.10.16

Member 3 – **Prof. Sangita D. Kumar** **Date:** 17.10.16

The modifications as per the examiners' comments have been incorporated in the respective portions of the thesis. Final approval and acceptance of this thesis is contingent upon the candidate's submission of the final copies of the thesis to HBNI.

I hereby certify that I have read this thesis prepared under my direction and recommend that it may be accepted as fulfilling the thesis requirement.

Date: 17.10 2016
Place: Mumbai

Dr. K. L. Ramakumar
(Guide)

STATEMENT BY AUTHOR

This dissertation has been submitted in partial fulfillment of requirements for an advanced degree at Homi Bhabha National Institute (HBNI) and is deposited in the Library to be made available to borrowers under rules of the HBNI.

Brief quotations from this dissertation are allowable without special permission, provided that accurate acknowledgement of source is made. Requests for permission for extended quotation from or reproduction of this manuscript in whole or in part may be granted by the Competent Authority of HBNI when in his or her judgment the proposed use of the material is in the interests of scholarship. In all other instances, however, permission must be obtained from the author.

Komal Chandra
Komal Chandra Shrivastava

DECLARATION

I, hereby declare that the investigation presented in the thesis has been carried out by me. The work is original and has not been submitted earlier as a whole or in part for a degree/diploma at this or any other Institution / University.

Komal Chandra

Signature of the Student

(Komal C. Shrivastava)

List of Publications arising from the thesis

Journal

1. "Determination of Deuterium Pick-Up in Zr-Nb Alloy by Hot Vacuum Extraction-Quadrupole Mass Spectrometry", **Komal Chandra**, P. S. Ramanjaneyulu, C. S. Yadav, A. S. Kulkarni, Y. S. Sayi, K. L. Ramakumar, Analytical Letters, **2012,** 45, 2136–2147.

2. "Determination of total gas content and its composition in Indian PFBR blanket pellets", P. S. Ramanjaneyulu, **Komal Chandra**, A. S. Kulkarni, C. S. Yadav, Abhijit Saha, M. K. Saxena, B. S. Tomar, K. L. Ramakumar, J Radioanal. Nucl. Chem., **2014**, 301, 117–124.

3. "Determination of diffusion coefficients of hydrogen and deuterium in Zr-2.5%Nb pressure tube material using hot vacuum extraction – quadrupole mass spectrometry", **Komal Chandra Shrivastava,** A. S. Kulkarni, P. S. Ramanjaneyulu, Saurav Sunil, M. K. Saxena, R. N. Singh, B. S. Tomar, K. L. Ramakumar, J. Nucl. Mater., **2015,** 461, 151–156.

4. "Palladium Nanoparticles Hosted on Hydrazine-grafted Magnetite and Silica Particles for Catalyzing the Reduction of Oxymetal Ions with Formic Acid", **Komal Chandra Shrivastava**, Sankararao Chappa, Arijit Sengupta, Amit P. Srivastava, Ashok K. Pandey, K. L. Ramakumar, Chem. Cat. Chem., **2016**, 8, 2981-2987.

Conferences

1. "Determination of Deuterium content in irradiated Zirconium alloy - Ageing Management", C. S. Yadav, P. S. Ramanjaneyulu, **Komal Chandra**, A. S. Kulkarni, Y. S. Sayi, K. L. Ramakumar, RAPT – **2010**, Anupuram, Chennai.

2. "Determination of Deuterium by HVE-QMS for Life Time Assessment of Zr-2.5%Nb Coolant Channels", K. L. Pandey, A. S. Kulkarni, **Komal Chandra**, P. S. Ramanjaneyulu, C. S. Yadav, Y. S. Sayi, K. L. Ramakumar, NUCAR **2011**, Visakhapatnam, INDIA.

3. "Determination of total gas content and its composition in PFBR Blanket Pellets", P. S. Ramanjaneyulu, **Komal Chandra**, A. S. Kulkarni, C. S. Yadav, M. K. Saxena, K. L. Ramakumar, NUCAR **2013**, Jabalpur, INDIA.

4. "Determination of Activation Energy of Hydrogen Diffusion in Zr-2.5%Nb Alloy", **Komal Chandra**, A. S. Kulkarni, P. S. Ramanjaneyulu, Sourav Sunil, C. S. Yadav, M. K. Saxena, R. N. Singh, B. S. Tomar, K. L. Ramakumar, THERMANS **2014** , TSH, BARC, Mumbai, INDIA.

5. "Thermal Conditioning of Palladium Nanoparticles Loaded Fe_3O_4", **Komal C. Shrivastava**, M. Phanindrakumar, S. K. Sali, K. L. Ramakumar, THERMANS **2016**, DEPARTMENT OF PHYSICS,INDIAN INSTITUTE OF TECHNOLOGY, B.H.U., Varanasi, INDIA.

Komal Chandra
Komal C. Shrivastava

DEDICATED

To

MY PARENTS

(Mrs. Seema Srivastava

&

Mr. Satish Chandra Srivastava)

And

MY HUSBAND

(Mr. Avinash Shrivastava)

for their endless love and unconditional support in my life

ACKNOWLEDGEMENTS

I express my sincere appreciation and gratitude to my guide, **Prof. K. L. Ramakumar**, Ex-Director RC&I Group, for giving me the chance to register for PhD under him, and for all the support, trust, encouragement and guidance over the last five years of this work. He encouraged me to not only grow as an experimentalist and a chemist but also as a person and an independent thinker. I acknowledge his excellent input and insightful comments during the preparation of this thesis.

I am also grateful to **Prof. V. Venugopal**, Chairman, Doctoral Committee, Ex-Director, Radiochemistry & Isotope Group, for his encouragement and enthusiasm. I also thank the Doctoral Committee members, **Prof. S. Kannan**, **Prof. R.N. Singh**, **Dr. Sangita D. Kumar** for the helpful advices and discussions.

I am privileged to thank **Prof. B.S. Tomar**, Director RC&I Group & Head, Radioanalytical Chemistry Division, for his unstinted support and encouragement. His advice and comments have been priceless and played a significant role in documenting my experimental work.

I take this opportunity to express my sincere regards and deepest appreciation to **Dr. Y. S. Sayi** (Former Head, High Temperature Analysis Group). His invaluable constructive criticisms and suggestions on academic level have always been extremely helpful to me.

I am grateful to **Dr. A. K. Pandey** for the enriching technical discussions on nanoparticles' preparation, characterization and applications.

Also, it is my utmost pleasure to express my sincere thanks to my colleagues in High Temperature Analysis Group (TEAS), **Mr. M. K. Saxena (Head, TEAS), Mr. C. S. Yadav, Dr. P. S. Ramanjaneyulu, Mr. A. S. Kulkarni, Mr. M. Phanindra**

Kumar, for their support and extended co-operation at different stages of my work.

I thank my co-authors for their help in various experiments.

My sincere thanks to all of my colleagues from Radioanalytical Chemistry Section for their help, suggestions and encouragement. I am thankful to all my friends for their encouragement and support. I greatly value their friendship and deeply appreciate their belief in me.

I cannot imagine my current position without the blessings of my teachers and will always be indebted to them.

Most importantly, I owe my heartfelt gratitude to **my parents** for their constant encouragement, care and never fading love. Their blessings and good wishes have helped me to achieve what I am today.

Finally, I would like to express my endless thanks and appreciations to my husband **Mr. Avinash Shrivastava**. I truly thank Avinash for sticking by my side, even when I was irritable and depressed. I feel that what we both learned a lot about life and strengthened our commitment and determination to each other and to live life to the fullest.

Komal Chandra

October, 2016

Komal C. Shrivastava

RACD, BARC, Mumbai

TABLE OF CONTENTS

CHAPTER-2

CHAPTER-3

CHAPTER-4

CHAPTER-5

CHAPTER-6

Synopsis

Nuclear Energy is one of the prominent sources for electricity generation all over the world. Understanding the limitations of materials in nuclear reactor applications under prolonged periods is the key for realising optimal safety and continuous operation of nuclear reactors. Behaviour and properties of materials may get affected over continuous severe and hostile operating conditions such as high temperature, neutron flux and exposure to radioactive decay products. One of the common concerns faced by material scientists is the material degradation due to which their performance is affected. Anticipated materials performance and their sustained behaviour is an important factor in designing any new reactor materials. Materials degradation can lead to increased maintenance, increased downtime, and increasedrisk. Understanding the long-term behaviour of materials in the reactor core, vessel, and many other subsystems is critical for safe, reliable, reactor operation.

The behaviour of hydrogen in metals and alloys has attracted considerable interest in various areas, particularly for understanding material degradation and energy conversion. The adverse effect of hydrogen on the mechanical properties of steel, zircaloy and other alloys has long been known and has prompted numerous studies of hydrogen pick up in metals and alloys aimed at understanding the processes leading to hydrogen embrittlement[1-3] Pressurized heavy water reactors (PHWRs) use zirconium and zirconium based alloys as clad and coolant tube material since its beginning [4]. Hydrogen ingress in the clad is not of concern since fuel, along with the clad, is replaced after attaining the maximum expected burn up. Since the coolant channel stays for maximum permissible time in the reactor, for economic reasons, it is essential to know Hydrogen equivalent (HEq) at regular time intervals, as the life of coolant channel is also dictated by the extent of hydride/deuteride formation [5,6]. The limiting solubility of hydrogen in zirconium at any temperature is called terminal solid solubility [7]. It is < 1 ppmw at room temperature and ~ 60 ppmw at 300°C.

Above the terminal solid solubility at a given temperature, zirconium hydride gets precipitated, which is brittle in nature. Though the initial hydrogen content in zircaloy is maintained at less than 5 ppm, these components later pickup hydrogen and deuterium during reactor operation. Therefore H_2 monitoring at regular time intervals is required as a part of ageing management of zirconium alloy components. Several methodologies like Differential Scanning Calorimetry (DSC) [8], Inert Gas Fusion (IGF) [9] etc. are available for the determination of hydrogen. However, if deuterium (isotope of hydrogen) also co-exists in the material, the determination of these isotopes individually becomes all the more difficult. Nuclear techniques [10,11,12] like Nuclear reaction analysis (NRA), Energy recoil detection (ERD) analysis are non-destructive and by far the most sensitive of all the methods available for hydrogen/deuterium determination, though, the requirement of accelerators or other ion beam sources is not always possible to realize. Hot Vacuum Extraction cum Quadrupole Mass Spectrometry (HVE-QMS) technique to determine hydrogen and deuterium is routinely employed for the determination of hydrogen and deuterium in metals and alloys. Hot vacuum extraction-mass spectrometry (HVE-MS) provides information on the concentration of hydrogen and deuterium simultaneously and has been used in the study of hydrogen and deuterium diffusion in Zr–2.5%Nb pressure tubes.

The steps in current uranium reprocessing include the following: dissolution of uranium materials in nitric acid, purification by solvent extraction, recovery of uranyl nitrate, denitration to give UO_3 with release of NO_x, and subsequent reduction to UO_2 under a hydrogen atmosphere at 500 °C. The UO_2 is converted to UF_4 by reaction with HF and reduced to metal with calcium. Direct low-temperature reduction of uranyl to give UO_2 as a precipitated product represents an attractive alternative for minimizing waste, eliminating NO_x generation, and avoiding the potentially hazardous hydrogen reduction step. The key step in uranium processing is conversion of U(VI) to U(IV). In general, formic acid with or without hydrazine is used for catalytic reduction of U(VI) to U(IV). However, the redox decomposition of formic acid in the presence Pdnanocatalyst (NC) occurs under similar condition resulting to formation of hydrogen. The catalytic activity for hydrogen production from formic has been found to enhance by alloy or core shell Ag-Pd NCs, addition of $CeO_2(H_2O)_x$ or hosting Pd NC in the $-N(CH_3)_2$ functional groups bearing macroreticular resin beads. Formic acid has been also used for the Pd NC catalyzed reduction of $Cr_2O_7^{2-}/CrO_4^{2-}$ anions to Cr^{3+} ions for remediation in a less toxic form. However, it has been reported that the reduction of UO_2^{2+} ions with formic acid requires initiation with another reducing agent hydrazine. Formic Acid has also been used for the catalytic reduction of Np(VI, V). It is interesting to note that Pd is not only a good catalyst but also has good hydrogen storage properties metal and stores hydrogen under ambient conditions. It is mentioned that the hydrogen storage properties of Pd nanoparticles vary depending on the particle sizes and the stabilizers.

Total gas content and its composition are important specifications for sintered nuclear fuel pellets particularly in the case of fast breeder reactor fuels [13,14]. During the manufacture of high purity metals and alloys, permanent gases like hydrogen and nitrogen are trapped in the interstitial spaces and cumulatively they are referred to as the Total Gas content [15]. In the case of the nuclear fuels, the total gas content is defined as the amount of non-condensable gases (converted to STP) released when the pellet is heated under vacuum at required temperature and time. Total Gas content and its composition is determined by hot vacuum extraction-quadrupole mass spectrometry (HVE-QMS). This is an important specification for nuclear fuel materials and is applied not only to fuel in the core but also in the blanket materials e.g. deeply depleted uranium oxide ($DDUO_2$) in prototype fast breeder reactor (PFBR). The excess pressure of the total gas that builds up during reactor operation alter the thermal conductivity of the cover gas, pressurize the clad, react with the clad and damage it. It may be noted that not only the information on the total gas content is required; it is also desirable to have the information on individual gas components in the total gas to properly understand their origin. Generally hydrogen (H_2), methane (CH_4), nitrogen (N_2), carbon monoxide (CO) and carbon dioxide (CO_2) are present in the gases released from the nuclear fuel pellets. The source for these gases in fuel pellets may be due to entrapment of gases during fabrication, sintering and also reaction products expected during these operations. Development of suitable analytical methodology is therefore desirable.

Thus there is lot of scope to extend the investigations in all three areas identified above, namely hydrogen/deuterium ingress, total gas content and hydrogen storage.

The work described in this thesis is divided into Seven Chapters.

CHAPTER ONE

Introduction

This chapter deals with India's three-stage nuclear power program [4], different types of Indian Nuclear Reactors specifically PHWRs and FBTR. All the three areas of investigation are briefly introduced in this chapter. Major reactor components like, Calandria tubes, Pressure tube, Fuel, Blanket etc. are described in brief. The effect of H_2/D_2 in Zr-2.5%Nb pressure tube and its importance is discussed in detail. Information on the chemical aspects of zirconium and zirconium based alloys [4], mechanistic principles of hydrogen/deuterium ingress into the pressure tubes during reactor service, and the deleterious effects of this ingress [5,6], identification of suitable analytical methodologies for precise and accurate determination of hydrogen/ deuterium (in wafer thin sliver samples carved out from the insides of pressure tubes in-situ without causing any structural damage) have been provided in this chapter.For the second stage of Indian nuclear energy programmei,e. prototype fast breeder reactor (PFBR), Deeply depleted uranium dioxide ($DDUO_2$) has been proposed as the blanket material. Total gas content and its composition are important specifications for sintered nuclear fuel pellets particularly in the case of fast breeder reactor fuels [13,14]. A brief description about total gas determination in DDUO$_2$ pellets has also been provided in this chapter.

The production of U^{4+} ions is required for various applications in the nuclear industries such as stripping of Pu^{4+} ions in PUREX process using U^{4+} as reductant without contaminating feed, preparation of UO$_2$ particles and UF$_4$, and so on. In general, the reduction of UO$_2^{2+}$ ions to U^{4+} ions by electrocatalytic, photocatalytic, sonolysis, and chemical reductions have been reported. In the chemical reductions, hydrazine and/or formic acids have been used with Pt/Pd catalysts in aqueous solutions having different acids such as HNO$_3$ and H$_2$SO$_4$. Hydrazine also prevents back oxidation by scavenging HNO$_2$ formed by the decomposition of HNO$_3$. It has been reported that the reduction of UO$_2^{2+}$ ions with formic acid requires initiation with another reducing agent hydrazine. Formic Acid has also been used for the catalytic reduction of Np(VI,V). However, the key issue of U(VI) reduction under mild conditions is reusability and easy retrieval of Pdnanocatalysts. Also, nanoparticles have the potential to show exotic hydrogen absorption properties, giving us many possibilities for discovering new kinds of storage media. Palladium (Pd) is a classical hydrogen-storage metal and shows exceptional features for practical use; for example, Pd absorbs hydrogen at ambient temperature and pressure. Many studies on hydrogen storage in Pd nanoparticles have been published, and several characteristics were ascertained [26,27]. Therefore, a brief review of hydrogen storage properties of Pd nanoparticles and nano-alloy has been given in this chapter.

CHAPTER TWO

Instrumental Techniques and Experimental Methods

This chapter deals with description of analytical techniques used for (i) investigating hydrogen/deuterium ingress, (ii) determination of total gas content in deeply depleted uranium dioxide, and (iii) chemical analysis by Gas determinators and Inductively Coupled Plasma-Atomic Emission Spectroscopy (ICP-AES) and physical characterisation by X-ray diffraction and transmission electron microscope techniques were employed for studying Pd nanoparticles hosted on Fe_3O_4 and SiO_2.

The Hot Vacuum Extraction - Quadrupole Mass Spectrometry (HVE-QMS) instrument is based on the extraction of gases from an inorganic sample (at 1273K temperature) under vacuum condition followed by quantitative determination of the gases. The HVE-QMS instrument consists of different components like Quadrupole Mass Spectrometer, Pumps, Capacitance Manometer, resistance furnace etc. In this chapter the working principle of all these components are discussed in detail.

Total Gas Analyser (TGA) is another HVE-QMS system. The major differences between Total Gas Analyser and a simple HVE-QMS system are- (i) In HVE-QMS maximum attainable temperature is 1200<C while in Total Gas Analyzer, the maximum temperature that can be achieved is 1670<C (ii) Nuclear core components like nuclear fuel, blanket pellet etc. being ±-active samples cannot be handled in HVE-QMS system but TGA can be used for their analyses as a Glove Box comes integrated with the TGA. The heating of samples in HVE-QMS is carried out inside the Glove box.

The samples taken from an inactive Zr-2.5%Nb pressure tube supplied from NFC Hyderabad were charged with hydrogen/deuterium using electrolytic charging and hence this charging method has been discussed in this chapter. Carbon and Nitrogen content in Palladium nanoparticles on Fe_3O_4 support was identified using Carbon & Nitrogen determinators and the loading capacity of Pd on Fe_3O_4 was measured by ICP-AES. This Chapter elaborates the theory, principle and instrumentation part of Carbon Determinater, Nitrogen Determinator and ICP-AES. In the characterization of formed nanoparticles, X-ray Diffraction (XRD) analysis and High Resolution Transmission Electron Microscopy (HRTEM) were also employed. So, a brief description about XRD and HRTEM has also been included. Sieverts apparatus was used for Hydrogen sorption on Pd nanoparticles and hence this chapter also contains brief information about Sieverts apparatus.

CHAPTER THREE

Determination of Deuterium pick-up in Zr-Nb alloy by Hot Vacuum Extraction - Quadrupole Mass Spectrometry

In pressurized heavy water reactors (PHWRs) zirconium-niobium alloy pressure tubes (also called coolant channels) are used with D_2O as the primary heat transport fluid. Due to continuous usage of the pressure tubes inside the reactor, heavy ingress of hydrogen/deuterium into the pressure tubes could occur resulting in hydrogen (or deuterium) embrittlement. Ageing management of pressure tube therefore requires the quantification of the deuterium pick-up rate, so that the remedial measures can be taken for the smooth operation of the reactor. Deuterium pick-up in Zr-Nb alloy was determined using hot vacuum extraction-quadrupole mass spectrometry (HVE-QMS) technique. Experimental conditions like temperature, time of extraction of liberated gases, and measurement methodology were optimized for obtaining desired result. Deuterium content (µg/g) of a Zr-Nb coolant channel at different distances from inlet end was determined and the precision of the methodology was found to be around 10%. Whereas enough literature is available on the determination of hydrogen or deuterium content in H/D charged zirconium samples [15,16, 17]. This work has been carried out on actual irradiated Zr-Nb coolant channel sample. A very large mass difference between hydrogen isotopes (a factor of 2 between H_2 and D_2) brings in significant mass discrimination during measurements which need to be taken into consideration for quantification of analytical results. Thus, Sensitivity factor of H_2, HD, D_2 gases in the quadrupole mass spectrometer were determined for the quantification of the analytical results. Also, detailed studies were carried out on the formation of hydrogen (or deuterium) molecular ion H_3^+ (D_3^+) in QMS as a function of pressure in the measurement system and its possible effect on the results.

CHAPTER FOUR

Determination of diffusion coefficients of Hydrogen and Deuterium in Zr-2.5%Nb pressure tube material using hot vacuum extraction-quadrupole mass spectrometry

This chapter deals with the determination of diffusion coefficients of Hydrogen and Deuterium in Zr-2.5%Nb pressure tube material. Although, extensive studies have been carried out in the past on the diffusion of hydrogen /deuterium in zirconium and its alloys [10,19,20,21,22] , but to the best of our knowledge no information is available in the literature about determination of diffusion coefficients of both H and D in Zr–2.5%Nb alloy in a single laboratory or employing the same methodology. It has also been reported that the solubility of hydrogen in zirconium and its alloys depends on the thermal treatment of the material and this could be one of the reasons for the variation in literature data. In view of this, it was decided to carry out the study of the diffusion of hydrogen and deuterium in Zr-2.5% Nb samples with the same thermal treatment and by the same method i.e. HVE-QMS. The diffusion coefficients of hydrogen and deuterium in the Zr-2.5%Nb alloy were measured in the temperature range of 523 to 673 K. One end of the Zr-2.5% Nb alloy specimens was charged electrolytically with the desired hydrogen isotope. After annealing at different temperature for a predetermined time, the specimens were cut into thin slices, which were analysed for their H_2/D_2 content using the HVE-QMS technique. The depth profile data were fitted into the equation representing the solution of Fick's second law of diffusion. The activation energy of hydrogen/deuterium diffusion was obtained from the Arrhenius relation between the diffusion coefficient and temperature. The temperature dependent diffusion coefficient can be represented as D_{H} = 1.41 x 10-7 exp (-36000/RT) and D_{D} = 6.16 x 10-8 exp (-35262/RT) for hydrogen and deuterium, respectively. Also, the Zr-2.5% Nb tube microstructure consists of elongated ±-Zr grains surrounded by thin layer of ² -Zr and the diffusivity of hydrogen in ² -Zr is about two orders of magnitude higher than in ±-Zr [23, 24]. Measured diffusivity values for hydrogen and deuterium at two temperatures were compared with literature [25] and the values were found out to be almost half of the reported values. There are minor differences in the fabrication route of Zr-2.5%Nb pressure tubes used in Indian PHWRs [24] and CANDU reactors [25]. These differences in the fabrication route can vary the micro-structural features of the PTs and this might be the reason for the observed difference in diffusivity values.

CHAPTER FIVE

Palladium Nanoparticles Hosted on Hydrazine-grafted Magnetite and Silica Particles for Catalyzing the Reduction of Oxymetal Ions with Formic Acid and for Hydrogen sorption

This chapter deals with the formation of the Pd nanoparticles anchored on Fe_3O_4 and SiO_2 particles using a new synthetic route, characterization of thus formed Pd NPs that also includes their hydrogen sorption properties because this may deactivate the catalytic propertied of Pd NCs , and finally reduction of UO_2^{2+} and $Cr_2O_7^{2-}/CrO_4^{2-}$ ions by formic acids was studied. The choice of Fe_3O_4 as a host matrix is based on the fact that nano-size Fe_3O_4 particles have superparamagnetic properties i.e. the particles are magnetized at low field but get de-magnetized if the field is cut off. In general, Pd nanoparticles in solid substrates are formed either by reduction in solution and subsequent nucleation/growth on the solid matrix or by loading Pd^{2+} ions via ion-exchange mechanism on solid matrix and subsequent reduction with a suitable reagent. Contrary to the above methods, in the present work, the reducing agent has been anchored on Fe_3O_4 by reacting hydrazine with (3-glycidyloxypropyl) trimethoxysilane coated Fe_3O_4. Thus, reduction of Pd^{2+} ions to Pd^0, nucleation and growth of the Pd nanoparticles takes place on the surface of the Fe_3O_4. The formed material was characterized by elemental (C,N) analysis, XPS, XRD and HRTEM. By following the same procedure, $SiO_2$was modified by covalently attaching the reducing agent (hydrazine) and then anchoring Pd nanoparticles on it. The Pd content loaded on Fe_3O_4 and SiO_2 particles was obtained by ICP-AES analyses. The Pd nanoparticles loaded Fe_3O_4 and SiO_2 has also been characterized for their hydrogen sorption properties, as Pd nanoparticles also catalyses redox decomposition of formic acid, used as reductant, for hydrogen production [28]. Finally, the Fe_3O_4@Pd and SiO_2@Pd synthesized in the present work has been applied for the quantitative reduction of U(VI) to U(IV) with formic acid at 50°C using. The Cr(VI) reduction was also carried to study the general application of Fe_3O_4@Pd and SiO_2@Pd as a redox catalyst. Also, Cr(VI) reduction is important for its remediation in the less toxic form Cr(III).

CHAPTER SIX

Determination of total gas content and its composition in Indian PFBR blanket pellets

This chapter discusses the determination of total gas content and its composition in Indian, PFBR blanket pellets. Total gas content and its composition are important specifications for sintered nuclear fuel pellets particularly in the case of fast breeder reactor fuels. Total gas content and its composition were determined by hot vacuum extraction-quadrupole mass spectrometry (HVE-QMS). A number of parameters in this methodology such as temperature, duration of heating for quantitative extraction of evolved gases, total volume of the system, gas analysis conditions etc. were optimized for reliable measurements. In addition, sensitivity factors for various gases like H_2, CH_4, N_2, CO, O_2 and CO_2 in quadrupole mass spectrometry required for quantification of results have also been determined and validated employing reference gas mixtures of known composition. Cracking pattern of gases CH_4, N_2, CO, and CO_2 was also determined at all pressure from the mass spectral intensities monitored during sensitivity factor determination. Cracking pattern of gases was used in determining their composition. The peak intensities of the parent peaks of hydrogen (2), methane (16), carbon monoxide (28), nitrogen (28), Oxygen (32) and carbon dioxide (44) were corrected for sensitivity. The sensitivity corrected peak intensity is directly proportional to the partial pressure of the gas and hence its mole fraction, the composition of the species (i) is given as

$$X_i = \frac{(\text{Peak Intensity})_i}{\sum(\text{Peak Intensity})_i}$$

where Xi is the mole fraction of the species i.

Employing these optimized conditions total gas content and its composition in blanket pellets (uranium oxide pellets) of Indian prototype fast breeder reactor was determined employing HVE-QMS. The relative expanded uncertainty (at a coverage factor k=2) in the measurement of total gas content excluding hydrogen was estimated as per ISO guidelines and it was found to be 9.2 %.

CHAPTER SEVEN

Summary, conclusions and future scope

In this chapter, the summary and conclusions of the present investigations are given. Also, the possibility of the further studies has been discussed.

The important highlights of the thesis are:

[1] Determination of deuterium pickup in actual irradiated Zr-Nb coolant channel sample was carried out. Sensitivity factors for hydrogen isotopes were determined for the quantification of analytical results.

[2] Studies were carried out on the formation of hydrogen (or deuterium) molecular ion H_3^+ (D_3^+) in QMS as a function of pressure in the HVE-QMS measurement system. It was observed that the molecular ions formation is negligible at system pressures less than 10 Pa.

[3] Diffusion coefficient of hydrogen and deuterium in Zr-2.5%Nb was determined with the sample having same thermal treatment and by the same method i.e. HVE-QMS. The temperature dependent diffusion coefficient can be represented as $D_H = 1.41 \times 10^{-7}\exp(-36{,}000/RT)$ and $D_D = 6.16 \times 10^{-8}\exp(-35{,}262/RT)$ for hydrogen and deuterium, respectively.

[4] A novel method was developed for the synthesis of Pd nanoparticles anchored on the Fe_3O_4 and SiO_2 particles.

[5] Fe_3O_4@Pd and SiO_2@Pd nanoparticles were used as a catalyst for reduction of U(VI) to U(IV) by formic acid.

[6] Employing optimized conditions total gas content and its composition in blanket pellets (uranium oxide pellets) of Indian prototype fast breeder reactor was determined by TGA system.

References

1. J. P. Hirth, Metall. Trans. 11A (1980) 861.
2. R. A. Oriani, Annu. Rev. Mater. Sci. 8 (1978) 327.
3. H. K. Birnbaum, Proceedings of the 1st International Conference on Environ ment-Induced Cracking of Metals , NACE, Houston, Texas, 1990, p. 21.
4. Gopalakrishnan, Ann. Rev. Energy Environ. 27 (2002) 395.
5. N. Saibaba, BRNS Theme Meeting on Assessment of Hydrogen Damage in PHWR Pressure Tubes, June 28 and 29, 2007, BARC, Mumbai.
6. R.N. Singh, R. Kishore, S. Banerjee, P. Stahle and C. Bjerken, Canadian Nuclear Society - 13th International Conference on Environmental Degradation of Materials in Nuclear Power Systems 2007 Vol. 2, 2007, Page 1139.
7. L. Lanzani and M. Ruch, J. of Nucl. Mater. 324 (2004) 165.
8. D. Khatamian, V.C.Ling, J. Alloys Compd. 253 (1997) 162-166.
9. Ramakumar, K. L., Y. S. Sayi, P. S. Shankaran, G. C. Chhapru, C. S. Yadav, and V. Venugopal, Indian J. Chem. Techn. 11 (2004) 865-868.
10. T. Laursen, M. Leger and J.L. Whitton, J. Nucl. Mater. 158 (1988) 49-56.
11. T. Laursen , M. Leger, Xin-Pei Ma, J.D. MacArther, G.R. Palmer, J.L.Whitton, J. Nucl. Mater. 165 (1989) 156-163.
12. D. Khatamian, J. Alloys Compd. 253-254 (1997) 471-474.
13. M.V. Ramaniah, Analytical chemistry of fast reactor fuels- A review, Pure and Appl. Chem. 54 (1982) 889.

14. C. Ganguly, R.N. Jayaraj, Characterization and quality control of nuclear fuels, Allied publishers: New Delhi (2002).
15. Sayi YS, Yadav CS, Shankaran PS, Chhappru GC, Indian J Chem Tech 11 (2004) 648–653.
16. G. L.Powell, J. B. Condon, Anal. Chem. 45 (1973) 2349–2354.
17. J.G.V.Raaphorst, A. Kout, F. Z. Anal. Chem. 291 (1978) 324–327.
18. Y. S. Sayi, K. L. Ramakumar, R. Prasad, C. S. Yadav, P. S. Shankaran, G. C. Chhapru, H. C. Jain, J. Radioanal. Nucl. Chem. 230 (1998) 5–9.
19. E.A. Gulbransen, K.F.Andrew, J.Electrochemical Society 101 (1954) 560-566.
20. A. Sawatzky, J. Nucl. Mater. 2 (1960) 62-68.
21. A. Sawatzky, J. Nucl. Mater. 2 (1960) 321-328.
22. J. J. Kearns, J. of Nucl. Mater. 43 (1972) 330-338.
23. A. Sawatzky and C.E. Ells, “Understanding Hydrogen in Zirconium” Zirconium in the Nuclear Industry: 12th International Symposium ASTM, STP 1354 , 32-50.
24. D. Srivastava, G. K. Dey, S. Banerjee, Metall. Trans. 26A (1995) 270-277.
25. D. Khatamian, J. Alloys Compd. 580 (2013) 558-562.
26. Miho Yamauchi, Hirokazu Kobayashi, Hiroshi Kitagawa, ChemPhysChem 10 (2009) 2566 – 2576.
27. Miho Yamauchi, Ryuichi Ikeda, Hiroshi Kitagawa, Masaki Takata, J. Phys. Chem. C 112 (2008) 3294-3299.
28. K. Mori, M. Dojo, H. Yamashita, ACS Catal. 3 (2013) 1114-1119.

LIST OF FIGURES

LIST OF TABLES

Chapter - 1

Introduction

Description of Present Investigation

1.1. Introduction

Energy is one of the most fundamental parts of our universe. Energy has come to be known as a `strategic commodity' and any uncertainty about its supply can threaten the functioning of the economy, particularly in developing economies. India has the world's second largest population of 1.24 billion in 2011 second only after China. The energy consumption in India is the fourth biggest after China, USA and Russia. Due to rapid economic expansion, India has one of the world's fastest growing energy markets and is expected to be the second-largest contributor to the increase in global energy demand by 2035, accounting for 18% of the rise in global energy consumption [1]. Given India's growing energy demands and limited domestic fossil fuel reserves, the country has ambitious plans to expand its energy production base, both conventional, nuclear and renewable sources. The Integrated Energy Policy (IEP) formulated by Government of India is the first comprehensive energy policy and oversees all energy sectors and addresses all aspects of energy use and supply including energy security, access, availability, affordability and pricing, as well as efficiency and environmental concerns [2]. One interesting aspect and philosophy of IEP is that it linked energy security with energy access, saying “India cannot be energy secure if her people remain without secure supply for lifeline needs.” The energy mix is the snapshot of a country's dependency on each energy source and provides a good indication of a country's energy challenges.

1.2.Option of nuclear power

According to experts, in India where low grade coal is used to generate thermal power, generation costs are now quite high and in the long term the cost of generating atomic energy will be lower and cheaper than coal. In addition, the fight against global warming is viewed as an argument in favor of nuclear power. The rapid growth and expansion of economies across the world has made it imperative that there are sources for meeting the increasing demands for power and electricity. The requirement for nuclear power in developing countries like India was also articulated by Yukiya Amano, Director General, International Atomic Energy Agency (IAEA), while delivering the Indian Nuclear Society Silver Jubilee lecture in Mumbai on March 12, 2013. Amano said "Nuclear power can help to improve energy security. For rapidly developing economy such as India, it (nuclear energy) can make a vitally important contribution to growth". Besides, nuclear power can also reduce the impact of volatile fossil fuel prices and mitigate the effects of climate change, he added. India's per capita electricity consumption is expected to double by 2020, with 6.3 per cent annual growth, to about 1700 TWh. It is expected to reach 8000 TWh/yr by 2050, ten times as much as today. Hence there is an acute demand for more and more reliable power supplies. This energy mix option recommended by the IEP document envisages increasing the contribution of nuclear power to overall electricity generation capacity building on the flourishing and largely indigenous nuclear power programme. This contribution is expected to have 14.6 GWe nuclear capacity by 2024 and 63 GWe by 2032 thus aiming at 25% of electricity from nuclear power by 2050.

1.3. Three Stage Nuclear Power programme

Even though the international civil nuclear cooperation facilitates import of nuclear power plants from other countries, the pressurised heavy water reactors (PHWRs) that India has been constructing for more than 40 years continue to be the work horses. Use of heavy water reactors has been particularly attractive for the nation because it allows Uranium to be burnt with little to no enrichment requirements. Further, India has also carried out extensive investigations on the development of a Thorium centred fuel cycle. While Uranium deposits in the nation are extremely limited, there are abundant reserves of Thorium. Due to the limited uranium resources and vast thorium resources, right at the inception of atomic energy programme in the country, Dr. Homi Jahangir Bhabha, the founder of atomic energy programme in India envisioned three stages of the Indian Nuclear Power programme.

The formulation of the long term, three stage Indian nuclear $^{\text{programme}}$ was based on judicious utilization of domestic reserves of uranium and abundant reserves of thorium. The emphasis of the programme was on self-reliance, with thorium utilization as a long term objective. The three stages of the Indian nuclear power programme are [3]:

> Stage I: This stage envisages construction of natural uranium fuelled, heavy water moderated and cooled pressurized heavy water reactors (PHWRs). Spent fuel from these reactors is reprocessed to obtain plutonium.
>
> India selected PHWRs for Stage I of its nuclear power programme because (i) there is no need for enrichment, which is capital intensive, (ii) uranium requirement for the PHWR is the lowest, (iii) plutonium production, required for FBRs (planned for the second phase of the Indian nuclear power programme), is the highest and (iv) the infrastructure available in the country was suitable for undertaking the manufacture of equipment for the PHWRs.
>
> Stage II: This stage envisages construction of fast breeder reactors (FBRs) fuelled by plutonium produced in Stage I. These reactors would also breed 233U from thorium.
>
> Stage III: This stage would comprise power reactors using 233U/thorium as fuel.

India has successfully constructed PHWRs and a Fast Breeder Test Reactor (FBTR) and these are operating well. A Prototype Fast Breeder Reactor, PFBR is under commissioning at Kalpakkam.

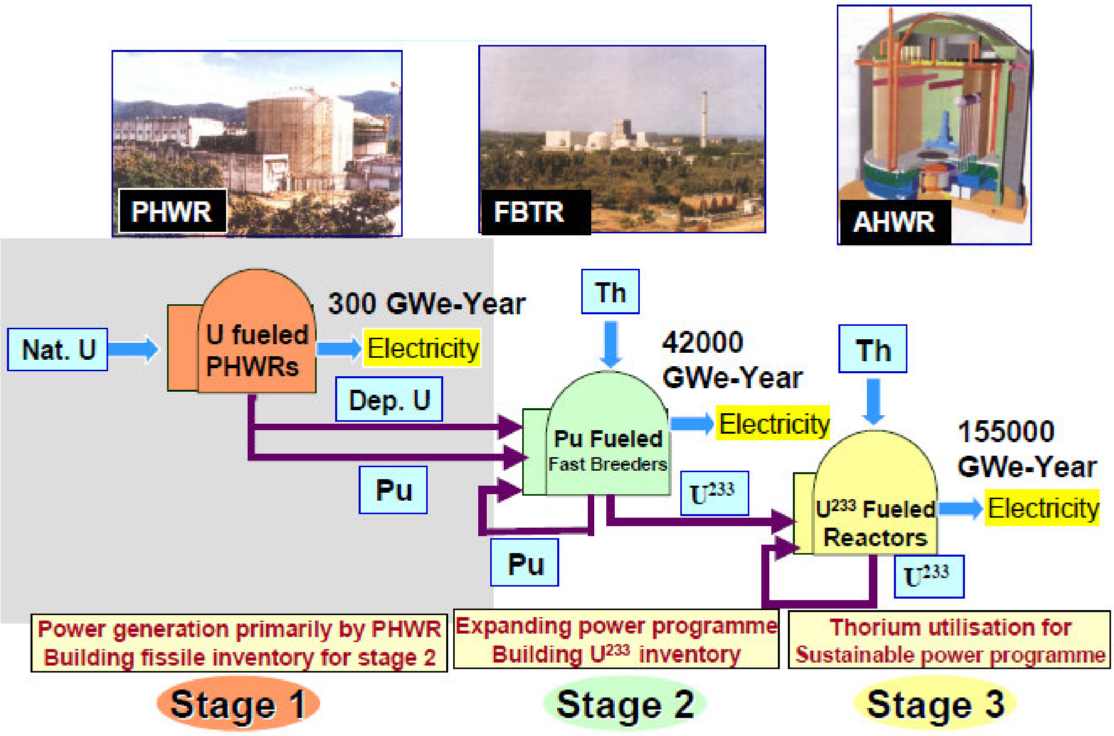

Figure 1.1. Three stage Indian Nuclear Power programme

With the expected commissioning of PFBR, India will be entering into the commercial phase of second stage of nuclear power programme. With advanced heavy water reactor planned in future with Th MOX fuel, the third stage of our nuclear power programme will be initiated. As mentioned earlier, major contribution to electricity generation from nuclear power is from PHWRs. With the anticipated construction of additional reactors, the PHWRs will continue to play major contributory role to our power programme.

1.4. Scope of present investigations

The present work mainly deals with three aspects of nuclear fuel cycle activities closely linked to our first and second stages of nuclear power programme. These are:

1. understanding the ingress of hydrogen and deuterium in zircaloy based materials used in PHWRs,

2. developing alternate methodologies for U(IV) production in reprocessing of spent fuel using Pd-based nanocatalysts loaded on Fe_3O_4 or SiO_2 host matrix and possible use of these nanoparticles for hydrogen storage, and
3. chemical quality control of fast reactor fuel materials especially total gas content.

The reasons for undertaking these investigations are given below:

1.4.1. Factors to be considered for sustained fail-safe operation of PHWRs

In PHWR, natural uranium is used as a fuel and heavy water (deuterium oxide D_2O) as its coolant and moderator. The heavy-water coolant is kept under pressure, allowing it to be heated to higher temperatures. While heavy water is significantly more expensive than ordinary light water, it yields greatly enhanced neutron economy, allowing the reactor to operate without fuel-enrichment facilities. PHWRs employ large number of horizontal fuel channel assemblies (> 300) (coolant channels), each surrounded by heavy water moderator within the calandria vessel. These pressure tubes / coolant channels (Zicaloy-2, Zircaloy-4, Zr-2.5%Nb) are supported at its ends by the calandria tube. Schematic of pressure tubes and calandria configuration is shown in Figure 1.2.The dimensions of the Indian PHWR (220 MW) Coolant Channels are 5.2 m long x 83 mm inner diameter with 4 – 5 mm thickness. Inside these channels a string of 12 fuel bundles each containing 19 fuel pins, through which pressurized heavy water passes, are located. The inlet and outlet temperatures of coolant are ~290°C and ~315°C respectively. The pH value of the coolant is maintained >7 by adding LiOD to minimise corrosion rate and also prevent peeling of oxide layer [6]. The pressure tube is rolled at each end into the hub of a stainless steel end fittings. This is connected to feeder pipes through couplings. The assembly is supported to the calandria by end fitting bearings and spacers called garter springs. The annulus between the calandria tube and the pressure tube is filled with carbon dioxide.

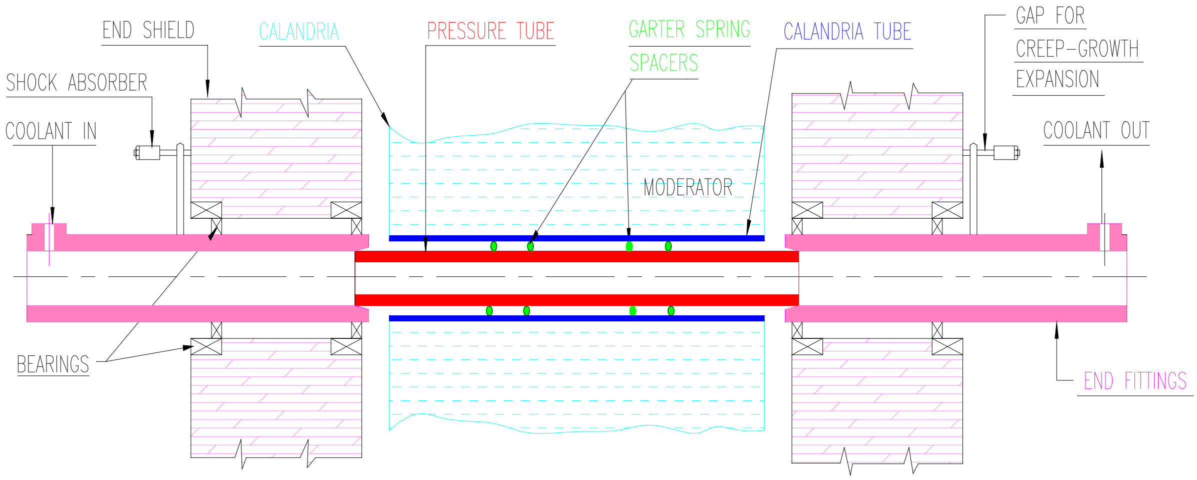

Figure 1.2.Schematic of PHWR Coolant Channel [4,5]

Mostof Failures in pressure tubes in the history of CANDU type PHWRs have hydrogen ingress as the root cause. Some examples are delayed hydrogen cracking at rolled joints and blister formation at cold spots, cracking of series of blisters and sudden rupture of pressure tubes. A 1983 pressure tube rupture event in Pickering Unit 2 led to the recognition of deuterium ingress into pressure tube material (hydriding) and the importance of avoiding contact between calandria and pressure tubes [7].The pressure tube failure was caused by a combination of hydriding of the Zirconium-2 pressure tube and contact between the pressure tube and calandria that surrounds the pressure tube. This led to concentration of hydride at the cooler location of contact, blistering of the pressure tube, and the resulting failure. With a view to bringing more understanding of the hydrogen/deuterium ingress, it may be desirable to discuss this aspect in more detail.

1.4.1.1. Formation of ZrH

The limiting solubility of hydrogen in zirconium at any temperature is called terminal solid solubility. It is < 1 ppmw (part per million weight) at room temperature and ~ 60 ppmw at 573 K. At any given temperature, if the levels of hydrogen exceeds the terminal solubility, zirconium hydride gets precipitated. Owing to the unique configuration of PHWRs and also due to irradiation, restraint at the ends and fuel bundles load, the coolant channels sag in due course of time. If the garter springs are slightly dislocated from the original place, the pressure tube may come in physical contact with the calandria tube (PT-CT contact) leading to reduction in PT-CT gap in the vicinity of the PT-CT contact point. In the region of point of contact and lower PT-CT gap, the outside surface of the pressure tube will be at a relatively low temperature (cold spot) forming temperature gradient and resulting in migration of hydrogen to the cold spot. Hydrogen accumulation at this point may lead to zirconium hydride blister which grows and cracks [8].

1.4.1.2. Source of hydrogen/deuterium in the pressure tube

Zirconium alloy has low neutron absorption cross-section, good corrosion resistance in aqueous media, adequate high temperature strength and microstructural & irradiation stability [9-17]. Due to these reasons it is used for making core structural material in water cooled nuclear reactor (PHWR, CANDU, RBMK). Initial hydrogen content of the core component kept as low as possible during their manufacturing [18] but the pressure tube and clad components may pick – up the hydrogen/deuterium evolved during service from any of the following sources [19-22] -

1) The reaction of zirconium with coolant heavy water (contains ~2.5 % light water) released Hydrogen/Deuterium,

   $Zr + 2D_2O = ZrO_2 + 4D$

2) Hydrogen / Deuterium evolved during the radiolytic decomposition of heavy water coolant,

   $D_2O = D + OD$

3) Deuterium added as scavenger for nascent oxygen evolved during radiolytic decomposition

   $2OD = D_2O + O$

4) Deuterium/ hydrogen evolved during the corrosion reaction between the corecomponents and the moisture present in the annulus gas (CO_2, N_2) and

5) Moisture present in UO_2 pellet (for fuel tubes only).

1.4.1.3. Mechanism of hydrogen pick-up by the pressure tube

Normally intentionally coolant channels are covered with thin layer of oxide to minimize its hydride formation. Hydrogen can enter through the oxide film only if it is damaged or degraded. The corrosion reaction $Zr + D_2O \rightarrow ZrO_2 + 4D$ takes place inside the surface of the coolant channel. Deuterium combines to form D_2 gas and released in to the Coolant but small portion of released deuterium (2-10%) is absorbed by the Zirconium metal. Over a time, deuterium concentration increases to such a large amount that it causes damaging effects. Kuwae et al [23] suggested the following mechanism of transport of hydrogen through the oxide layer-

Water is dissociated on the surface of the metals during oxidation and O^{2-}ions are formed. These ions diffuse through the oxide film and reacts with zirconium at the metal-oxide interface producing electrons. Since ZrO_2 has low electrical conductivity, migration of protons takes place in preference to electrons. These protons form hydrogen atoms and then hydrogen gas at the metal-oxide interface. The oxide layer brakes when the pressure of hydrogen gas exceeds the mechanical strength of ZrO_2. Zirconium metal will then be exposed to hydrogen free radicals/ hydrogen atoms. They react and form zirconium hydride.

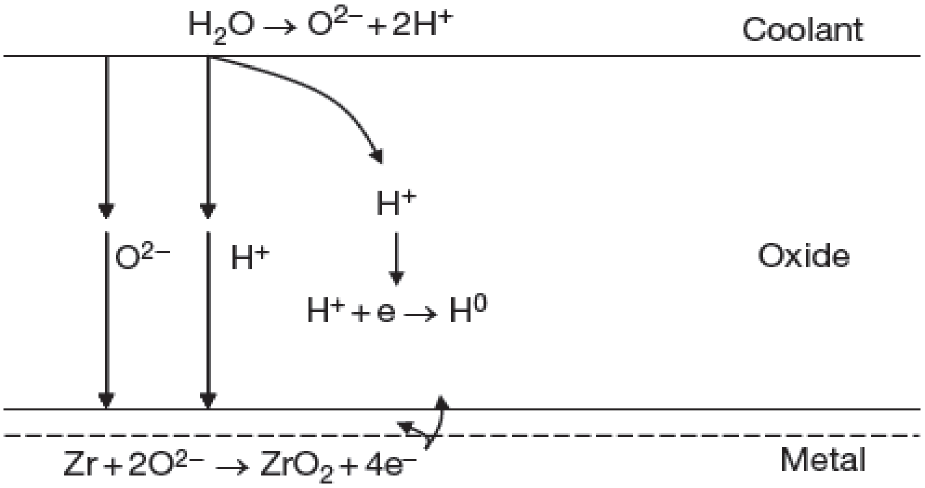

Figure 1.3. Schematic presentation of the corrosion of the zirconium alloys. (Corrosion of zirconium alloys in nuclear power plants; TECDOC-684; International Atomic Energy Agency, Vienna, Austria, Jan 1993.)

Thus, hydriding was identified as an important lifelimiting parameter of Zircaloy-2 pressure tubes and therefore required continuous monitoring.Lot of work has been carried out throughout the world in this respect. Zirconium alloy is used both as clad and coolant channel material. Hydrogen ingress in the clad is not of concern since fuel, along with the clad, is replaced after attaining the maximum expected burn up. Since the coolant channel stays for maximum permissible time in the reactor, for economic reasons, it is essential to know HEq at regular time intervals, as the life of coolant channel is also dictated by the extent of hydride/deuteride formation.

1.4.1.4. Hydrogen equivalent (Heq)

The metallurgical properties of zirconium matrix depend on the extent of the total hydrogen species present as zirconium hydride/deuteride, since effect of both hydrogen and deuterium in the Zr-H/D is same. Therefore it is convenient to express both hydrogen and deuterium as hydrogen equivalent (HEq). HEq is given as H + D/2 if both hydrogen and deuterium concentration was expressed in weight % (since the atomic weights of hydrogen and deuterium are 1 and 2 respectively).

From the above literature it is evident that understanding the limitations of materials in nuclear reactor applications under prolonged periods is the key for realising optimal safety and continuous operation of nuclear reactors. Behaviour and properties of materials may get affected over continuous severe and hostile operating conditions such as high temperature, neutron flux and exposure to radioactive decay products. Since the coolant channel stays for maximum permissible time in the reactor, for economic reasons, it is essential to know Hydrogen equivalent (HEq) at regular time intervals, as the life of coolant channel is also dictated by the extent of hydride/deuteride formation [24].Though the initial hydrogen content in zircaloy is maintained at less than 5 ppm, these components later pickup hydrogen and deuterium during reactor operation. Therefore H_2 monitoring at regular time intervals is required as a part of ageing management of zirconium alloy components.

1.4.1.5. Methodologies for the Determination of Hydrogen and Deuterium in zircaloy samples

The initial hydrogen content in zircaloy pressure tube is maintained less than 5 ppm during the manufacturing process. However, the pressure tube picks-up additional hydrogen and deuterium during reactor operation. Therefore monitoring of hydrogen/deuterium at regular time intervals is required as a part of ageing management of zirconium alloy components.

Techniques such as Differential Scanning Calorimetry (DSC), Inert Gas Fusion (IGF), nuclear techniques, Spark Source Mass Spectrometry (SSMS) and Hot Vacuum Extraction - Quadrupole Mass Spectrometry (HVE - QMS) [24]have been employed for the determination of hydrogen. Brief discussion about the methodology and pros and cons of each technique is given below.

1.4.1.5.1. Differential Scanning Calorimetry (DSC)

DSC is a non-destructive technique. It is based on the functional relationship between the hydride dissolution temperature and hydride content in the matrix. It is a well-established fact that the Terminal Solid Solubility for hydride Precipitation (TSSP) during cooling down is higher than the Terminal Solid Solubility during Dissolution (TSSD) when the specimen is heated. Moreover it has been observed that the TSSD values are very close to the thermodynamic equilibrium values. The reproducibility of the technique is good and the average values for different series agrees within the experimental error. The standard dispersions are low and variance analysis indicates that the values of TSSD and TSSP do not depend on the heating and cooling rates. As mentioned above, the determination of hydrogen by DSC depends on the heat of dissolution of zirconium hydride in the zirconium matrix. The solubility of hydrogen in zirconium depends on the temperature. The Terminal Solid Solubility (TSS) and the temperature are related by the Arhenius equation:

$$\mathbf{TSS = A\ e^{-Q/RT}}$$

The temperature at which zirconium hydride completely dissolves into solution is a measure of hydrogen content. The process of dissolution is monitored by DSC. In a typical analysis for the determination of TSS, known amount of sample is sandwiched in high purity tin cup and lid and similarly a reference is also prepared. Both sample and reference are placed over two identical metal pans of the DSC system. The pans are provided with independent thermocouples and heaters. The entire sample arrangement is flushed with dry and high purity argon gas. The temperature of both reference and sample are increased / decreased by uniform heat flow. During heating / cooling the sample may undergo physical or chemical changes. In the zirconium alloy samples, dissolution / precipitation of zirconium hydride in zirconium matrix takes place, which is an endothermic / exothermic reaction, resulting in cooling / heating in the sample. The temperature of both sample and reference are maintained same by the supported heaters electronically. A typical DSC curve between the heat flow and time is shown in Figure1.4.In this figure T_1corresponds to the terminal solid solubility in dissolution (TSSD), T_2 corresponds to the end of effect of phase transformation on heat flow [25]. The derivative of the DSC plot gives a point of inflexion corresponding to the complete dissolution / precipitation of zirconium hydride. This point (T_3) of inflexion is a measure of hydrogen content. A linear calibration curve is plotted between the inverse of T_3 and log [amount of hydrogen present in the sample] by analyzing several zirconium alloy samples containing known amount of hydrogen (hydrogen standards). The amount of hydrogen in the unknown sample is computed from the DSC run and the point of inflexion.

DSC has the added advantage of detecting only the hydride / deuteride. However the difference between the enthalpy of dissolution of zirconium hydride and zirconium deuteride is so small that DSC cannot distinguish between hydride and deuteride.

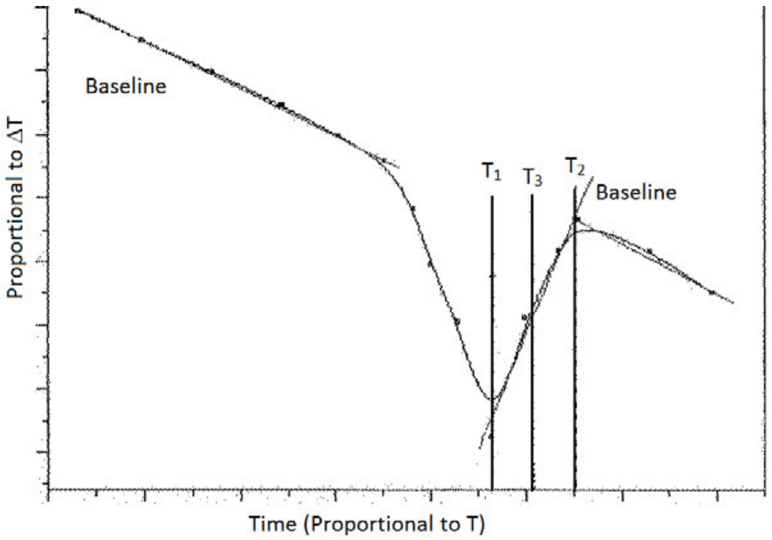

Figure 1.4. Typical DSC plot for determination of hydrogen in zirconium alloys

1.4.1.5.2. Inert Gas Fusion (IGF)

Inert Gas Fusion–Thermal Conductivity Detection (IGF–TCD) methodology involves fusion of the sample in a graphite crucible in presence of tin as flux, under flowing Nitrogen gas atmosphere at about 2273 K. Hydrogen, in whatsoever form, is released as H_2. Nitrogen and oxygen present in the sample, in all the forms, are released as N_2 and CO. Carbon monoxide is selectively oxidized to carbon dioxide at room temperature by Schutze reagent (I_2O_5). Caron dioxide is trapped by ascarite (NaOH) and anhydrone (anhydrous magnesium perchlorate). Hydrogen and nitrogen are separated by zeolite gas chromatography column. Hydrogen being the lighter gas comes out first and is detected by a thermal conductivity detector. Thermal conductivity cell has the ability to detect the difference in the thermal conductivity of the reference and measure gas. The advantage of IGF-TCD method is short time taken for analysis. This method has some disadvantage also like in this method at least 100 mg of sample is required and the isotopic information on hydrogen cannot be arrived at employing the above methodologies [26].

1.4.1.5.3. Nuclear techniques

Nuclear techniques are non-destructive and by far the most sensitive of all the methods available for hydrogen determination. Nuclear techniques have an added advantage that they are not dependent on the chemical nature / bond and matrix. Lanford [27] has published an excellent review on the analysis for hydrogen by nuclear reaction and energy recoil detection, in which the use of MeV ion beams to measure hydrogen concentration profiles have been reviewed. Generally nuclear techniques fall into two categories viz. nuclear reaction analysis (NRA) and energy recoil detection (ERD).

Nuclear reaction analysis (NRA)

In NRA, the sample containing hydrogen (target) is bombarded with high energy ions and the prompt gammas emitted in nuclear reaction are monitored by suitable detector. The most common representation of the nuclear reactions for hydrogen determination and signal detection are given below:

$$^{1}\mathrm{H} + {}^{19}\mathrm{F} \rightarrow {}^{4}\mathrm{He} + {}^{16}\mathrm{O} + \text{gamma ray (gamma ray monitoring)}$$

$$^{1}\mathrm{H} + {}^{15}\mathrm{N}^{4} \rightarrow \mathrm{He} + {}^{12}\mathrm{C} + \text{gamma ray (gammaray monitoring)}$$

$$^{1}\mathrm{H} + {}^{7}\mathrm{Li}^{4} \rightarrow \mathrm{He} + {}^{4}\mathrm{He} + \text{gamma ray (gamma ray monitoring / } {}^{4}\text{He monitoring)}$$

Deuterium content in zircaloy can also be determined by the following nuclear reaction [28]

$$\mathrm{D}\,({}^{3}\mathrm{He},p) \rightarrow {}^{4}\mathrm{He}$$

However, the requirement of accelerators or other ion beam sources required for NRA is difficult to realize.

Energy recoil detection (ERD)

Cohen and co-workers [29] described a method for hydrogen profiling in thick (~ 100 μm) foil. In this method the target was bombarded with protons (17 MeV) and the incident and recoil proton are detected by two detectors at ±45° to the beam direction in coincidence. For every proton detected on one detector which comes from an elastic scattering from hydrogen in the target there must be another proton detected in coincidence in the other detector. Thus, there must be two protons detected simultaneously in the two detectors. The depth profile depends on the total energy lost in the target. The energy detected in both detectors is summed. It is observed that the highest energy events comes from scattering at the back edge of the foil and the lowest energy events come from scattering at the front side. The advantage of this method is its high sensitivity and detection well below 1 ppm concentration. The disadvantage of this method is that it requires samples in form of film thin enough to transmit the protons. If the thickness is more, high energy protons are required to be employed.

1.4.1.5.4. Rutherford backscattering

Among the ion beam analytical techniques used, Rutherford backscattering spectrometry is the most versatile and widely employed one [30]. The methodology involves measurement of energy and yield of backscattered ions. The ratio of energy of the ion backscattered from the target atom to the incident beam energy is a function of the masses of projectile and the target. This technique is less sensitive to elements having low mass and more sensitive to elements with high mass. However, with certain limitations, this method can be employed for estimation of H/D content in Zr samples and their depth profile.

1.4.1.5.5. Spark Source Mass Spectrometry (SSMS)

The application of spark source mass spectrometry (SSMS) technique for the determination of hydrogen and deuterium present in the zircaloy samples, by two-level exposure technique has been successfully developed and demonstrated by Ramakumar et al.

[31]. SSMS with conventional photo plate detection system can be considered as an attractive solid sample analysis technique despite having some limitations. In the two-level exposure technique, the photo plate is exposed at two different magnetic field settings. One longitudinal half is exposed to cover the m/z values from 6 to 240 and the other half is exposed to cover the mass range from m/z 1 to 30 by varying the electronics accordingly. Hydrogen is determined with respect to an internal reference material (IRM) like nitrogen, carbon or even a multiply charged Zr^{+n} mass peak and the results for hydrogen and deuterium are computed. This two-level exposure technique has been successfully employed for the analysis of a failed zircaloy clad sample.

1.4.1.5.6. Hot Vacuum Extraction

Development and application of hot vacuum extraction methodology for hydrogen in zirconium alloys dates back to 1953 wherein Mc Geary [32] reported the determination of hydrogen in zircaloy. This technique has minimum blank and no other material is added to get the hydrogen released from the sample. Raaphorst and Kout [33] have first time employed vacuum extraction coupled with mass spectrometry for the determination of hydrogen and deuterium in zircaloy. The methodology involves heating the sample to 1000°C and extraction of gases released into known volume by ejector pump (sealed turbo molecular pump), measurement of the pressure showed by capacitance manometer and its composition by mass spectrometry. Both irradiated and un-irradiated zircaloy materials were analysed for their hydrogen and deuterium content.

Several methodologies like Differential Scanning Calorimetry (DSC) [25], Inert Gas Fusion (IGF) [27] etc. are available for the determination of hydrogen. However, if deuterium (isotope of hydrogen) also co-exists in the material, the determination of these isotopes individually becomes all the more difficult. Nuclear techniques [27] like Nuclear reaction analysis (NRA) [28], Energy recoil detection (ERD) [29] analysis are non-destructive and by far the most sensitive of all the methods available for hydrogen/deuterium determination, though, the requirement of accelerators or other ion beam sources is not always possible to realize. Hot Vacuum Extraction cum Quadrupole Mass Spectrometry (HVE-QMS) technique to determine hydrogen and deuterium is routinely employed for the determination of hydrogen and deuterium in metals and alloys. Hot vacuum extraction-mass spectrometry (HVE-MS) provides information on the concentration of hydrogen and deuterium simultaneously and has been used in the study of hydrogen and deuterium diffusion in Zr–2.5%Nb pressure tubes.

1.4.2. Pd-based nanocatalysts for U reduction at reprocessing stage and for hydrogen storage

The steps in current uranium reprocessing include the following: dissolution of uranium materials in nitric acid, purification by solvent extraction, recovery of uranyl nitrate, denitration to give UO_3 with release of NO_x, and subsequent reduction to UO_2 under a hydrogen atmosphere at 500°C. The UO_2 is converted to UF_4 by reaction with HF and reduced to metal with calcium. Direct low-temperature reduction of uranyl to give UO_2 as a precipitated product is an attractive alternative for minimising waste, eliminating NO_x generation, and avoiding the potentially hazardous hydrogen reduction step. The key step in uranium processing is conversion of U(VI) to U(IV). In general, formic acid with or without hydrazine is used for catalytic reduction of U(VI) to U(IV). The potential advantages of Pd nanocatalyst have been exploited in the redox decomposition of formic acid in the spent fuel reprocessing to directly produce U(IV). A new synthetic route for preparation of Pd nanoparticles anchored on Fe_3O_4 and SiO_2 particles has been proposed. In general, Pd nanoparticles in solid substrates are formed either by reduction in solution and subsequent nucleation/growth on the solid matrix or by loading Pd^{2+} ions via ion-exchange mechanism on solid matrix and subsequent reduction with a suitable reagent. In contrast to the above method, in the present work, the reducing agent has been anchored on Fe_3O_4 by reacting hydrazine with (3-glycidyloxypropyl) trimethoxy silane coated Fe_3O_4. Thus, reduction of Pd^{2+} ions to Pd^0, nucleation and growth of the Pd nanoparticles takes place on the surface of the Fe_3O_4. Finally, the Fe_3O_4@Pd and SiO_2@Pd synthesized in the present work has been applied for the quantitative reduction of U(VI) to U(IV) with formic acid at 50°C. The studies were also extended to investigate (a) Cr(VI) reduction to Cr(III) as an effective bioremediation and (b) hydrogen storage under ambient conditions as literature reports that the hydrogen storage properties of Pd nanoparticles vary depending on the particle sizes and the stabilizers.

1.4.3.Specification analysis for chemical quality control

Total gas content and its composition are important specifications for sintered nuclear fuel pellets particularly in the case of fast breeder reactor fuels [34-36, 51]. During the manufacture of high purity metals and alloys, permanent gases like hydrogen and nitrogen are trapped in the interstitial spaces and cumulatively they are referred to as the Total Gas content [51]. In the case of the nuclear fuels, the total gas content is defined as the amount of non-condensable gases (converted to STP) released when the pellet is heated under vacuum at required temperature and time. Total Gas content and its composition is determined by hot vacuum extraction-quadrupole mass spectrometry (HVE-QMS). This is an important specification for nuclear fuel materials and is applied not only to fuel in the core but also in the blanket materials e.g. deeply depleted uranium oxide ($DDUO_2$) in prototype fast breeder reactor (PFBR). The excess pressure of the total gas that builds up during reactor operation alters the thermal conductivity of the cover gas, pressurises the clad, reacts with the clad and damage it. It may be noted that not only the information on the total gas content is required; it is also desirable to have the information on individual gas components in the total gas to properly understand their origin. Generally hydrogen (H_2), methane (CH_4), nitrogen (N_2), carbon monoxide (CO) and carbon dioxide (CO_2) are present in the gases released from the nuclear fuel pellets. The source for these gases in fuel pellets may be due to entrapment of gases during fabrication, sintering and also reaction products expected during these operations. Development of suitable analytical methodology is therefore desirable.

Thus there is lot of scope to extend the investigations in all three areas identified above, namely hydrogen/deuterium ingress, total gas content and reprocessing. Systematic experiments carried out to realise the goals of the investigations are given in subsequent sections.

1.5. Hydrogen/Deuterium Charging on Zirconium Alloy

The method used for charging of hydrogen/deuterium on the Zirconium alloy was similar to that described by Singh et.al. [37]**.**For introducing controlled amount of hydrogen in Zr-alloys [38], gaseous hydrogen charging and electrolytic hydrogen charging techniques are generally used. In gaseous hydrogen charging technique, Zr-alloy samples are heated in hydrogen atmosphere either under constant pressure for different time-periods or in a constant volume system. In the first case i,e. constant hydrogen partial pressure system, time-period for which the sample is exposed determines the hydrogen concentration. While in the constant volume system, the average hydrogen concentration of the sample is estimated from the product of system volume and the difference between the initial and final partial hydrogen pressure of the system. In the gaseous hydrogen charging technique, the samples can be hydrided completely i.e. the amount of hydrogen charged is not limited to the terminal solid solubility of hydrogen in the alloy. In electrolytic hydrogen charging technique [39] an adequately thick and adherent layer of hydride is deposited over the sample. The sample with hydride layer is homogenized at a pre-determined temperature to attain equilibrium. After homogenization, the excess hydride layer is removed by machining. In this technique, the amount of hydrogen charged into the sample cannot exceed the TSS at the homogenization temperature.

1.5.1. Gaseous hydrogen charging

Metal when exposed to hydrogen gas can absorb certain amount of hydrogen in solution. The equation of dissolution of hydrogen gas in zirconium metal can be written as:

$$\mathbf{1/2\ H_2 \rightarrow H_{Zr}}$$

Where, H_{Zr} is the hydrogen dissolved in zirconium metal. The concentration of dissolved hydrogen is calculated by Sievert's law:

$$\mathbf{[H_{Zr}] = (p_{H2})^{1/2} \exp(-\Delta G^o/RT)}$$

Where, $\Delta G^o = \Delta H^o - T\Delta S^o$ is the standard free energy change of the reaction;

p_{H2} is the gas pressure,

R is the gas constant,

T is the temperature.

ΔH^o is a measure of the ability of the metal to absorb hydrogen.

The above Equationcan be rewritten as:

$$\mathbf{[H_M] = (p_{H2})^{1/2} \exp(\Delta S^o/R) \exp(-\Delta H^o/RT)}$$

The more negative ΔH^o is, the higher is the hydrogen solubility for a given external hydrogen pressure. Zirconium and titanium have been declared as exothermic hydrogen occluders [40] since ΔH^o is negative for them. The pressure composition isotherm at various temperatures is shown schematically in Figure 1.5 [40]

From the T_1 isotherm it can be seen that as hydrogen dissolves in the metal phase, the hydrogen pressure in equilibrium with this phase increases. When metal getssaturated at the terminal solid solubility (TSS) point, C_1, addition of more hydrogen to the system will cause the formation of hydride phase, at a fixed composition MHx. When more hydrogen is added the volume fraction of MHx increases until, at C_{hyd}, where all the metal gets converted to hydride. The hydrogen pressure remains constant over this plateau, as a consequence of phase rule. This dissociation pressure is a measure of the stability of the hydride phase. Additions in excess of C_{hyd} value causes the pressure to rise again as hydrogen is now taken into solution by the hydride.

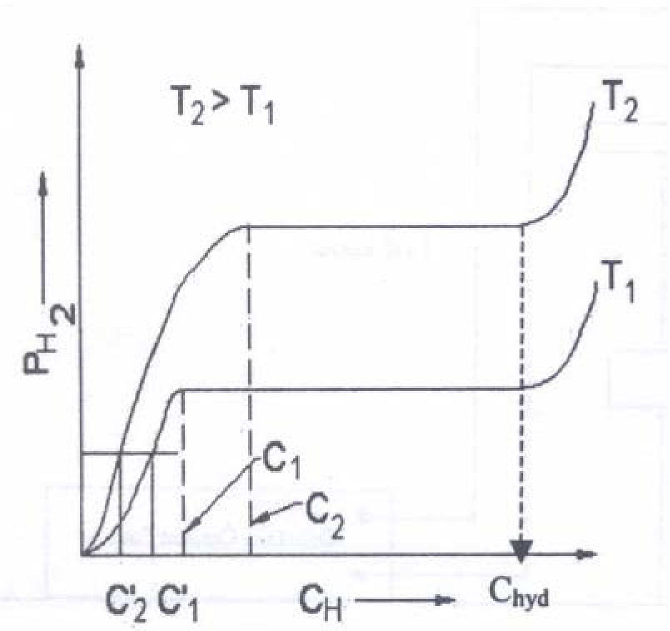

Figure 1.5. Typical pressure composition isotherm at various temperatures.

It can be seen that in the absence of hydride, the solubility of hydrogen, in equilibrium with hydride (TSS) increases with increasing temperature (endothermic); this is reflected by the increase in TSS from C_1 to C_2 as the temperature is increased from T_1 to T_2. In addition, it is important to mention that in a system where several hydride phases can occur, the pressure-composition curve shows several plateau. It can also be seen from Figure 1.5 that for a given partial pressure of hydrogen, solid solubility increases with decreasing temperature. The solid solubilities $C_2' < C_1'$ for $T_2 > T_1$, where Ci' are the solid solubility for the hydrogen for constant partial pressure of hydrogen P_{H2} at temperatures Ti respectively. This is a contamination free process and ensures uniformity of hydrogen / hydride distribution [38]. Traces of oxygen in the gaseous methods are to be avoided which otherwise leads to an oxide scale on the surface.

Construction: This system consists a hydrogen source, two glass chambers to hold the specimen, a vacuum pumping system, a capacitance-based manometer and a couple of resistance heated furnaces for heating the specimen and hydrogen source (pure Zirconium hydride) (as shown in Figure 1.6).

Working: The system is first evacuated to a dynamic vacuum of the order of 10^{-5}torr using an oil diffusion pump. The hydrogen source is then heated using the resistance heated furnace. Once the source temperature of 823 K is attained, the system is isolated and heating of source is continued. The amount of the hydrogen evolved is proportional to the pressure indicated by the capacitance-based manometer. Hydrogen is released up to a predetermined pressure depending upon the weight of the sample, the source tube is isolated and source heating is discontinued. The specimen chamber is subsequently heated to a temperature in the range of 623 to 673 K. Amount of the hydrogen picked up by the specimen, is indicated by the pressure in manometer. The amount of hydrogen picked up by the sample is computed from the difference between initial and final pressure readings recorded at ambient temperature.

Calculation

Estimation of internal volume of hydrogen charging system: Let the total internal volume of hydrogen charging system be *V*cc. The value of a part of system volume 'v' was estimated directly by measuring the volume of water required to fill it completely. With the help of diaphragm valves volume ‘v’ can be isolated from rest of the system. The total volume, *V,* of the system was estimated indirectly using Boyle’s law. The system was evacuated to a vacuum level of 10^{-5}torr. The part of system having volume ‘v’ was isolated from the pumping system and the remaining volume of the system. The hydrogen source tube is heated to release hydrogen to an initial pressure of *p*. After this the source tube is isolated and heating is discontinued and initial pressure reading is recorded. The valve isolating volume ‘v’ from the remaining volume of the system is opened and the gas is allowed to expand to a final pressure *P*. From the Boyle’s law, for a given amount of gas at a fixed temperature

$$pv = PV$$

For $p = 105.44$ torr, v = 647 cc and $P = 12.12$ torr, we have from

$$V = pv / P = 5629\text{cc}$$

Estimation of weight (ppm) of hydrogen absorbed by the specimen: Let the difference between the initial and final room temperature pressure readings be ” P torr, the total internal volume of the system be Vcc and the weight of the sample be W grams. Using gas laws, the number of moles of hydrogen absorbed by the sample is given by:

$$\mathrm{n} = \frac{\Delta \mathrm{P\,V}}{\mathrm{R\,T}} = \frac{\Delta \mathrm{P} \times 13.6 \times 981 \times 5629}{8.3144 \times 10^{8} \times 298} = 3.031 \times 10^{-4}\,\Delta \mathrm{P}$$

Weight of hydrogen absorbed by the sample will be

Hydrogen = 2n = 2 x 3.301 x $10^{-4}\Delta P$ grams

Hence the weight (ppm) of hydrogen is $[\mathrm{H}]_{\mathrm{Zr}} = \frac{3.031\times10^{-4}\,\Delta \mathrm{P}}{\mathrm{W}} \times 10^{6} = \frac{606.2\,\Delta \mathrm{P}}{\mathrm{W}}$ ppm

Thus, the average concentration of hydrogen picked up by the sample can be estimated with a reasonable accuracy knowing the weight of the sample and the difference between the initial and final hydrogen pressure.

Figure 1.6. Photograph of gaseous hydrogen charging facility

1.5.2. Electrolytic hydrogen charging

Sample preparation: A Zr-2.5%Nb coupon of dimension (12 x 4.6 x 60) mm is taken. 2mm thickness from one end is polished with 120, 400, 600, 800, and 1200 grit emery papers to prepare an oxide free surface. After grinding, the samples are pickled in a solution containing 5%HF + 45%HNO_3 + 50%H_2O for 1 minute to get a surface totally free of oxides having good surface finish. The samples are then thoroughly washed in distilled water. Subsequently the samples are cleaned ultrasonically in acetone for 15 minutes to remove any trace of grease and finally in methanol for 5 minutes to remove any residue of acetone.

Anode preparation: The anode is prepared from pure lead strips of 1mm thickness and imparting them the curvature of pressure tube, with the sample to curved anode distance, maintained at a predetermined distance. This ensures that the samples are hydrided uniformly on both the sides. The lead anodes are suspended into the electrolyte solution by riveting it to 3mm thick strip of pure lead. Prior to hydriding, the lead anodes are polished using 600 grit emery paper and subsequently ultrasonically cleaned in acetone for 5 minutes.

Electrolysis: 0.4N Sulphuric acid solution, prepared by diluting 22ml of sulphuric acid (S.G. 1.84) to two litres by adding distilled water, is used as an electrolyte for hydriding. Uniform bath temperature of 338±5 K is ensured by magnetic stirring throughout the campaign. The electrolyte bath needs to be covered on top with a Perspex sheet to avoid excessive loss of water due to evaporation. Few holes are drilled into the top cover, which helps in suspending the anode, sample and thermometer into the solution. The current is supplied to the samples with the help of stainless steel rod of 3 mm diameter, which can be screwed to the sample at one end. To prevent the immersed part of the steel rod from coming in direct contact with the solution, it is normally covered with Teflon tape. A constant current power supply is used to supply the requisite current needed for electrolytic hydrogen charging of the samples. A current density of 0.2 A/cm^2 is sufficient for this purpose. The required current to be supplied is calculated depending upon the area of the sample. The solution level is maintained by adding distilled water intermittently. The sample should be immediately dipped into the hot solution after ultrasonic cleaning so as to prevent the oxide film formation. The duration of electrolytic charging is varied according to the required hydride layer thickness which in turn is decided based on the target hydrogen concentration [39]. Electrolytically depositing the hydride layer on Zr-2.5% Nb alloy sample is shown in Figure 1.7.

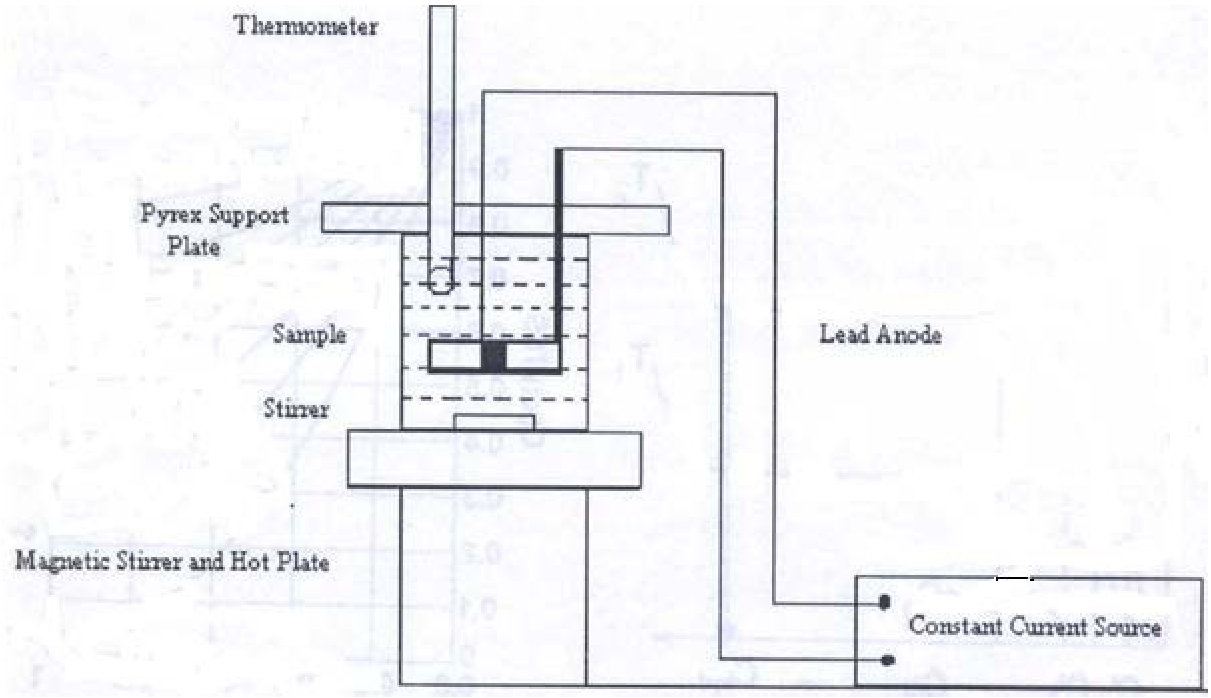

Figure 1.7. Electrolytically depositing the hydride layer on Zr-2.5% Nb alloy sample

1.6. Laws of Diffusion & Determination of diffusion coefficients

Diffusion- Diffusion is the process by which matter is transported from one to another part of the system as a result of random molecular motions. Diffusion is governed by Fick's laws.

Fick's first law - It states that the diffusion flux (amount of the substance per unit area per unit time) goes from the regions of high concentration to regions of low concentration, with a magnitude that is proportional to the concentration gradient.

$$\mathbf{J = -D\,\frac{\partial C}{\partial x}}$$

J = diffusion flux, of which the dimension is amount of substance per unit area per unit time, so it is expressed in such units as $\frac{\mathrm{mol}}{\mathrm{m^2 s}}$.

C = concentration of diffusing substance of which the dimension is amount of substance per unit volume. It might be expressed in units of $\frac{\mathrm{mol}}{\mathrm{m^3}}$.

x = space coordinate measured normal to the section the dimension of which is length. It might thus be expressed in the unit m

D = diffusion coefficient. Its dimension is area per unit time, so typical units for expressing it would be $\frac{\mathrm{m}^2}{\mathrm{sec}}$.

Fick's second law - Fick's second law predicts how diffusion causes the concentration to change with time.

$$\frac{\partial \mathbf{C}}{\partial \mathbf{t}} = \mathbf{D}\frac{\partial^2 \mathbf{C}}{\partial \mathbf{x}^2}$$

C = the concentration in dimensions of [(amount of substance) length^{-3}, example$\frac{\mathrm{mol}}{\mathrm{m}^3}$]

t = time [s]

x = length [m]

D = diffusion coefficient in dimensions of [length^2 time^{-1}, example $\frac{\mathrm{m}^2}{\mathrm{s}}$]

Determination of diffusion coefficients

Hydride/deuteride once formed on the zirconium alloy surface by the electrolytic chargingis annealed at different temperature so that diffusion of hydrogen/deuterium to the bulk of zirconium takes place. Thereafter, the diffusion coefficient of hydrogen/deuterium in zirconium alloy matrix can be found out. Fick’s second Law of diffusion has been used to determine Diffusion Coefficient of hydrogen/deuterium in Zr-2.5%Nb alloy.

1.7. General Aspect of Nanoparticles

Nanoparticles (or nanopowder or nanocluster or nanocrystal) are microscopic ensembles typically on the nanometer scale ranging from 1 and 100 nm. These are characterized by the unique nanoscale properties that originate from their highly reduced dimensions, and distinguish them from the bulk or individual particles. In the present work, Bottom-Up approach that is building the unit size of interest by assembling the building blocks (such as atoms or molecules) as shown in Figure 1.8was adopted to synthesise the Pd nanoparticles.

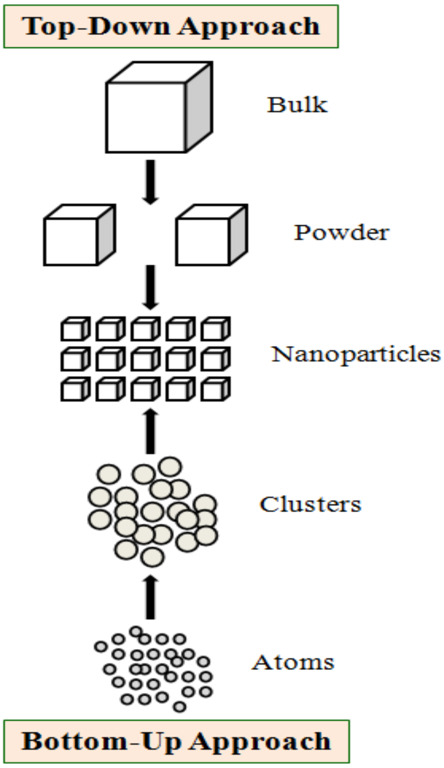

Figure 1.8. Schematic representation of the building up of nanoparticles

The bottom-up approach usually employs solution-phase colloid chemistry for the synthesis. Due to the flexibility in selecting different reducing agents, particle capping agents, solvent systems as well as synthesis conditions, colloidal synthesis offers a great variety of options for composition, shape, size and surface chemistry control. The bottom-up approach is also suitable for controlling monodispersity of the nanoparticles. An advantage of the bottom-up approach is the better possibilities to obtain nanostructues with less defects and more homogeneous chemical compositions. General mechanism for the formation of nanoparticles is shown in Figure 1.9.

Once the nanoparticles are synthesised they have to be immobilised to prevent agglomeration. Immobilisation on a solid support has been adopted in the present work. Various solid supports like TiO_2, SiO_2, Fe_3O_4can be used for this purpose. But with TiO_2 and SiO_2being non-magnetic, there is difficulty in retrieving them from the system

(Recyclabilty/Reusabilty). So, Fe_3O_4 is chosen as a solid support.On the solid support (Fe_3O_4), metal (Pd) loading capacity is low as well as its non – reproducible. To avoid this difficulty a new synthesis root has been developed i.e. grafting the reducing agents on the solid support (Fe_3O_4) so that the metal ion (Pd^{2+}) reduction as well as nucleation takes place, on the solid support. Fe_3O_4 solid support was chosen because the prepared Pd nanoparticles anchored on Fe_3O_4 support can be retrieved easily from a solution using a magnet. A similar approach was adapted to anchor Pd nanoparticles on SiO_2.

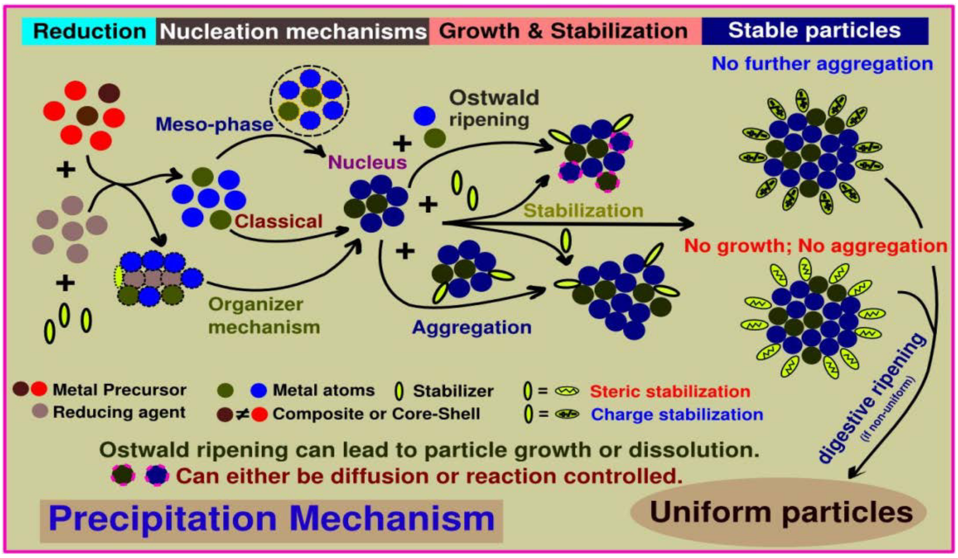

Figure 1.9. Schematic representation of the steps involved in the formation of nanoparticles during reduction in solution

The Fe_3O_4 NPs having nanometer size have superparamagnetic properties i.e. they get magnetized by applying external magnetic field but demagnetize as soon as magnetic field is withdrawn [41,42]. Thus, the Fe_3O_4 NPs can be collected by applying external magnetic field and re-dispersed in the reaction medium.

The Pd nanoparticles thus synthesised were tested for their catalytic activity [43-45] in the reduction of reduce U(VI) to U(IV) as well as Cr(VI) to Cr(III). In addition, their characteristics for hydrogen sorption [46-48] were also investigated.

1.8. Specification analysis for total gas content in UO_2

Total/occluded/residual gases are important specification for sintered nuclear fuel pellets. Total gas content is defined as the amount of non-condensable gases released when the pellet is heated under vacuum at required temperature and time and converting the gas content to STP[49].If the pressure of these gases increases over a certain critical value, the intergranular structures of the pellet materials suddenly deforms, which in course of time leads to embrittlement.

Entrapment of Total Gas-

1) During the manufacture of high purity metals and alloys permanent gases like hydrogen and nitrogen are trapped in the interstitial spaces. These trapped gases are known as total / occluded or residual gases.

2) During the fabrication of these fuels, to maintain specified O/M or C/M, they are subjected to high temperature sintering in reducing gas environment (Ar + 8%H_2 or N_2 + 8%H_2). During this cycle, some gases get trapped. These gases will be released during the operating conditions of the reactor. They may pressurise the clad or alter the thermal conductivity of cover gas (gap between the pellets and the clad is filled by suitable cover gas) or react with the clad and cause damage. Hence it is of importance to have a precise knowledge of the total gas content and its composition.

Total gas content of the fuel pellet will depend upon the nature of the fuel and the type of reactor in which it is used. The temperature at which fuel pellet is heated depend upon the central line temperature of the fuel pellet during the operation of the reactor and the easiness with which the gases come out of the pellet. For example the central line temperature of carbide pellets (used in FBTR) is 1273 K whereas for oxide pellets, central line temperature reaches to 1923 K. The oxide pellets are highly sintered and have high density compared to the carbide pellets. Therefore, high temperatures are required to extract the gases from the interstitial spaces in the oxide pellets as compared to carbide pellets.

1.8.1. Time of heating

Time up to which each pellet is heated has been determined by Sayi et al [50] using HVE-QMS instrument. In this process the MOX pellets with and without annular hole were heated at 1923 K and the pressure of the gases evolved was monitored at regular intervals up to 2 hours. The gas content was calculated at each time interval, after correcting for the blank. It can be seen from the Figure 1.10 (without annular hole) and 1.11 (with annular hole) that within 10 minutes of heating all the gases were released. Hence, heating the pellet for 15 minutes was more than adequate for the release of gases from the oxide pellets. Similarly, the release pattern of gases in MC pellets was studied at 1273 K up to 4 hours. It is obvious from the Figure1.12 that 30 minutes of heating and extraction was sufficient for the quantitative extraction of gases. Hence, the time of extraction of gases released was confined to 15 minutes and 30 minutes for oxides and carbides respectively.

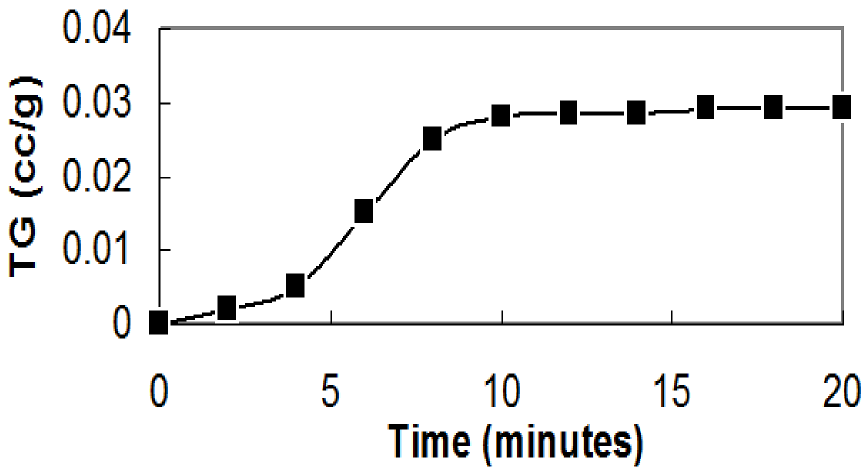

Figure 1.10. Time vs. TG(cc/g) in MOX pellet

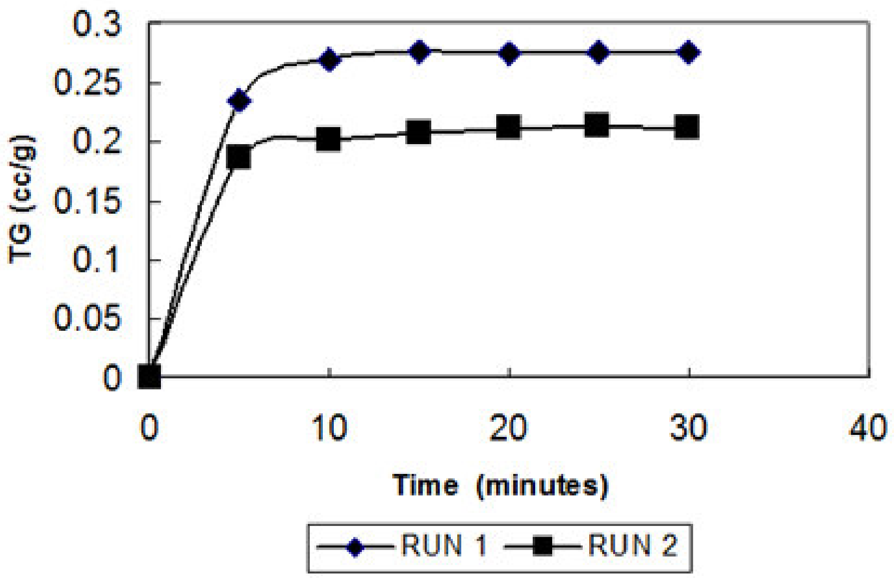

Figure 1.11. Time vs. TG (cc/g) in MOX pellets (with ann. hole)

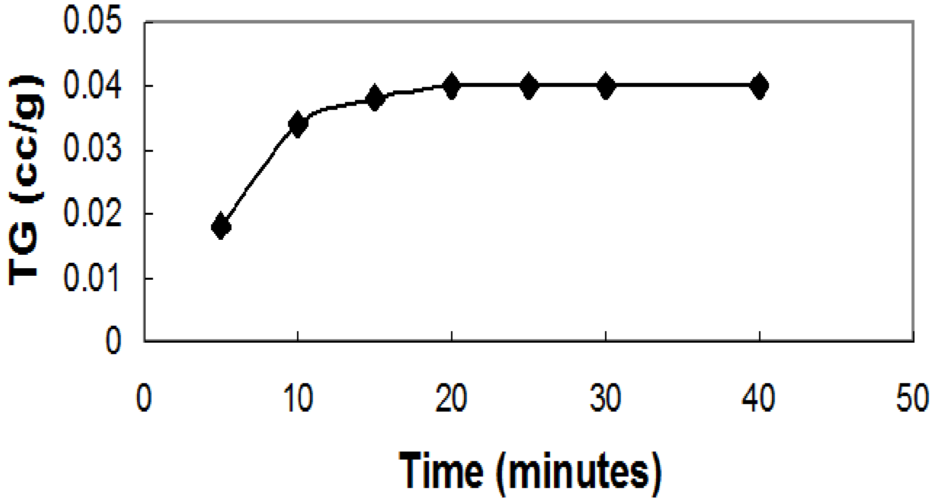

Figure 1.12. Time vs. TG(cc/g) in MC pellet

It was observed that the main constituent of the occluded gases was hydrogen (>95%). The rest of the gases were a mixture of carbon monoxide, nitrogen and carbon dioxide. The total gas content of carbide fuels pellets and MOX fuel pellets with the annular hole was high (>0.1 L/Kg). These fuel pellets are employed in fast breeder reactors, wherein the clad is of stainless steel. It is known that hydrogen diffuses out of stainless steel at elevated temperatures[51]. Hence there may not be pressure build up in the fuel pin due to the hydrogen released from the pellets. However, hydrogen content in oxide pellets used in thermal reactor is less (0.04 L/Kg), this is because clad used in the thermal reactor is zirconium alloy in which excess H_2 will lead to hydrogen embrittlement.

Chapter -2

Instrumental Techniques and Experimental Methods

2.1. Introduction

A number of analytical instruments, both indigenously fabricated as well as commercially available have been employed during the course of current investigations. Some of these techniques are common to more than one investigation. For example, the hot vacuum extraction-quadrupole mass spectrometry (HVE-QMS) has been employed for determination of hydrogen/deuterium in Zircaloy matrix described in Chapter 3, for determination of diffusion coefficients for hydrogen and deuterium described in Chapter 4, and for determination of total gas content in PFBR blanket pellets enunciated in Chapter 6. Instead of describing the principles of this technique each time in subsequent individual chapters, general description is given in this Chapter. The experimental details, as applicable are given in the respective Chapters.

In addition, a number of other techniques have also been employed as supporting tools to generate the requisite information on the samples investigated. These techniques were employed for characterizing the Pd nanocatalysts synthesized, the details of which are given in Chapter 5. This information includes morphology of samples, their chemical composition and surface characteristics. Details of such techniques are also given in this Chapter.

Table 2.1 Details of equipment employed and samples investigated

Samples investigated	Technique employed	Materials/reagents used
Chapter 3: Determination of Deuterium pick-up in Zr-Nb alloy by Hot Vacuum Extraction - Quadrupole Mass Spectrometry		
Zr-2.5% Nb sliver samples from a PHWR	HVE-QMS	Standard gas calibration mixtures of H_2/D_2
Chapter 4: Determination of diffusion coefficients of hydrogen and deuterium in Zr-2.5%Nb pressure tube material using hot vacuum extraction – quadrupole mass spectrometry		
Zr-2.5% Nb from a fuel fabrication facility	HVE-QMS Optical microscopy	Standard gas calibration mixtures of H_2/D_2
Chapter 5: Formation of Pd Nano-catalyst on Inorganic host materials for U(VI) reduction by formic acid		
Palladium Nanoparticles coated on Fe_3O_4 host. Palladium Nanoparticles coated on SiO_2 host.	Carbon determinator Nitrogen determinator Inductively coupled Plasma atomic emission spectrometry X-Ray diffraction High resolution transmission electron microscopy Field Emission - Scanning electron microscopy(FE-SEM) Energy-dispersive X-ray spectroscopy (EDS) Vibrating sample magnetometer Sievert apparatus X-Ray photo electron spectroscopy Mossbauer spectrometry Fourier transform infrared spectroscopy (FTIR) UV-Visible Spectrophotometry	Fe_3O_4 SiO_2 Hydrazine Hydrate Potassium Dichromate Formic Acid (3-Glycidyloxypropyl) trimethoxysilane $PdCl_2$

Table 2.1 (Continued) Details of equipment employed and samples investigated

Chapter 6: Determination of total gas content and its composition in Indian PFBR blanket pellets		
PFBR $DDUO_2$ blanket pellets	HVE-QMS	Standard gas calibration mixtures

2.2. Details of the Instrumental techniques employed

2.2.1. Equipment used in the investigations described in Chapters 3, 4 and 6.

2.2.1.1. General description of a Mass Spectrometer

A mass spectrometer is an instrument which sorts out ions according to their mass to charge (m/e) ratio by the action of electric or magnetic fields measures these ratios and determines the abundance of various ions. Every mass spectrometer, regardless of its design is comprised of four functional parts [52]

(i) the ion source where a beam of ions representative of the sample is generated, accelerated and collimated after suitable ion optics,

(ii) the analyser in which ions are separated according to their mass to charge ratio,

(iii) the detector where the resolved ions are detected and counted, and

(iv) the vacuum system which provides the environment for these purposes. In addition, a sample introduction system is necessary to admit the samples to be studied to the ion source while maintaining the high vacuum requirements ($\sim10^{-6}$ to 10^{-8} mm of mercury) of the technique; and an online data acquisition and analysis system.

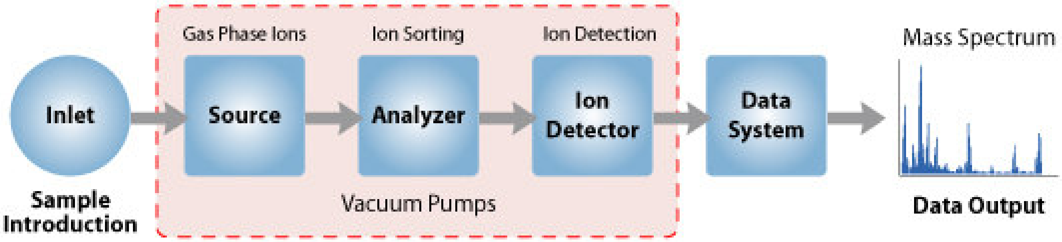

Figure 2.1. Schematic of a Mass Spectrometer

In the present work a quadrupole mass spectrometer has been employed. In this system ions are separated under the influence of electric fields. Further description that follows is limited to these quadrupole mass spectrometers.

2.2.1.2. Quadrupole Mass Spectrometer

A quadrupole mass spectrometer consists of an ionizer (bombardment by electrons from a hot filament), an ion accelerator, and a mass filter consisting of four parallel metal rods arranged as shown in Figure 2.2. Two opposite rods have an applied potential of $(U+V\cos(\omega t))$ and the other two rods have a potential of $-(U+V\cos(\omega t))$, where U is a dc voltage and $V\cos(\omega t)$ is an ac voltage. The applied voltages affect the trajectory of ions traveling down the flight path centered between the four rods. For given dc and ac voltages, only ions of a certain mass-to-charge ratio pass through the quadrupole filter and all other ions are thrown out of their original path. A mass spectrum is obtained by monitoring the ions passing through the quadrupole filter as the voltages on the rods are varied. There are two methods: varying ω and holding U and V constant, or varying U and V with (U/V) fixed for a constant angular frequency, ω. By a suitable choice of RF/DC ratio, the two directions together give a mass filter which is capable of resolving individual atomic masses. The attractive features of the quadrupole as a mass analyser are: the quadrupole provides a convenient filter which can be tuned to the desired mass by varying the amplitude of the RF voltage, V; the mass selectivity (i.e. resolution can also be varied electronically by simply adjusting the DC/RF ratio. Simultaneously varying the amplitude of the DC and RF voltages (at fixedω) allows the entire mass spectrum to be scanned.

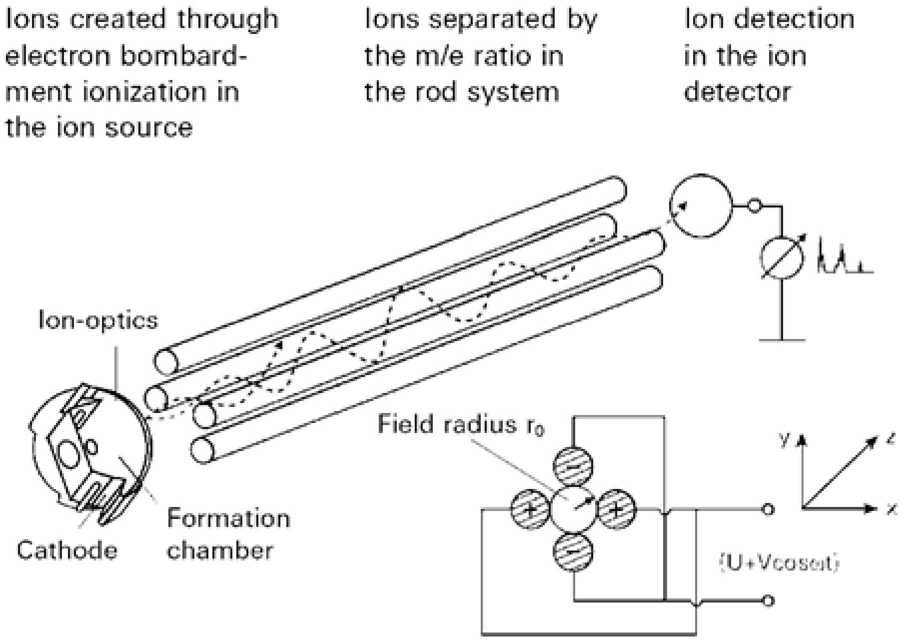

Figure 2.2. Schematic of a Quadrupole Mass Spectrometer

(i) Ion sources

Before gases can be analysed in a mass filter, they must first be ionized in an ion source by means of electron bombardment (Figure 6.6). Electrons are emitted from an electrically heated cathode (filament). A voltage is applied between anode and cathode, which accelerates the electrons. Neutral gas molecules that are present in the formation space between the anode and cathode are ionized by collisions between electrons, forming single and multiple positive ions. The energy of the colliding electrons exerts a significant influence on both the

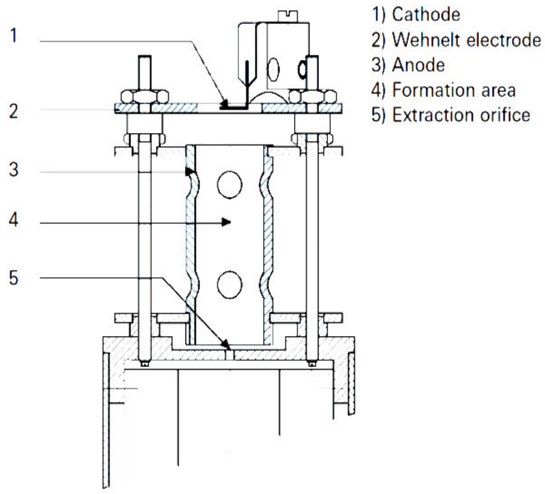

Figure 2.3. Cross section of electron bombardment ion source

number and type of ions that will be formed. Ionization of the neutral particles commences at a minimum electron energy of between 10 and 30 eV (appearance potential). The number of formed ions quickly increases as electron energy rises (acceleration voltage), reaches a maximum at 50 to 150 eV depending upon the type of gas in question, and slowly declines again as energy continues to rise. Since the yield in ions, and thus the sensitivity of the mass spectrometer, should be as large as possible, electron energies between 70 and 100 eV are typically used.

(ii) Detectors

The ions that are separated in the rod system on the basis of their mass-to-charge ratio can be electrically detected with various types of detectors. Detector selection will primarily be based upon requirements that relate to detection sensitivity, detection speed and signal-to-noise ratio. However it will also be governed by other application-specific requirements that relate to stability, thermal and chemical resistance, as well as space requirements. We have used a Faraday cup detector.

In the simplest case, the ions strike a Faraday collector (Faraday cup), where they give up their electrical charge.

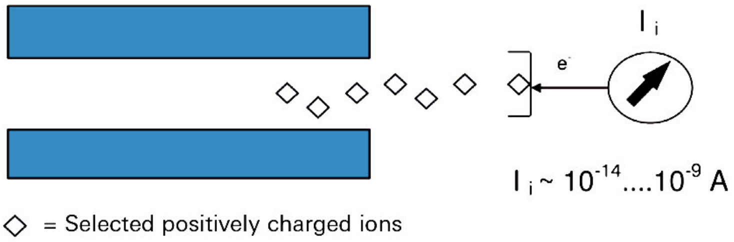

Figure 2.4. Operating principle of a Faraday Cup

The resulting current is converted to a voltage that is proportional to the ion current by means of a sensitive current-to-voltage converter (electrometer amplifier). Partial pressures in the order of 10^{-10} Pa can be detected. In addition to its simple, robust design, a Faraday detector is characterized by its long-term stability and its ability to withstand high temperatures. To keep the time constants small and to avoid other interfering effects, the electrometer amplifier is connected directly to the analyser and its output signal is supplied directly to the data analysis system.

2.2.2. Equipment used in the investigations described in Chapter 5

Different analytical techniques have been employed in the studies of synthesis of Pd nanocatalysts, their characterization and application described in chapter 5. In the experiments described in chapter 5, Pd nanoparticles were synthesized by coating of (3-glycidyloxypropyl)trimethoxysilane on Fe_3O_4 and then covalently linking them with hydrazine. The (3-glycidyloxypropyl)trimethoxy silane contains 7 number of carbon atoms, so the quantity of (3-Glycidyloxypropyl)trimethoxysilane having an epoxy ring in 1g of Fe_3O_4 was obtained by the use of Carbon determinater technique. To ensure that one hydrazine molecule has reacted with one epoxy ring of silane, nitrogen content was obtained using Nitrogen determinator technique. The above formed material was reacted with $PdCl_2$ so as to reduce Pd^{2+} ions to Pd^{o}. Inductively coupled Plasma atomic emission spectrometry was then used to determine the loading of Pd nanoparticles present in Fe_3O_4 and SiO_2. Techniques likes X-Ray diffraction, High resolution transmission electron microscopy, Fourier transform infrared spectroscopy (FTIR), X-Ray photo electron spectroscopy etc. were used for Pd nanocatalysts characterization. These Pd nanoparticles were studied for their catalytic activity in the reductions of representative oxymetal ions such as UO_2^{2+} and $Cr_2O_7^{2-}$ ions with formic acid. For this purpose UV - Vis Absorption Spectrometry technique is used because as it gives absorption which is directly related to the concentration of the oxymetal ions. For hydrogen storage application by the Pd nanoparticles, Sievert apparatus and Mössbauer spectrometry were used.

2.2.2.1. Carbon Determinator

(i) Principle

The sample is heated to high temperature in the presence of purified oxygen. After removing the other evolved gases and moisture, mixture of CO and CO_2 produced is passed over heated CuO and the total CO_2 formed is measured by IR detector.

(ii) Instrument

Horiba, Japan made carbon determinator (model 320 V) has been used in the present studies. A schematic of the instrument is shown in Figure 2.5.

(iii) Procedure

Known mass of sample **(Fe_3O_4@(3-Glycidyloxypropyl) trimethoxysilane)**was taken with 1g of tungsten (which acts as accelerator) in alumina crucible. The crucible was then taken inside the induction furnace. The carrier gas oxygen from a cylinder was purified by allowing it to pass through ascarite (asbestos soaked with NaOH) and then through anhydrone (anhydrous Mangnesium Perchlorate) to remove CO_2 and moisture.

$$2NaOH + CO_2 \rightarrow Na_2CO_3 + H_2O$$

$$Mg(ClO_4)_2 + xH_2O \rightarrow Mg(ClO_4).\ x\ H_2O$$

The purified gas was then passed over the alumina crucible in the induction furnace. The crucible was then head to ~ 1300 K when the carbon present in the sample is converted to CO + CO_2 by combustion in presence of oxygen. The evolved gases were then passed over hot

CuO at 737 K to convert CO to CO_2.The CO_2 was then passed through the anhydrone filter to remove the moisture present, if any.

$$2CuO + CO \rightarrow CO_2 + Cu_2O$$

$$2CuO + H_2 \rightarrow H_2O + Cu_2O$$

$$Mg(ClO_4)_2 + xH_2O \rightarrow Mg(ClO_4).\ x\ H_2O$$

Purified $CO_2$was detected by IR detector.

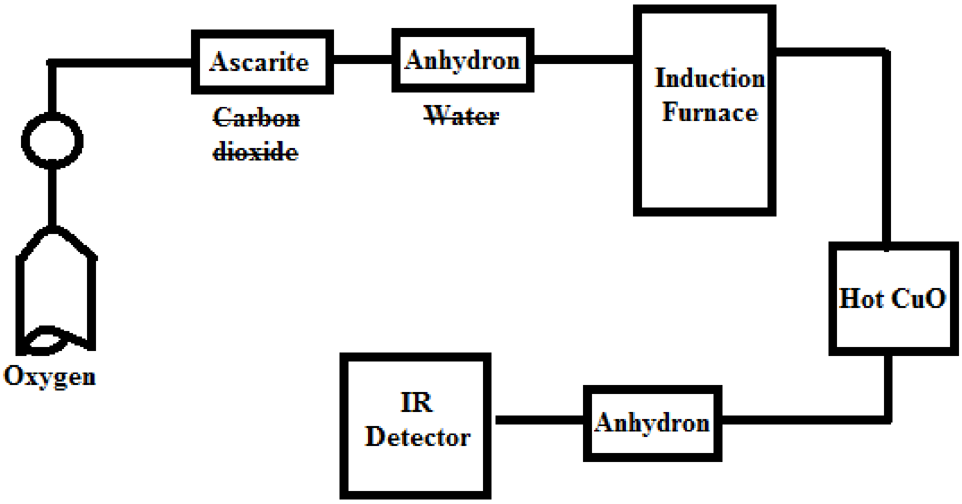

Figure 2.5. Schematic of Carbon determinator

A separate blank measurement was carried out by taking empty alumina crucible along with tungsten accelerator and repeating the analysis procedure. To arrive at detection limit of the method, ten independent blank measurements were carried out. The detection limit was found to be 10 μg/g at 3σlevel. Prior to the sample analysis, the instrument performance was checked by analysing NIST steel reference materials with known carbon content. Replicate analyses (minimum 5 measurements). The precision of the methodology was 10% at 2 σ level (3 replicate measurements).

(iv) Calculation

Multi-point calibration of the instrument was done.

Carbon concentration of **Fe_3O_4@(3-Glycidyloxypropyl)trimethoxysilane** was

- 1.518% = 15180 ppm
- 1.458% = 14580 ppm
- 1.486% = 14860 ppm

Average Carbon Concentration was 1.487% or 1.5% or (15000 ± 1500) ppmw

15000 ppmw = 15000 μg/g = $\frac{15000}{7 \times 12}$ μmol/g = 178 μmol/g

Therefore 1g of Fe_3O_4 contains 178 μmol of (3-Glycidyloxypropyl)trimethoxysilane having an epoxy ring.

2.2.2.2. Nitrogen Determinator

(i) Principle

The sample is heated to high temperature in presence of an inert gas such as Helium. The sample gets fused. During fusion, oxygen reacts with graphite to give CO, while nitrogen and hydrogen, irrespective of the form, (free or combined), give N_2 and H_2. The carrier gas sweeps all these gases and the gaseous mixture is dried over anhydron and then passed through hot CuO catalyst column, where CO and H_2get converted to CO_2 and H_2O respectively. These are then trapped employing sodium hydroxide coated asbestos granules (ascharite) and anhydrous magnesium perchlorate (anhydron) respectively. Nitrogen is determined by thermal conductivity detector (TCD).

(ii) Instrument

Chromatography and Instrument Company (CIC), Vadodara, India, make N, O determinator has been employed to determine nitrogen content. A schematic flow sheet in the form of block diagram is shown in Figure 2.6.

(iii) Procedure

First the graphite crucible which is used for sample loading is degassed at 2800 K under flow of purified Helium gas. Known mass of sample (**Fe_3O_4@silane@NHNH$_2$**) was encapsulated in a high purity Nickel capsule which was then inserted in a degassed graphite crucible. This graphite crucible was then loaded into the impulse furnace. The carrier gas Helium from a cylinder was passed through hot CuO, ascarite and anhydrone filters to remove the impurities (CO, CO_2, H_2O). The purified He gas was then passed over the graphite crucible in the impulse furnace. The crucible was then heated to ~ 2800 K when it gets fused. The evolved gases were then passed through hot CuO, ascarite and anhydrone to remove CO_2 and moisture. Oxygen was measured by NDIR and nitrogen by thermal conductivity detection.

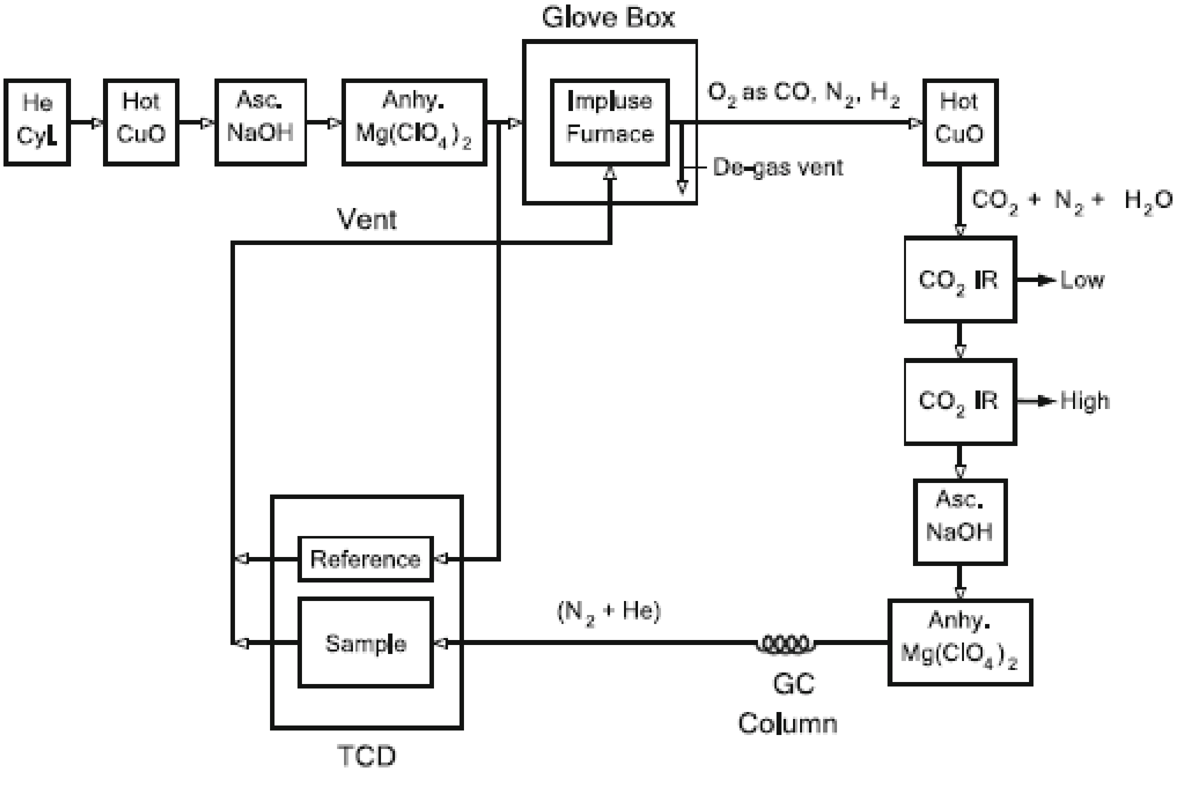

Figure 2.6. Block diagram of the nitrogen and oxygen determinator

A separate blank measurement was carried out by taking Nickel capsule in the empty degassed graphite crucible and repeating the analysis procedure. To arrive at detection limit of the method, ten independent blank measurements were carried out. The detection limit was found to be 11µg/g at 3σlevel. Prior to the sample analysis, the instrument performance was checked by analysing NIST steel reference materials with known nitrogen content. Replicate analyses (minimum 5 measurements). The precision of the methodology was 10% at 2 σ level (3 replicate measurements).

(iv) Calculation

Multi-point calibration of the instrument was done.

Total Nitrogen concentration in **Fe_3O_4 @ silane@$NHNH_2$** was

- (5100 ± 510)ppmw
- (4980 ± 500)ppmw
- (5300 ± 530)ppmw

Average of Nitrogen concentration was (5130 ± 510) ppmw

5130 ppmw = 5130 µg/g= $\frac{5130}{2 \times 14}$ µmol/g= 183 µmol/g

Therefore 1g of Fe_3O_4 contains 183 µmol of hydrazine (NH_2NH_2).

Epoxy conc.=178µmol/g based on C analysis

Hydrazine = 183 µmol/g based on N analysis

It showed that one hydrazine is reacted with one epoxy ring of silane.

2.2.2.3. Inductively Coupled Plasma-Atomic Emission Spectroscopy (ICP-AES)

(i) Principle

Inductively Coupled Plasma-Atomic Emission Spectrometry (ICP-AES) is one of the most common techniques for elemental analysis. Its high specificity, multi-element capability and good detection limits result in the use of the technique in a large variety of applications. All kinds of dissolved samples can be analysed, varying from solutions containing high salt concentrations to diluted acids. A plasma source is used to dissociate the sample into its constituent atoms or ions, exciting them to a higher energy level. They return to their ground state by emitting photons of a characteristic wavelength depending on the element present. This light is recorded by an optical spectrometer. When calibrated against standards the technique provides a quantitative analysis of the original sample. Three important components of ICP-AES are (a) sample introduction, (ii) plasma, and (iii) spectrometer and detector.

Sample introduction: A solid sample is normally first dissolved and mixed with water. The technique is robust enough to allow direct analysis of liquids. The sample solution is transformed into an aerosol by a nebuliser. The bigger droplets are separated from the smallest in a specially spray chamber. The smallest droplets (1-10 µm) are transferred by an argon flow into the heart of the ICP-AES, the argon plasma. The bigger droplets (>90%) are pumped to waste.

Plasma: To produce strong atomic emission from all chemical elements it is necessary to attain temperatures considerably above in the range of 7,000 K to 10,000 K. A convenient means of obtaining these temperatures is to generate an inert-gas plasma. When the aerosol droplets enter the hot area of the plasma (front page) they are converted into salt particles by desolvation. These salt particles are split into individual molecules that will subsequently fall apart to atoms and ions which get excited to higher energy levels. When these excited atoms and ions return to their ground state or to lower excitation states they will emit electromagnetic radiation in the ultra-violet/visible range of the spectrum. Each excited element emits specific wavelengths and the intensity of the radiation is proportional to the element concentration.

Spectrometer and Detector: A spectrometer, a multi-component part containing mirrors, prisms etc.are used to separate the specific wavelengths of interest. Because atomic emission lines are very narrow lines, a high-resolution detector is essential. Simultaneous detection makes it possible to measure all elements of interest at the same time. This is an advantage because it limits signal variations introduced by sample preparation. Most often a CCD detector is used, which provides both advantages (high resolution and simultaneous detection).

A typical layout of ICP-AES is shown in Figure 2.7

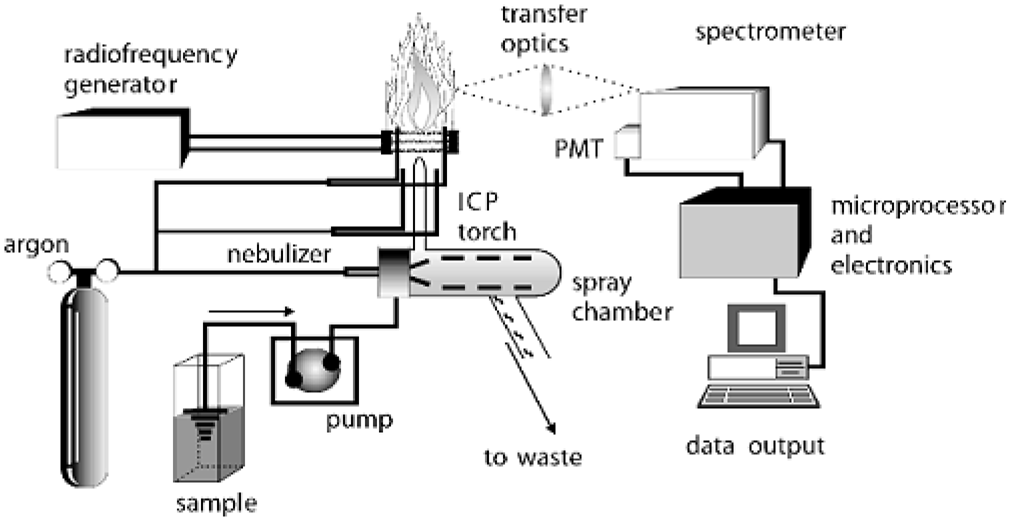

Figure 2.7. Typical layout of ICP-AES

(ii) Instrument

A computer controlled, high resolution, simultaneous atomic emission spectrometer (Spectro Arcos, Germany) with ICP and DC Arc as excitation sources and a charged coupled device (CCD) as detector was employed for carrying out all the analytical experiments. The instrumental specification and experimental parameters are summarized in Table 2.2. The detector system, consisting of linear arrays of CCD detectors (3648 pixels/array), thermally stabilized together with an optical system, provides the ability to choose the alternate analytical lines.

Table 2.2 InstrumentalSpecification & Experimental Parameters

Optical design	Paschen-Runge mounting, Circular design
Focal length	750 mm
Grating	Holographic
Groove density	1800 grooves/mm (1), 3600 grooves/mm (2)
Wave length range	130-800 nm
Entrance slit width	15 microns
Resolution (FWHM)	0.01 nm from 130-450 nm 0.02 nm from 450-800 nm
Thermal regulation	Controlled to 30 ± 1˚C
Frequency	27.12 MHz
Pump	Dual channel peristaltic pump
Detector	Linear arrays of CCD (3648 pixels/array)
Nebulizer	Concentric nebulizer with cyclonic spray chamber
ICP-torch	Demountable, radial viewing
Operating condition	
Coolant flow	16 L/min
Auxiliary flow	0.6 L/min
Total timeof measurement	28 s
Pump speed	30 Rpm
RF power out put	1.2 kW
Input power	230 V AC

(iii) Procedure

<u>*The amounts of Pd^0 deposited on the Fe_3O_4*</u>: (3-Glycidyloxypropyl) trimethoxy silane was coated on Fe_3O_4 and then reacted with hydrazine to covalently link it with anchored epoxy ring on Fe_3O_4. These particles were retrieved using a magnet, washed with acid-water (pH 1-2), ethanol and then dried. 0.005M $PdCl_2$ solution was prepared and 10 mL of this solution was kept as stock solution. Another 10 mL of the solution was added in silane and hydrazine coated Fe_3O_4. The material was left for 48h for equilibration. Loading of Pd in this sample was monitored by Inert coupled plasma – Atomic emission Spectroscopy (ICP-AES) before and after equilibration

<u>*The amounts of Pd^0 deposited on the SiO_2*</u>: Since SiO_2 was used as the inert support and not Fe_3O_4 (which was retrievable by magnetic field), a different method was adopted for estimating Pd loading on Silica by ICP-AES. In this method, 500 mg of the Pd loaded silica was taken and 8ml of aqua regia (3:1- HCl-HNO_3) was added to it. The mixture was stirred with the help of magnetic stirrer for 3hrs and then filtered such that SiO_2 remained on the filter paper. The filtrate was evaporated in IR-Lamp and Pd (solid) remained in the beaker.10 ml HNO_3 (pH=1) solution was added in the beaker and the sample was analysed by ICP-AES.

The samples were analysed in triplicate after multi-point calibration.

2.2.2.4. X-ray diffraction (XRD)

(i) Principle

XRD is an experimental technique used to determine the crystal structure of solids[53], including lattice constants and geometry, identification of unknown materials, orientation of single crystals, preferred orientation of polycrystals, defects, stresses, etc. In XRD, a collimated beam of X-rays, with a wavelength typically ranging from 0.7 to 2 A^0, is incident on a specimen and is diffracted by the crystalline phases in the specimen. Consider crystal planes as shown in Figure 2.8. AO and CP are the two incident X-rays on two consecutive crystal planes. OB and PD are the corresponding diffracted rays of AO and CP respectively. OK and OL are the perpendiculars drawn from O on CP and PD respectively. d_{hkl} is the distance between two consecutive crystal planes.

The path difference between rays can be given as,

$$KP+PL = 2d_{hkl} \sin \theta$$

For constructive interference the Bragg’s law should be satisfied which is given as

$$2d_{hkl} \sin \theta = n \lambda \text{.......................Bragg's Law}$$

Where, n is the order of diffraction and λ is the wavelength of X-ray used. Important function of XRD is to measure the diffraction beam intensity and the d-spacings of crystalline materials which is used for phase identification of a crystalline material and can provide information on unit cell dimensions and crystal structure of the crystalline material. Due to this similarity, they are useful for determining crystal structures by X-ray Crystallography

The crystallite size of the particles is measured using the Scherer’s equation [54].

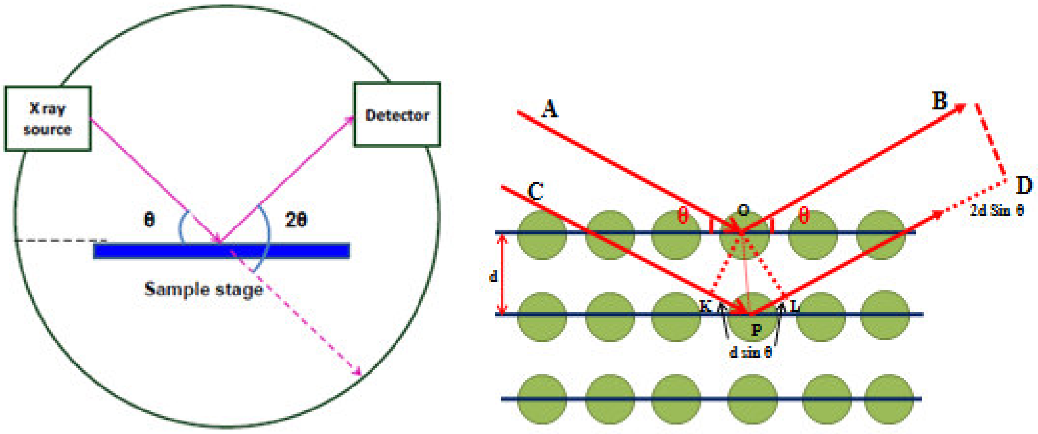

Figure 2.8. Schematic of X-ray diffractometer and Bragg's law of diffraction pattern

Homogeneous or uniform elastic strain shifts the diffraction peak positions. From the shift in peak positions, one can calculate the change in d-spacing, which is the result of the change of lattice constants under a strain. Inhomogeneous strains vary from crystallite to crystallite or within a single crystallite resulting in broadening of the diffraction peaks that increase with Sinθ.

If there is no inhomogeneous strain, the crystallite size, D, can be estimated from the peak width with the Scherrer's formula:

$$t = \frac{K\lambda}{B \cos \theta_B}$$

Where, t is the crystallite size of the particles, K is a dimensionless constant that may range from 0.89 to 1.39 depending on the specific geometry of the scattering objects. For a perfect two-dimensional lattice, where every point on the lattice emits a spherical wave, numerical calculations yield the lower bound of 0.89 for K [55]. A cubic three-dimensional crystal is best described by K = 0.94, while analytical calculations for a perfectly spherical object yield K = 1.33 [56]. B is the full width at half maxima, θ_B is the angle of diffraction and λ is the wavelength of the X-ray source (for Cu Kα, λ=1.5416Å). As the crystallite size decreases the range $(\theta_2 - \theta_1)$ increases hence the peaks broadens as the size of the crystals reduces gradually. However, owing to the fact that nanoparticles often form twinned structures, Scherrer's formula may produce results different from the true particle sizes. In addition, X-ray diffraction only provides the collective information of the particle sizes and usually requires a sizeable amount of powder. It should be noted that since the estimation would work only for very small particles, this technique is very useful in characterizing nanoparticles. Similarly, the film thickness of epitaxial and highly textured thin films can also be estimated with XRD.

(ii) Instrument

A Rigaku Miniflex-600 instrument was used having $\theta - 2\theta$ geometry for XRD measurements. The diffraction pattern was obtained using Cu-Kα (λ= 1.54 Å) radiation. Scan range of 10^0 - 70^0 was used and scan rate of 4^0/min was maintained for each measurement.

2.2.2.5. Electron microscopy

Electron microscopy techniques are of two types- Scanning electron microscopy (SEM) and Transmission electron microscopy (TEM). Both the techniques have been employed in the present investigations to solicit information on Pd nanocatalysts. The basic differences between these two electron microscopy techniques are-

- SEM is based on scattered electrons while TEM is based on transmitted electrons.
- SEM focuses on the sample's surface and its composition whereas TEM provides the details about its internal composition. Therefore, TEM can show many characteristics of the sample, such as morphology, crystallization, stress or even magnetic domains. On the other hand, SEM shows only the morphology of samples.
- The sample in TEM has to be cut into very thin slice whereas there is no such need with SEM sample.
- TEM has much higher resolution (0.05 nanometer) than SEM (0.4 nanometer).
- SEM allows for large amount of sample to be analysed at a time whereas with TEM only small amount of sample can be analysed at a time.
- SEM is used for surfaces, powders, polished & etched microstructures, IC chips, chemical segregation whereas TEM is used for imaging of dislocations, tiny precipitates, grain boundaries and other defect structures in solids.
- In TEM, final images are formed on fluorescent screens whereas in SEM, images are formed on a monitor.

- SEM gives a very clear 3-dimensional image while TEM provides a 2-dimensional picture.

2.2.2.5.1. **Scanning electron microscopy (SEM)**

(i) Principle

The scanning electron microscope (SEM) has been used to produces images of a sample by scanning it with a focused beam of electrons. A Scanning Electron Microscope provides details surface information by tracing a sample in a raster pattern with an electron beam.The process begins with an electron gun (either a simple tungsten filament electrically heated or field emission) generating a beam of energetic electrons down the column and onto a series of electromagnetic lenses. The energetic electron beam is focused onto the sample. When the incident electrons come in contact with the sample, they interact with the sample’s atoms, producing various signals that contain information about the sample's surface topography and composition.

Energetic electrons are released from the surface of the sample. The scattered patterns made by the interaction yield information on size, shape, texture and composition of the sample. A variety of detectors are used to attract different types of scattered electrons, including secondary and backscattered electrons as well as X-rays.

Backscatter electrons are incidental electrons reflected backwards; images provide composition data related to element and compound detection.

Diffracted backscatter electrons determine crystalline structures as well as the orientation of minerals and micro-fabrics.

X-rays, emitted from beneath the sample surface, can provide element and mineral information.The number and energy of the X-rays emitted from the specimen can be measured by an energy-dispersive spectrometer (EDS).EDS allows the elemental composition of the specimen to be measured [57]. SEM analysis is considered to be "non-destructive"; that is, X-rays generated by electron interactions do not lead to volume loss of the sample, so it is possible. A schematic of SEM is shown in Figure 2.9.

SEM produces black and white, three-dimensional images. Image magnification can be up to 10 nanometers and the intense interactions that take place on the surface of the specimen. For Energy dispersive spectrometric studies, OXFORD instrument was used. Sample (Fe_3O_4@Pd, SiO_2@Pd) suspension was prepared in acetone. A drop of suspension was placed on a glass slide and then coated with gold. Pd& Fe composition in Fe_3O_4@Pd and Pd& Si composition in SiO_2@Pd were obtained.

FE-SEM analyses were carried out using Zeiss make AURIGA model. Sample (Fe_3O_4@Pd, SiO_2@Pd) suspension was prepared in acetone.A drop of suspension was placed on a glass slide and then coated with gold.

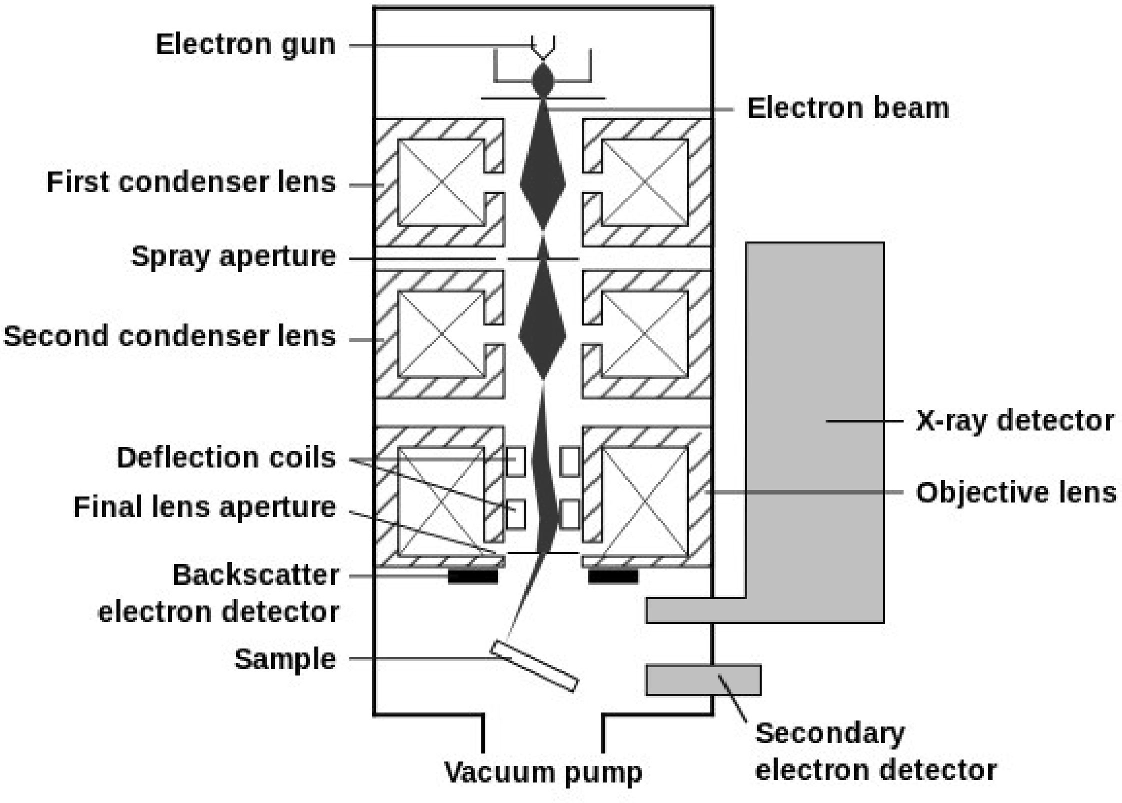

Figure 2.9. Schematic of scanning electron microscopy

2.2.2.5.2. Transmission Electron Microscopy (TEM)

The transmission electron microscope (TEM) forms an image by accelerating a beam of electrons that pass through the specimen. The image is magnified and focused onto an imaging device, such as a fluorescent screen, on a layer of photographic film, or detected by a sensor such as a CCD camera. In TEM, electrons are accelerated to 100 KeV or higher (up to 1MeV), projected onto a thin specimen (less than 200 nm) by means of the condenser lens system, and penetrate the sample thickness either undeflected or deflected. The greatest advantages that TEM offers are the high magnification ranging from 50 to 10^6 and its ability to provide both image and diffraction information from a single sample. Figure 2.10 shows schematic of a typical TEM.

The scattering processes experienced by electrons during their passage through the specimen determine the kind of information obtained. Elastic scattering involves no energy loss and gives rise to diffraction patterns. Inelastic interactions between primary electrons and sample electrons at heterogeneities such as grain boundaries, dislocations, second phase particles, defects, density variations, etc., cause complex absorption and scattering effects, leading to a spatial variation in the intensity of the transmitted electrons. In TEM one can switch between imaging the sample and viewing its diffraction pattern by changing the strength of the intermediate lens.

The high-resolution transmission electron microscopy (HRTEM) uses both the transmitted and the scattered beams to create an interference image. It is a phase contrast image and can be as small as the unit cell of crystal.

HRTEM investigations are carried out using Zeiss Libra 200 FE TEM. A drop of the sample (Fe_3O_4, Fe_3O_4@Pd, SiO_2@Pd) dispersion was placed on a carbon coated copper grid (0.3 cm diameter, mesh size of 200 holes/cm) and left to dry overnight at room temperature.

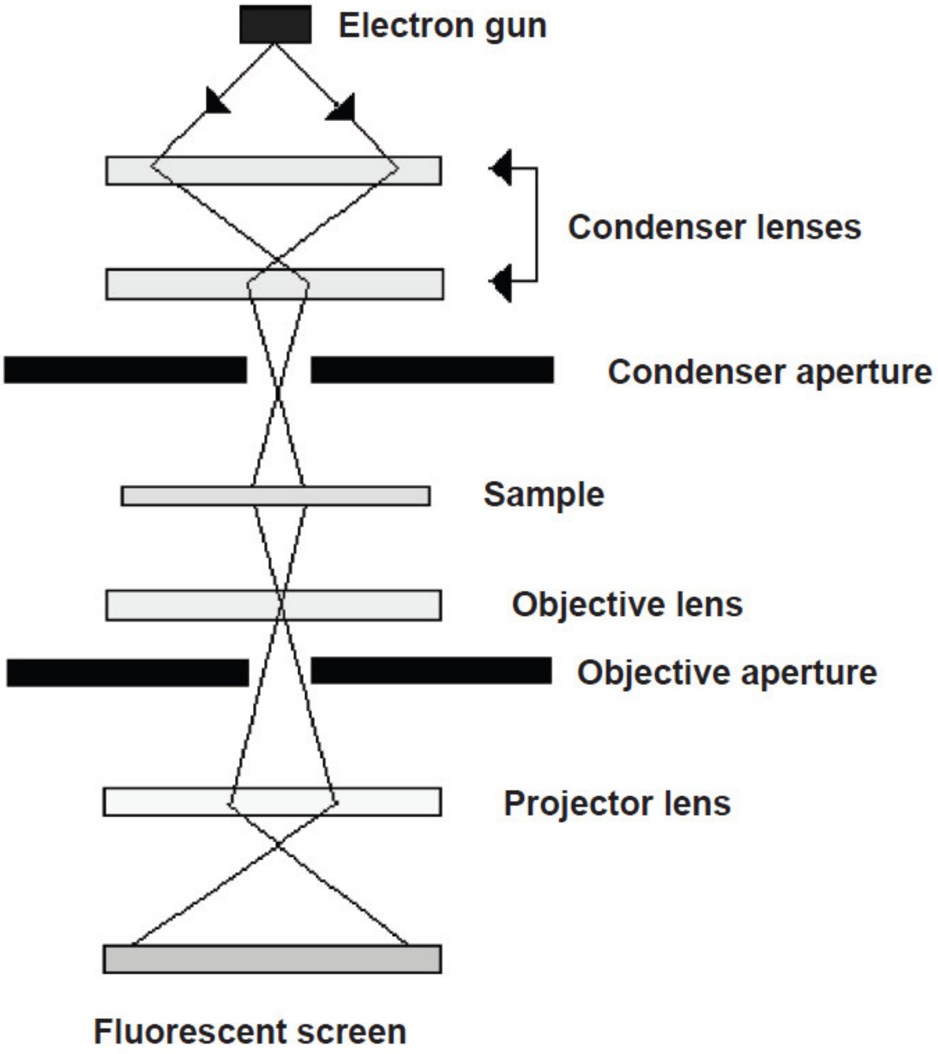

Figure 2.10. Schematic diagram of TEM

2.2.2.6. Vibrating Sample Magnetometer

A vibrating sample magnetometer (VSM)measures magnetic properties of magnetic materials [58].It operates on **Faraday's law of induction i.e. a changing magnetic field produces an electric field**[59] and this electric field can give information about the changing magnetic field. A schematic of vibrating scanning magnetometer is shown in Figure. 2.11.

A sample is placed inside the uniform magnetic field. If the sample is magnetic, this constant magnetic field will magnetize the sample by aligning the magnetic domains, or the individual magnetic spins, with the field. If the constant magnetic field is high, the magnetization will be much larger. The magnetic dipole moment of the sample will create a magnetic field around the sample, called the magnetic stray field. By the use of **a piezoelectric material the sample is then physically vibrated sinusoidally.** As the sample is moved up and down, this magnetic stray field is changing as a function of time that is sensed by a set of pick-up coils. The oscillating magnetic field will cause an electric field in the pick-up coils according to Faraday's law of induction. This current will be proportional to the magnetization of the sample. The induction current is amplified by a trans-impedance amplifier and lock-in amplifier. The various components are controlled by a computer interface. The magnetic moment of the sample is measured in terms of electromagnetic unit (emu). Later, the magnetic moment is converted to emu/g scale and plotted against the applied magnetic field. The magnetic hysteresis measurement was carried out using a vibrating sample magnetometer (VSM) (Cryogenic Ltd., UK) at room temperature (300 K) over +9 to -9 Tesla applied magnetic fields.

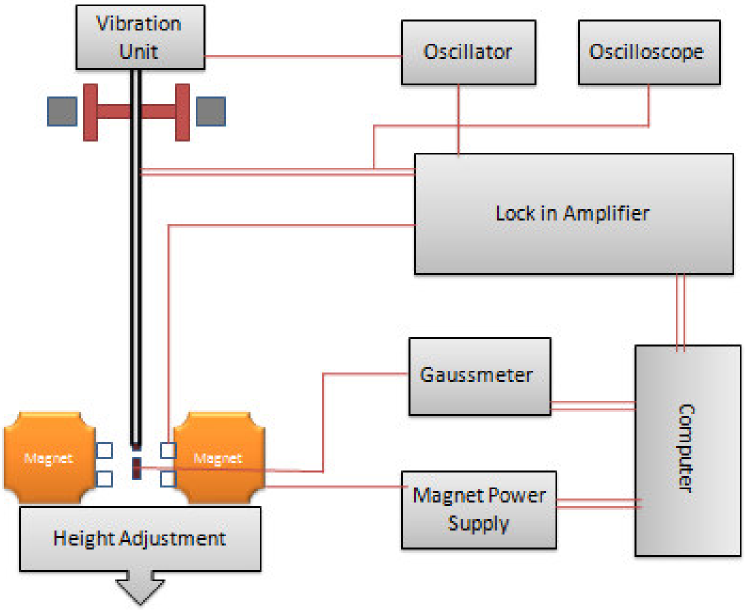

Figure 2.11. Schematic diagram of vibrating sample magnetometer

]

2.2.2.7. Sievert’s Type Setup

Sievert’s apparatus determines the hydrogen storage capacity of a material by measuring the pressure change resulting from adsorption after exposing the sample to hydrogen at constant volume and temperature. The schematic diagram of Sievert’s apparatus is given in Figure 2.12 [60]. The apparatus consists of a high-pressure manifold connected to the pressure transducer, vacuum line, a high pressure cylinder and hydriding reactor. In order to have high temperature and pressure resistance, the instrument is made of SS316.The reactor is cylindrical type, with ~24 mm inner diameter, ~37mm outer diameter and ~210 mm height. The reactor is connected with the manifold using a screw connection and Viton “O” ring is placed at the screw connection for leak tightness. The Viton “O” ring is cooled externally bypassing water through the Copper coil to prevent its damage at high temperature. In the connection line between reactor and manifold, a filter (200 mesh size) is put to prevent entering of fine hydride particles into the system. Reactor is joined with manifold using an on-off valve (**V5**). On-off valve is used to expose the sample in hydrogen atmosphere. For heating (during high temperature hydrogen absorption-desorption study) the reactor is placed into a tubular furnace. The temperature of the reactor is measured by Chromel-alumel thermocouple. The rotary and diffusion pumps are connected with the manifold through the valve V4.

Initially the whole apparatus is evacuated under diffusion vacuum. The sample is then heated under diffusion vacuum (10^{-6} mbar) for 2 hours at 673 K. This is done to prevent hydrogen sorption by the sample prior to heat treatment. Sample after heat treatment (in vacuum) is cooled to the working temperature under vacuum. The manifold is then purged with little quantity of hydrogen repeatedly and then evacuated completely. For hydrogen absorption study, at the experimental temperature, hydrogen pressure is created by opening the valve **V1**, keeping the reactor isolated by putting off the **V5** valve. The valve **V5** is then opened to equilibrate hydrogen gas between reactor and manifold. As the volume of the reactor, manifold and the total volume is calibrated, so from the final pressure (equilibrium pressure) of the system, the amount of absorbed hydrogen gas in the sample can be calculated. During the desorption study the reverse procedure is followed. Small amount of hydrogen is taken out from the manifold using rotary pump by opening valve **V4**, and keeping valve **V5** closed. The valve **V5** is opened and the sample reactor is allowed to equilibrate. The amount of desorbed hydrogen can be calculated from the increase in the equilibrium pressure. When the equilibrium pressure is plotted against the amount of hydrogen absorbed/desorbed we get the pressure-composition isotherm.

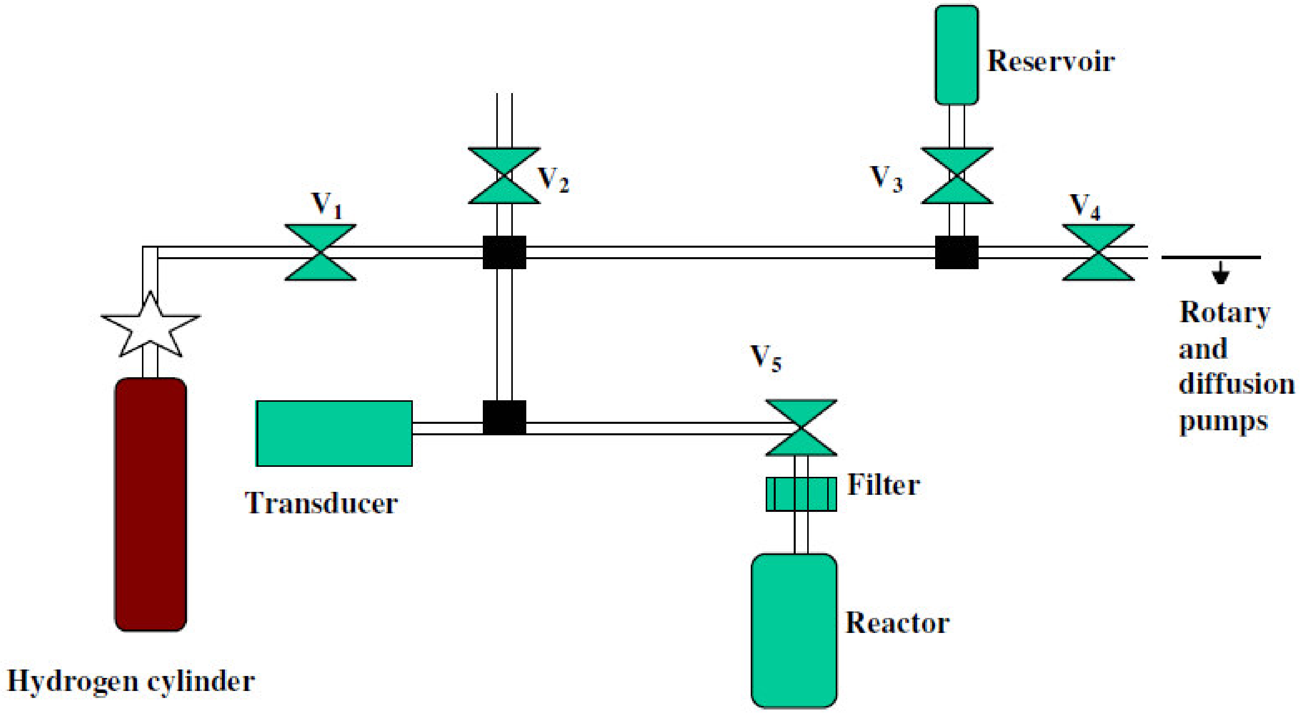

Figure 2.12. Sievert’s type hydriding setup

Hydrogen sorption – desorption experiments were carried out with different samples (Fe_3O_4, Fe_3O_4@Pd, SiO_2@Pd)using Sievert’s Apparatus.

2.2.2.8. X-ray photoelectron spectroscopy (XPS)

Principle

XPS is a technique used to investigate the composition of deposited films by ionizing surface atoms and measuring the energy of ejected photoelectrons. A beam of aluminium or magnesium X-rays irradiate the sample material and simultaneously measures the binding energy and number of electrons that escape (intensity of a photoelectron peak) from the top 0 to 10 nm of the sample material [61]. The method requires the sample of interest to be bombarded with low energy X-rays, produced from an aluminium or magnesium source, with energy of hv. These X-rays cause electrons to be ejected from either a valence or inner core electron shell. The energy of the electron, E, is given by $E = hv - E_1 - \phi$, where E_1 is the binding energy of the atom and ϕ is the work function of the sample. Thus, it is possible to calculate the binding energy of the ejected electron, and therefore identify the atom (and its chemical state) from which the electron originates. In order to prevent surface contamination, analysis is carried out under ultrahigh vacuum ($< 10^{-10}$ Torr).Elements like hydrogen (Z=1) and helium (Z=2) due to their low probability of electron emission cannot be detected by XPS.

As Figure 2.13 illustrates, X-rays are directed onto the sample and the resulting photoelectrons are then focused onto the entrance slit of a concentric hemispherical analyser. Here a negative and positive potential are applied to the outer and inner cylinders, respectively, such that the central line between the cylinders is a line of zero potential. Scanning the potentials allows control of the energy of electrons that are allowed to pass through the analyser and onto the detector, usually a channel electron multiplier (channeltron).

One major disadvantage is the low spatial resolution of the technique, in most cases the analysed area is required to be of the order of a few square mm. Another problem is that only the surface of a sample can be analysed, thus little information relating to the bulk is obtained. This problem can be minimised by carrying out depth profiles in which a beam of argon ions is used to etch away the surface between XPS analyses. In such a way the bulk of a sample can be investigated with XPS.

For X-ray Photoelectron Spectroscopy (XPS) analysis, MgK_α (1253.6 eV) X-ray source and a DESA-150 electron analyser (M/s. Staib Instruments, Germany) were employed for recording the spectra. The binding energy scale was calibrated to Au-$4f_{7/2}$ line of 83.95 eV. The XPS spectra were fitted using XPSPEAK41 software.

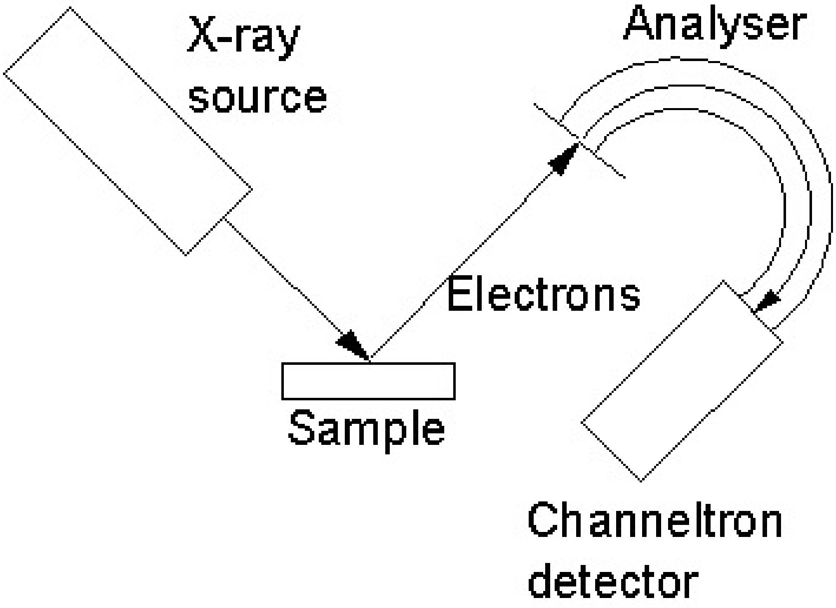

Figure 2.13. Schematic of XPS apparatus

2.2.2.9. Mössbauer Spectroscopy

The Mössbauer effect is the *recoilless nuclear resonance absorption and emission of γ -rays.* A nucleus with Z protons and N neutrons in an excited state of energy E_e and mean lifetime τ of typically 100 ns undergoes transition to the ground state of energy E_g by emitting a γ -quantum of energy $E_g = E_e - E_g$. The γ-quantum may be absorbed by a nucleus of the same kind (same Z and N) in its ground state, whereby transition to the excited state of energy E_e, takes place (resonance absorption). The subsequent transition to the ground state emits again a γ-quantum (resonance fluorescence) or a conversion electron e^- (with nearly tentimes higher probability than γ-emission). The mean lifetime τ determines the width, Γ, of the resonance lines by$\Gamma \times \tau = \hbar$ ($\hbar = h/2\pi$ which is Planck's constant).

Resonance absorption is observable only if the emission and absorption lines overlap sufficiently. No resonance is possible between free atoms or molecules. The Mossbauer Effect cannot, therefore, be observed for freely moving atoms or molecules (gaseous or liquid state). In the solid state, recoilless emission and absorption of $\gamma -$ quanta is possible, and the transition lines can, at least partially overlap and nuclear resonance absorption can be observed. The main components of a Mössbauer spectrometer are shown in Figure 2.14.

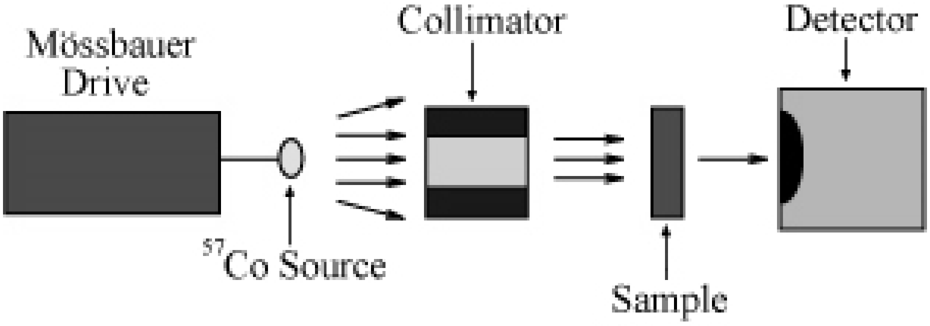

Figure 2.14. Schematic of Mossbauer Spectrometer

Mössbauer spectroscopy can give a quick answer on the valence state (oxidation state, spin state), local symmetry or magnetic properties of a Mössbauer atom contained in the material of interest. It has also proved invaluable in the study of electronic structure, bonding properties, molecular symmetry, magnetic behavior and phase transitions in the solid state [62]. Mössbauer spectroscopy allows for non-destructive phase analysis, which is often employed routinely as a “fingerprint” method. The use of synchrotron radiation instead of radioactive nuclides as sources has opened new pathways for studies of special problems.

Typically, radioactive ^{57}Co with 271 days half-life, which may be generated in a cyclotron and diffused into a noble metal like rhodium, serves as a gamma radiation source for ^{57}Fe Mössbauer Spectroscopy (Figure 2.15). ^{57}Co decays by e - capture (EC from K-shell, thereby reducing the proton number, from 27 to 26 corresponding to ^{57}Fe) and initially populates the 136 keV nuclear level of ^{57}Fe with nuclear spin quantum number I = 5/2. This 136 keV excited state decays after 10 ns and populates - with 91% probability the 14.4 keV level by emitting 122 keV gamma quanta and with 9% probability that it decays directly to the ground state of ^{57}Fe. The 14.4 keV nuclear state has a half-life of 100ns. Both the half-life and the emitted gamma quanta of 14.4 keV energy are ideally suited for ^{57}Fe Mössbauer Spectroscopy. Nuclides suitable for Mössbauer Spectroscopy should possess excited nuclear states with lifetimes in the range of 10^{-6} to 10^{-11}s and transition energies between 5 -180 KeV. Longer (shorter) lifetimes than indicated lead, according to the Heisenberg Uncertainty Principle, to too narrow (broad) emission and absorption lines, which no longer effectively overlap. When the atoms are within a *solid matrix* the effective mass of the nucleus is very high. The recoiling mass is now effectively the mass of the whole system, so if the gamma-ray energy is small enough the recoil of the nucleus is too low to be transmitted as a phonon (vibration in the crystal lattice) and so the whole system recoils, making the recoil energy practically zero: a *recoil-free event*. Transition energies beyond 180 keV cause too large recoil effects which destroy the resonance. Gamma quanta with energies smaller than 5 keV will mostly be absorbed in the source and absorber material.

Doppler shifts are provided to the 14.4 keV $\gamma -$ ray coming from the source by using small mechanical motions and tuning them through the nuclear resonance of the absorber (Figure 2.16).

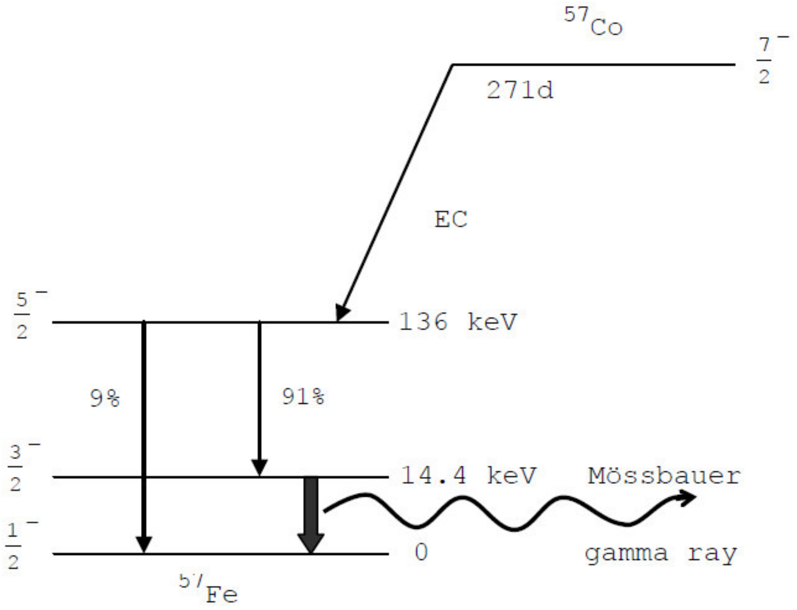

Figure 2.15. Nuclear decay scheme of ^{57}Co showing the transition giving the 14.4 keV Mössbauer gamma ray

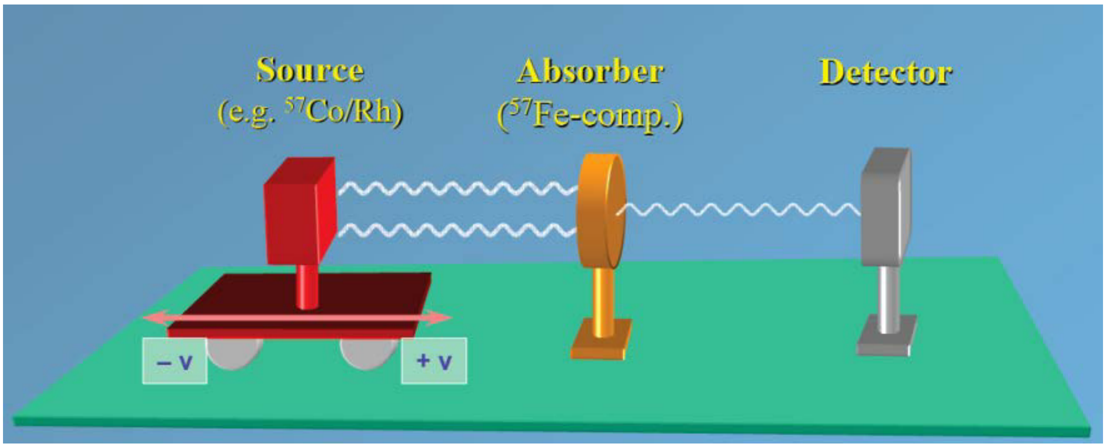

Figure 2.16. Mössbauer Experiment – Source and absorber are moved relative to each other with Doppler velocity

Mössbauer spectra give quantitative information on “hyperfine interactions,” which are small energies from the interaction between the nucleus and its neighbouring electrons. Mössbauer spectra at room temperature were recorded using a Mössbauer spectrometer operated in constant acceleration mode (triangular wave) in transmission geometry. The source employed was Co-57 in Rh matrix of strength 50 mCi. The calibration of the velocity scale was done by using an enriched α-^{57}Fe metal foil with effective nuclear hyperfine field (H_{eff}) value of 331 kOe at room temperature. The outer line width of calibration spectra was0.29 mm.s^{-1}. The Mössbauer spectra were fitted by using Win Normos fit programme with Lorentzian distribution. The results of isomer shift were relative to $\alpha - \mathrm{Fe}$ metal foil (δ = 0.00 mm.s^{-1}).

2.2.2.10. Ultraviolet (UV) - Visible Absorption Spectrophotometry

UV - Visible Spectrophotometry covers 200 nm - 800nm region of the Electromagnetic Spectrum. When a beam of monochromatic radiation of a suitable frequency passes through a solution, it is absorbed by the solution. As a result, the intensity of light when it finally emerges from the solution is considerably reduced. In other words, when the energy of the incident photon matches with the energy of the excited state of an atom (or a molecule, radical or an ion) resonance occurs, and the intensity of the transmitted light is decreased. Depending on the energies of the excited states and the absorbed photons, absorption band is observed.

The intensity of the beam is defined as the energy falling on unit area perpendicular to the beam per unit time. It is proportional to the number of photons incident on unit area in unit time.

The two laws governing absorption are known as Beer-Lambert law. According to Lambert's law when a monochromatic radiation passes through a transparent medium, the rate of decrease in intensity with the thickness of the medium is proportional to the intensity of the radiation i.e. the intensity of the emitted light decreases exponentially as the thickness of the absorbing medium increases arithmetically. Mathematically the law is expressed as

$$\mathrm{I_t} = \mathrm{I_0}\, \mathrm{e}^{-\mathrm{kl}}$$

Where,

'I_0' is the intensity of the incident light of wavelength λ,

'l' is the thickness of the medium

'k' is a proportionality factor for the wavelength and the absorbing medium used.

According to Beer's law the intensity of a beam of monochromatic radiation decreases exponentially as the concentration of the absorbing substance increases arithmetically. This is written as

$$I_t = I_o e^{-k'c}$$

Where, 'c' is the concentration.

Combining the two equations and changing the logarithmic scale, we have

$$A = \log\left(\frac{I_0}{I_t}\right) = \varepsilon cl$$

According to this equation, the intensity of a beam of monochromatic radiation decreases exponentially with increase in the thickness- l and the concentration- c of the absorbing medium. Here, if c is expressed in mol L^{-1} and l in cm, µ is known as the molar absorption coefficient or molar absorptivity. For a given specimen, µ depends on the wavelength of the incident radiation, the temperature and the solvent employed. Log (I_o/I_t) is the absorbance (A) of the medium. I_t/I_o is the fraction of the radiation transmitted by a thickness l of the medium and is called the transmittance, T.

$$A = \log(\frac{1}{T})$$

$$A = \log(\frac{100}{\%T})$$

$$A = 2 - \log(\%\,T)$$

Instrument

A double beam UV - Visible Spectrophotometer (K-MAC Technology, South Korea) was used for absorption measurement in the case of Cr(VI) and U(VI) reduction by formic acid using Pd Nanocatalyst coated on Inorganic host materials (Fe_3O_4 and SiO_2). The schematic is shown in Figure 2.17.

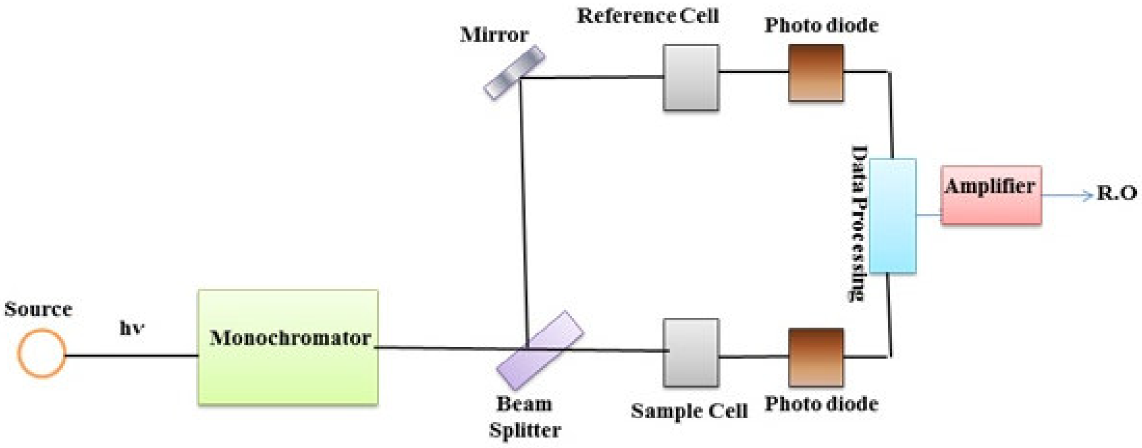

Figure 2.17. Double-beam Ultraviolet-Visible Spectrophotometer

Procedure

To understand the kinetics of reduction process, the successive UV-Vis spectra were recorded to monitor the characteristic absorbance related to the concentration of Cr(VI) and U(VI) ions respectively. 10 mL of 7mM of Cr(VI) (using $K_2Cr_2O_7$) and 10 ml of 70mM formic acid were taken in a beaker and pH of the solution was adjusted to 2. The temperature of the solution was raised to 323 K using constant temperature bath. Since, Pd@Fe_3O_4 contained12 mg of Pd/gm of Fe_3O_4 thus 100mg of Pd@Fe_3O_4 (containing 1 mg of Pd) was added to the above solution. The absorbance of Cr(VI) was measured at different time intervals (0, 1, 5, 10, 15, 30. 45, 90 min) by taking 1mL sample of the solution mixture in a cuvette and diluting it to 3mLby adding distilled water.

In the similar way, Pd@SiO_2 contained 20 mg of Pd/gm of SiO_2, hence 50mg of Pd@SiO_2(containing 1 mg of Pd) was added to the above solution and the experimental procedure was repeated as mentioned above.

The reduction U(VI) was also studied in a similar fashion using the reaction solution prepared by mixing equal volumes (8 mL) of 0.1 mol L^{-1} $UO_2(NO_3)_2$ solution at pH=2 and 1mol L^{-1} formic acid.

2.2.2.11. Fourier Transform Infrared Spectroscopy

Infrared radiation causes atoms and group of atoms of compounds to vibrate faster about the covalent bonds which connect them and thus causes net change in their dipole moment [63]. The alternating electrical field of the radiation interacts with fluctuations in the dipole moment of the molecule. If the frequency of the radiation matches with the vibrational frequency of the molecule the radiation will be absorbed, causing a change in the amplitude of molecular vibration. Molecular vibrations are divided into stretching and bending. Fourier transform infrared spectroscopy is preferred over dispersive methods of infrared spectral analysis for several reasons:

- It is a non-destructive technique.
- It provides a precise measurement method which requires no external calibration.
- It can increase speed, collecting a scan every second.
- It can increase sensitivity – one second scans can be co-added together to ratio out random noise.
- It has greater optical throughput.
- It is mechanically simple with only one moving part.

It is vital that the wavenumbers, and hence peak positions, in an infrared spectrum be measured reproducibly. FTIR contains a laser that acts as an internal wavenumber standard, which gives rise to a precision of ±0.01 cm^{-1}.

A common FTIR spectrometer consists of a source, interferometer, sample compartment, detector, amplifier, A/D convertor, and a computer. The source generates radiation which passes the sample through the interferometer and reaches the detector. The signal is then amplified and converted to digital signal by the amplifier and analog-to-digital converter, respectively. Eventually, the signal is transferred to a computer in which Fourier transform is carried out. Figure 2.18 is a block diagram of an FTIR spectrometer.

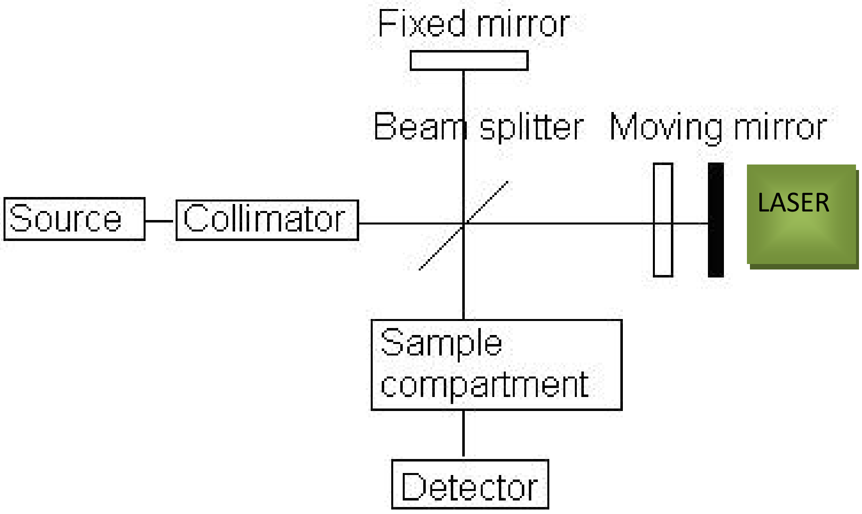

Figure 2.18. Block diagram of an FTIR spectrometer

The major difference between an FTIR spectrometer and a dispersive IR spectrometer is the Michelson interferometer. The Michelson interferometer, which is the core of FTIR spectrometers, is used to split one beam of light into two so that the paths of the two beams are different. The Michelson interferometer then recombines the two beams and conducts them into the detector where the difference in the intensity of these two beams is measured as a function of the difference of the paths.

A typical Michelson interferometer consists of two perpendicular mirrors and a beamsplitter. One of the mirror is stationary and another one is movable. The beamsplitter is designed to transmit half of the light and reflect half of the light. Subsequently, the transmitted light and the reflected light strike the stationary mirror and the movable mirror, respectively. When reflected back by the mirrors, two beams of light recombine with each other at the beamsplitter. The single light beam that leaves the interferometer, interacts with the sample, and strikes the detector. The resulting signal is called an interferogram which has the unique property that every data point (a function of the moving mirror position) which makes up the signal has information about every infrared frequency which comes from the source. The measured interferogram signal cannot be interpreted directly because the analyst requires a frequency spectrum (a plot of the intensity at each individual frequency) in order to make identification. The "decoding" of individual frequencies are accomplished by Fourier transformation.

FTIR analyses were carried out using JASCO FT-IR/420 (JAPAN) make model. The samples were mixed with anhydrous KBr in the 5:95 weight percentages and pressed into pellets under high pressure and used for FTIR analysis. The % transmittance of the samples was measured at different wavenumbers in the range between 400-4000 cm−1 by averaging 16 scans for each spectrum.

Chapter -3

Determination of Deuterium pick - up in Zr - Nb alloy by Hot Vacuum Extraction - Quadrupole Mass Spectrometry

3.1. Introduction

Dilute zirconium alloys are used as coolant channels (also known as pressure tubes) (Table 3.1) in Pressurized Heavy Water Reactors (PHWRs) because of their adequate aqueous corrosion resistance, low neutron absorption cross-section, good mechanical properties at elevated temperature, and irradiation stability [64].

Table 3.1 Dilute Zirconium Alloys for PHWR coolant channels [65]

Zr alloys	Chemical Composition						Short-comings
	Sn wt%	**Fe wt%**	**Cr wt%**	**Ni wt%**	**Nb wt%**	**Zr**	
Zircaloy-2	1.5	0.15	0.1	0.05	-	Rest	Nickel accelerates the absorption of hydrogen into zirconium
Zircaloy-4	1.5	0.2	0.1	0.0075	-	Rest	Corrosion under aggressive condition
Zr-2.5% Nb alloy	-	-	-	-	2.5	Rest	Better corrosion behaviour, lower absorption of hydrogen

These coolant channels are coated with a thin layer of oxide to prevent hydride formation. Though the initial hydrogen content (H) in the coolant channels is maintained less than 5 ppm, these components later pickup additional hydrogen/deuterium (D) during service. If hydrogen/deuterium concentration exceeds that of terminal solid solubility, it will precipitate as zirconium hydride/deuteride [66]. This causes embrittlement of the host matrix through phenomena-like stress orientation of hydrides, delayed hydride cracking, and hydride blister formation. Ageing management of coolant channels therefore, requires knowledge of extent of deuterium pick-up as well as pick-up rate along with its quantification to assess the integrity of coolant channel for its continuous use or take appropriate remedial measures including its replacement. If the pick-up rate is available, then it would be possible to predict the time required for the ingressed deuterium to reach terminal solid solubility limit at the operating temperatures.As the utility of the zircaloy coolant channels is dictated by hydrogen/deuterium content, its monitoring at regular time intervals is essential. It may be mentioned that during the operation of PHWRs only deuterium will be picked-up [67]. The whole exercise, therefore, is to determine deuterium pick-up in wafer-thin sliver samplesscraped from the interior of the coolant channels after removing the protective oxide layer, so that the integrity of the channel can be ensured for its continued usage. It is desirable to take sliver samples at multiple points from the interior of the coolant channels to cover as many vulnerable locations as possible. Figure 3.1 shows typical locations for taking sliver samples.

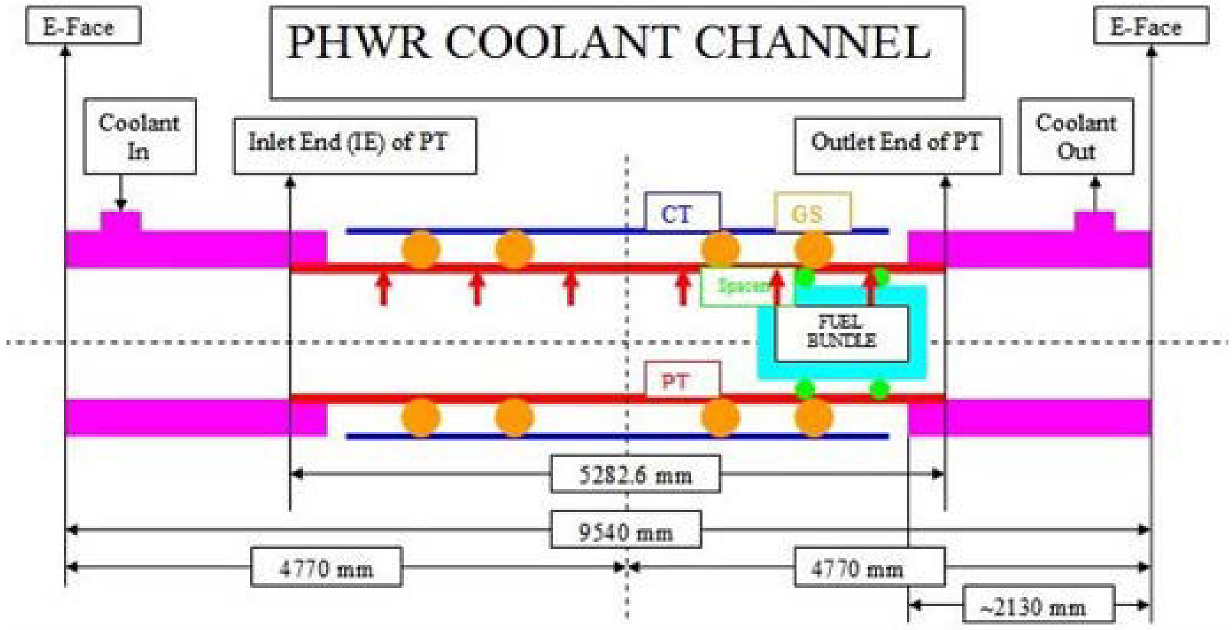

Figure 3.1. Probable Slivering locations of a coolant channel

The sliver samples are taken using a special tool designed for this purpose [68]. The tool has spring loaded cutters which scrape the sample by application of calculated amount of pressure. Slivering is done in wet condition. Figure 3.2 shows a picture of sliver sampling tool.

Figure 3.2. Sliver Sample scraping tool[68]

Front cutter scrapes off & holds oxide layer whereas back cutter follows for metallic layer at same location with small dimensions. A reasonably oxide free metallic sliver sample of 60-110 mg is retrieved. It is essential that oxide layer should be completely removed from the sliver sample. Otherwise the results will be erroneous. Figure 3.3 shows scraped Zr-2.5% alloy sample.

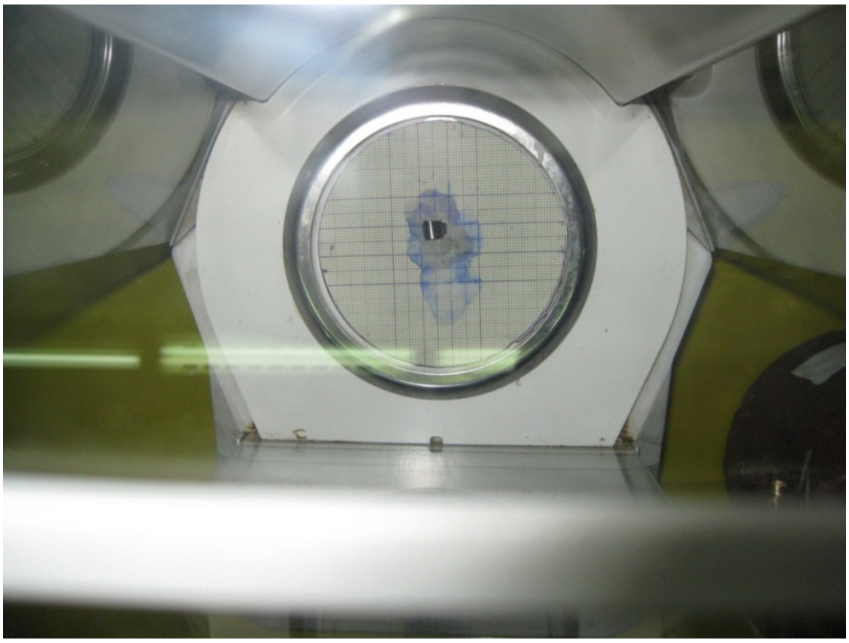

Figure 3.3. Scraped/Slivered metal sample[Obtained from RAPS # 4]

3.2. Methodologies available for hydrogen determination

The inert gas fusion (IGF) method with thermal conductivity detection (TCD) is commonly used to measure hydrogen content in metals and alloys including zirconium alloys [69]. TheIGF -TCD instruments are commercially available for this purpose. This method though simple and fast, but the results for hydrogen could be erroneous if the analysed gas also contains the heavier isotope deuterium. For the same number of moles, the response of TCD for deuterium will be less than for hydrogen as thermal conductivity of deuterium is about 30% less than that of hydrogen. This results in an underestimate of results. Further, in these dedicated instruments, the response of TCD is converted into concentration units (µg/g of sample) and this introduces another error because entire gas being measured is assumed to be only hydrogen gas with molecular weight equal to 2. No allowance is made for the presence of deuterium and its molecular weight 4. Thus, the weight concentration of deuterium is measured as half of the expected value. This underestimation is proportional to the isotopic content of deuterium. Further, IGF – TCD gives only total hydrogen + deuterium content and not isotopic information. Correction methodologies have been reported in literature to account for deuterium in the sliver samples when IGF-TCD technique is employed [26]. However, the correction needs information on mole fractions of deuterium and hydrogen in the sample. This calls for another independent measurement technique.

Since, it is necessary to maintain the integrity of the coolant channel even after taking out some sample for the analysis, only very small quantity of sliver sample (~ 10 - 20 mg of zircaloy) will be available for the analysis. Therefore, IGF-TCD cannot be employed mainly due to two reasons viz. i) low sliver sample size and ii)for applying the correction factor, one more aliquot of the same sample has to be analysed (for determination of X_D)by using Hot Vacuum Extraction – Quadrupole Mass Spectrometer method. Further, oxide layer if present, results will not correspond to hydrogen/deuterium content in the virgin surface.

Differential Scanning Calorimetry (DSC) has also been employed for determination of hydrogen/deuterium in the sliver samples [70]. One advantage of DSC is that the results are not affected due to the presence of oxide layer. However, it also suffers from the limitation of not being amenable to provide isotopic information.

Nuclear techniques involving neutron scattering or heavy ion induced reactions are time consuming and cannot be applied for routine analysis.

Only hot vacuum extraction mass spectrometry(HVE-MS) can determine hydrogen and deuterium contents separately [71-74]. Previous investigations carried out in our laboratory [75] reported the feasibility of adopting HVE-QMS for the determination of hydrogen and deuterium. Only standardization and validation of the methodology was reported. However, quantification of analytical results for both hydrogen and deuterium in the case of actual irradiated samples was not carried out. While enough literature is available on the determination of hydrogen or deuterium content in zircaloy samples, most of the work was related to the H/D charged zirconium samples and very few are on the actual irradiated coolant channels [76]. The majority of them focused on either modelling studies or the effects of oxide layers or impurities on ingress, with little details on the measurement methodology for determination of hydrogen/deuterium.

3.3. Present Studies

The present studies have therefore been directed to:

(i) Optimization of conditions for the determination of hydrogen and deuterium content in a typical irradiated Zr-Nb coolant channel employing hot vacuum extraction-quadrupole mass spectrometer (HVE-QMS),

(ii) Determination of sensitivity factors for hydrogen and deuterium for quantification of results when using QMS. This is due to the fact that the very large mass difference between hydrogen isotopes (a factor of 2 between H_2 and D_2) brings in significant mass discrimination during measurements. This is an essential requirement in calculating ingress of deuterium in coolant channels of PHWRs,

(iii) Measurements on sliver samples from coolant channels for hydrogen and deuterium,

(iv) Study the formation of molecular ion (H_3^+) in quadrupole mass spectrometer and its effect on measurements.

3.4. Experimental

3.4.1.Hot Vacuum Extraction - Quadrupole Mass Spectrometry (HVE-QMS)

Hot vacuum extraction of gases from Zircaloy samples was carried out using a indigenously designed and fabricated set up. This set up has been coupled to a commercial Quadrupole mass spectrometer [75]. A schematic of the setup is shown in Figure 3.4.

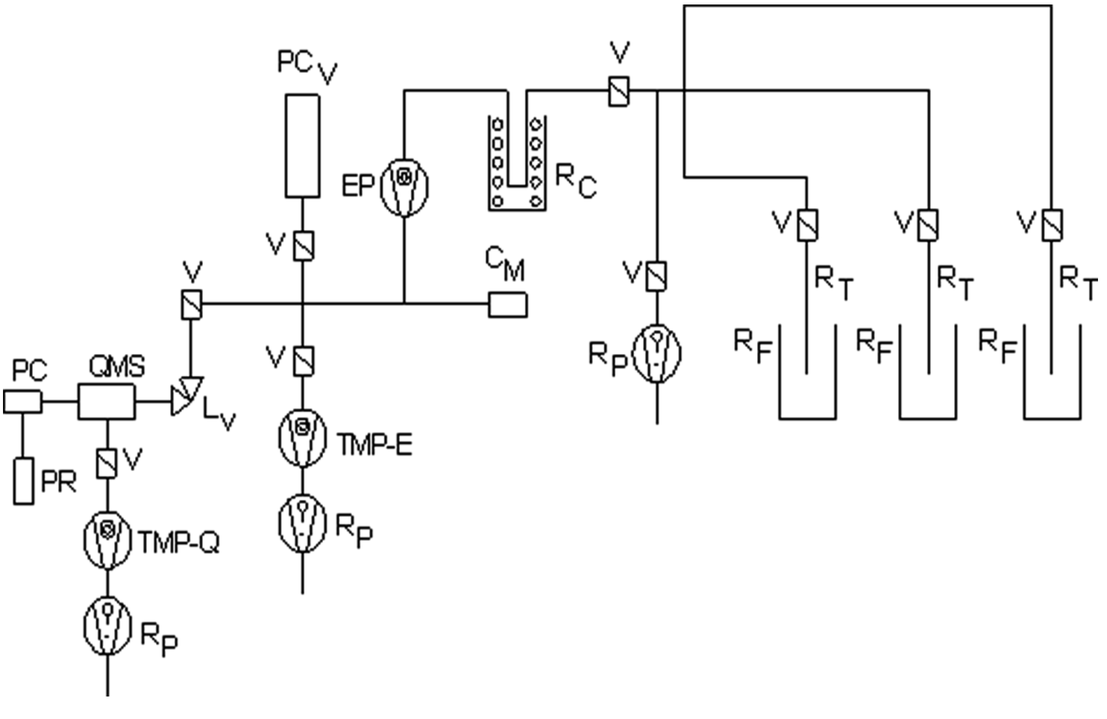

Figure 3.4. Schematic diagram of Hot Vacuum Extraction -Quadrupole Mass Spectrometry (HVE-QMS) System

The hot vacuum extraction system is made up of stainless steel tubing impervious to gas diffusion. Only NWCF type joints and all metal valves are used in this equipment. HVE-QMS system has quartz reaction tubes (R_T) in which sample is heated under vacuum, a resistance furnace (R_F) to heat the sample to required temperature, a turbo molecular pumping system (TMP-E) to evacuate the system, a nude and sealed turbo molecular pump as an ejector pump (EP) to extract the gases, dry rotary pumps (R_P) as back-up pumps to the TMP, refrigeration coil (RC) to condense the condensable gases, a pre-calibrated volume (PCV) into which the gases are extracted, and a high precision capacitance manometer (CM) to measure the pressure accurately. Extracted gases, after measurement of the pressure, are fed into HAYDEN, UK make quadrupole mass spectrometer (QMS) through a micro-leak valve (LV) to measure the gas composition. A turbo molecular pumping station (TMP-Q) evacuates the QMS. QMS works at 10^{-2}Pa pressure. Pressure tolerated by micro-leak valve is 10^{-3}Pa/s. For taking one spectra (five repetitive scans) 5 minutes (300s) are required. So, through micro-leak valve 0.3 Pa(10^{-3} Pa/s x300s) pressure is entered into the QMS which is more than the pressure that QMS bears (10^{-2}Pa). Therefore a turbo molecular pumping station is provided to evacuates the QMS and maintain its working pressure. The entire system and the tubing arewrapped in heating jackets to maintain the temperature constant at353 K to prevent occlusion of moisture inside the tubing. An on-line personal computer acquires the data in peak select mode and the gas composition is computed employing an off-line program.

With a view to increasing the sample throughput, four resistance furnaces are connected in parallel and the samples are heated in sequence one after the other thus reducing the time required for sample change over.

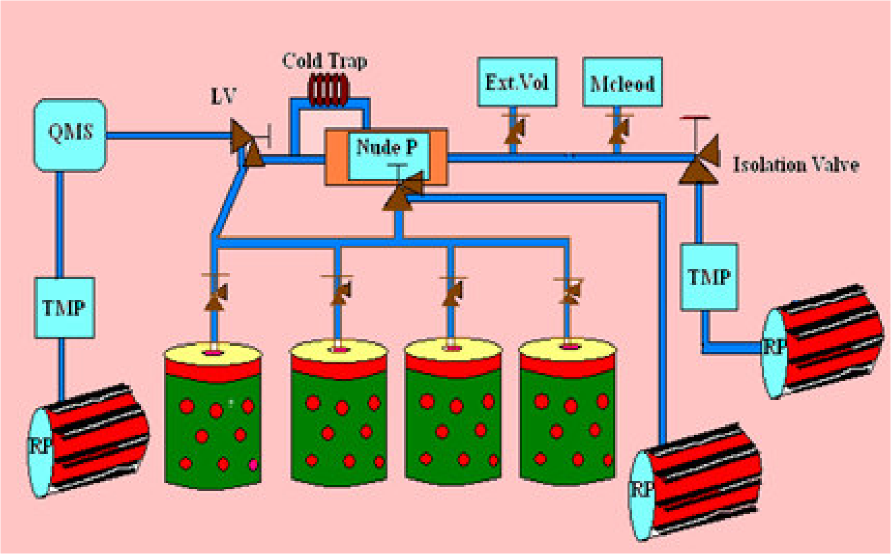

Figure 3.5. Multiple sample analysis module

3.4.2. Sensitivity Factors of Hydrogen and Deuterium in QMS

For determination of sensitivity factors of hydrogen and deuterium, H_2 and D_2in pure gaseous form were taken in the system at various pressures (10^{-1} to 8 Pa), separately. The respective gas cylinder was connected to the system and the gas was allowed to fill the expansion chamber of known volume (pre-calibrated earlier) at a particular pressure. The pressure was monitored by a capacitance manometer. The gas was then fed into QMS through micro leak valve and intensities at various m=z values (1, 2, 3, 4, 18, 28, 32, and 44) are monitored.

3.4.3. Samples

For standardization and validation of analytical results, reference materials for hydrogen (Ti steel and Zr) were employed. Sliver samples received from irradiated Zr-Nb pressure tubes were analysed for deuterium determination. These were cleaned with pure carbon tetrachloride in an ultrasonic cleaner to remove the contamination with oil and loose particles. They were then air dried at room temperature prior to the analysis.

3.4.4. Procedure

The sliver sample weighing about 50 mg was taken in the quartz tube which was then connected to the system with CF 16 joint employing oxygen free high conducting (OFHC) copper gasket. Initial evacuation was carried out with a rotary pump to remove atmospheric gases and then evacuated by TMP-E to a vacuum better than 10^{-4}Pa. The quartz tube, containing the sample, was then heated by the resistance furnace employing a temperature programmer. Degassing of the sample was carried out at 373 K for removing moisture and surface contamination due to organic materials. The outlet valve at the quartz tube end was closed and the temperature was slowly raised at the rate of 283 K/min up to 1323 K and maintained at this temperature for 10 minutes. The valve was then opened and the evolved gases were extracted into the known volume for 10 minutes, by the nude TMP through refrigeration trap for condensing the condensable gases. The pressure exerted by the non-condensable gases was measured by employing a high precision capacitance manometer. The gases were then fed to the on-line quadrupole mass spectrometer through the micro leak valve. A typical mass spectrum is shown in Figure 3.6(i). Peak intensities at m/z =1, 2, 3, 4, 18, 28, 32, and 44 corresponding to H^+, H_2^+/D^+,HD^+, D_2^+, H_2O^+, CO^+/N_2^+, O_2^+ and CO_2^+, respectively, were monitored. A blank experiment was also carried out without sample i.e. with only quartz tube connected to the system and following the aforementioned procedure. The signal intensities at different m/z values were corrected for the corresponding blank contribution (recorded prior to the sample analysis) Figure 3.6(ii). The blank corrected intensities were divided with respective relative sensitive factors to arrive at the true intensities. From these data the mole fraction of hydrogen and deuterium was calculated as

$$X_H = \frac{(I_2 + \left({}^{I_3}\!/_{2} \right))}{({}^{I_1}\!/_{2} + I_2 + I_3 + I_4 + I_{18} + I_{28} + I_{32} + I_{44}}$$

$$X_D = \frac{({}^{I_3}/_2 + I_4)}{({}^{I_1}/_2 + I_2 + I_3 + I_4 + I_{18} + I_{32} + I_{44})}$$

Where $I_i$is the true peak intensity at m/z value of ''i''. Partial pressure of hydrogen or deuterium is arrived at by multiplying total pressure with respective mole fractions. Hydrogen and deuterium content was calculated employing ideal gas equation from partial pressure and total volume of the system.

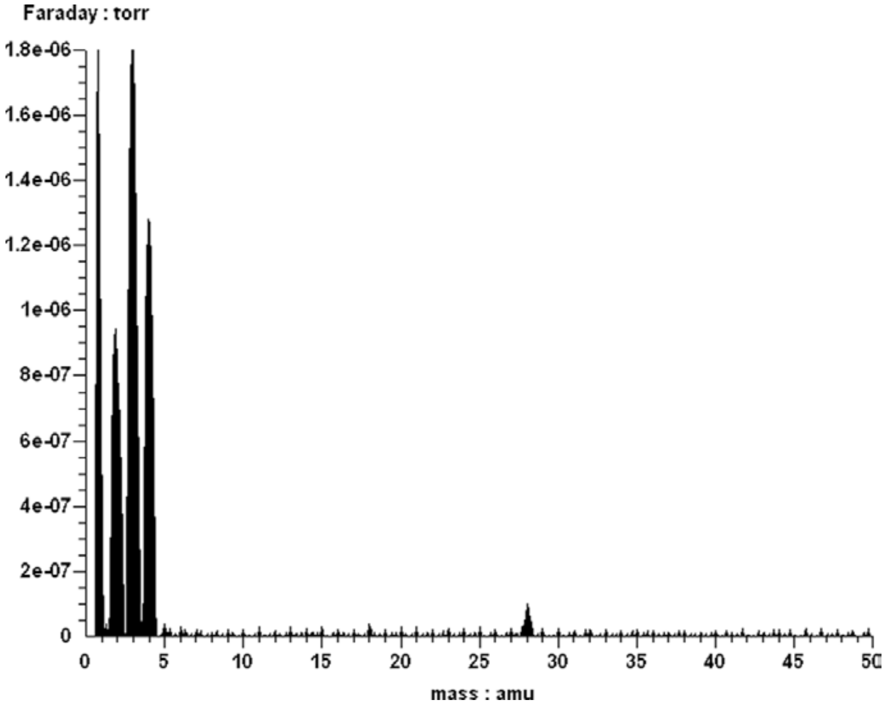

Figure 3.6 (i). Typical mass spectra of gases released from the sliver sample of irradiated Zr-2.5%Nb alloy coolant channel

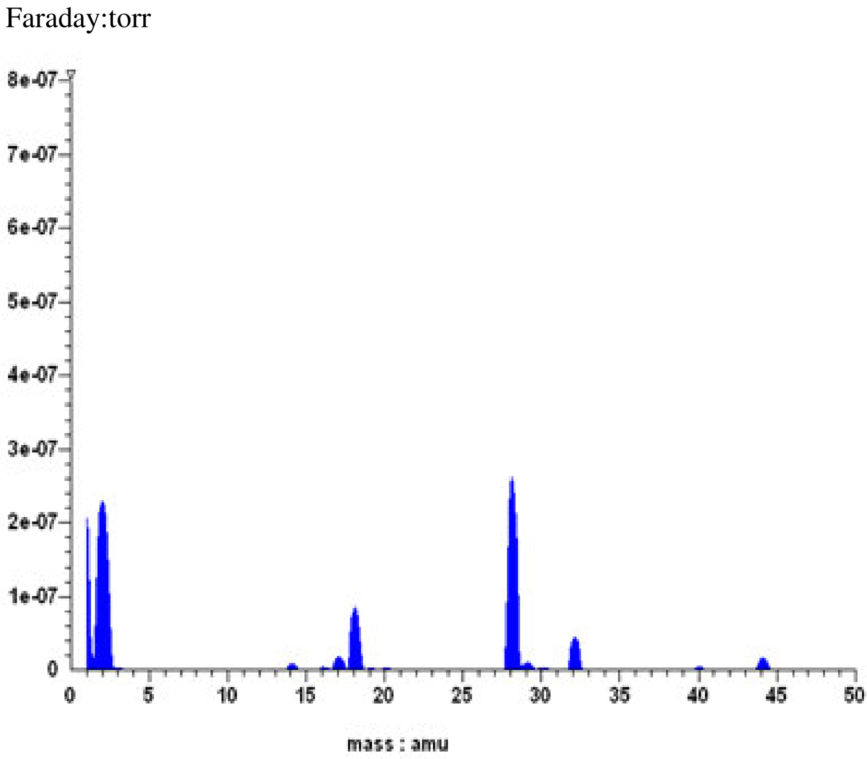

Figure 3.6 (ii). Typical mass spectra of the Blank

3.4.5. Calculation

Hydrogen and deuterium content is calculated employing ideal gas equation from partial pressure and total volume of the system.

Partial Pressure of Hydrogen/Deuterium = $X_{H/D}$ x P

Where, P = total pressure obtained by HVE.

$X_{H/D}$ = mole fraction of hydrogen/deuterium

Hydrogen Content is

$$\mathbf{C = \frac{I_{H2}}{I_{Tot}} \times \frac{PV}{RT} \times \frac{2}{W_{Sam}}}$$

Deuterium Content is

$$\mathbf{C = \frac{I_{D2}}{I_{Tot}} \times \frac{PV}{RT} \times \frac{4}{W_{Sam}}}$$

where,

C = Concentration

$I_{H2/D2}$= Peak intensity due to hydrogen/deuterium

I_{Tot}= Total peak intensity

P = Corrected pressure exerted due to the gases released from the sample

V = Volume into which the gases are collected

T = Room temperature

R = Gas constant

W = Weight of the sample

3.5. Results and Discussion

3.5.1. Requirement of Relative Sensitivity Factors (RSFs)

Typically in a quadrupole mass spectrometer, the ion intensities (m/z) of individual gaseous species are measured and these are then correlated to their partial pressures and then to gas composition. The gas composition has to be derived from the peak intensities at various m/z values after blank correction. The peak intensity of any gas recorded in QMS analysis depends on its nature such as its molecular mass, ionization potential and ionization cross section, and also such other physical actors like diffusion through micro leak, vacuum pump characteristics and acceleration for ion focusing in QMS. This necessitates the determination of sensitivity factors for various gases in QMS. Due to very large difference between the relative masses (a factor of 2 between H_2 and D_2), the isotopic intensities by QMS for H_2^+, HD^+, D_2^+ are not expected to be same even for same partial pressures of the species. Theoretically, the sensitivity factor for any gas I with mass number M, in QMS is the ratio of blank-corrected intensity at m/z value of M and partial pressure of the gas I in the mixture (I_M/P_I) [78].Normally the sensitivity factors for gases are determined relative to Nitrogen (RSF = 1).

3.5.2. Pressure and Volume Calibration

Accurate pressure and volume measurements are key parameters for the analysis. Pressure is measured with capacitance manometer (10^{-3} Pato 11 Pa) with an accuracy of 0.5% of reading and repeatability of ±0.003 Pa. The volume of the collection chamber was arrived at by expanding dry nitrogen gas of pre-calibrated volume after measuring its pressure. The pressure was measured again after expanding nitrogen in the pre-calibrated volume into the collection chamber. Employing ideal gas equation, the volume of entire collection chamber including pre-calibrated volume was measured. This procedure was repeated for five times. The total volume of the collection chamber was found to be 2100mL with standard deviation of 70mL.

3.5.3. Quantitative Extraction

Initial experiments were carried out to optimize the temperature and time of extraction. The gases were released from the sample from 1173 K onward, but the quantitative extraction as measured by the constancy in pressure measurement took almost 60 minutes. When the temperature was 1473 K or more, the extraction was over in less than 5 minutes, but at such high temperature, the structural integrity of quartz tube deteriorated rapidly. As a compromise, a temperature of 1323 K was used and extraction time of 10 minutes was found to be optimum.

3.5.4. Mass Spectra for H_2+D_2

Whenever both hydrogen and deuterium are present in the sample, the mass spectrum reveals peaks at m/z's 1 (due to H^+), 2 ($H_2^+ + D^+$), 3 (HD^+), and 4 (D_2^+). During heating of the sample, nascent H and D are released and they combine to form H_2, HD, and D_2. The atom fraction of deuterium [D] is calculated using the expression $[D] = [D_2] + \frac{1}{2}[HD]$ [77]. It may be mentioned that while calculating the total intensity due to hydrogen isotopes, it was assumed that the intensity at m/z=2 is completely due to H_2^+ and the contribution from the atomic D^+ is ignored. This is justified, as the ratio of corrected intensities at m/z 2 and 4 in the mass spectra of pure D_2 was found to be less than 0.01. Similar observation was also made in the case of pure hydrogen where $I_1/ I_2 \leq 0.01$. Hence the uncertainty associatedwhile ignoring the contribution from D at m/z=2 is expected to be negligible.

3.5.5. Sensitivity Factors

In all the experiments, it was observed that the blank-corrected intensities at m/z values 18, 28, 32, and 44 were found to be zero. This may be due to the fact that the operating temperature (1323 K) used for extracting hydrogen without any accelerators or flux, might not be sufficient [79] to release the gases like N_2, CO, O_2 and CO_2 from refractory materials such as the Zr-Nb alloys.

The sensitivity factor (S_i) for H_2as well as for D_2, was determined at various pressures from 10^{-1} to 8 Pa. As the mass spectral intensity is plotted in the units of torr in the on-line data processing unit of QMS, the pressure is also expressed in units of torr. Mass spectral intensity versus pressure of the gas in the collection chamber was plotted for both hydrogen and deuterium. The plots are shown in Figure 3.7 and 3.8 for hydrogen and deuterium respectively. From the slope of linear regression data, the sensitivity factors were determined. The S_{H2} value for H_2 was found to be 1.79×10^{-5} with standard deviation of 0.18×10^{-5}. Similarly sensitivity factor for D_2 (S_{D2}) was found to be $1.18 \times 10^{-5}$with standard deviation of 0.07×10^{-5}. Due to practical difficulty in the preparation of pure HD gas, sensitivity factor for HD was calculated as arithmetic mean of sensitivity factors of H_2 and D_2. Therefore, the calculated sensitivity factor for HD (S_{HD}) is $(1.48 \pm 0.19) \times 10^{-5}$. The relative sensitivity factors with respect to hydrogen for H_2, HD, and D_2 are 1.000, 0.83 and 0.66respectively. It may be mentioned that Pyper et al. determined sensitivity factors employing pure H_2, D_2, and HD and their results indicated that sensitivity factor for HD is very close to arithmetic mean of S_{H2} and S_{D2} .

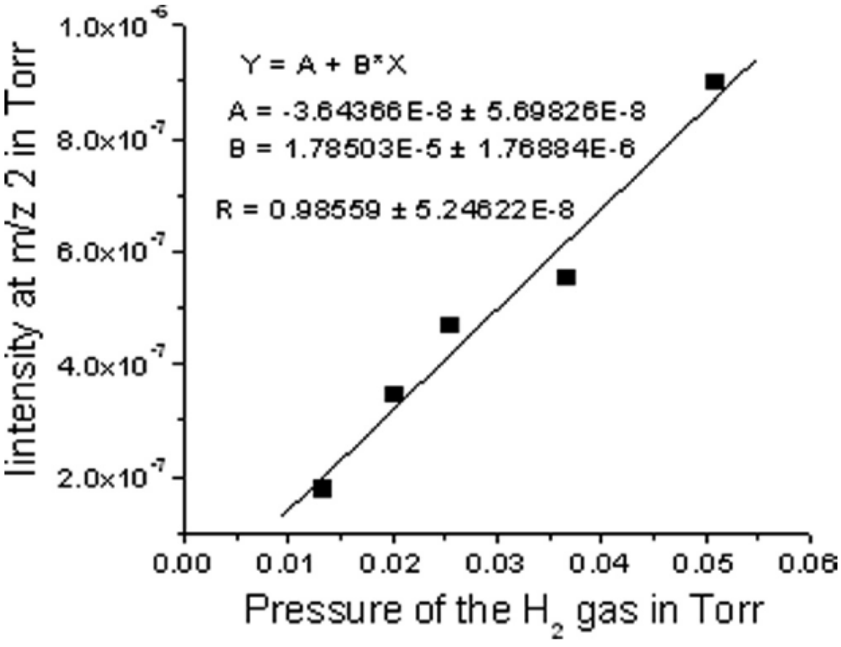

Figure 3.7. Plot between intensity versus pressure of H_2 gas in collection chamber.

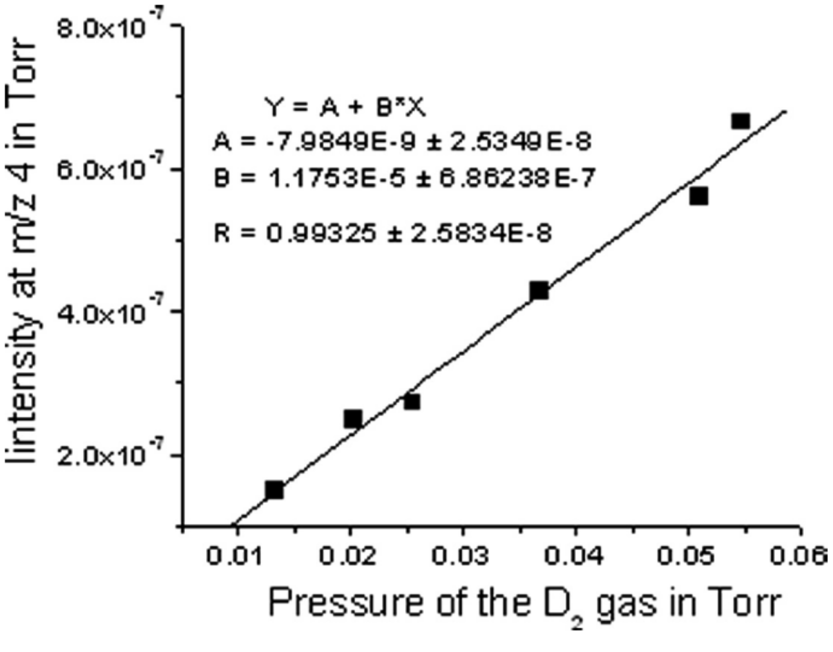

Figure 3.8. Plot between intensity versus pressure of D_2 gas in collection chamber.

To validate these relative sensitivity factors, mixtures of $H_2$and $D_2$with varying mole fractions were prepared. Hydrogen and deuterium gases were produced by reducing H_2O and D_2O in known mole ratios with calcium metal (as shown in Figure 3.9). High purity calcium metal freshly taken out of an inert glove box was used for reduction. The evolved gaseous mixture was dried by passing through anhydrous magnesium perchlorate, collected in the pre-calibrated volume at 0.5 Pa pressure, and then fed into QMS through the micro leak valve at the same leak rate as was used for calibration experiments.

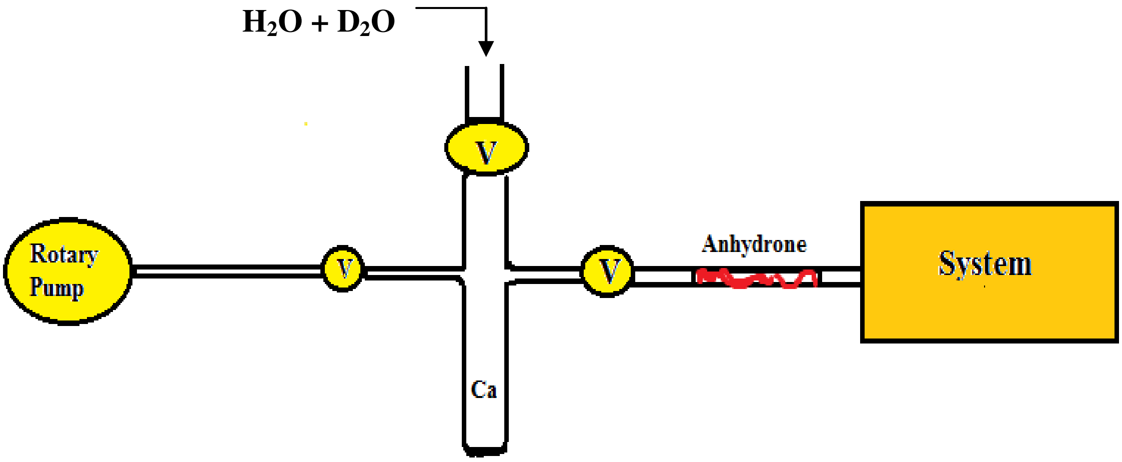

Figure 3.9. Reduction of H_2O and D_2O

Blank-corrected intensities for H_2, HD and D_2 were calculated and composition of the gas (mole fraction of H_2 and D_2) was determined employing relative sensitive factors as mentioned in the Experimental section. Results are given in Table 3.2. From the table, it can be seen that there is no difference between observed and the expected values, confirming the validation of the sensitivity factor measurements.

Table 3.2 Determination of composition of H_2 and D_2 mixture

Sr. No.	Water composition (mole fraction)		Observed Gas Composition (mole fraction)[a]	
	H_2O	D_2O	H_2	D_2
1.	0.60	0.40	0.59±0.06	0.41±0.04
2.	0.50	0.50	0.49±0.05	0.51±0.05
3.	0.30	0.70	0.31±0.03	0.69±0.07
4.	0.90	0.10	0.92±0.09	0.08±0.01

[a] Mean of four determinations with standard deviation.

3.5.6. Molecular ion formation

As discussed previously, the partial pressure of hydrogen and deuterium was calculated from the peak intensities at m/z 2, 3 and 4. Peak at m/z = 3 was assumed to be due to HD^+. Depending upon the partial pressure of hydrogen in the ion source region, the existence of H_3^+, due to ion-molecular reaction $H_2 + H_2^+ \leftrightarrow H_3^+ + H$, is also possible. Thus, the peak at m/z=3 may correspond to either HD^+ or H_3^+. Similarly deuterium exhibits peak at D_3^+. If hydrogen is present in deuterium, depending on its concentration, D_2H^+ and $H_2D^+$are also possible. Formation of these molecular ion peaks have to be taken into account for the accurate calculations of hydrogen and deuterium. It is known that the formation of the molecular ion is directly proportional to the square of the exerting pressure [80]. Hence, it is essential to determine the formation of these molecular ion peaks as a function of pressure of the system. Hydrogen and deuterium gases were produced by reducing H_2O and D_2O respectively, with calcium metal as previously described. The hydrogen gas generated with pure H_2O was filled into the system at a pressure >500 Pa (pressure at above 10 Pa level was measured with an oil manometer specially incorporated for the purpose) and was allowed to enter the quadrupole mass analyzer at a fixed leak rate. Mass spectra were recorded at m/z = 1, 2 and 3. The pressure was then reduced in steps and spectra were recorded upto a pressure of 10^{-2} Pa. The experiment was repeated several times. Similar studies have been carried out with deuterium, which was produced by reduction of pure D_2O(>99.9%) with pure calcium metal, the peaks at m/z 1, 2, 3, 4, 5 and 6 were monitored. It was observed that the molecular ions formation is negligible at system pressures less than 10 Pa. In the analysis of zircaloy samples, the pressure of the gases released is in the range 5 x10^{-2} Pa to 5 Pa. At these pressures, the molecular ions are not formed. If the pressure is more than 10 Pa, it should be suitably manipulated and brought down to <5 Pa before feeding the gas to mass analyser.

3.5.7. Repeatability, Reproducibility and Accuracy of the Methodology

Five independent aliquots of hydrogen standard in zirconium matrix were analysed. Reproducibility and accuracy of the methodology was found to be 5%.Repeatability of the methodology for a single sample with multiple measurements was found to be 1% (i.e., mole fraction of hydrogen determined from five different mass spectra scans). As no standards are available for deuterium or hydrogen and deuterium together, in zirconium or titanium matrix, accuracy in the measurements could not be determined. But, reproducibility of the methodology for the determination of H and D in charged samples was determined and it was found to be 10%.

3.5.8. Standardization and Validation of the Methodology

For the standardization of the methodology, typical alloy sample coupons where initial hydrogen impurity content was known (12μg.g^{-1}) were selected. In these coupons, hydrogen and deuterium were charged with two different mixtures, one containing 50% H_2 and 50% D_2 another one containing 35% $H_2$and 65% D_2.Hydrogen and deuterium content in these coupons of Zr-Nb alloy were determined. After subtraction of initial hydrogen content from the measured hydrogen content, percentage of charged H and D were determined.

For example consider the case where coupon in which hydrogen and deuterium was charged with 35% H_2 and 65% D_2 mixture.

Observed hydrogen Charged content = 73 $\mu g.g^{-1}$

Observed deuterium Charged content = 202 $\mu g.g^{-1}$

Initial hydrogen impurity content present in the coupon = 12$\mu g.g^{-1}$

Exact hydrogen charged content = (73 -12) $\mu g.g^{-1}$ = 61 $\mu g.g^{-1}$

H_{eq} = (H+D/2) = (61+ 202/2) = 162 $\mu g.g^{-1}$

Composition of charged content was H_2 (%) = $\frac{61}{162} \times 100 = 37$

D_2 (%) = 100 - 37 = 63

Results for other charged samples are given in Table 3.3.

Table 3.3 Determination of hydrogen and deuterium in charged samples

S. No.	Charged gas composition (Mole %)		Observer gas composition (µg/g)		Blank-corrected composition of the charged content (Mole %)	
	H_2	D_2	H_2	D_2	H_2	D_2
1	50	50	54	71	54	46
2	50	50	57	75	54	46
3	35	65	73	202	37	63
4	35	65	81	270	34	66
5	35	65	30	62	37	63

FromTable3.3 it can be seen that composition of gases employed for charging and composition of absorbed H and D content were agreed well within 10%. It may be mentioned that the difference in kinetics of absorption of H and D in Zr-Nb alloy matrix has been neglected.

Reference materials for deuterium in zirconium matrix were not available for method validation. Hence, the developed methodology has been validated by analysing several certified standards for hydrogen in zirconium and titanium matrix obtained from Micro elemental Analysis, U.K. The results are given in Table 3.4. As can be seen, by applying statistical treatment of the data (t test), there is no significant difference (95% confidence interval) between the results obtained in the present work and the recommended reference values.

Table 3.4 Validation of the methodology

S.No.	**Part No. of Std.**	**Host matrix**	**Reference value (ug/g)**	**Obtained Value(ug/g)[a]**
1	B2460	Zirconium	11.0±1.0	10.6±0.6
2	B2601	Titanium	47.0±4.0	48.5±2.3
3	B2632	Stainless Steel	6.24±0.60	6.15±0.40
4	AR 555	Stainless Steel	2.35±0.30	2.38±0.21

[a]Mean of 4 determinations with standard deviation.

3.5.9. Determination of Hydrogen and Deuterium Content in Irradiated Zr-Nb Coolant Channels

A number of sliver samples, received from irradiated Zr-Nb coolant channels from a typical PHWR were analysed. In PHWRs, heavy water is used as a primary heat transport fluid; hence only deuterium will be picked up during service of coolant channel, as discussed earlier. The effect of total hydrogen could be calculated from the data of initial hydrogen content present in coolant channel and deuterium picked up during service. As the effect of both hydrogen and deuterium in the Zr-H/D is the same, it is convenient to express the concentration (µg g^{-1}) as the hydrogen equivalent (Heq), which is given as [H] + [D]/2 with the understanding that the concentrations are expressed in µg g^{-1}. The typical results of deuterium content for a particular coolant channel operated for 8.5 effective full power years (EFPY) is shown as a pictorial form in Figure 3.10.

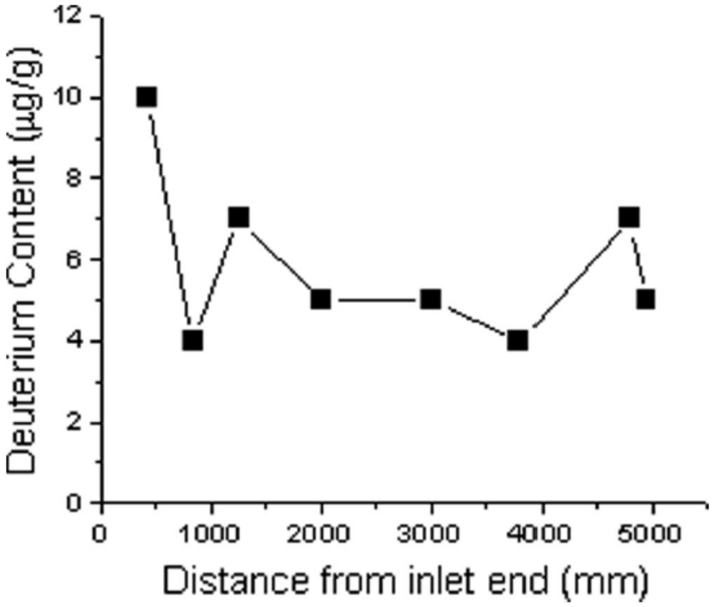

Figure 3.10. Deuterium content of a Zr-Nb coolant channel operated for 8.5 EFPY with distance from inlet end

3.5.10. Estimation of Uncertainty

The term uncertainty (of measurement) is defined as:

"A parameter associated with the result of a measurement which characterises the dispersion of the values that could reasonably be attributed to the measurand"[81].When a physical quantity i.e. the measurand (in this case, deuterium) is measured then it is essential to give quantitative indication of the excellence of the result to those who employ it so that they assess its reliability.

3.5.10.1. Systematic and Random Errors

All measurements have a degree of uncertainty regardless of precision and accuracy. This is caused by two factors, the limitation of the measuring instrument (systematic error) and the skill of the experimenter making the measurements (random error). Random error sometimes called human error, are compensated by repeated measurements. Systematic errors tend to be consistent in magnitude and/or direction. If the magnitude and direction of the error is known, accuracy can be improved by additive or proportional corrections. **Additive correction** involves adding or subtracting a constant adjustment factor to each measurement; **proportional correction** involves multiplying the measurement(s) by a constant. This correction factor is obtained by analyzing standards. However, these standards may be having certain uncertainty, which also has to be accounted for.

3.5.10.2. Type A and Type B uncertainties

A Type A evaluation of standard uncertainty may be based on any valid statistical method for treating data. When a set of several repeated readings has been taken, the mean‘x’ and estimated standard deviation‘s’ can be calculated for the set. From these, the estimated standard uncertainty ‘u’ of the mean (standard deviation of the mean) is calculated from:

$$u = \frac{s}{\sqrt{n}}$$

Where n was the number of measurements in the set.

A Type B evaluation of standard uncertainty is usually based on scientific judgment using all of the related information available, which may include:

- previous measurement data,
- experience with, or general knowledge of, the behaviour and property of relevant materials and instruments,
- manufacturer's specifications,

- data provided in calibration and other reports, and
- uncertainties assigned to reference data taken from handbooks.

When the information is limited, one might only be able to estimate the upper and lower limits of uncertainty and then has to assume that the value is equally likely to fall anywhere in between, i.e. a rectangular or uniform distribution. The standard uncertainty for a rectangular distribution is found from:

$$u = \frac{a}{\sqrt{3}}$$

Where ‘a’ is the semi-range (or half-width) between the upper and lower limits.

3.5.10.3. Combining standard uncertainties

For addition and subtraction -

$Y = X_1 - X_2 + \dots\dots\dots\dots\dots\dots + X_n$

Combined standard uncertainty, $u_c(y) = \sqrt{x_1{}^2 + x_2{}^2 + \cdots + x_n^2}$

Where, $x_1, x_2, x_3 \dots\dots\dots, x_n$ are standard uncertainty for $X_1, X_2, X_3, \dots\dots, X_n$

For multiplication or division -

$Y = \frac{X_1 X_2}{X_3 X_4}$

Combined standard uncertainty, $u_c(y) = Y \text{ x } \sqrt{(\frac{x_1}{X_1})^2 + (\frac{x_2}{X_2})^2 + (\frac{x_3}{X_3})^2 + \left(\frac{x_4}{X_4}\right)^2}$

Relative standard uncertainty, $\frac{u_c(y)}{Y} = \sqrt{(\frac{x_1}{X_1})^2 + (\frac{x_2}{X_2})^2 + (\frac{x_3}{X_3})^2 + \left(\frac{x_4}{X_4}\right)^2}$

Where, x_1, x_2, x_3, x_4 are standard uncertainty for X_1, X_2, X_3, X_4.

3.5.10.4. Uncertainty in the measurement

Uncertainty in weighing the sample, volume calibration, total pressure measurement, ionic current measurement, conversion into partial pressures, calculation of moles etc. are required for obtaining uncertainty for the calculation of deuterium content by HVE-QMS.

The formula for determination of concentration of deuterium is:

$$\mathbf{C} = \frac{\mathbf{I_{D2}}}{\mathbf{I_{Tot}}} \times \frac{\mathbf{PV}}{\mathbf{RT}} \times \frac{\mathbf{4}}{\mathbf{W_{Sam}}}$$

Where,

C = Concentration

I_{D2} = Peak intensity due to deuterium

I_{Tot}= Total peak intensity

P = Corrected pressure exerted due to the gases released from the sample

V = Volume into which the gases are collected

T = Room temperature

R = Gas constant

W = Weight of the sample

Uncertainty of I_{D2}, I_{Tot}, P, V, T, W were determined in the following manner for obtaining the overall uncertainty.

Weight of the sample (B type uncertainty)

Electronic balance was used for weighing of the sample. The uncertainty quoted by the manufacturer of the balance is 0.2 mg over the entire range (10 mg - 180 mg).

Weight of the sliver Sample = 0.1103 g

Standard Uncertainty = 0.2 mg = 0.0002 g

Relative Standard Uncertainty (u_w) $= \frac{0.0002}{0.1103} \times 100$

= 0.18 %

Volume Measurement (A type uncertainty)

Volume of entire collection chamber (V1) was arrived by expanding dry N_2 gas of pre-calibrated volume (V) after measuring its pressure (P). Again the pressure (P1) was measured after expanding nitrogen in the pre - calibrated volume into the collection chamber.

$$PV = P1V1 \quad \text{(By ideal gas equation)}$$

$$\Rightarrow V1 = PV/P1$$

The above procedure was repeated five times. The total volume of the collection chamber was 2.1 Lwith standard deviation of 0.07 L.

Volume of the system = 2.1 L

Standard Deviation = 70mL = 0.07L

Number of volume measurement = 5

Standard Uncertainty $= \frac{0.070}{\sqrt{5}} = 0.031\text{L}$

Relative Standard Uncertainty (u_V) $= \frac{0.031}{2.1} \times 100$

$= 1.48\%$

Pressure Measurement (Sample pressure ⇒ B type uncertainty; Blank pressure⇒A type uncertainty)

Pressure of blank (mb) – 5 No. of measurement

0.0047

0.0046

0.0046

0.0045

0.0048

Average = 0.0046 mb = 0.46 Pa

Std. Deviation = 0.0001mb = 0.01 Pa

Std. uncertainty of blank (z) = std.deviation / $\sqrt{5}$ Pa

= 0.01/2.25 Pa

= 4.44x 10^{-3}Pa

Pressure of sample = 0.0518 mb = 5.18 Pa

Pressure was measured by Capacitance manometer with an accuracy of 0.5% of reading.

Standard Uncertainty of the sample (y) = 0.5 x 5.18 /100 Pa = 0.03Pa

Combining standard uncertainties of (sample – blank) was,

$$U_p = \sqrt{y^2 + z^2}$$

$$\Rightarrow U_p = \sqrt{(0.03)^2 + (4.44 \times 10^{-3})^2} \text{ Pa} = 0.03\text{Pa}$$

Relative Standard Uncertainty of Pressure (u_p) = U_p x 100/ (sample pressure – blank pressure)

= 0.03x 100 / (5.18 – 0.46) = 0.60 %

Temperature Measurement (B type uncertainty)

Room temperature was 298 K

Standard uncertainty was 1K

Relative Standard uncertainty (u_T) = 1 x 100/298 = 0.34 %

Uncertainty in partial pressure of deuterium (A type uncertainty)

The partial pressure of deuterium was obtained from the peak intensities at m/z 3 and 4 ($p_{3/2}$+ p_4), $\sum p_i$were pressure exerted by the released gases. Uncertainty encountered in peak intensities measurement were obtained by taking the mass spectral scan for three times.

Table 3.5 Peak Intensities Measurement for Sample and Blank

Measurement no.	**Sample spectrum**			**Blank spectrum**		
	m/z = 2 (Insu. Units)	**m/z = 3 (Insu. Units)**	**m/z = 4 (Insu. Units)**	**m/z = 2 (Insu. Units)**	**m/z = 3 (Insu. Units)**	**m/z = 4 (Insu. Units)**
1	2.05×10^{-7}	4.28×10^{-7}	3.16×10^{-7}	2.98×10^{-8}	3.98×10^{-11}	0.00
2	1.96×10^{-7}	4.15×10^{-7}	3.07×10^{-7}	2.82×10^{-8}	6.58×10^{-11}	0.00
3	1.91×10^{-7}	4.05×10^{-7}	2.98×10^{-7}	2.74×10^{-8}	2.11×10^{-11}	7.70×10^{-12}
Average	1.97×10^{-7}	4.16×10^{-7}	3.07×10^{-7}	2.85×10^{-8}	4.22×10^{-11}	7.70×10^{-12}
Std.Deviation (σ)	7.09×10^{-9}	1.15×10^{-8}	9.00×10^{-9}	1.22×10^{-9}	2.24×10^{-11}	1.33×10^{-11}

By employing Relative Sensitivity factors to the blank corrected sample intensities, true intensities were obtained (as shown in Table 3.6).

Table 3.6 Corrected peak intensities

	Average of Sample Intensity (I_s) = M	Average of blank Intensity (I_b) = N	Relative Sensitivity Factor (RSF)	(I_s - I_b) / RSF
H_2	1.97×10^{-7}	2.85×10^{-8}	1	1.69×10^{-7}
D_2	3.07×10^{-7}	7.70×10^{-12}	0.66	4.65×10^{-7}
HD/2	2.08×10^{-7}	2.11×10^{-11}	0.83	2.51×10^{-7}
HD	4.16×10^{-7}	4.22×10^{-11}	0.83	5.01×10^{-7}

Intensity of H_2, $I_{H_2} = \frac{I_{2_{Samp}} - I_{2_{blan}}}{RSF_{H_2}} + \frac{I_{3/2_{Samp}} - I_{3/2_{blan}}}{RSF_{HD}}$……………..(1)

$= 4.19 \times 10^{-7}$

Intensity of D_2, $I_{D_2} = \frac{I_{4_{Samp}} - I_{4_{blan}}}{RSF_{D_2}} + \frac{I_{3/2_{Samp}} - I_{3/2_{blan}}}{RSF_{HD}}$…………….(2)

$= 7.16 \times 10^{-7}$

Intensity of HD, $I_{HD} = \frac{I3_{Samp} - I3_{blan}}{RSF_{HD}}$ ……………………....(3)

$= 5.01 \times 10^{-7}$

Total Intensity = $I_{H_2} + I_{D_2} + I_{HD} = 1.64 \times 10^{-6}$

Standard Uncertainty and Relative Standard Uncertainty (expressed as 'a') of (I_{samp} - I_{bla}) were given in Table 3.7.

Table 3.7 Relative Standard Uncertainty(a) of (I_{samp} - I_{bla})

	σ_{samp}	σ_{bla}	σ^2_{samp}	σ^2_{bla}	Y= $\sqrt{\sigma^2 \text{sam} + \sigma^2 \text{bla}}$	Standard Uncertainty $Y/\sqrt{3} = P$	Rela.Std. Uncertainty(a) $=P/I_s-I_b$
H_2	7.09×10^{-9}	1.22×10^{-9}	5.03×10^{-17}	1.49×10^{-18}	7.19×10^{-9}	4.16×10^{-9}	2.47×10^{-2}
D_2	9.00×10^{-9}	1.33×10^{-11}	8.10×10^{-17}	1.77×10^{-22}	9.00×10^{-9}	5.20×10^{-9}	1.69×10^{-2}
HD/2	5.75×10^{-9}	1.12×10^{-11}	3.31×10^{-17}	1.25×10^{-22}	5.75×10^{-9}	3.32×10^{-9}	1.60×10^{-2}
HD	1.15×10^{-8}	2.24×10^{-11}	1.32×10^{-16}	5.02×10^{-22}	1.15×10^{-8}	6.65×10^{-9}	1.60×10^{-2}

Since, the Relative sensitivity Factors of H_2, D_2 and HD with respect to H_2 are given by

$$RSF_{H_2} = \frac{SF_{H_2}}{SF_{H_2}}$$

$$RSF_{D_2} = \frac{SF_{D_2}}{SF_{H_2}}$$

$$RSF_{HD} = \frac{SF_{HD}}{SF_{H_2}}$$

Thus, Standard Uncertainty and Relative Standard Uncertainty (expressedas 'b') of RSF were shown in Table 3.8.

Table 3.8 Relative standard uncertainty (b) of RSF

	Sensitivity Factor (SF)	Std Deviation of SF	S.D/$\sqrt{3}$ = x (rectangular Distribution)	(x/SF)*(x/SF)	Relative std. uncertainty=b	Std. Uncertainity = RSFx b
H_2	1.79 x 10^{-5}	1.77 x 10^{-6}	1.02 x 10^{-6}	m=3.27 x10^{-3}	$\sqrt{m+m}$ = 8.09 x 10^{-2}	8.09 x 10^{-2}
D_2	1.18 x 10^{-5}	6.86 x 10^{-7}	3.96 x 10^{-7}	n=1.14 x 10^{-3}	$\sqrt{m+n}$ = 6.64 x 10^{-2}	4.38 x 10^{-2}
HD/2	1.48 x 10^{-5}	1.90 x 10^{-6}	1.10 x 10^{-6}	p=5.49 x 10^{-3}	$\sqrt{m+p}$ = 9.36 x 10^{-2}	7.76 x 10^{-2}
HD	1.48 x 10^{-5}	1.90 x 10^{-6}	1.10 x 10^{-6}	p=5.49 x 10^{-3}	$\sqrt{m+p}$ = 9.36 x 10^{-2}	7.77 x 10^{-2}

From Table 3.7 and 3.8, Relative Standard uncertainty of $\frac{I_{Sample} - I_{blank}}{RSF}$ was $\sqrt{a^2+b^2}$.

Thus, Relative Standard uncertainty of $\frac{I_{2_{Samp}} - I_{2_{blan}}}{RSF_{H_2}} = \sqrt{(2.47 \text{ x } 10^{-2})^2 + (8.09 \text{ x } 10^{-2})^2}$

$= 8.46 \text{ x } 10^{-2}$

Standard uncertainty of $\frac{I_{2_{Samp}} - I_{2_{blan}}}{RSF_{H_2}} = 1.69 \text{ x } 10^{-7} \text{ x } 8.46 \text{ x } 10^{-2}$

$= 1.43 \text{ x } 10^{-8}$……………………………………..(4)

Relative Standard uncertainty of $\frac{I_{4_{Samp}} - I_{4_{blan}}}{RSF_{D_2}} = \sqrt{(1.69 \text{ x } 10^{-2})^2 + (6.64 \text{ x } 10^{-2})^2}$

$= 6.85 \text{ x } 10^{-2}$

Standard uncertainty of $\frac{I_{4_{Samp}} - I_{4_{blan}}}{RSF_{D_2}} = 4.65 \text{ x } 10^{-7} \text{ x } 6.85 \text{ x } 10^{-2}$

$= 3.19 \text{ x } 10^{-8}$………………………………..(5)

Relative Standard uncertainty of $\frac{I_{3/2_{Samp}} - I_{3/2_{blan}}}{RSF_{HD}} = \sqrt{(1.60 \text{ x } 10^{-2})^2 + (9.36 \text{ x } 10^{-2})^2}$

$= 9.49 \text{ x } 10^{-2}$

Standard uncertainty of $\frac{I_{3/2_{Samp}} - I_{3/2_{blan}}}{RSF_{HD}} = 2.51 \text{ x } 10^{-7} \text{ x } 9.49 \text{ x } 10^{-2}$

$= 2.38 \text{ x } 10^{-8}$……………………………….(6)

Relative Standard uncertainty of $\frac{I3_{Samp} - I3_{blan}}{RSF_{HD}} = \sqrt{(1.60 \text{ x } 10^{-2})^2 + (9.36 \text{ x } 10^{-2})^2}$

$= 9.50 \text{ x } 10^{-2}$

Standard uncertainty of $\frac{I3_{Samp} - I3_{blan}}{RSF_{HD}} = 5.01 \text{ x } 10^{-7} \text{x } 9.50 \text{ x } 10^{-2}$

$= 4.76 \text{ x } 10^{-8}$………………………………….(7)

From eq (4) and (6)

Standard uncertainty of $I_{H2} = \sqrt{(1.43 \times 10^{-8})^2 + (2.38 \times 10^{-8})^2} = 2.77 \text{ x } 10^{-8}$

From eq (5) and (6)

Standard uncertainty of $I_{D2} = \sqrt{(3.19 \times 10^{-8})^2 + (2.38 \times 10^{-8})^2} = 3.98 \text{ x } 10^{-8}$

From eq (7)

Standard uncertainty of $I_{HD} = 4.76 \text{ x } 10^{-8}$

Standard uncertainty of $I_{Total} = \sqrt{[(2.77 \times 10^{-8})^2 + (3.98 \times 10^{-8})^2 + (4.76 \times 10^{-8})^2]}$

$= 6.79 \text{ x } 10^{-8}$

$$\text{Relative Std. Uncertainty } (u_D) \text{ of } {}^{I_{D_2}}\!/_{I_{Total}} = \sqrt{(\frac{u_{D_2}}{I_{D_2}})^2 + (\frac{u_{Total}}{I_{Total}})^2}$$

$$= \sqrt{(\frac{3.98 \times 10^{-8}}{7.16 \text{ x } 10^{-7}})^2 + (\frac{6.79 \times 10^{-8}}{1.64 \text{ x } 10^{-6}})^2}$$

$$= \sqrt{3.09 \times 10^{-3} + 1.72 \times 10^{-3}}$$

$= 6.94 \text{ x } 10^{-2}$ or 6.94%

Relative combined uncertainty =

$$\sqrt{(\text{rsu of Weight})^2 + (\text{rsu of Volume})^2 + (\text{rsu of Pressure})^2 + (\text{rsu ofTemp})^2 + (\text{rsu of} \frac{I_{D2}}{I_{Total}})^2}$$

$$= \sqrt{{u_W}^2 + {u_V}^2 + {u_P}^2 + {u_T}^2 + {u_D}^2}$$

$=\sqrt{(0.18)^2 + (1.48) + (0.6)^2 + (0.34)^2 + (6.94)^2}$

= 7.13 %

% Relative combined uncertainty in measurement of deuterium (at coverage factor of 2)

= 2 x 7.13

=14.26%

Hence, the relative expanded uncertainty (at coverage factor k=2) in measurement of Deuterium content is 14 %.

Chapter – 4

Determination of Diffusion Coefficients of hydrogen and deuterium in Zr-2.5%Nb pressure tube material using Hot Vacuum Extraction – Quadrupole Mass Spectrometry

4.1. Introduction

Reaction of hydrogen/deuterium with zirconium is known to be diffusion controlled with the surface oxide layer acting as a barrier [82]. The Zr-2.5% Nb tube microstructure consists of elongated α-Zr grains surrounded by thin layer of β-Zr and the diffusivity of hydrogen in β-Zr is about two orders of magnitude higher than in α-Zr [83, 84].

The coolant channels also known as pressure tubes for the Indian PHWRs are manufactured at Nuclear Fuel Complex (NFC), Hyderabad, following a fabrication route similar to but not identical to the modified route II developed for the pressure tubes of CANDU reactors [84].The modified route II consists of two cold working steps (instead of one cold working step for the conventional route followed for CANDU Pressure Tubes) and an intermediate annealing step. The intermediate annealing step(823 K for 6 h)is required to attain recovery so as to facilitate second stage of cold working. However, there are three differences between modified route II developed for CANDU pressure tubes and that being practiced at NFC. These are:

(i) the mode of hot working,

(ii) amount of cold work imparted during first cold working stage of tube fabrication (50–55% at NFC as compared to 20% for CANDU tubes) and

(iii) mode of imparting cold work (pilgering at NFC as compared to cold drawing practiced for CANDU tubes).

Fabrication routes for Indian PHWR pressure tubes, CANDU pressure tubes and modified route II pressure tubes are given in Figure 4.1 [85]. The method hot working for breaking the cast structure for CANDU pressure tubes is forging, whereas the method used for Indian PHWR pressure tubes is extrusion. However both CANDU and Indian PHWR pressure tubes are fabricated by hot extrusion of the hollow billet.

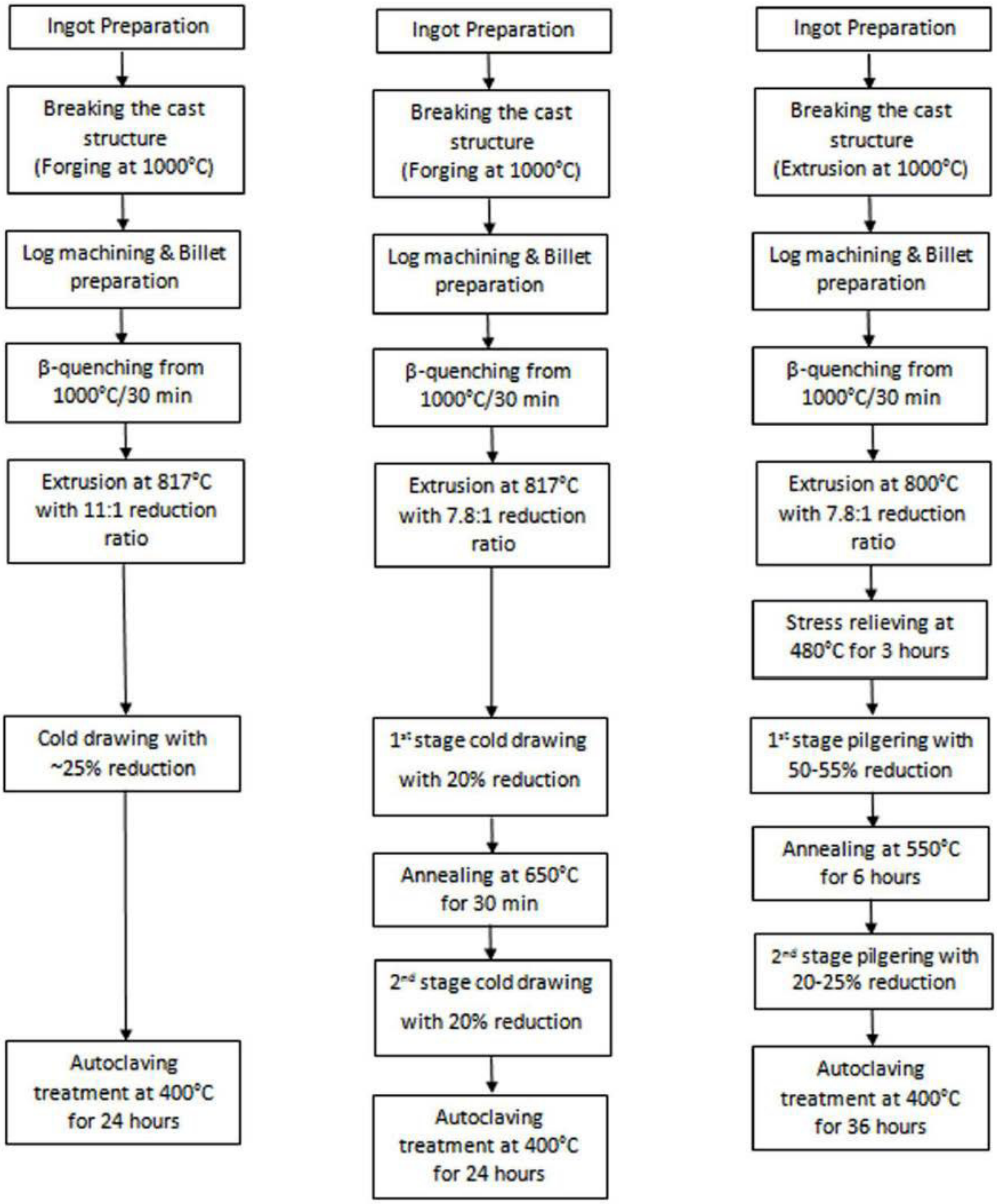

Conventional CWSR route of CANDU PTs

Modified CWSR route-2 of CANDU PTs

CWSR route of IPHWR220 PTs

Figure 4.1. Fabrication routes for conventional CANDU pressure tubes; modified route II developed by AECL for pressure tubes and Indian PHWR pressure tubes

4.2. Reported work

Extensive studies have been carried out in the past on the diffusion of hydrogen /deuterium in zirconium and its alloys but to the best of our knowledge no report is available in the literature about determination of diffusion coefficients of H and D in Zr-2.5% Nb alloy in a single laboratory or employing same methodology. Sawatzky and coworkers studied the solubility and diffusion of hydrogen in alpha phase of Zirconium alloy [86-88]. Kearns et al. studied the diffusion of hydrogen in α-Zr, Zircaloy-2 and Zircaloy-4 in different directions (longitudinal and transverse) and did not find any effect of the alloy composition or the microstructure on the diffusivity [89, 90].

Different techniques have been employed for the determination of hydrogen/deuterium in the zirconium alloys. The earliest studies on reaction of hydrogen with zirconium were based on vacuum microbalance [82]. Differential scanning calorimetry (DSC) has been used to study solubility of hydrogen in zirconium alloys by Khatamian and Ling [91].Wipf et al. used mechanical spectroscopy to measure hydrogen concentration while investigating hydrogen diffusion in Zirconium alloys [92]. However, these techniques provide total hydrogen content, and hence isotopic diffusion data cannot be obtained. Laursen et al. used nuclear reaction analysis (NRA) to estimate the levels of deuterium in Zirconium alloys [93]. This technique is based on the nuclear reaction $^{2}D(^{3}He,p)^{4}He$. The technique has also been used for diffusion of deuterium in Zr-2.5% Nb [93, 94]. For the study of diffusion of hydrogen, another nuclear reaction, namely, $^{1}H(^{15}N,\alpha\gamma)^{12}C$ was used [95].As different nuclear reactions are used to probe depth profile of hydrogen and deuterium, comparison of diffusion coefficient of the two isotopes is subject to the differences in the stopping power, depth resolution and sensitivity. Hot Vacuum Extraction -Mass Spectrometry (HVE-MS) provides the information about the concentration of hydrogen and deuterium simultaneously

[96] and has been used in study of deuterium diffusion in Zr-2.5%Nb pressure tubes by Khatamian [97].

The literature reports on diffusion of hydrogen and deuterium show large variation in the activation energy (E_A) of diffusion. The earliest study on H/D diffusion in high purity zirconium showed E_A = 47 kJ.mole^{-1} [82] for both the isotopes, while Sawatzky's group reported the E_A value as 35 kJ.mole^{-1} for diffusion of hydrogen in alpha phase of zircaloy-2 [86, 87]. These are at variance with those reported by Schwartz and Mallett [98] (24 kJ.mol^{-1}) and those reported by Mallett and Albrecht [99] (30 kJ.mol^{-1}). Kearns et al. obtained E_A=45 kJ.mol^{-1} for diffusion of deuterium in α-Zr, Zircaloy-2 and Zircaloy-4 [90]. The literature data on activation energy of diffusion and pre-exponential factor for diffusion are compiled and given in Table 4.1.

Table 4.1 Literature data of activation energy and pre-exponential factor for diffusion

Hydrogen Isotope	**Material**	**E_A (kJ/mol)**	**D_0 (m^{2}s^{-1})**	**Method**	**Ref**
Hydrogen	Zircaloy-2	35.05	2.17×10^{-7}	HVE	[86]
Hydrogen	Zircaloy-2	35.05	2.17×10^{-7}	HVE	[87]
Hydrogen	α-Zirconium, Zircaloy-2 Zircaloy-4	45.27	7.73×10^{-7}	HVE	[90]
Hydrogen	Zirconium	47.65	1.09×10^{-7}	vacuum microbalance	[82]
Deuterium			0.73×10^{-7}		
Hydrogen	Zirconium	47.28	-	mechanical spectroscopy	[92]
Deuterium^a	Zr-2.5%Nb	-	D = 1.13×10^{-10} at 573K D = 1.23×10^{-10} at 623K	NRA	[93]
Deuterium	Zr-2.5%Nb	39.01	2.61×10^{-7}	HVE-MS	[97]

4.3. Present Studies

It has also been reported that the solubility of hydrogen in zirconium and its alloys depends on the thermal treatment of the material and this could be one of the reasons for the variation in literature data. In view of this, it was decided to carry out the study of diffusion of hydrogen and deuterium in Zr-2.5% Nb samples with the same thermal treatment and by the same method, that is, HVE-QMS. In this work, the Zr-2.5%Nb alloy samples were obtained from IPHWR pressure tubes, which are fabricated using a different route [84, 85] than CANDU pressure tubes [97, 100] in order to examine the role of fabrication route, on diffusivity of hydrogen isotopes in this alloy. The results in the current study were compared with the literature data.

4.4. Experimental

4.4.1. Sample Preparation

Rectangular pieces of Zr-2.5% Nb pressure tube material having length, width and height equal to 67, 12and 4.6 mm respectively, were used for the present study. One end of the specimen (2 mm) was polished with emery papers of 120,400, 600, 800, 1200 grit size. After polishing, the sample was pickled with 5% HF+ 45% HNO_3+50% H_2O for 1 minute to get a surface totally free of oxides formed during polishing. The samples were washed with distilled water and subsequently cleaned with acetone and methanol ultrasonically.

4.4.2. Charging of Hydrogen/Deuterium and annealing of the sample

The samples were obtained from the pressure tube and had initial hydrogen concentration of 3.5±0.3 ppmw. A hydride/deuteride surface layer was formed electrolytically at one end of the specimen. The electrolytic charging condition was chosen in such a way so as to ensure enough hydrogen/deuterium in solution at the annealing temperature and to act as source of hydrogen/deuterium for diffusion. Standard electrolytic charging procedure was followed for charging of H/D and diffusivity measurement [101, 102].In this methodology, the Zr-2.5% Nb alloy and lead were taken as cathode and anode, respectively(Figure 4.2is the schematic diagram and Figure 4.3 shows the electrolytic charging set up).The electrolytes were 0.4 N H_2SO_4 in normal water in the case of hydrogen, while in the case of deuterium, the medium chosen was heavy water (Purity 99.5%)[100].Low hydrogen content was determined in all deuterided specimens, the highest concentration of hydrogen was found to be 8.6 and 14.2 ppmw at 523 and 673 K respectively. The temperature of electrolytes and current density were maintained at 340 K and 0.2 A/cm^2, respectively. The alloy piece was electrolytically charged for about 100 hours. To avoid charging of the unpolished surface, it was covered and sealed with teflon tape. After the charging of the hydrogen / deuterium, the alloy sample was vacuum sealed in a quartz tube, which was then annealed in a resistance heated furnace at the required temperatures ranging from 523 to 673 K for about 100 hours. After annealing, the hydride distribution was assessed by metallographically examining the sample as a function of distance from the electrolytically charged end. For metallography the samples were polished, swab etched with $HF:HNO_3:H_2O$::2:9:9 for ~22 seconds.

4.4.3. Determination of hydrogen/deuterium

Electrolytically charged and annealed Zr-2.5%Nb samples were cut as 2 mm thick slices from the charged end using a diamond cutter employing silicon oil as a lubricant. After polishing with emery papers, these slices of alloy were cleaned with CCl_4 and dried at room temperature for about 2 hours. Hydrogen and Deuterium content in each slice was determined employing HVE-QMS.

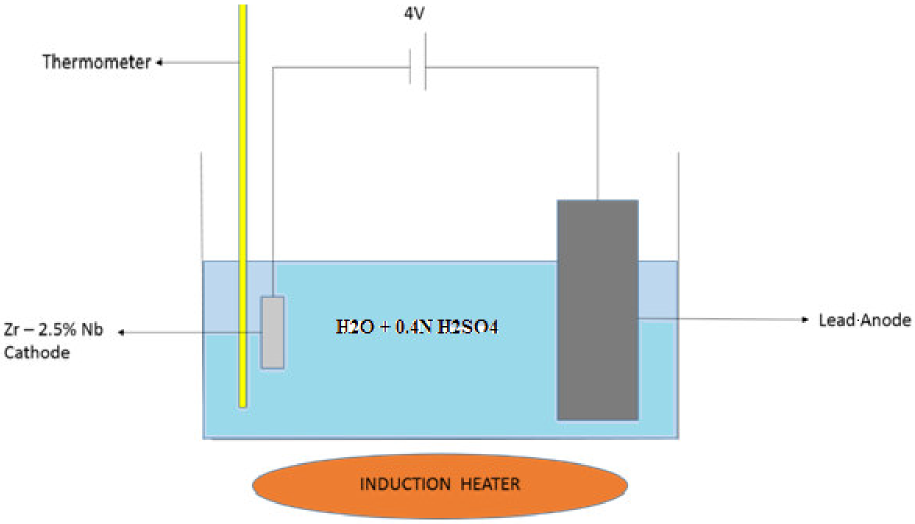

Figure 4.2. A Schematic diagram of electrolytic charging set up

Figure 4.3. Electrolytic charging set up

4.4.4. Hot Vacuum Extraction – Quadrupole Mass Spectrometer (HVE-QMS) analysis

The detailed description of the equipment (see the schematic diagram in Figure 3.4), procedure of operation and analysis by HVE-QMS has been described in detail in Section 3.4. The cleaned and dried 2 mm slices of Zr-2.5%Nb sample were weighed and then placed in a quartz tube of the HVE-QMS system. The tube was pre-evacuated with a rotary pump and then connected to the main system by opening the isolation valve. The entire system was then evacuated to a vacuum higher than 10^{-4} Pa. The quartz tube, along with the sample, was heated in a resistance furnace employing a programmable temperature controller. Degassing of the sample was carried out at 373 K to remove moisture and surface contamination of organic materials. The outlet valve at the end of the quartz tube was closed and the temperature was slowly raised at a rate of 283 K/minute to 1273 K and maintained at this temperature for 10 minutes. The equilibrium condition was maintained for 10 minutes to ensure the breaking of methane, if it was formed. The valve was then opened and the evolved gases were extracted into a known volume by an ejector pump (Nude and Sealed TMP) through a liquid nitrogen trap to condense the condensable gases. The extraction was carried out until a constant pressure reading was obtained (about 10 minutes). The pressure exerted by the non-condensable gases was measured by employing a capacitance manometer. The gases were then fed to an on-line quadrupole mass spectrometer through a micro leak valve. Peak intensities were monitored at m/z =1, 2, 3, 4, 18, 28, 32 and 44 corresponding to H^+, H_2^+ / D^+, HD^+, D_2^+ , H_2O^+, CO^+ / N_2^+, O_2^+ and CO_2^+ respectively. A typical spectrum is given in Figure 4.4(i) and (ii). The blank corrected intensities are divided with respective relative sensitivity factors to arrive at the true intensities.

Mole fraction of hydrogen and deuterium are calculated as

$$X_H = \frac{\left(I_2 + (I_3/2)\right)}{\left(I_2 + I_3 + I_4 + I_{18} + I_{28} + I_{32} + I_{44}\right)} \qquad \ldots\ldots\ldots \qquad (1)$$

$$X_D = \frac{\left(I_3/2 + I_4\right)}{\left(I_2 + I_3 + I_4 + I_{18} + I_{28} + I_{32} + I_{44}\right)} \qquad \ldots\ldots\ldots \qquad (2)$$

Where,

I_2= intensity of H_2,

I_3= intensity of HD,

I_4= intensity of D_2,

I_{18}= intensity of H_2O,

I_{28}= intensity of N_2,

I_{32}= intensity of O_2 and

I_{44}= intensity of CO_2

From the total pressure exerted by these gases, the volume of the collection chamber and the mole fraction of hydrogen and deuterium, their concentration was calculated employing an ideal gas equation [103].

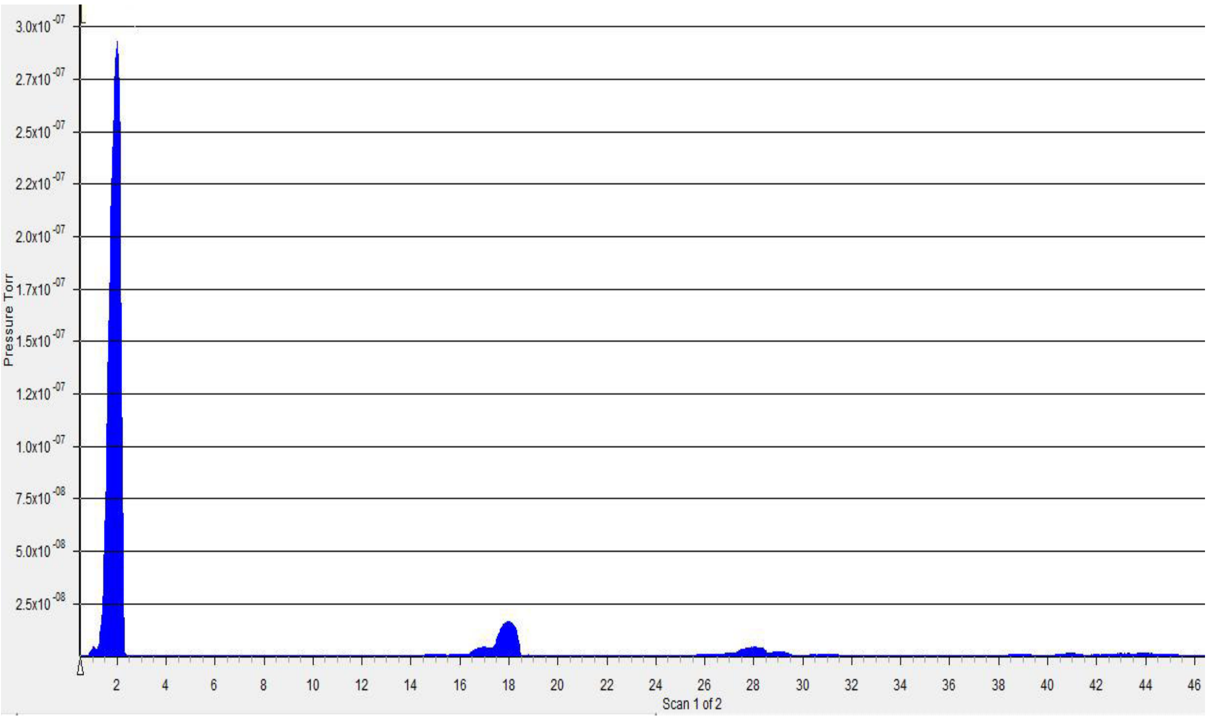

Figure 4.4(i). Typical Mass spectrum in analysis of hydrogen charged piece

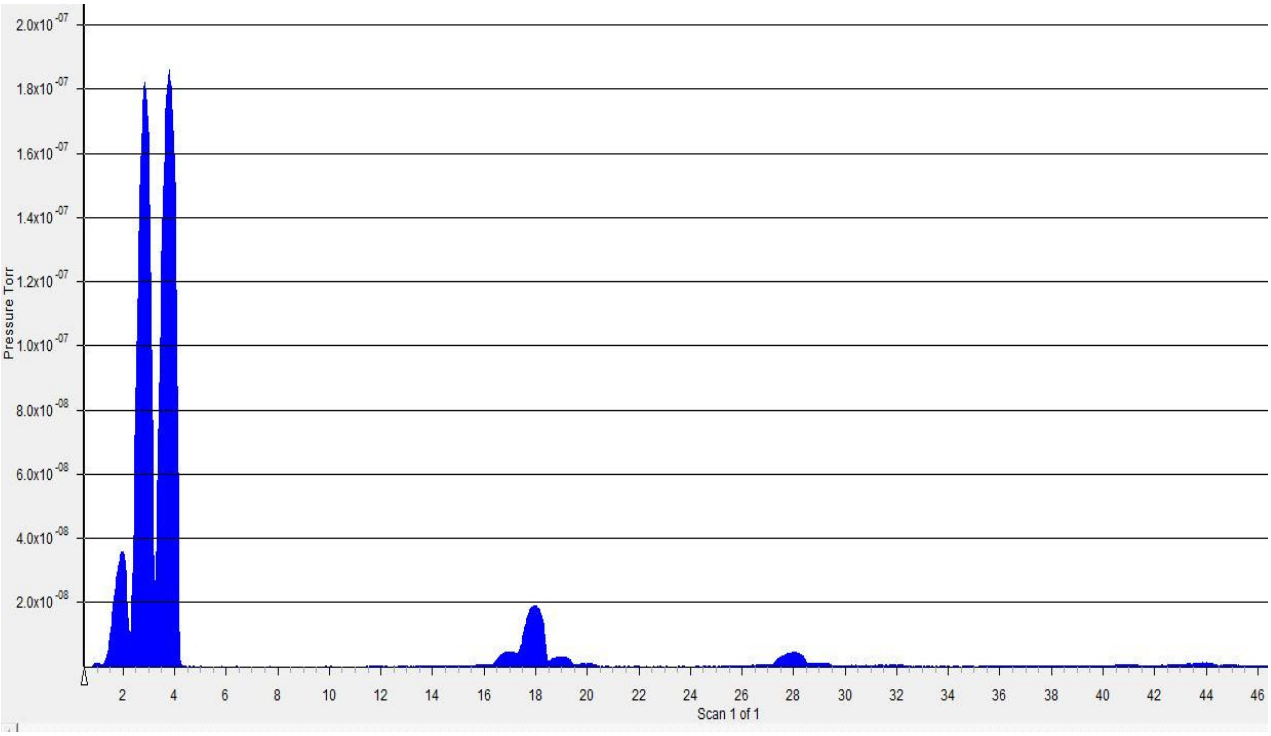

Figure 4.4(ii). Typical Mass spectrum in analysis of deuterium charged piece

4.4.5. Determination of relative sensitivity factors

Due to the large difference of the relative masses between H_2 and D_2 , the isotopic intensities in QMS for H_2^+, HD^+ and D_2^+ are not expected to be the same, even for same partial pressure of the species. Theoretically, the sensitivity factor for any gas, in the QMS is the ratio of blank corrected intensities at m/z values of M and partial pressure of the gas I in the mixture (I_M /P). The sensitivity factor (S_i) for H_2, as well as for D_2, was measured at various pressures from 10^{-1} to 8 Pa [103]. Mass spectral intensity versus pressure of the gas in the collection chamber was plotted for both hydrogen and deuterium. The plots are shown in Figure 4.5 for both hydrogen and deuterium. From the slope of linear regression of the data, the sensitivity factors for H_2 (S_{H2}) and D_2 (S_{D2}) were determined. Due to the practical difficulty in the preparation of pure HD gas, the sensitivity factor for HD was calculated as an arithmetic mean of the sensitivity factors of H_2 and D_2. It should be mentioned that Pyper et al. [78] determined sensitivityfactors employing pure H_2, D_2, and HD and their results indicated that the sensitivityfactor for HD is very close to the arithmetic mean of S_{H2} and S_{D2}.

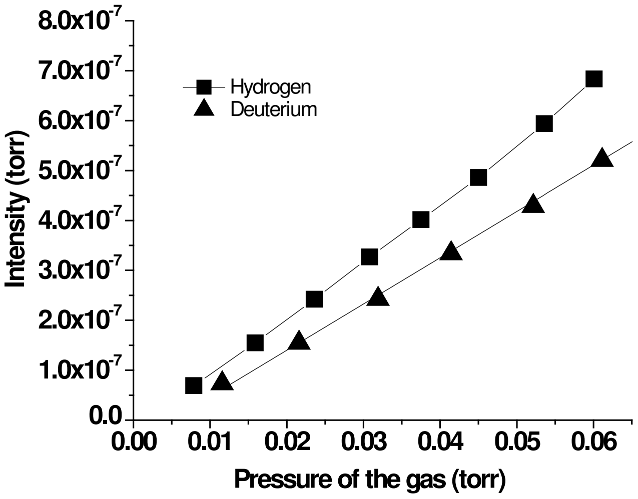

Figure 4.5. Plot between molecular peak intensity(at m/e 2 for H_2& 4 for D_2) versus pressure of H_2 & D_2 gas in collection chamber

4.5. Results and discussion

The $S_{H2}$and S_{D2}were found to be (1.17 ± 0.02) x 10^{-5} and (9.27 ± 0.12) x 10^{-6}, respectively. The calculated sensitivity factor for HD (S_{HD}) was (1.05 ±0.01) x 10^{-5}. The relative sensitivity factors with respect to hydrogen for H_2, HD, and D_2 were 1.000, 0.90 and 0.79, respectively. For the determination of activation energy of hydrogen/deuterium diffusion, charged alloy pieces were annealed at four temperatures 523, 573, 623 & 673 K. Hydrogen and deuterium concentration at different depths of alloy from the charged end was determined employing HVE-QMS. The depth profile of hydrogen and deuterium at all temperatures are represented in Figure 4.6 and 4.7, respectively. The uncertainty in the concentrations is about 14%, which is mainly due to the uncertainty in measurement of pressure and computation of mole fraction of the isotopes. The solid lines represent the fitted curves. Micrographs of hydride distribution along the axial-radial plane of the tube taken at three different locations from the electrolytically charged end are also shown in Figure 4.7. It is evident from these micrographs that as one moves away from the electrolytically charged end, the hydride (dark lines in the micrograph) area fraction decreases.

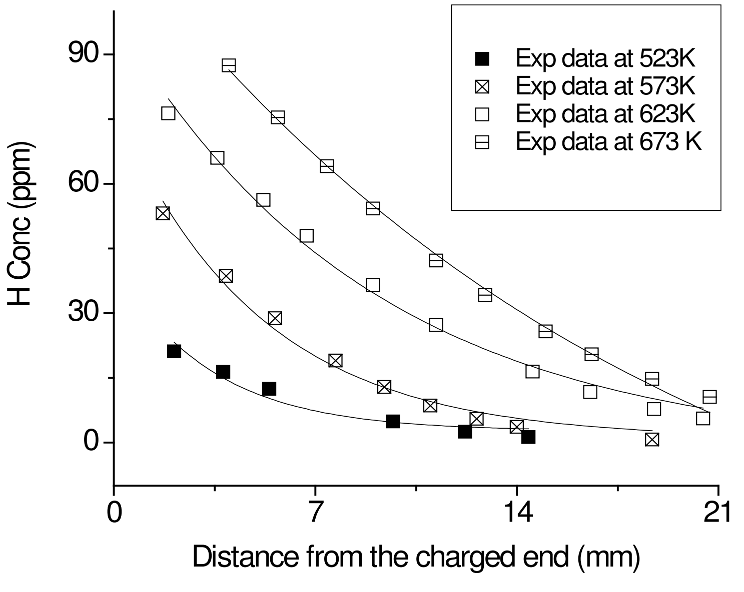

Figure 4.6. Depth profile of hydrogen in Zr-2.5%Nb annealed at various temperatures

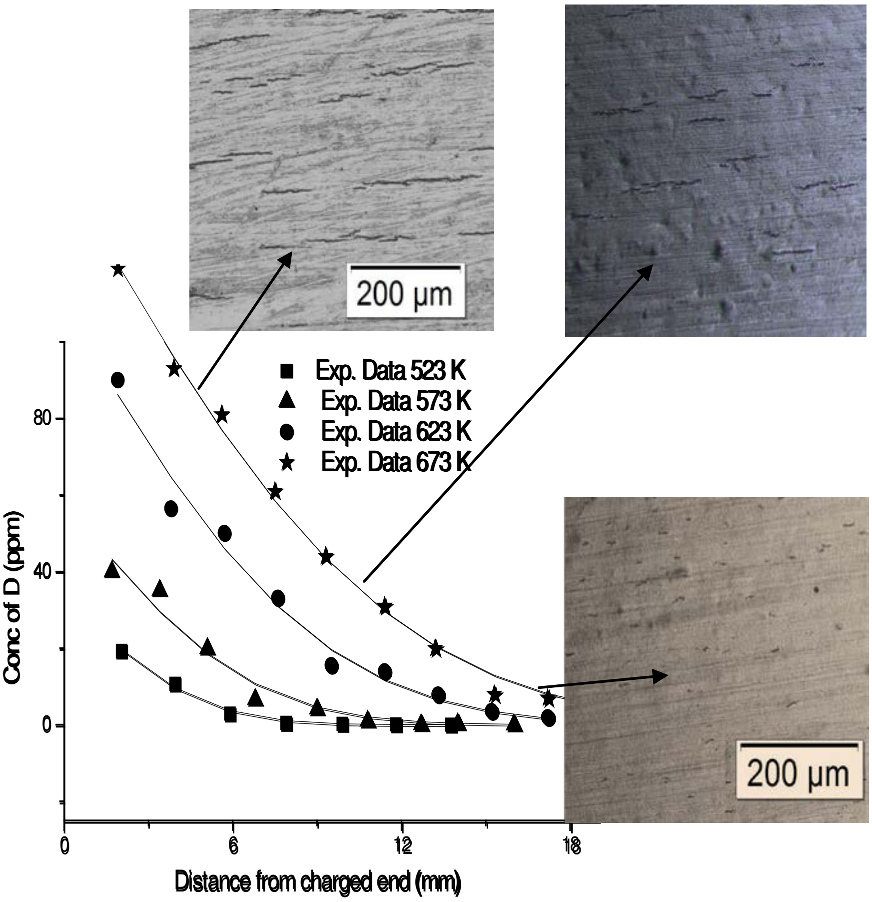

Figure 4.7. Depth profile of deuterium in Zr-2.5%Nb annealed at various temperatures. Also shown in this figure are hydride micrograph taken at three locations as a function of distance from the electrolytically charged end.

It is possible to determine TSS for dissolution of hydrogen and deuterium from the equilibrium concentration of H/D at the interface of hydride layer and the bulk sample annealed at different temperatures using equation 1. The equilibrium hydrogen isotope concentration at the interface of hydride layer and bulk sample can be determined by extrapolating the depth profile data to zero diffusion distance.

$$\mathrm{TSSD}(T) = A \exp[(-\Delta H_s/RT)] \qquad \ldots\ldots\ldots \quad (1)$$

Where,

TSSD = terminal solid solubility for dissolution (ppmw),

A = constant (ppmw),

ΔH_s = enthalpy of dissolution of zirconium hydride/deuteridein the matrix (kJ/mol), R = universal gas constant (8.314 kJ/mol K),

T = absolute temperature (K).

The TSSD of hydrogen and deuterium obtained by extrapolation are shown in Table 4.2 along with the literature data [89, 104, 105]. However the equilibrium hydrogen isotope concentration determined by extrapolation is very sensitive due to large uncertainty associated with sampling near the interface between hydride layer and the bulk sample and also the curve fitting of the data. Therefore, it will not be advisable to determine the TSS by extrapolation.

Table 4.2 Solubility Equations for TSSD from this work and with the data in literature

Reference	**Terminal Solid Solubility for Dissolution (TSSD) equation**	
	Hydrogen (μg/g)	**Deuterium (μg/g)**
This Work	$C_H = 2.8283 \times 10^4 \exp[-27903/RT]$	$C_D = 8.8430 \times 10^4 \exp[-33223/RT]$
Pan[22]	$C_{H.} = 8.080 \times 10^4 \exp[-34520/RT]$	
Kearns[8]	$C_H = 1.200 \times 10^5 \exp[-35900/RT]$	
Slattery[23]	$C_H = 6.860 \times 10^4 \exp[-33570/RT]$	

C_H = Concentration of hydrogen

C_D = Concentration of deuterium

The approach adopted by Laursen et al. [93] was followed to derive diffusion coefficients for H/D from the experimental data on the depth profile of $H_2/D_{2.}$ An analytical expression for the hydrogen/deuterium concentrations C(x,t) by solving the diffusion equation with the suitable boundary conditions are -

$$C(x,t) = \frac{C_s}{(1+\mathrm{erf}\lambda)}\left[1 - \mathrm{erf}\left(\frac{x}{2(Dt)^{\frac{1}{2}}}\right)\right], \quad \text{for } x > X$$

$$C(x,t) = C_s, \quad \text{for } x > X$$

Where λ is a solution of

$$\lambda \exp(\lambda^2)\,(1+\mathrm{erf}\lambda) = \frac{C_S}{(C_T - C_S)\pi^{1/2}}$$

X is given by

$$X = -\,2\,\lambda\,(Dt)^{1/2}$$

Where,

C_s = hydrogen/deuterium concentration in solution defined by the equilibrium with the hydride/deuteride layer.

D = diffusion coefficient

C_T = the average hydrogen/deuterium concentration on a cross-section of the sample containing the hydride/deuteride layer.

It is assumed by this equation that the diffusion is taking place only in the axial direction and that the interface between an initially hydride/deuteride part of the sample and the unhydride/undeuteride region is x = 0. The hydride/deuteride coating is the source of hydrogen/deuterium and as it dissolves, the position of the end of the deposition recedes to position X at time t.

The concentration versus depth profile was fitted using a non-linear least square fitting procedure with the above equation based on Fick's second law of diffusion. In the fitting procedure, Cs and *D* were kept as free parameters which were obtained by the chi square minimization procedure in the fitting process. Diffusion coefficients (*D*) at different temperatures are given in Table 4.3.

Table 4.3 Diffusion coefficient of Hydrogen and Deuterium in Zr-2.5%Nb measured by HVE-QMS

Temperature (K)	D_{H} **(m^2.s^{-1})**	D_{D} **(m^2.s^{-1})**
673	2.09×10^{-10}	1.13×10^{-10}
623	1.79×10^{-10}	6.97×10^{-11}
573	6.62×10^{-11}	3.63×10^{-11}
523	3.84×10^{-11}	1.88×10^{-11}
Pre-exponential factor, D_0 (m^2/s)	1.41×10^{-7}	6.16×10^{-8}
Activation Energy, E_A (kJ/mol)	36.00	35.26

Figure 4.8 show the Arrhenius plot (log D vs 1/T) for hydrogen and deuterium, respectively. The data were fitted into the equation,

$$D = D_0 \exp(-E_A/RT) \quad \ldots\ldots\ldots\ldots\ldots\ldots \quad (2)$$

Where,

D= diffusion coefficient(m^2/s),

D_0 = pre-exponential factor (m^2/s),

E_A = activation energy for diffusion (kJ/mol),

R = universal gas constant (8.314 kJ/mol.K),

T = absolute temperature (K).

The E_A values for diffusion of Hydrogen and Deuterium in Zr-2.5%Nb alloy, were found to be nearly same i.e, 36 ± 5 kJ.mol^{-1} and 35 ± 1 kJ.mol^{-1}, respectively. Gulbransen and Andrew [82] also reported nearly same value of E_A for hydrogen and deuterium for diffusion in Zr, though the magnitude of E_A was much higher than that obtained in the present study.

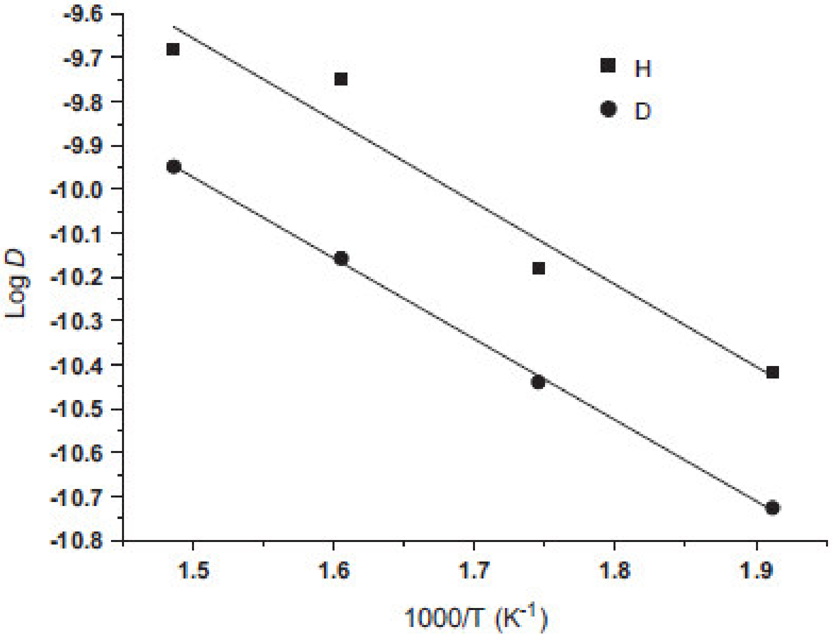

Figure 4.8. Log *D* versus 1000/T plot for hydrogen and deuterium

The E_A values obtained in the present work are close to those reported by Khatamian [97] for diffusion along longitudinal and transverse directions. The diffusivity of Deuterium in Zr-2.5%Nb alloy was measured by Khatamian [97] using HVE-QMS as was the case in present investigation. As was pointed out earlier there are differences in the fabrication route of Zr-2.5%Nb pressure tubes used in Indian PHWRs [84, 85] and CANDU reactors [97, 100]. It is reported that the microstructure of the Indian pressure tubes do not possess continuous film of ^{2}-phase along the grain boundary and hence the diffusivity of hydrogen isotopes in Indian PHWR pressure tube is expected to be lower than the corresponding values for CANDUPressure tubes. This indeed was the case as the diffusivity values obtained in the present investigation were almost half the values reported by Khatamian **[**97**]** at 523 and 573 K (as shown in Table 4.4) [106,107].

The higher diffusion coefficient (*D*) of hydrogen than that of deuterium at any temperature is attributed to the pre-exponential factor (D_0), which was found to be higher for hydrogen than that for deuterium by a factor of 2.3, in line with the mass dependence ($1/\sqrt{m}$)

of jump frequency. The reaction of H_2O/D_2O with Zr-2.5% Nb through cracks in the oxide layer has also been found to be a potential route of hydrogen/deuterium pick up [108],which need to be modeled to obtain a realistic estimate of the hydrogen/deuterium ingress in the alloy [109].

Table 4.4 Comparison of measured diffusion coefficients for deuterium (D_D) with literature report based on HVE-MS

Annealing temperature (K)	D_D ($m^2.s^{-1}$) Present work	D_D ($m^2.s^{-1}$) Ref. [16]
523	1.88×10^{-11}	3.3×10^{-11}
573	3.63×10^{-11}	7.2×10^{-11}

Chapter – 5

Palladium Nanoparticles Hosted on Hydrazine-grafted Magnetite and Silica Particles for Catalyzing the Reduction of Oxymetal Ions with Formic Acid and for Hydrogen sorption

5.1. Introduction

Palladium metal finds extensive applications in catalysis, hydrogen technology and electrochemical devices. The functional properties of Pd metal in these applications are further enhanced when dimension of Pd metal is in nano-scale range [110].It is known that the nano-scale materials have high surface area, with desirable effect on the catalytic properties [110-112]. For example, palladium nano-particles (Pd NPs) catalyse electrochemical oxidation of alcohol, formic acid and hydrogen [113-117], cross-coupling and other synthetically useful organic reactions[118, 119]and inorganic reductions such as Cr(VI) to Cr(III) etc. [120-126], resulting in their extensive use in organic synthesis, fuel cells, sensors and environmental remediation.

In general, the PdNPs can be prepared by physical methods (sputtering methods, Ion- and electron-beam-induced deposition methods and laser ablation method), hydrothermal methods, electrodeposition methods and chemical reductions methods[110, 127-129].The sonolysis, radiolysis and photolysis are also used for generating reducing species and/or facilitating the chemical reduction of precursor metal ions[130-132].It is possible to control the formation of Pd NPs having desirable shapes and dimensions [133-139]. The bimetallic, core-shell and hollow nanostructures have been reported for different potential applications including catalysis [140-142]. The major hurdles in the applications of Pd NPs as the catalyst are their physical and chemical stabilities. To some extent, these problems could be overcome by appropriate choice of the capping agents. However, the recyclability of the catalyst, easy retrieval from the system/process and product contamination with Pd NPs remains the bottleneck in their large scale commercial applications.

5.2. Reported Work

The host matrices such as carbon nanomaterials [142-146], inorganic particles [147-151] and synthetic/bio-polymer [152] may address stability and recyclability problems of PdNPs. The polymer films/membranes have been proposed as dip catalyst [153-157]. However, the accessibility of NPs to the reactants is a major issue necessitating the use of highly porous matrices. Egg-shell membrane has highly fibrous structure. This bio-membrane takes up precursor metal ions, reduce and stabilize them leading to formation of Pd NPs of high catalytic activity [158, 159]. The silica can also be a good host as it can be obtained in different forms like mesoporous molecular sieves with high surface area and void volume, stable at elevated temperatures, pressure and chemical environment, and is easily available. The Pd NPs immobilized on the silica matrices are being used in organic synthesis as heterogeneous catalyst[160-162]. The silanol groups on silica can be used for the covalent attachment of functional groups. The Pd NPs on super-paramagnetic particles such as Fe_3O_4 are magnetically recoverable and have been envisaged for sustainable technology[148]. The alkoxysilane coating on Fe_3O_4 can impart chemical stability and provide precursor sites for anchoring the desirable nanocatalysts. The Pd NPs immobilized on anatase TiO_2 finds application as a photocatalyst[149, 163].

There are three general chemical reduction routes for the formation of noble metal NPs on the SiO_2, Fe_3O_4 and TiO_2[110, 148, 160-162]. First one involves the formation of seeds during the reduction of precursor ions in the solution and subsequent nucleation and growth of NPs on the active sites on the host inorganic particles. In another one, the precursor ions have to be loaded on the host particles by the ion-exchange or complexation mechanism and subsequent reduction using appropriate reducing agent. It is also possible to incorporate metal salts during synthesis of host particles, and hydrothermal reduction leading to the formation of NPs on to the host particles itself [110]. However, a major problem associated with these methods is very low nanocatalyst loading, loss of costly noble metal precursor ions, complicated synthesis procedure, no- control over NPs formation process. Recently, an interesting method has been reported which involves grafting of reducing agent *N*-methyl-*D*-glucamine itself in pores of the synthetic membrane for formation of noble metal nanoparticles[164].

5.3. Present Studies

In the present work, a new synthetic route has been developed that involves reduction, nucleation and growth of Pd NPs on the hydrazine grafted SiO_2 and Fe_3O_4 particles. The different steps involved in this synthesis procedure have been monitored by the elemental analyses, and Pd NPs thus formed on inorganic host particles have been characterized by microscopy and elemental mappings. The catalytic activities of these Pd NPs anchored SiO_2 and Fe_3O_4 particles have been tested in the formic reduction of Cr(VI) and U(VI) ions.

5.4. Experimental

5.4.1. Reagents and Apparatus

Fe_3O_4 (20-30nm) was purchased from J.K. Impex, Mumbai (INDIA). SiO_2 was obtained from Spectrochem Private Ltd. Mumbai (INDIA), (3-Glycidyloxypropyl) trimethoxysilane and Palladium chloride ($PdCl_2$) were purchased from Sigma – Aldrich (Germany). Formic Acid and Hydrazine Hydrate ($NH_2.NH_2.H_2O$) were procured from SD Fine Chemicals, Mumbai (INDIA). Potassium dichromate was obtained from Sigma-Aldrich (Germany). Other chemicals such as ethanol and ammonia were acquired from Chemco Fine Chemical, Mumbai (INDIA). All chemicals were of analytical grade and were used as received, without further purification.

Horiba, Japan make carbon determinator model 320 V was used for determination of carbon. Chromatography and Instrument Company (CIC), Vadodara, India, make

Nitrogen,determinator was employed to determine nitrogen content based on IGF-TCD (Inert Gas Fusion – Thermal Conductivity Detector) principle. Pd present in the Pd nanoparticles coated on Fe_3O_4 and SiO_2 was determined by Spectro Arcos, Germany make Inductively Coupled Plasma-Atomic Emission Spectroscopy (ICP-AES). For characterization of the nanoparticles following instruments were used - X-ray diffraction (XRD) (Rigaku Miniflex-600 instrument, Japan), High resolution - Transmission Electron Microscopy (Zeiss Libra 200 FE TEM), Field Emission Gun-Scanning Electron Microscopy (FEG - SEM) (Zeiss make AURIGA model), Energy-dispersive X-ray spectroscopy (EDS) (OXFORD Instrument), Vibrating Sample Magnetometer (VSM) (Cryogenic Ltd., UK), Sievert's Apparatus (HYDEN Isocicma, U.K.), Mössbauer spectrometer (NUCLEONIX Systems Pvt. Ltd. Hyderabad), X-ray Photoelectron Spectroscopy (XPS) (Staib Instruments, Germany), Fourier transform infrared spectroscopy (FTIR)(JASCO FT-IR/420 (JAPAN).Pdnanocatalysts were used for reduction of oxymetal ions by formicacid. For absorbance studies of oxymetal ions UV - Vis absorption spectrophotometer (K-MAC Technology, South Korea) was employed.

5.4.2. Synthesis of Pd nanocatalyst coated on Fe_3O_4 and SiO_2

A new synthetic method was developed to anchor Pd nanoparticles on inorganic solid support Fe_3O_4. In this synthetic route Fe_3O_4 was dispersed in 60mL of ethanol and 100µL of ammonia ultrasonically. 3mL of (3-Glycidyloxypropyl)trimethoxysilane was added to it and the solution was stirred for 20 hours with magnetic stirrer. The prepared precursor Fe_3O_4 particles were retrieved using a magnet. These were washed with water then ethanol and dried. The sample was analysed for carbon by Combustion-cum-IR detection technique and it was found that carbon concentration was 1.5% or 15000 ppmw(15000 µg/g). Since precursor Fe_3O_4 does not containany carbon atom so carbon concentration of 15000 µg/g was due to epoxy silanemoiety which contained 7 carbon atoms, therefore corresponding epoxy concentration $=\frac{15000}{7 \times 12}$ µmol/g = 177 µmol/g.These silane coated Fe_3O_4 particles were mixed in 25mL hydrazine in a 50 mL beaker and stirred for 20 hours. Silane coated Fe_3O_4 particles reacted with hydrazine and covalently linked hydrazine with anchored epoxy ring on Fe_3O_4. These particles were retrieved using a magnet, washed with acid-water (pH 1-2), ethanol and then dried. The sample was analysed for nitrogen content, using Inert Gas Fusion - TCD detection technique. Nitrogen content was found to be 0.51% or 5100 ppmw (5100 µg/g). Based on nitrogen analysis, the hydrazine content was found to be $\frac{5130}{2 \times 14}$ µmol/g = 180 µmol/g.

0.005M $PdCl_2$solution was prepared. 10 mL of this solution was kept as stock solution and another 10 mL was added in the above inorganic material. The material was left for 48hours for equilibration. Loading of Pd in this sample was monitored by Inert coupled plasma – Atomic emission Spectroscopy (ICP-AES) before and after equilibration.

Pd nanoparticles were loaded on an inert support (SiO_2) using similar type of procedure as used for Fe_3O_4 support. Since $SiO_2$was used as the inert support and not Fe_3O_4 (which was retrievable by magnetic field), a different method was adopted for estimating Pd loading on Silica by ICP-AES. In this method, 500 mg of the Pd loaded silica was taken and 8ml of aqua regia (3:1- HCl:HNO_3) was added to it. The mixture was stirred with the help of magnetic stirrer for 3hrs and then filtered such that SiO_2 remained on the filter paper. The filtrate was evaporated in IR-Lamp and Pd (solid) remained in the beaker.10 ml HNO_3 (pH=1) solution was added in the beaker and the sample was analyzed by ICP-AES.

BeingsuperparamagneticFe$_3$O$_4$and Pd coated Fe_3O_4 showed sigmoidal behaviour when magnetization was plotted against the external magnetic field that was applied. The images of Fe_3O_4@Pd and SiO_2@Pd particles were obtained by FE-SEM (Zeiss make AURIGA model). Elemental mappings were done using EDS (OXFORD instrument).

Fe_3O_4@Pd /SiO_2@Pd particle samples for FE-SEM and EDS were prepared by making their solution in acetone. A drop of the solution was put on glass slide and coated with gold.The particle sizes were determined from HRTEM images using software Image J.For obtaining size distributions of Pd NPs on the Fe_3O_4 and SiO_2 particles, a high resolution transmission electron microscopy (Zeiss Libra 200 HR TEM) was used. The samples for HR TEM imaging were prepared by dispersing the sample (Fe_3O_4@Pd /SiO_2@Pd particles) in acetone kept in a beaker and ultrasonicating it for 15-20 minutes. One drop of thus prepared solution was put on a carboncoated copper grid (200 mesh size) and dried before loading it to the HR TEM instrument.

Figure 5.1. Formation of Pd NP's on inert support (SiO_2) using same protocol

Fourier transform infrared spectroscopy (FTIR) were done by JASCO FT-IR/420 (JAPAN). The samples were mixed with anhydrous KBr and pressed into pellets under high pressure and used for FTIR analysis. The % transmittance of the samples was measured at different wavenumbers in the range between 400-4000 cm^{-1} by averaging 16 scans for each spectrum. The reduction of Cr(VI) to Cr(III) was studied using reactant solution consisting of 10 mL of 7 mmol L^{-1} of Cr(VI) (using $K_2Cr_2O_7$) and 10 mL of 70 mmol L^{-1} formic acid. The reduction of UO_2^{2+} ions was carried out in double jacketed glass vessel kept at 323 K using thermostat bath. After attaining constant temperature, the known amount of Fe_3O_4@ /SiO_2@Pd having 1 mg Pd NPs catalyst was added and reduction was carried out with constant stirring (300 rpm) using magnetic stirrer. The reduction was monitored by taking out aliquot and measuring absorbance at 348nm at regular time intervals using miniature UV-Vis spectrophotometer (K-MAC Technology, South Korea). The reduction U(VI) was also studied in a similar fashion using the reaction solution prepared by mixing equal volumes (8 mL) of 0.1mol L^{-1} $UO_2(NO_3)_2$solution at pH=2 and 1 mol L^{-1} formic acid.

5.5.Results and Discussion

5.5.1. Synthesis

The precursor host particles were prepared by coatings of (3-glycidyloxypropyl)trimethoxysilane covalently attached to –OH groups on the hydrolyzed surfaces of Fe_3O_4 and SiO_2 particles. In subsequent step, the hydrazine units were attached by creation of branching due to epoxy ring opening. The representative chemical reactions are shown in Figure 5.2.

The amounts of (3-glycidyloxypropyl)trimethoxysilane anchored and subsequent attachment of hydrazine on the host particles were determined by total carbon and nitrogen analyses. Based on the carbon content, it was observed that 177±5 μmol g^{-1} (3-

glycidyloxypropyl)trimethoxysilane was coated on the Fe_3O_4 particles. The nitrogen content of hydrazine-grafted Fe_3O_4 particles was found to be 180±8 μmol g^{-1} indicating nearly complete conversion of epoxy units with hydrazine as shown in Figure 5.2. The Pd NPs were formed spontaneously by equilibration of hydrazine grafted Fe_3O_4 and SiO_2 particles in a well-stirred $PdCl_2$ solution kept at room temp. This is similar to electro-less deposition of noble metals on the self-reducing polymer support [158, 159, 164]. The amounts of Pd^0 deposited on the host particles were determined, either by measuring the change in concentration of Pd^{2+} ions before and after equilibration of the hydrazine-grafted Fe_3O_4 particles in the solution or leaching out Pd content of the hydrazine grafted SiO_2 particles in aqua-regia as described in the experimental section. The amount of Pd^0 anchored on the hydrazine grafted Fe_3O_4 and SiO_2 particles were found to be 12 and 20 mg g^{-1}, respectively.

It is interesting to note from the nitrogen analysis that bonded hydrazine was not fully utilized for the Pd NPs formation as reported elsewhere for free hydrazine [165]. For example, the nitrogen content on Pd coated Fe_3O_4 particles was found to be≈178 μmol.g^{-1}. The amount of Pd (113 μmol g^{-1}) deposited on Fe_3O_4 was lower than the quantity expected from the hydrazine consumption. This seems to suggest that all the Pd^0 was not utilized in the formation of Pd NPs and some of the Pd^0 got lost during washing etc. However, the amount of Pd (189 μmol g^{-1}) deposited on SiO_2 was similar to the quantity of hydrazine consumed indicating no significant loss of Pd^0 content from host particles.

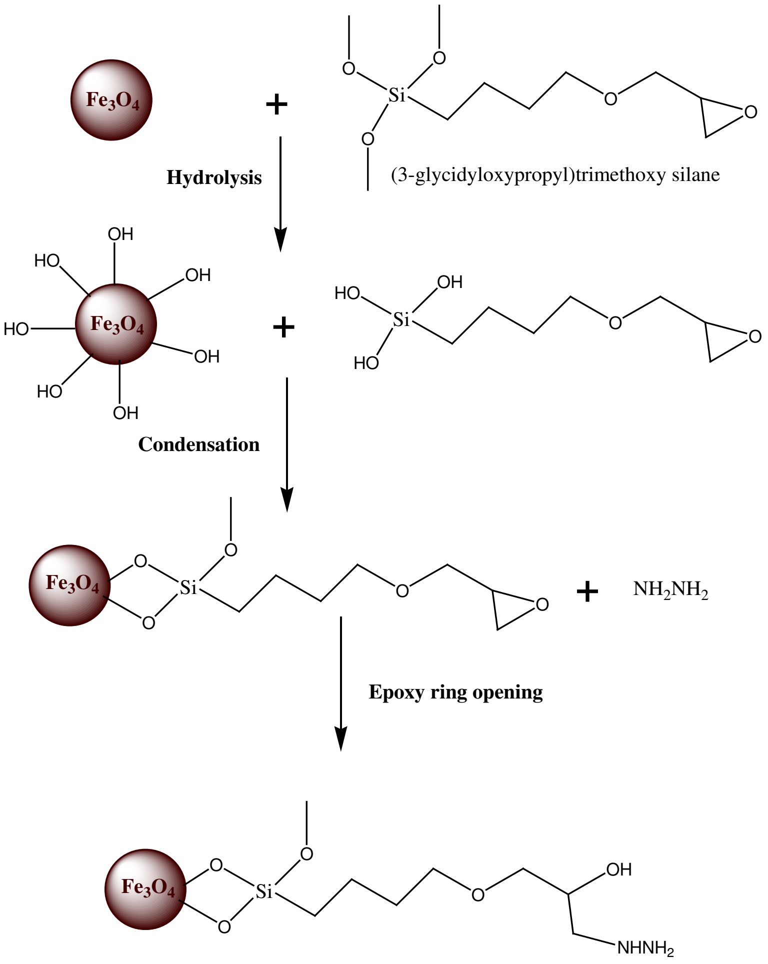

Figure 5.2. Chemical modifications involved in the formation of self-reducing particles

5.5.2. Characterizations

The presence of functional groups before and after the formation of Pd NPs on the Fe_3O_4 particles were studied by Fourier transformed infrared spectroscopy (FTIR). It is seen from FTIR spectra taken before and after formation of Pd NPs that the vibration bands corresponding to glycidyl units disappeared and –OH & -NH groups appeared in FTIR spectrum of the final product, shown in Figure 5.3. FTIR spectra of pristine Fe_3O_4 showed the characteristic Fe-O absorption bands at around 580cm^{-1} and 640cm^{-1}. For (3-glycidyloxypropyl)trimethoxysilane coated Fe_3O_4, the IR band of Si-O-Si at 1094 cm^{-1} merged with the band of epoxy/oxirane group of for (3-glycidyloxypropyl)trimethoxysilaneat

1129 cm^{-1}, and also at 2926cm^{-1} C-H stretching frequency was observed. This indicated that epoxy group bearing silane ((3-glycidyloxypropyl)trimethoxysilane) was coated successfully on to the Fe_3O_4. The FTIR spectrum of hydrazine grafted particles, formed by reaction of epoxy rings of precursor particles with hydrazine, indicates that the epoxy group IR absorption band has decreased. Increased intensity of the absorption band between 3200-3500cm^{-1} was observed due to O-H, N-H groups, formed during the epoxy group opening with the hydrazine. In addition to this, an absorption peak at 1360 cm^{-1} corresponding to C-N stretching frequency was also seen. After formation of the Pd NPs, the IR spectra found to be similar indicating that the N-H groups remained in the host particles.

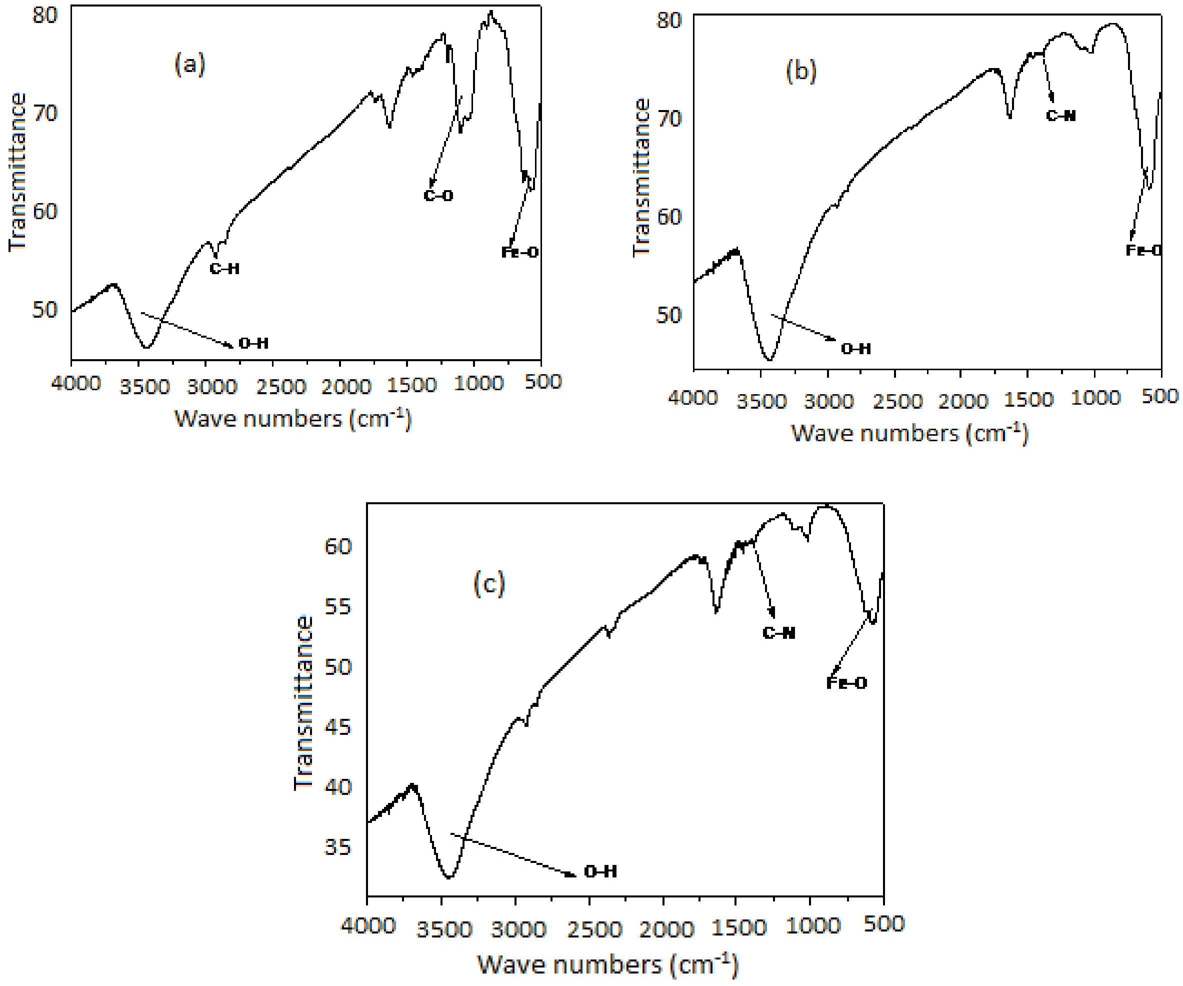

Figure 5.3. FTIR spectra of (3-glycidyloxypropyl)trimethoxysilane coated Fe_3O_4 particles (a), hydrazine grafted Fe_3O_4 particles (b), and Pd NPs embedded particles (c)

Based on these experimental evidences, the possible chemical reaction involved in the formation of Pd NPs is shown in Figure 5.4.

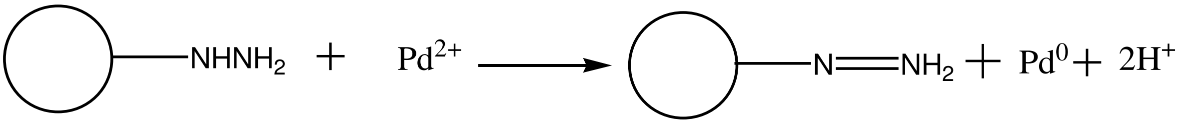

Figure 5.4. Chemical reaction involved in the formation of Pd nanoparticle on hydrazine grafted SiO_2 and Fe_3O_4 particles

As can be seen from X-ray photoelectron spectroscopy (XPS) spectra shown in Figure 5.5, the peaks at 335.9 eV and 341.1 eV are matching with 335.7 (Pd $3d_{5/2}$) and 341.0 eV (Pd $3d_{3/2}$) reported elsewhere for Pd^0[57].

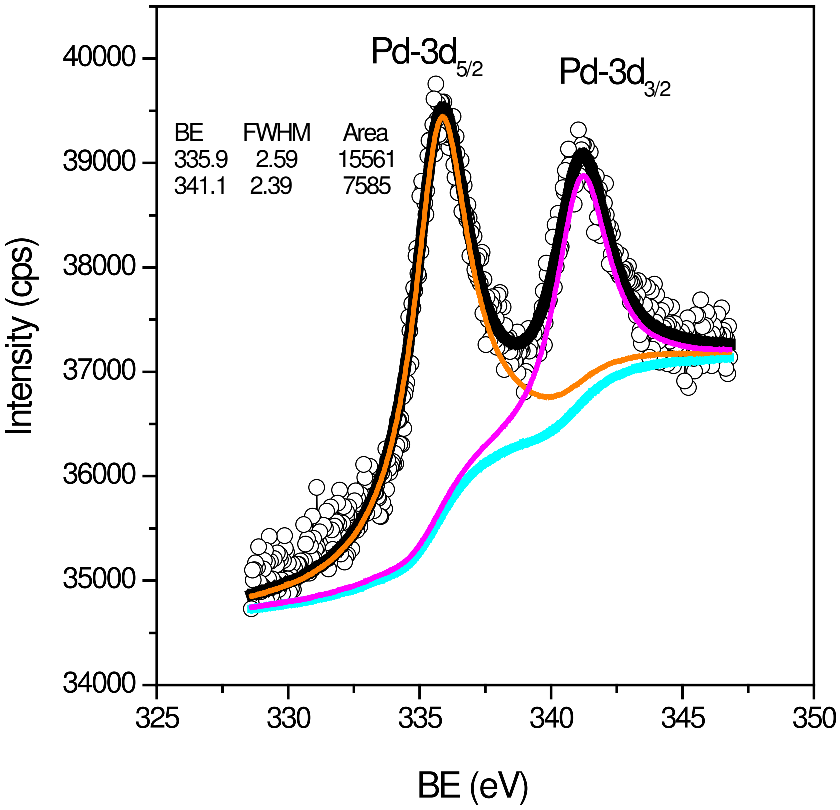

Figure 5.5. Deconvoluted core level Pd_{3d} XPS spectrum of Pd NPs embedded Fe_3O_4 particles

The XRD pattern shown in supporting information: Figure 5.6 confirmed that the Pd NPs formed on the inorganic host particles are crystalline as expected.

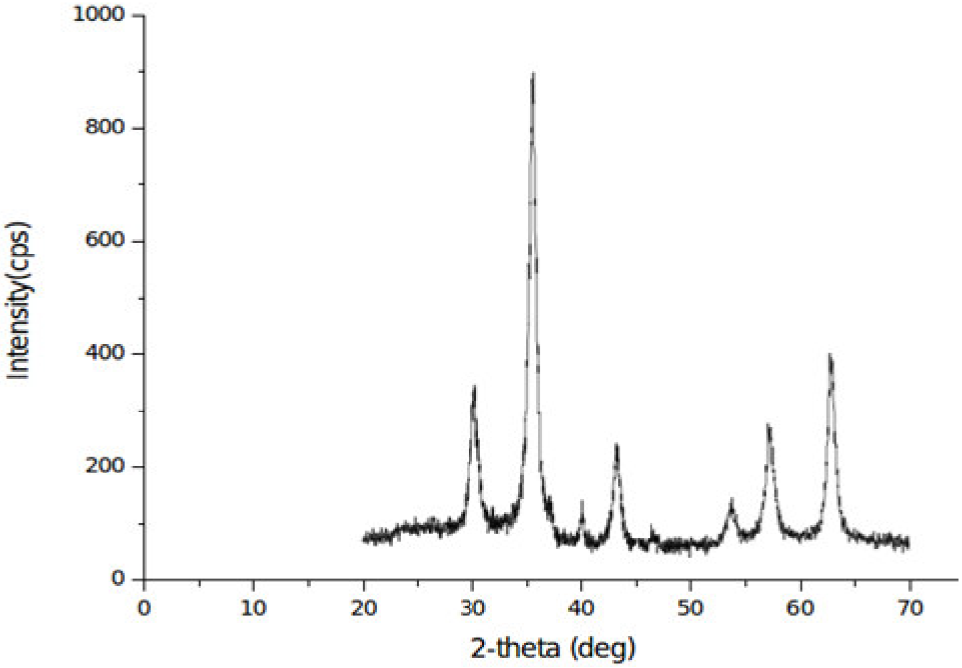

Figure 5.6. Powder XRD pattern of Fe_3O_4@Pd particles showing peaks at 40.08æand 46.7æ corresponding to planes of Pd FCC crystal

The effect of silane coating and subsequent formation of Pd NPs on the superparamagnetic properties of the Fe_3O_4 NPs was studied due to its importance in withdrawing the catalyst from the reaction solution. The variations of magnetization (M) as a function of magnetic field (H) recorded at room temperature for the pristine Fe_3O_4 and Pd NPs embedded Fe_3O_4 particles are shown in Figure 5.7.

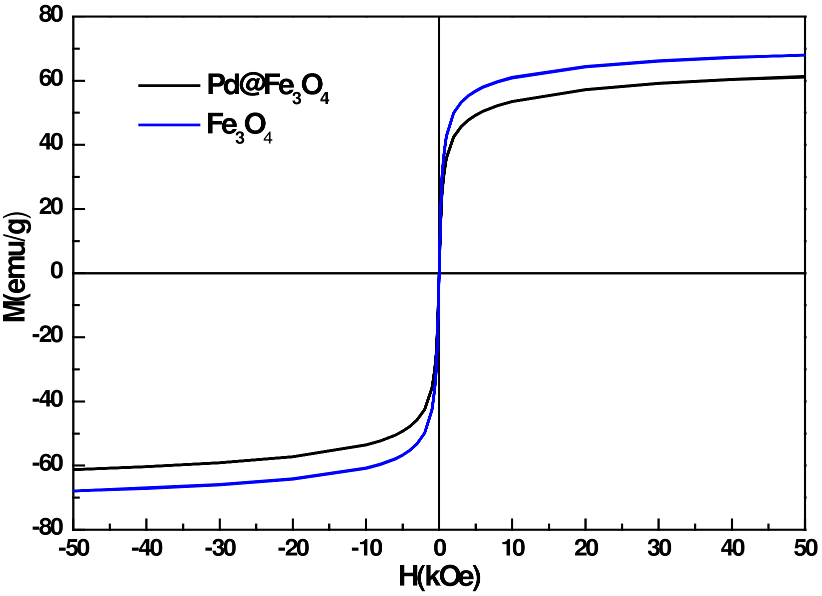

Figure 5.7. Magnetization (M) vs. magnetic field curves of pristine Fe_3O_4 and Pd NPs embedded Fe_3O_4 particles

It is evident from the magnetization curves that the final Pd NPs embedded Fe_3O_4 particles had no remanence and coercivity, and there was a slight decrease in the magnetization saturation with respect to pristine Fe_3O_4 particles. The magnetization saturation of the final Pd NPs embedded Fe_3O_4 particles was still very high (≈60 emu g^{-1}) indicating a very thin coating on Fe_3O_4 formed during anchoring of Pd NPs. Thus, the catalyst could be easily retrieved by applying an external magnetic field.

The morphology of the Pd NPs embedded host particles were studied by field emission scanning electron microscopy (FE-SEM) and elemental mappings by energy-dispersive spectroscopy (EDS). It is seen from the FE-SEM images given in Figure5.8 a)& b)that Pd NPs anchored on the SiO_2 (SiO_2@Pd) and Fe_3O_4 (Fe_3O_4@Pb) host particles were spherical having 60-100 nm and 15-30 nm sizes, respectively. The host particles size distribution histograms are in Figure 5.9.

It is evident from the elemental mappings on the host particles by EDS shown in Figure5.10that the Pd NPs were uniformly distributed on the surfaces of both SiO_2 and Fe_3O_4 host particles.

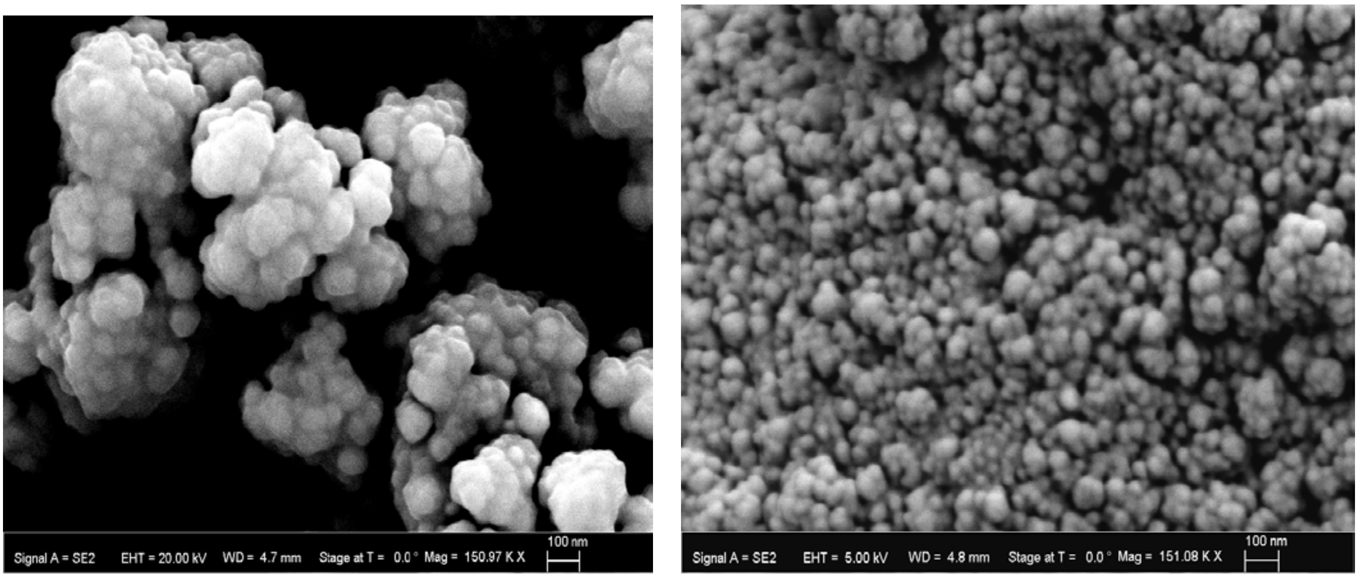

(a) (b)

Figure 5.8. FE-SEM images of Pd NPs embedded SiO_2 particles (a) and Fe_3O_4 particles (b)

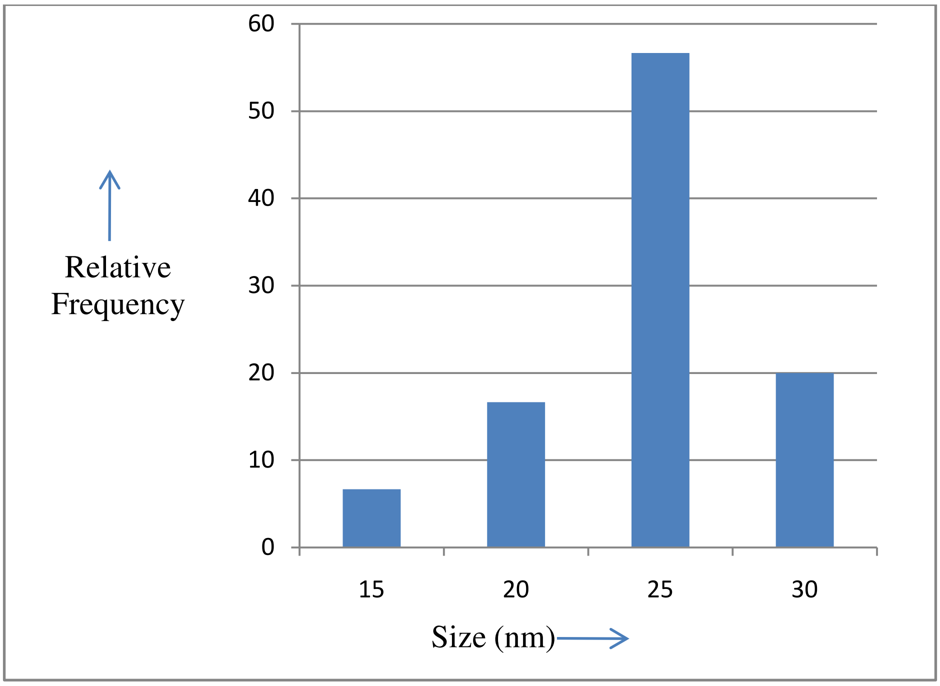

(a)

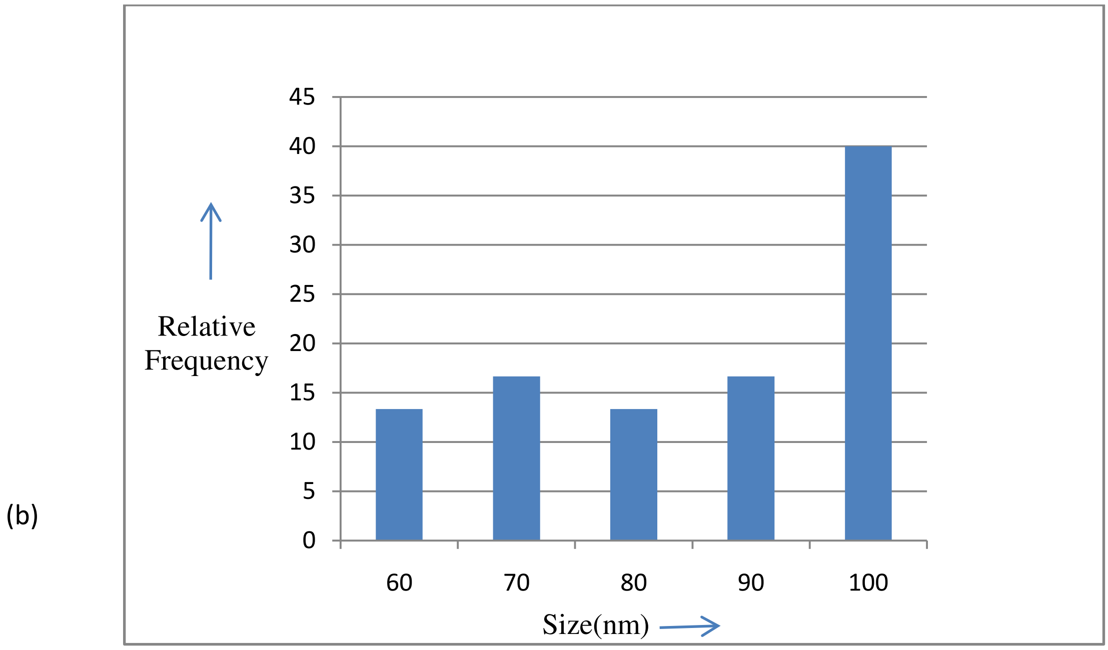

Figure 5.9.Fe_3O_4@Pd (a) and SiO_2@Pd (b) particles size distribution histograms obtained from the analyses of FE-SEM images

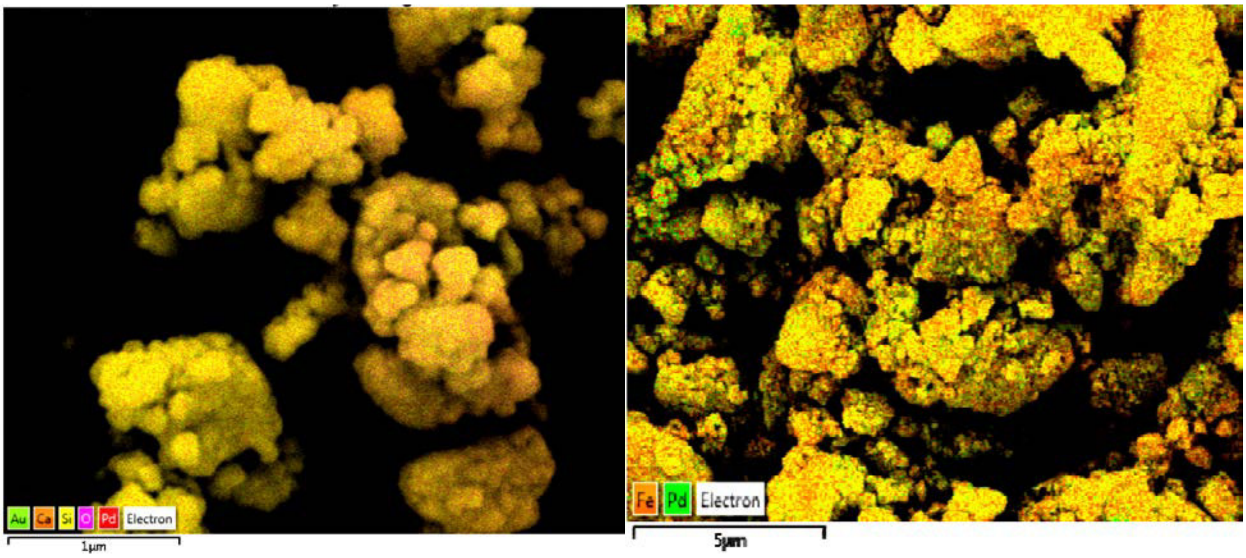

(a) (b)

Figure 5.10. Elemental mappings of Pd and Si on Pd NPs embedded SiO_2 particles (a) andPd and Fe on Pd NPs embedded Fe_3O_4 particles (b) by EDS

The particles were subjected to a high resolution electron transmission microscopy (HR-TEM). The representative HR-TEM images are shown in Figure 5.11 and size distribution histograms are given in Figure 5.12. The sizes of Pd NPs were found to be in the range of 0.1-0.5 nm on Fe_3O_4 particles. However, the sizes of Pd NPs on the SiO_2 particles were relatively bigger and ranged from 0.5-2.0 nm with 1 nm median. The bigger size Pd NPs formation could be attributed to higher loading of Pd^0 content on SiO_2 particles (20 mg g^{-1}) as compared to Fe_3O_4 particles (12 mg g^{-1}). This seems to suggest that Ostwald repining would have operated during spherical Pd NPs growth on the surfaces of both host particles.

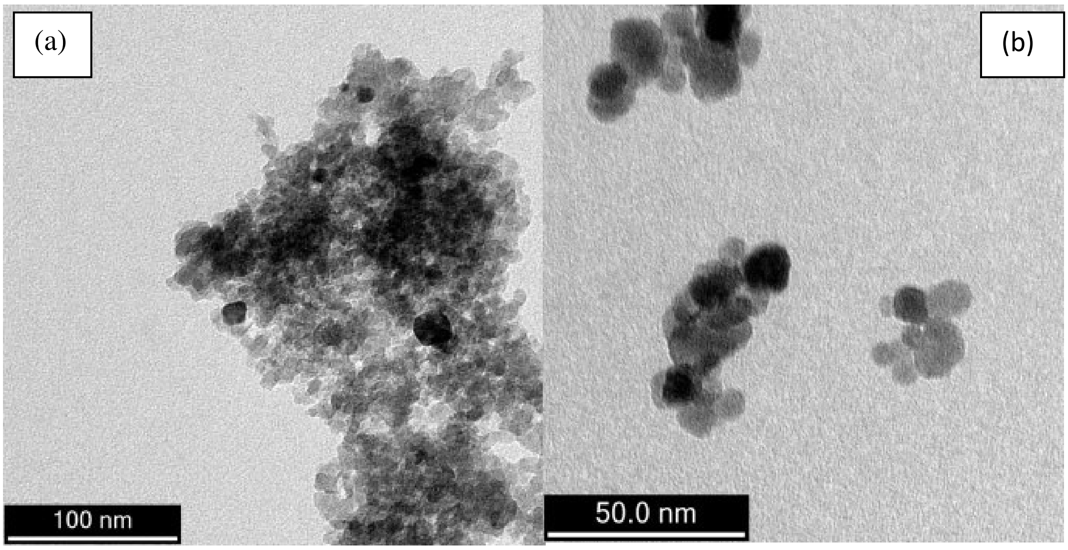

Figure 5.11. Representative HR-TEM images of Pd NPs embedded SiO_2 particles (a) and Fe_3O_4 particles

(a)

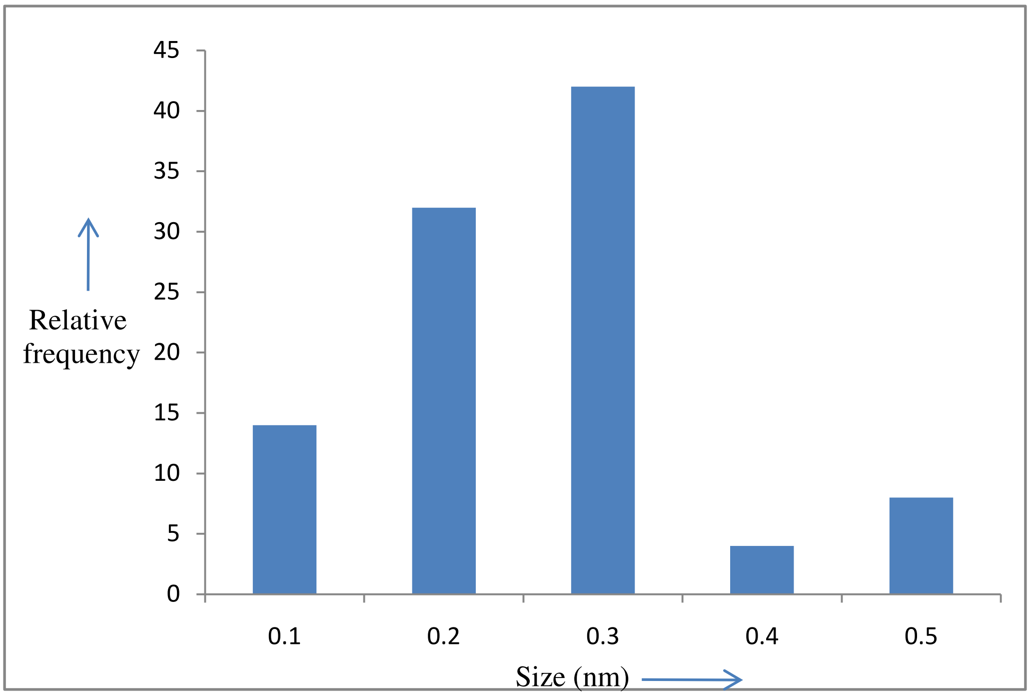

(b)

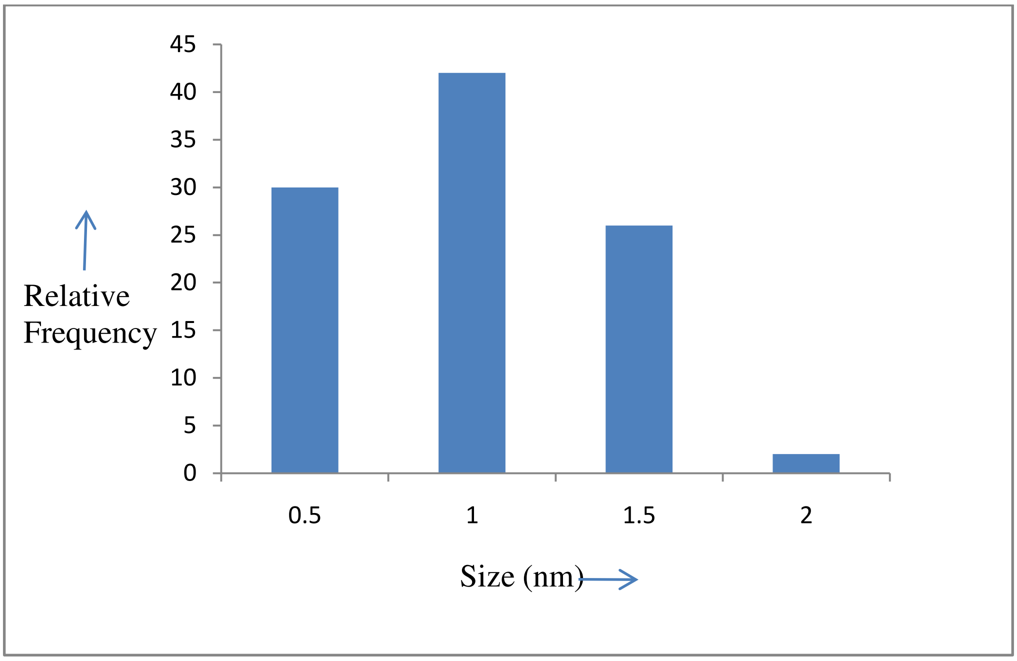

Figure 5.12. Pd nanoparticles size distribution histograms on Fe_3O_4 (a) and SiO_2 (b) obtained by analyses of HRTEM images

5.5.3.Catalytic applications

The catalytic activities of the Pd NPs on the host SiO_2 and Fe_3O_4 particles were examined in the reductions of Cr(VI) ($Cr_2O_7^{2-}$) and U(VI) (UO_2^{2+}) ions with formic acid at 50°C temperature. These reductions are not observed at room temperature, and proceed at elevated temp in the presence of catalyst[120-126, 167, 168]. This seems to suggest that a high activation energy barrier in the reduction of U(VI) and Cr(VI) are overcome by the use of efficient catalysts such as Pd NPs. It is interesting to note that formic acid also decomposes to H_2 and other gaseous products under similar condition [169-171].

The possible reactions involved are:

$HCOOH \longrightarrow CO_2 + 2H^+ + 2e^-$ (1)

$HCOOH \longrightarrow H_2 + CO_2$ (2)

$HCOOH \longrightarrow H_2O + CO$ (3)

The redox potentials for Cr(VI)/Cr(III) and U(VI)/U(IV) couples are 1.33 V and 0.41V vs. NHE, respectively. The redox potential for HCOOH /CO_2, $2H^+$ couple is -0.199 V. In present work, the formic acid concentration was kept 10 times more than oxymetal ions. Under these conditions, the reduction process was reported to follow pseudo-first-order kinetics [172]. To understand the kinetics of reduction process, the successive UV-Vis spectra were recorded to monitor the characteristic absorbance related to the concentration of oxymetal ions. As can be seen from Figure 5.13, the absorbance at 348 nm corresponding to concentration of Cr(VI) continuously decreased with time during reduction of Cr(VI) with formic acid in the presence of Pd NPs loaded on both Fe_3O_4 (Fe_3O_4@Pd) and SiO_2 (SiO_2@Pd) particles at 50°C. It is obvious from Figure5.13 that the reduction of Cr(VI) was faster in the presence of Fe_3O_4@Pd catalyst.

There is a possibility that reduction rate may follow pseudo-second order or diffusion controlled kinetics in the presence of matrix supported catalyst as reactants have to approach active sites of the Pd catalyst. Therefore, the reduction rates in both the cases were analyzed using linearized equations (eq.) for pseudo-first-order kinetics (eq.4), pseudo-second order (eq.5) and diffusion controlled reduction (eq. 6) given below [173-175]:

$$\ln\left(\frac{[A]_t}{[A]_0}\right) = -K_1 t \qquad (4)$$

$$\frac{t}{[A]_t} = \frac{1}{K_2[A]_0^2} + \frac{t}{[A]_0} \qquad (5)$$

$$[A]_t = K_d\, t^{1/2} \qquad (6)$$

Where $[A]_t$ and $[A]_0$ represent absorbance of Cr(VI) ions (348 nm) at time t and initially, respectively. K_1, K_2 and K_d are the apparent pseudo-first-order, pseudo-second-order rate constants and apparent diffusion rate constant, respectively, and t is the reduction time. Absorbance was taken in above equations as it represent concentration of Cr(VI).

It is seen from Table 5.1 that the best correlation coefficients were obtained from pseudo-first-order (K_1/Pd wt. =0.5146 s^{-1} g^{-1}) and pseudo-second-order (K_2/Pd wt. = 24.6 mol^{-1} cm^3 sec^{-1} g^{-1}) models in the presence of catalyst Fe_3O_4@Pd and SiO_2@Pd, respectively, under identical chemical conditions *i.e.* same Pd amount (1mg) reactants conc. and 323 K. This seems to suggest that the catalytic activity of the Pd NPs influenced the kinetics of the reduction. The higher catalytic activity of Pd NPs on Fe_3O_4 particles could be attributed to their lower sizes (0.1-0.5 nm) as compared to that on SiO_2 particles (0.5-2.0 nm). The lower sized Pd NPs would have larger surface area and also higher number of defects that may act as active sites for catalyzing the reduction.

The reduction of U(VI) with formic acid is more difficult than Cr(VI) due its lower redox potential (0.41V vs. NHE) and high activation energy barrier. It was observed that U(VI) reduction with formic acid occurred in the presence of SiO_2@Pd under similar conditions used for Cr(VI) reduction, see Figure 5.14. However, it was surprising that there was no significant reduction of U(VI) with formic acid in the presence of Fe_3O_4@Pd. This could be only possible when decomposition of formic acid denoted in eqs. 2&3 would be faster than the reduction of U(VI) ions (eq.1). The hydrogen thus formed would form hydride with palladium (PdH_x) leading to poisoning of Pd NPs catalytic activity [176]. This problem did not occur in the case of SiO_2@Pd which has inherently lower catalytic activity due to larger sized Pd NPs formed on SiO_2 host particles.

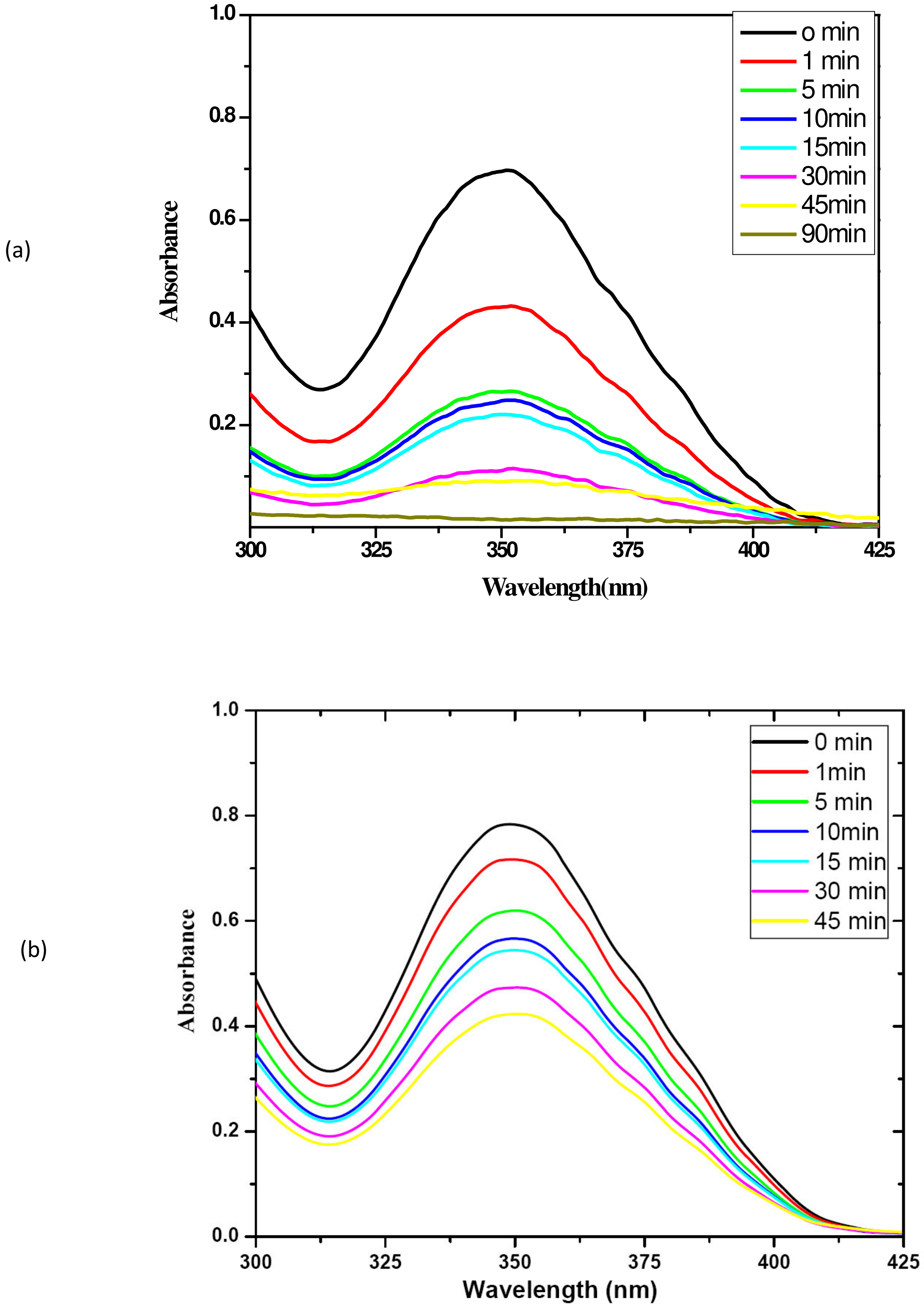

Figure 5.13. Successive UV-Vis spectra showing decrease in absorbance at 348 nm corresponding to Cr(VI) concentrations during it reduction with formic acid in the presence of Fe_3O_4@Pd (a) and SiO_2@Pd (b) at 323 K

Table 5.1 Analyses of reduction rate of Cr(VI) ions with formic acid in the presence of Fe_3O_4@Pd or SiO_2@Pd at 323 K with different kinetics model.

Catalyst Used	Plot	Correlation coefficient (R^2)	kinetics of sorption
Fe_3O_4@Pd	ln $[A]_t$vs. t	0.94967	pseudo-first-order
	t/A_tvs. t	0.78167	pseudo-second-order
	$A_t$vs. $t^{1/2}$	0.77164	diffusion controlled
SiO_2@Pd	ln $[A]_t$vs.t	0.84125	pseudo-first-order
	t/A_tvs. t	0.99537	pseudo-second-order
	$A_t$vs. $t^{1/2}$	0.95772	diffusion controlled

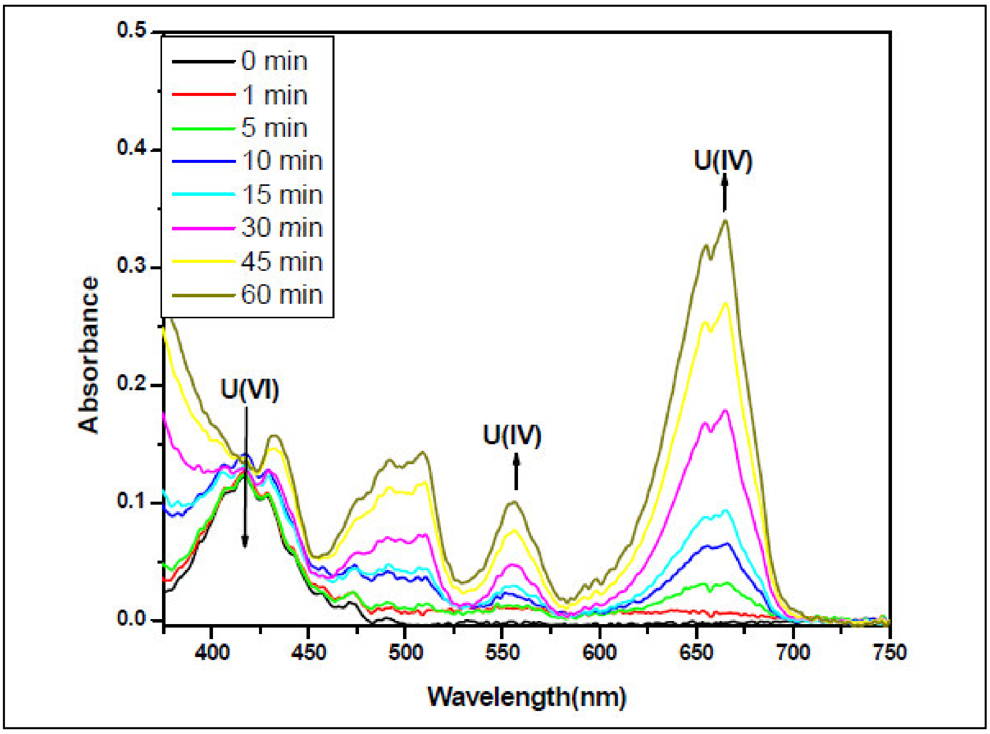

Figure 5.14. Successive UV-Vis spectra recorded during reduction of U(VI) with formic acid in the presence of SiO_2@Pd (b) particles at 323 K. The growth of new absorbance peaks corresponding to f-f transitions of U(IV) indicate the reduction of U(VI) as a function of time

5.5.4. Hydrogen sorption studies

Formic acid decomposition catalyzed by Pd catalyst shown in eq. 2 is being explored for hydrogen production for fuel cell. Pd metal also can be used as hydrogen sober and storage. As discussed in section 5.5.3, the Fe_3O_4@Pd appears to have accelerated decomposition of formic acid that has affected the reduction of U(VI) ions by formic acid resulting into formation of palladium hydride, which poison catalytic activity of the Pd NPs. Therefore, it is interesting to examine hydrogen sorption properties of Pd NPs anchored on the Fe_3O_4 and SiO_2 host particles.

The hydrogen sorption on Fe_3O_4@Pd and SiO_2@Pd were studied at four different temperatures (373K, 303K, 273K & 173K) using Sievert apparatus.The hydrogen sorption profiles as a function of pressure at different temperatures are shown in Figure 5.15. It is seen from Figure 5.15(a) that the hydrogen sorption increases with increase in pressure, and hydrogen profiles in SiO_2@Pd follow normal trend of decrease in hydrogen sorption with increasing temperature at a given pressure *i.e.* 173 K > 273K > 303K > 373K. It is interesting to note from Figure 5.15(b) that this trend of hydrogen sorption is followed in Fe_3O_4@Pd up to 303K but hydrogen sorption is abnormally high at 373 K and saturated at 2500 mbar. This seems to suggest that there may be some chemical reaction occurring during hydrogen sorption in Fe_3O_4@Pd at 373 K. Below 373 K, it is seen from the comparison of hydrogen sorption profiles of the SiO_2@Pd and Fe_3O_4@Pd that hydrogen sorption at a given temperature and pressure is lower in theFe_3O_4@Pd with respect to SiO_2@Pd, see Figure 5.15. This could be attributed to lower Pd content in the Fe_3O_4@Pd (12 mg g^{-1}) as compared to SiO_2@Pd(20 mg g^{-1}).

To study the hydrogen sorption on bare Pd NPs, the Fe_3O_4@Pd was also subjected to heating at 1033 K in Ar atmosphere for removing the organic coating. The hydrogen sorption was normalized with Pd weight for the comparison of hydrogen sorption in Pd bulk metal and

NPs reported in the literature at 373K temperature and 1MPa pressure where hydrogen sorption in Fe_3O_4@Pd was found to be abnormal. The hydrogen sorption on bare Fe_3O_4 particles and silane coated Fe_3O_4 particles were found to be negligible under similar temp and pressure. The comparison of data shown in Table 5.2seems to suggest that hydrogen sorption in Pd NPs, Pd metal andSiO_2@Pd is comparable ranging from 0.45 wt.% to 0.52 wt.% but very high in pristine (26 wt.%) and burnt Fe_3O_4@Pd (3.8 wt.%) particles.Contrary to this, the hydrogen sorption in Fe_3O_4@Pdat 303 K (0.47 wt.%) is comparable with the Pd NPs as such (0.40 wt.%), bulk metal (0.59 wt.%) and SiO_2@Pd (0.54 wt.%), see Table 5.2. Thus, the abnormally higher sorption of hydrogen in Fe_3O_4@Pd at 373K may be due to chemical reaction catalyzed by Pd NPs.

(a)

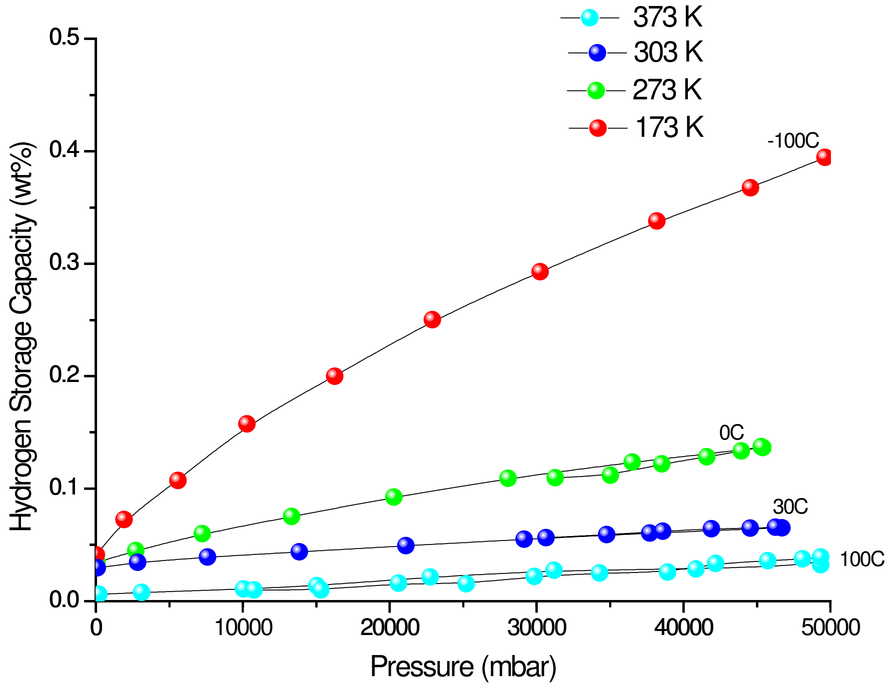

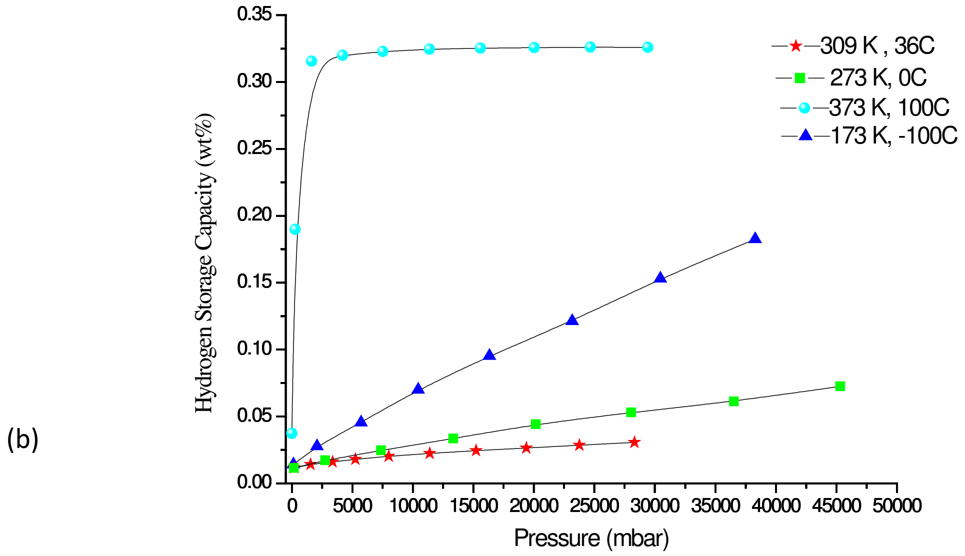

Figure 5.15. H_2 sorption by SiO_2@Pd (a), Fe_3O_4@Pd (b) at four different temperatures

Table 5.2 Comparison of wt %of hydrogen sorption on Pd NPs and bulk metal reported in lliteratureand obtained in the present work at 373& 303K temperature and 1MPa pressure

Temp. (K)	**Literature**		**Present Work**		
	Pd NPs	Pd Metal (black)	Fe_3O_4@Pd	Fe_3O_4@Pd burnt in Ar atmosphere	SiO_2@Pd
373	0.45 wt.% (177)	0.52 wt. % (178)	26 wt. %	3.8 wt.%	0.51 wt.%
303	0.40 wt.% (177)	0.59 wt. % (178)	0.47 wt.%	0.33 wt.%	0.54 wt.%

To understand the physical and chemical changes occurred during hydrogen sorption at 373 K, the Fe_3O_4@Pd loaded samples were subjected to high resolution transmission electron microscopy (HRTEM), Mössbauer spectroscopy and XPS before and after hydrogen sorption experiments. It was observed from HRTEM images of pristine and burnt Fe_3O_4@Pd that particles were agglomerated during heating at 1033 K in Ar atmosphere; see representative

HRTEM images given in Figure 5.16. This would give rise to inaccessibility of Pd NPs in Fe_3O_4@Pd particles and resulted in lower hydrogen sorption with respect to pristine Fe_3O_4@Pd as observed in Table 5.2.

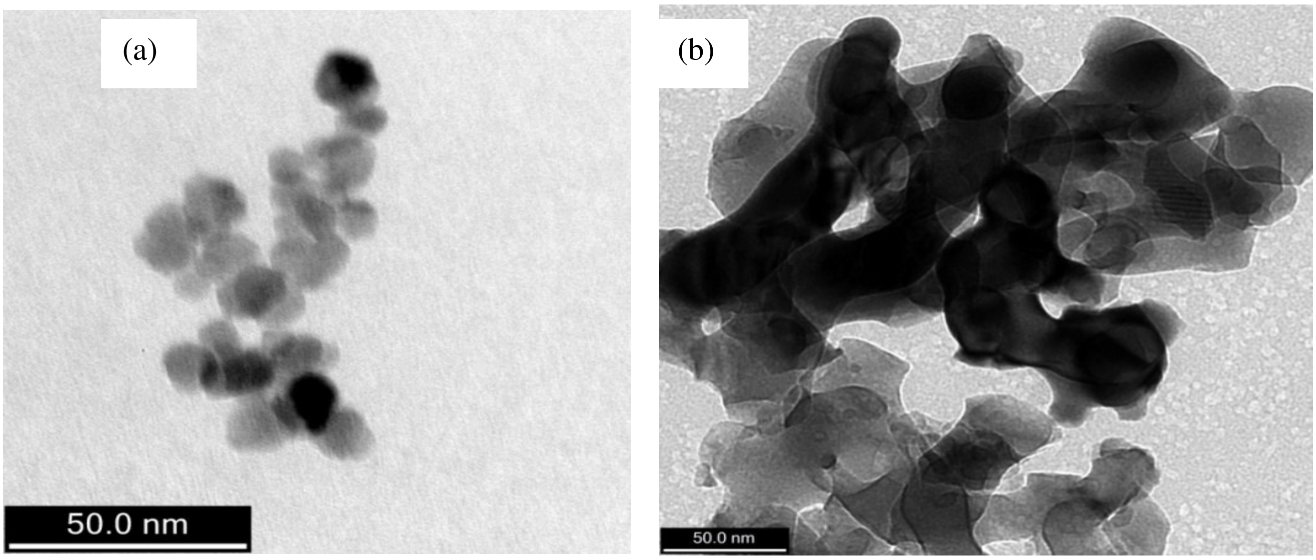

Figure 5.16. Representative HRTEM of the pristineFe_3O_4@Pd (a) and Fe_3O_4@Pd burnt at 1033 K in Ar atmosphere (b)

In HRTEM spectra number of fringes was observed. Analyses of fringes of pristine Fe_3O_4@Pd showed the d-spacing of Pd crystals were 2.261 A$^{\circ}$ which is matched 2.2516 A$^{\circ}$for (1,1,1) lattice plane of Pd, see Figure 5.17 (a).The analyses of fringes of burnt Fe_3O_4@Pd showed that the d-spacing were 2.077 A$^{\circ}$which is matched 1.945 A$^{\circ}$for (2,0,0) lattice plane of Pd (Figure 5.17 (b)). The same d-spacing of Pd crystals was observed in the burnt Fe_3O_4@Pd sample indicating Pd NPs remained unaffected.

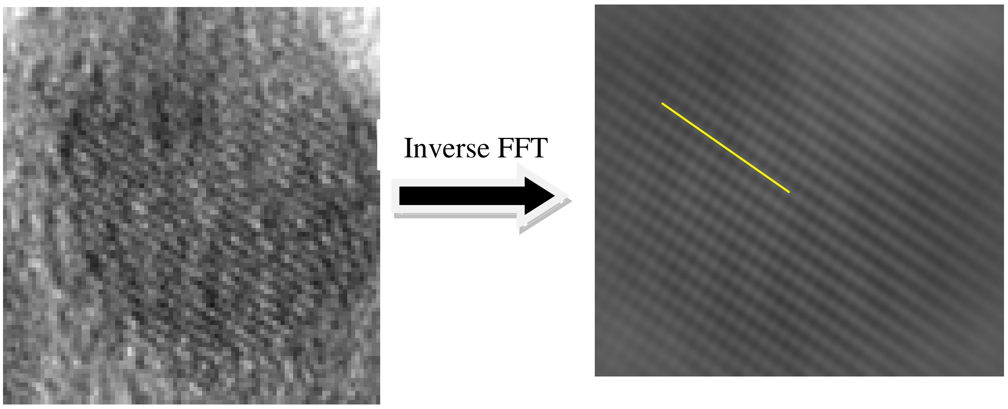

$$\frac{l}{No.of\ fringes}$$

= 3.392/15 nm

= 2.261 A^0

Figure 5.17 (a) Fringes of Fe_3O_4@Pd and its Inverse Fast Fourier Transformation (FFT) observed from HRTEM image

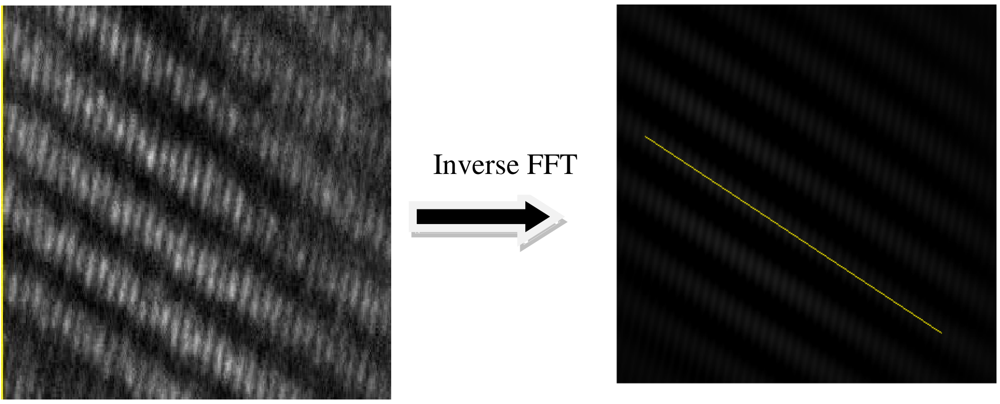

$$\frac{l}{No.offringes}$$

= 8.517/41 nm

= 2.077 A^0

Figure 5.17 (b) Fringes of burnt Fe_3O_4@Pd and its Inverse Fast Fourier Transformation (FFT) observed from HRTEM image

The possibility of changes in oxidation states of Fe^{2+} and Fe^{3+} ions in Fe_3O_4 during hydrogen sorption in Fe_3O_4@Pd at 373 K and 1MPa pressure was studied by subjectingFe_3O_4, hydrogen loaded Fe_3O_4coated with silane and hydrogen loaded Fe_3O_4@Pd to Mössbauer Spectroscopy, see Figure 5.18. It is seen from this figure that there is no significant change in Mössbauer spectra of these three samples (Fe_3O_4, hydrogen loaded Fe_3O_4coated with silane and hydrogen loaded Fe_3O_4@Pd) i.e. no change in isomer shift (δ) indicating no change in relative amount of $Fe^{3+}$and Fe^{2+} in Fe_3O_4. This eliminated the possibility of utilization of hydrogen in Fe^{3+} reduction during sorption in Fe_3O_4@Pd at 373 K.

The chemical changes during hydrogen sorption in the Fe_3O_4@Pd were studied by XPS. It is seen from Figure 5.19 that there were no significant changes in the core level XPS spectra of Pd ($3d_{5/2,3/2}$), N(1S) and Si(2p) taken before and after hydrogen loading in Fe_3O_4@Pd. TheFe_3O_4@Pd sample burnt in Ar atmosphere indicated that there was no oxidation of Pd and N content was completely removed during pyrolysis of Fe_3O_4@Pdin inert atmosphere (Figure 5.20). It is interesting to observe from Figure 5.21 that there were significant changes in XPS spectra of pristine Fe_3O_4, silane coated Fe_3O_4 and Fe_3O_4@Pd after hydrogen loading. The XPS spectrum of pristine Fe_3O_4 showed three binding energy peaks (Figure 5.21 (a)) corresponding to Fe-$2p_{3/2}$, Fe-$2p_{1/2}$ and satellite peak that are characteristics of Fe_3O_4. After silane coating on Fe_3O_4, three additional peaks appeared due to formation of Fe-O-Si bonds. After hydrogen loading, the XPS spectrum of Fe_3O_4@Pd was modified as shown in Figure 5.21 (c). The intensity of additional peaks corresponding to Fe-O-Si bonds decreased indicating breaking ofFe-O-Si bond by hydrogen at 373 K that may lead to the formation of -Fe-OH and SiH_x-. The comparison of deconvoluted Fe_{2p} XPS spectra showed that ratio of the area of the peak at B.E. ~ 710 eV to B.E. ~ 713 eV was 1.04 and B.E. ~ 723 eV to B.E. ~725 eV was 1.06 in the silane coated Fe_3O_4, which increased to 1.27 and 1.21 in "hydrogen loaded Fe_3O_4@Pd NP, respectively. Thus, XPS studies of pristine Fe_3O_4, hydrogen loaded Fe_3O_4@silane and hydrogen loaded Fe_3O_4@Pd showed that the Fe-O-Si bond breaks at 373K, resulting in anomalous sorption of hydrogen at this temperature.It has been reported in literature [179] that heating SiO_2 and $LiAlH_4$ at 373 K results to the formation of SiH_4. However, further studies is needed to confirm the cleavage of Fe-O-Si bond by hydrogen in the presence of Pd NPs

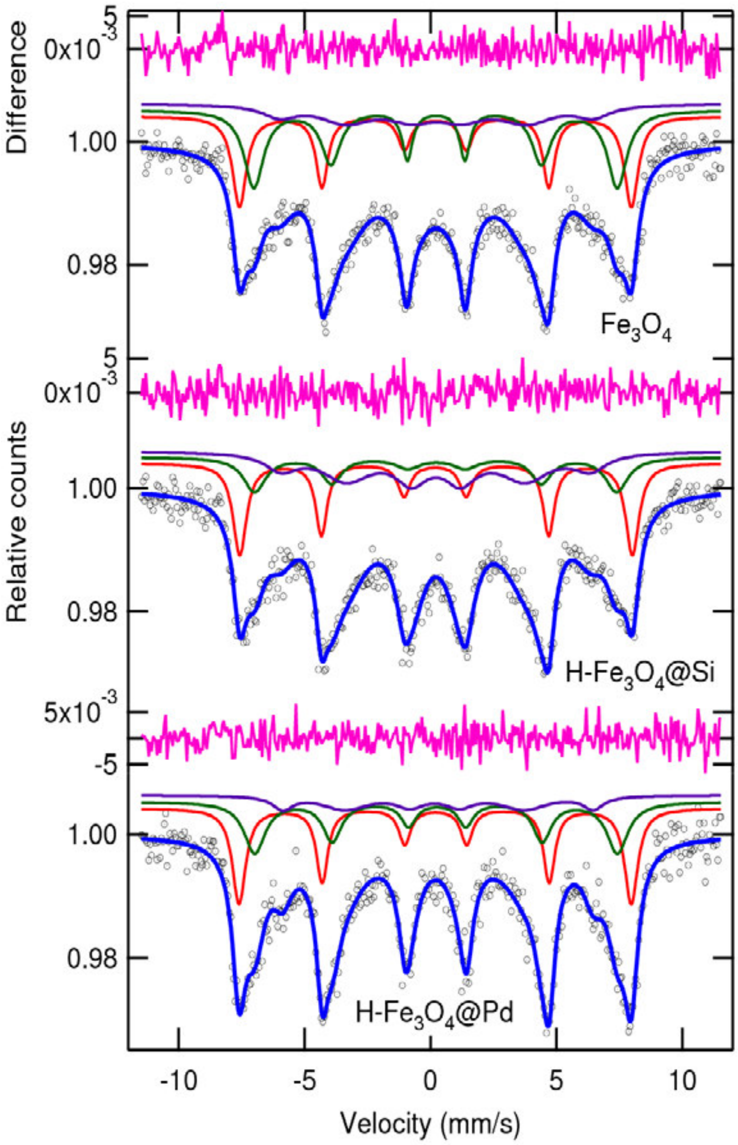

Figure 5.18. Mössbauer spectra of pristine Fe_3O_4, hydrogen loaded "Fe_3O_4 coated with silane" and hydrogen loaded "Fe_3O_4@Pd"

Before Hydrogen loading

After Hydrogen loading

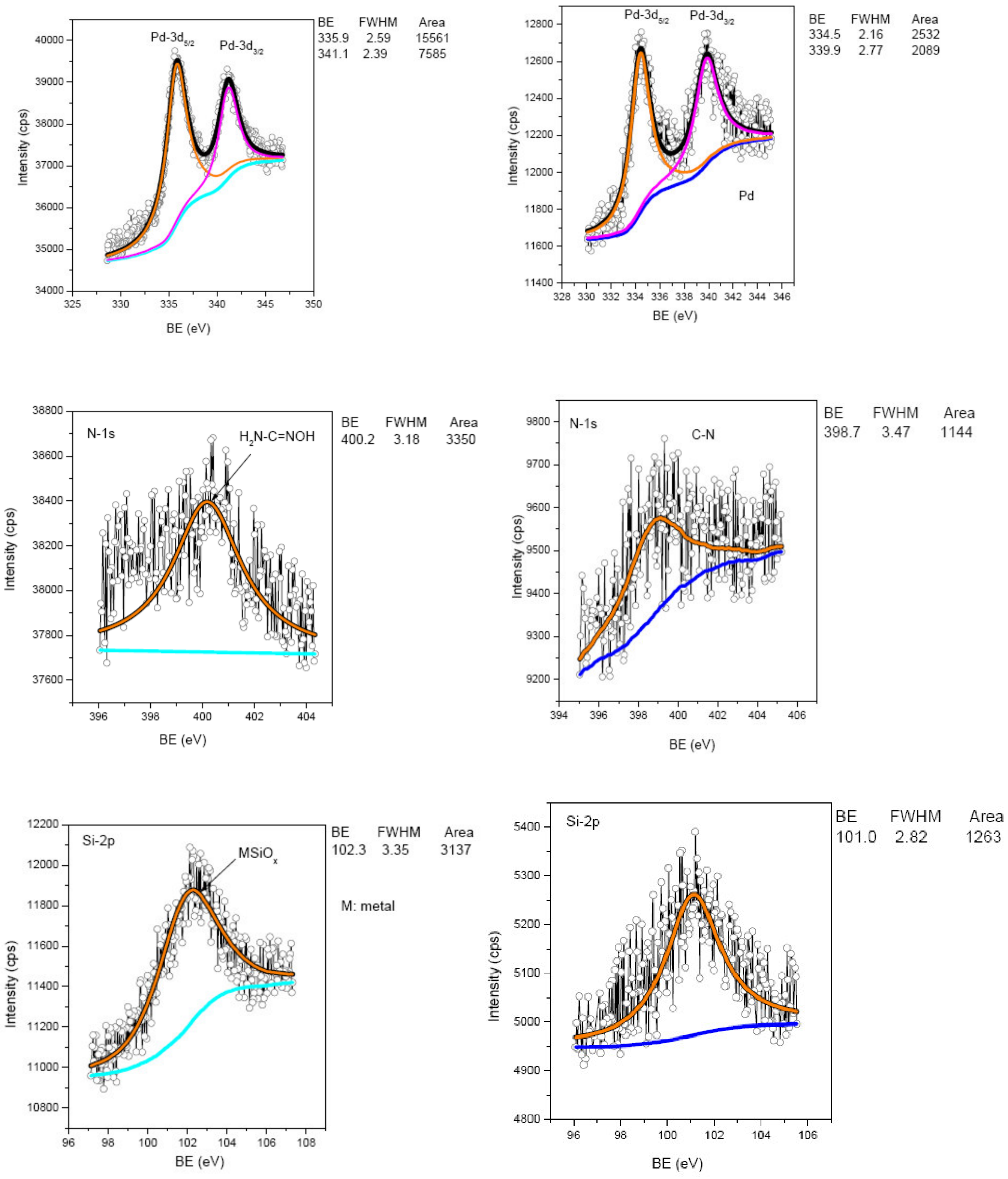

Figure 5.19. Core-levelXPS spectra of Pd ($3d_{5/2,3/2}$), N(1S) and Si(2p) taken before and after hydrogen loading in Fe_3O_4@Pd

(a)

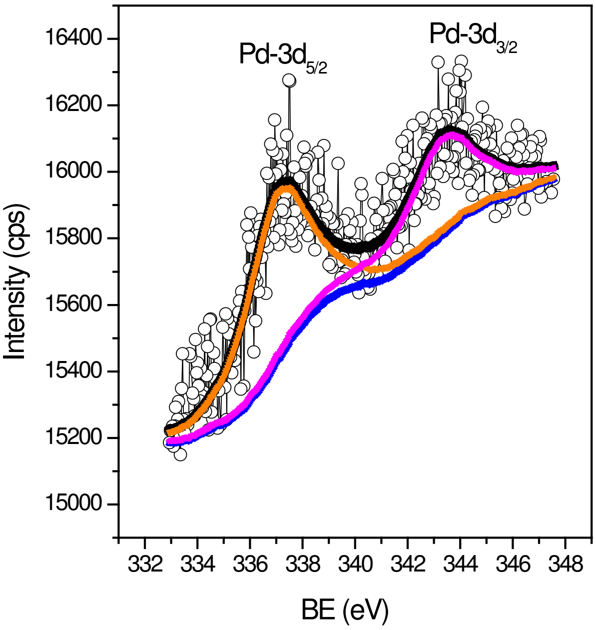

(b)

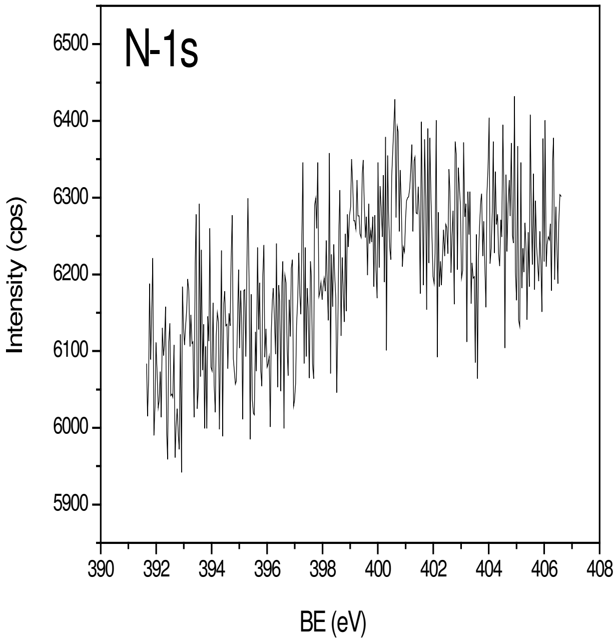

Figure 5.20. XPS of Pd (a) and N (b) content after doing pyrolysis of Fe_3O_4@Pdin inert atmosphere

(a)

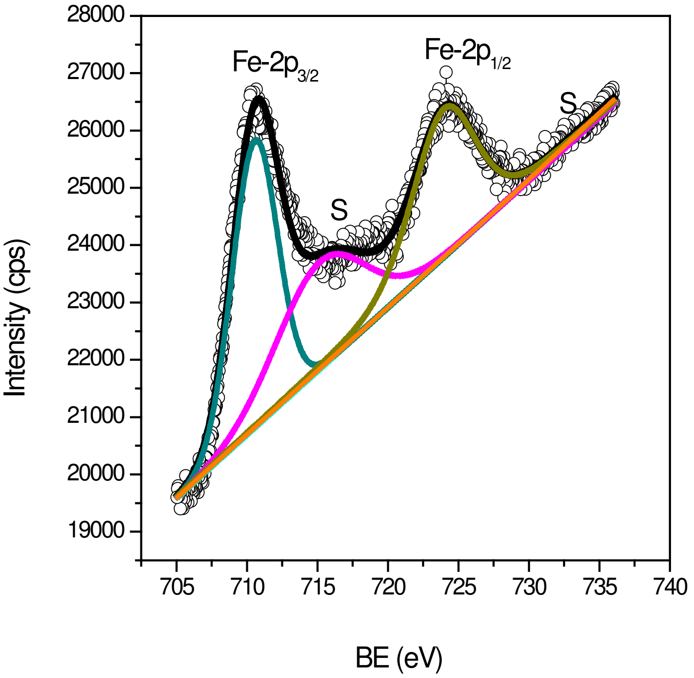

(b)

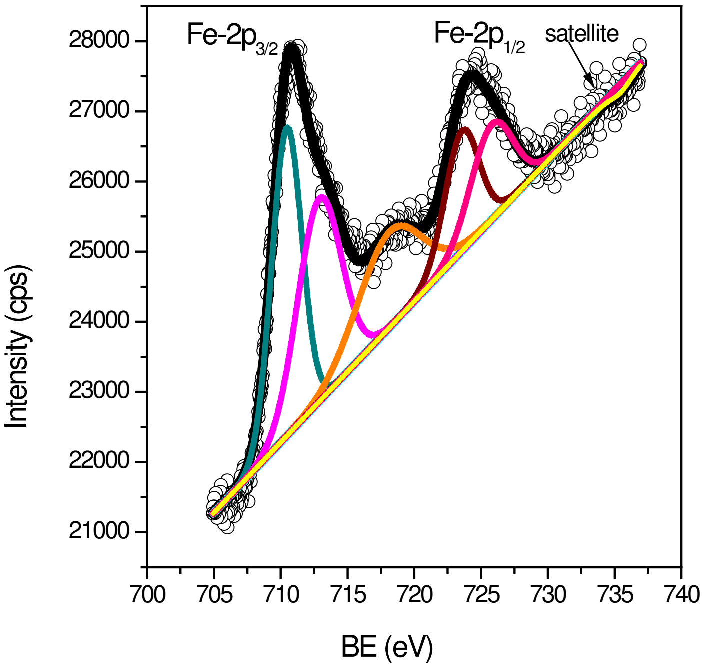

BE	FWHM	Area
710.4	2.66	12396
712.8	3.85	11820
718.1	5.59	8108
723.5	3.01	5611
725.8	3.73	5321
735.4	0.5	416

(c)

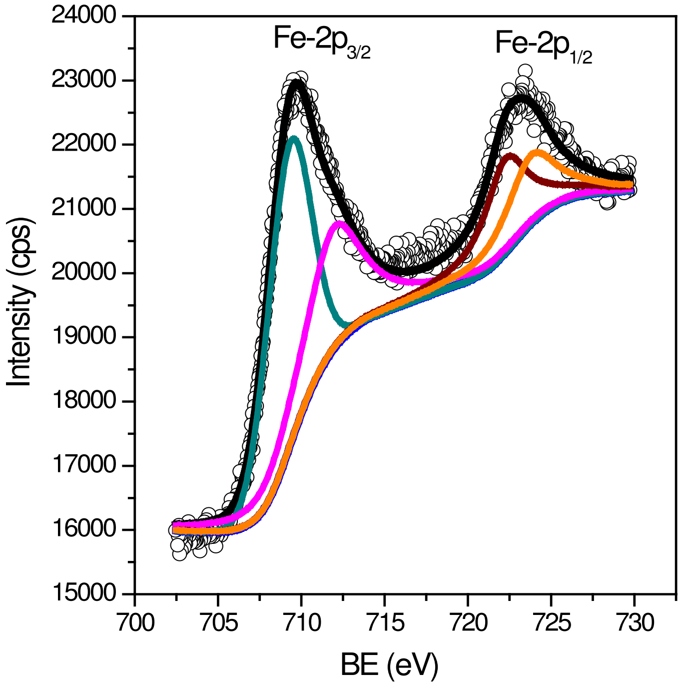

BE	FWHM	Area
709.5	3.08	15439
712.1	4.09	12177
722.5	3.21	7386
724.1	3.66	6131

Figure 5.21.XPS of Pristine Fe_3O_4(a), Fe_3O_4 coated with silane (b),hydrogen loaded Fe_3O_4 @Pd (c)

Chapter – 6

Determination of Total Gas Content and its Composition in Indian PFBR blanket pellets

6.1. Introduction

Deeply depleted uranium oxide ($DDUO_2$) has been proposed as blanket material in prototype fast breeder reactor (PFBR), heralding the initiation of second stage of Indian nuclear energy programme.

Prototype Fast Breeder Reactor (PFBR) is a sodium-cooled nuclear reactor and its core is composed of different subassemblies. The reactor is under pre-commissioning stage at Kalpakkam near Chennai in the state of Tamil Nadu. PFBR fuel subassemblies are mainly distributed in two zones viz. inner and outer zones. The inner zone is housed with ~ 21 % PuO_2 fuel subassemblies whereas, the outer zone is housed with subassemblies having relatively higher enrichment ~ 28 % PuO_2. Surrounding these fuel subassemblies, radial blanket sub assembles containing depleted Uranium oxide are arranged in two rows. In these Blanket Subassemblies, some of the U-238 is converted to fissile Pu-239 by the process of breeding.

$$^{238}_{92}\mathrm{U} + ^{1}_{0}\mathrm{n} \rightarrow ^{239}_{92}\mathrm{U} \xrightarrow[23.45\ \mathrm{min}]{\beta-} ^{239}_{93}\mathrm{Np} \xrightarrow[2.3565\ \mathrm{d}]{\beta-} ^{239}_{94}\mathrm{Pu}$$

PFBR core has 120 radial blanket subassemblies and each blanket subassembly contains 61 numbers of blanket fuel pins. Fast neutrons coming out from fuel subassemblies hit the nuclei of U-238 in $DDUO_2$ pellets in the blanket pins and convert it to fissile isotope Pu-239.

For optimal performance, certain chemical specifications are stipulated for the fuels and total gas content is one of these specifications. During the manufacture of high purity metals and alloys permanent gases like hydrogen and nitrogen are trapped in the interstitial spaces. Also, for maintaining O/M during the fuel fabrication, the fuel materials are subjected to high temperature sintering in reducing gas environment ($Ar + 8\%H_2$ or $N_2 + 8\%H_2$) and in this process some gases get trapped. These gases get released during operation of the reactor.Also, reaction products expected during reactor operating conditions are additional source besides entrapment of gases during fuel fabrication and sintering process[50]. The accumulation of significant quantity of gaseous impurities may pressurise the clad or alter the thermal conductivity of cover gas or react with the clad and cause damage. Hence, it is of importance to have a precise knowledge of the total gas content and its composition. Incase of nuclear fuels, the total gas content is defined as the amount of non-condensable gases released when the pellet is heated under vacuum at required temperature and time and converting the evolved gas content to STPcondition [49]. Depending upon the nature of the fuel pellet, the temperature up towhich it has to be heated is arrived at. This temperature is arrived on the basis of the central line temperature of fuel pellet during the operation ofreactor, and the ease with which the gases are released out of the pellets. For example, the centre line temperature of the oxide and carbide fuel pellets reaches 1923 K and 1273 K respectively. Also, since the oxide pellets are highly sintered and have high density compared to the carbide pellets, high temperatures are required to extract the gases from the interstitial spaces in the oxide pellets. The specification of the total gas content in various types of fuels is given in Table 6.1.

Table 6.1 Specifications for total gas content in different fuels

OXIDES (THERMAL)	**OXIDES (FAST)**	**CARBIDES (FAST) (70%Pu)**	**CARBIDES (FAST) (55%Pu)**	**OXIDES (FAST) Central hole:1.6mm**
0.04 L/Kg at 1923 K for 15 minutes	0.09 L/Kg at 1923 K 1650°C for 15 minutes	0.1 L/Kg at 1273 K for 30minutes	0.1 L/Kg at 1273 K for 30 minutes	0.1 L/Kg (excl. H_2) at 1923 K for15 minutes

The specification for the fast reactor fuel pelletsisthat thevolume of the released gases excluding hydrogen should be less than 0.1 L/kg of the pellet calculated for STP conditions, when the whole pellet (~20 g) is heated at 1,920 K under vacuum (maximum pressure of 133

Pa) for 30 minutes.Hence, the Total Gas Content has to be determined as a part of chemical quality assurance of nuclear fuels. Generally hydrogen(H_2), methane (CH_4), nitrogen (N_2), carbon monoxide (CO) and carbon dioxide (CO_2) are present in the gases released from the nuclear fuel pellets. Hydrogen is excluded as it is expected to escape out of SS clad of reactor operating condition and does not contribute to the total gas content and its effect.

6.2. Reported Work

Two methods have been reported in the literature for the determination of the total gas content and its composition in nuclear fuels. One of these methods is the hot vacuum extraction-gas chromatography (HVE-GC) and the other one is hot vacuum extraction-quadrupole mass spectrometry (HVE-QMS). In both the methods, the evolved gas is extracted from the sample under static vacuum at the stipulated high temperature. The composition of released gases is determined in the first method by gas chromatograph with thermal conductivity detector and in the second method by quadrupole mass spectrometer. Iwai et al.[35] determined thetotal gas content in uranium and plutonium mixed carbide fuels employing HVE-GC. As different gases have different thermal conductivity, prior to the experiment, GC has to be calibrated with standard gas mixtures for determination of gas composition quantitatively. However, details of calibration of GC have not been reported. Hiyama et al. [180] determined total gas content and its composition in uranium-plutonium mixed oxide fuel pellets employing HVE-GC with specially designed and developed gas sampling unit to feed the gasesinto GC. Even though, GC has been calibrated with pure individual gases, validation of methodology with mixture of gases was not reported. One of the major limitations of HVE-GC technique is the requirement of special injectors to feed the released gases at sub-atmospheric pressure into GC column at relatively high pressures. This limitation does not exist in HVE-QMS, as the released gases can be fed to the QMS directly without using any special equipment. Vega et al. [181] determined the total gas content and its composition in UO_2 pellets employing HVE-QMS, and the results were reported without considering the relative sensitivities of different constituent gases. It is well-known that several factors influence the sensitivity of the gases in QMS like molecular mass of the gas, characteristic features of electron impact ion source (filament current, electron energy, electronic current), electronic density of the gas, acceleration energy of the ions for focusing, pumping speed of the vacuum pumps etc. [182]. Hence, the sensitivity factors for different gases need to be determined for accurate gas composition calculations [183, 103]. Earlier total gas compositionwas being reported from our laboratory using relative sensitivity factors (RSFs) (sensitivity factors normalisedto nitrogen) as given in the QMS manufacturer manual [50]. As a new gas extraction system with differentQMSis now being used for total gas analysis, it became essential to determine RSFs in the new system for gas composition calculations. Further, to increase the confidence on RSFs, sensitivity factors were determined inentire range of operational pressures(1–8 Pa).

6.3. Present work

The present paper deals with the (i) validation of temperature measuring device, (ii) optimization of experimental conditions for quantitative extraction of gases (e.g. time of heating of sample), (iii) determination and validation of RSFs for various gases when analysed employing QMS, (iv) determination of total gas content and its composition in sintered PFBR blanket pellets and finally (v) estimation of uncertainty in measurement of total gas content excluding hydrogen employing bottom-up approach.

6.4. Experimental

6.4.1. Total gas analyser

The total gas extraction and analysis system was designed in-house and was fabricated by Vacuum Techniques Pvt., Ltd., Bengaluru, India. The entire system is made up of stainless steel and only CF type joints and all-metal valves are used. A schematic of the system is shown in Figure 6.1. For simplicity, the equipment is divided into two parts, viz., sample loading part and gas extraction part separated by a gate valve (GV). In the sample loading part, sample port (SM) is used to load the sample under inert gas flow. Turbo molecular pumping system (TMP-L) evacuates the loading part. Angular (AM), vertical (VM) and horizontal (HM) vacuum manipulators bring the crucible holder along with the crucible in required direction and position for transporting from the SM to the heating zone of the extraction part and vice versa. The extraction part contains a double walled water cooled quartz reaction tube (RT) in which the tungsten crucible (C) along with the sample is heated under vacuum. Programmable induction furnace (IC) heats the sample to required temperature and for the required time. Turbo molecular pumping system (TMP-E) evacuates the entire system including extraction part. Turbo molecular pump (NTP) sealed with CF flanges is used as an ejector pump to extract the gases from sample to collection chamber. Dry rotary pumps (RP) are used as back-up pumps to all the TMPs. Refrigeration system (RS) condenses the condensable gases during extraction. High precision capacitance manometer (CM) is used to measure the pressure exerted by the collected gases. An extra volume (EV) is provided to bring the pressure of released gases in the operational range of capacitance manometer (10^{-3}–11 Pa). A micro-leak valve (LV) feeds the gas to quadrupole mass spectrometer (QMS) to measure the gas composition. A turbo molecular pumping station (TMP-Q) evacuates the QMS. A personal computer is used to acquire the data from QMS and to control the operational parameters of QMS. After continuously baking the entire system at 373 K for 24 h, the pressure was raised at room temperature (298 K) from 10^{-3} to 2 x 10^{-2} Pa for an hour and raised to 3 x 10^{-1} Pa for 24 h under static vacuum condition (GV, LV, V2 and V6 are closed and remaining valves are in open condition).

6.4.2. Quadrupole mass spectrometer

M/s Hiden Analytical Limited, England, make quadrupole mass analyzer with model No. HAL 7 RC 51 is used for the present studies. Length of QMS rods is 90 mm. Resolution of theQMS is $M/\Delta M \geq M$ at 10 % valley. Ions in the mass analyser are produced employing electron impact ionsource with energy of 80eV using thoria quoted iridium as a filament. The mass range of the system is 1–50amu. The ion currents are measured employing a Faraday cup detector. The pressure in the QMS chamber maintained at about 10^{-3}Pa by continuous evacuation with TMP-Q system

6.4.3. Optical pyrometer

In the total gas analyzer system, theheating of the sample (taken in tungsten crucible) was carried out employing water cooled induction furnace. The temperature is varied by suitably selecting the anode current and anode voltages of the induction coil. The maximum required temperature isattained within 30s. Laser optical pyrometer was employed for measuring the temperature of the sample/ crucible.

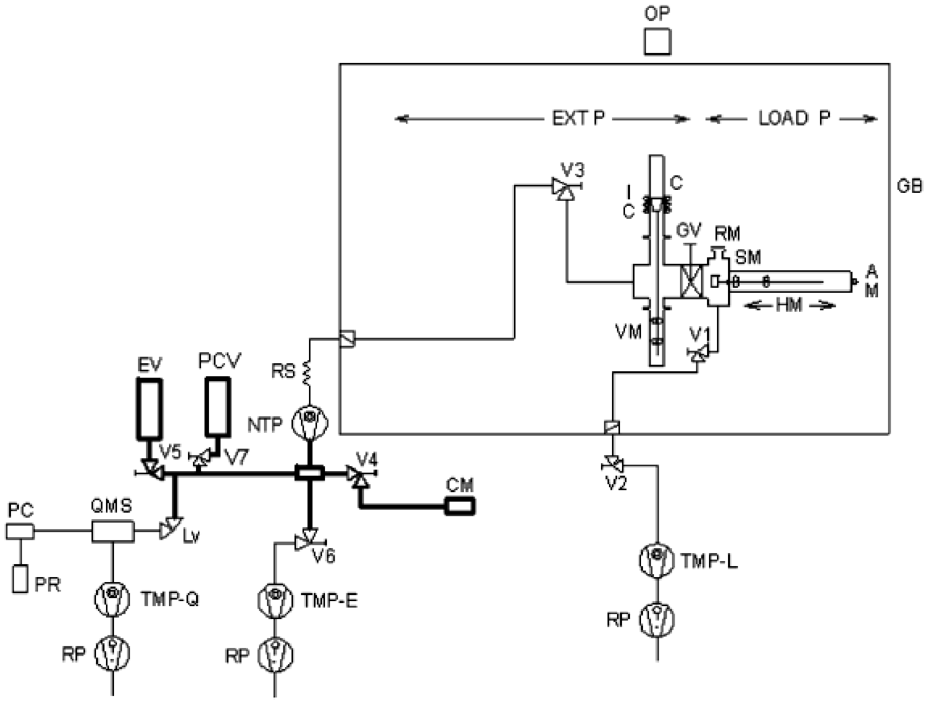

Figure 6.1. Schematic diagram of total gas analyzer system. Load P sample loading part, Extn. P gas extraction part, SM sample port, HM/AM/VM/RM horizontal/angular/vertical/rotational vacuum manipulator, GV gate valve, C tungsten crucible, IC induction coil, CM capacitance manometer, NTP nude turbo pump, TMP turbo molecular pump (L-Loading part evacuation, E-main evacuation, Q-QMS evacuation), RP rotary pump, V1–V7 all metal valves, LV leak valve, EV extra volume, PCV pre-calibrated volume, RS refrigeration system, QMS quadrupole mass spectrometer, PC personal computer, PR printer, GB glove box, Bold line gas collection chamber

6.4.4. Procedure

Adsorbed gases, if any on the surface of the tungsten crucible were removed by degassing repeatedly at 1,920K(3-4 times for 15 min), by opening all the valves except GV and LV. To load the sample, the crucible was taken to the sample loading port employing horizontal, vertical and angular manipulators. The loading part was isolated from the extraction part and vacuum pump TMP-L by closing the GV and V1 respectively. The SM was opened in flowing argon environment and the pre-weighed sample (about 21–22 g) was carefully dropped into the crucible. The sample dropping port was then closed and evacuated to 10-3Pa employing the turbo molecular pumping station TMP-L by opening V1. The crucible was then moved to the gas extraction part and was isolated from the loading part by closing the GV. At this juncture, impurity gases, if any present in Argon that could have been adsorbed during sample loading, were removed by degassing the crucible and the sample in it at room temperature for 2 h with TMP-E system (all valves are in open condition except GV & LV).

After isolation of the system from vacuum pumping station by closing valve V6, the sample loaded crucible was heated to 1,920 K employing induction furnace for 30 min. Throughout this period, the released gases were continuously extracted into pre-calibrated volume via the refrigeration coil to trap the condensable gases, employing the sealed turbo pump (NTP). After the 30 min heating, the pressure of the extracted gas was measured employing high precision capacitance manometer. To determine the accumulated gas composition, the gas was fed to the on-line quadrupole mass spectrometer through a micro leak valve. The peak intensities at m/e 2 (H_2^+), 12 (C^+), 14 (N^+/CH_2^+), 15 (CH_3^+), 16 (O^+/CH_4^+), 28(N_2^+/CO^+), 32(O_2^+) and 44 (CO_2^+) were recorded.

A separate blank experiment was carried out with degassed tungsten crucible alone under identical experimental conditions employed for the sample. The released gases were extracted into the collection chamber and then pressure was measured. These gases were fed to the online QMS and peak intensities were monitored at various m/z values as mentioned above.

6.4.5. Determination of sensitivity factors and cracking pattern of gases in QMS

The gas composition has to be derived from the peak intensities at various m/z values after blank correction. The peak intensity of any gas recorded in QMS analysis depends on its nature such as its molecular mass, ionization potential and ionization cross section, and also such other physical factors like diffusion through micro leak, pumping with TMP and acceleration energy for ion focusing in QMS. This necessitates the determination of sensitivity factors for various gases in QMS.

For the determination of sensitivity factors for hydrogen, methane, nitrogen, carbon monoxide, oxygen and carbon dioxide, the corresponding pure gas was taken in the system at various pressures separately in a collection chamber (highlighted with bold line in Figure 6.1). The pressure was measured by the capacitance manometer. The gas was then fed into QMS through the micro leak valve and intensities at various m/z values (1, 2, 12, 13, 14, 15, 16, 18, 28, 32 and 44) were measured.

It is well-known that polyatomic gases undergo fragmentation in addition to ionization when bombarded with electrons of energy ~80 eV and can interfere with other mass peaks. For example at the parent peak intensity of methane (m/z value 16), fragmented ions from other gases like O_2 (O^+), CO (O^+) and CO_2 (O^+) also contribute at this m/z. Therefore peak intensity at m/z 16 cannot be used directly for methane partial pressure calculation. Moreover nitrogen and carbon monoxide are not normally resolved as both will give parent peak intensity at the nominal m/z value 28. It has been reported that the fragmentation pattern could be used to calculate the individual contributions of carbon monoxide and nitrogen at m/z value of 28 [184]. In the present study fragmentation pattern of various gases were determined by taking pure gases and were used to get the correct parent peak intensities of CH_4, CO and N_2.

6.4.6. Calculation of total gas content

Knowing the volume of the system, the pressure exerted by the released gases and partial pressure of hydrogen calculated from mass spectral data (explained below), the total gas content excluding hydrogen was calculated employing gas laws:

$$\mathbf{V_T} = \frac{(\mathbf{P_S} - \mathbf{P_B})\mathbf{V_S}\ \mathbf{T_{STP}}}{\mathbf{T_R}\mathbf{P_{STP}}\ \mathbf{1000}\ \mathbf{W_S}} (\mathbf{1} - \mathbf{X_H})$$

where, V_T is the volume of total gas excluding hydrogen (L/Kg), P_S is the pressure of the gases released during sample analysis (atm), P_B is the pressure of the gases released during blank analysis (atm), V_S is the volume of the collection chamber (19.43 ± 0.27 L), T_{STP} is the standard temperature (273 K), T_R is the room temperature (298 K), P_{STP} is the pressure at STP (1 atm), W_S is the mass of the sample (g) and X_H is the mole fraction of hydrogen.

6.5. Results and discussion

6.5.1. Pressure and volume calibration

Accurate pressure and volume measurements are key parameters for the analysis. Pressure is measured using Pfeiffer make capacitance manometer model No.CMR 365 (10^{-3}–11 Pa full range) with an accuracy of0.5 % of reading and repeatability of ±0.003 Pa. For the determination of volume of collection chamber, dry nitrogen gas was taken in pre-calibrated volume at known pressure. The pressure was measured again after expanding nitrogen in the pre-calibrated volume into the entire collection chamber. Employing ideal gas equation, the volume of entire collection chamber including pre-calibrated volume was measured. This procedure was repeated five times. The total volume of the collection chamber (highlightedwith bold line in Figure 6.1) was found to be 19.43 L with standard deviation of 0.27 L.

6.5.2. Validation of temperature measurement

The temperature measuring device (optical pyrometer) was validated employing incipient melting temperature technique. For this purpose pure metals, such as, nickel(M.P. 1,723 K) and titanium (M.P. 1,933 K) were used. Nickel was taken in tungsten crucible and anode potential of the induction furnace was raised in steps. At each step temperature was measured by optical pyrometer and the crucible was physically checked for melting of nickel. The same procedure was repeated by taking titanium metal in crucible. It was observed that temperature indicated by the optical pyrometer when these metals melted, agreed within ±20 K of their melting point temperatures.

6.5.3. Duration of heating for complete release of gases

To optimize the duration of heating for complete release of gases from PFBR blanket pellet, a single pellet (DDUO$_2$ pellet) was loaded to tungsten crucible as mentioned in the experimental section. After degassing at room temperature for 2 hours, the temperature was raised to 1,920 K and the released gases were constantly extracted. The pressure was monitored regularly at an interval of 2 minutes up to 30 minutes. Similarly pressure was also monitored during the blank experiment. The total gas content was calculated as mentioned above. A plot was constructed between the amount of the cumulative total gas released and the corresponding cumulative duration of heating as shown in Figure 6.2. From the figure it can be seen that complete release of gases was obtained within 22 minutes. However, in all further experiments, the time of extraction was fixed as 30 minutes to ensure quantitative extraction.

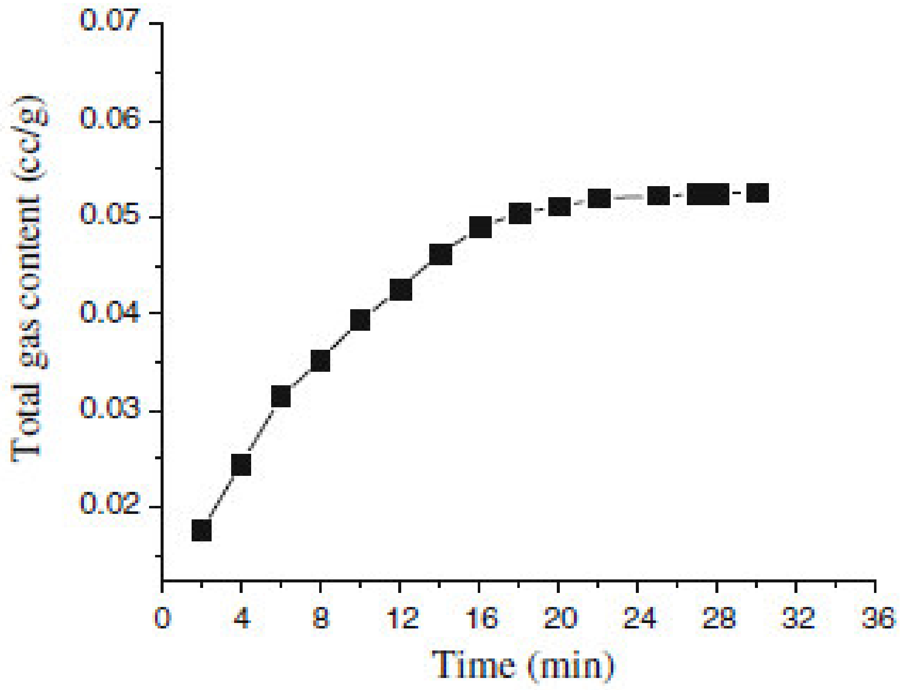

Figure 6.2. Release of gases with time

6.5.4. Relative sensitivity factors and cracking pattern of gases

Sensitivity factor (S_i) for any gas (I) with mass number M, in QMS, is the ratio of blank-corrected intensity at m/z=M and its partial pressure P_I in the mixture (I_M/P_I) [78]. For the determination of sensitivity factors for gases H_2, CH_4, CO, N_2, O_2 and CO_2, parent molecular ion peak intensity versus pressure of the corresponding gas in the collection chamber was plotted and is shown in Figure 6.3. From the slope of linear regression data, the sensitivity factors were determined for all the gases. RSFs were then calculated by normalising these sensitivity factors with respect to nitrogen and are given in Table 6.2. To validate these RSFs, commercially available reference gas mixtures were analysed. Even though, Argon and Helium will not be present in gases released from nuclear fuel pellets, RSFs of 'He' and 'Ar' were determined for reference and validation purpose (Table 6.2). Results of gas composition determined employing present method agreed well with the certified values (Table 6.4). This clearly shows that corrections for fractionation of the gas [185, 186] due to mass dependent diffusion through micro leak valve and pumping with

TMP-Q are not required as the computation of RSF includes the possible mass dependent fractionation.

From the mass spectral intensities monitored during sensitivity factor determination, fragmentation pattern of gases CH_4, N_2, CO, and CO_2 was also determined at all pressure ranges studied. The yield of various fragments with respect to parent ion along with standard deviation is given in Table 6.3(Mean value of yield was arrived from the data at all pressures and SD by propagation formulae). In obtaining the percentage of fragmentation coefficients of above gases, only mono positive molecular ion and containing the most abundant isotopes of the element were considered.

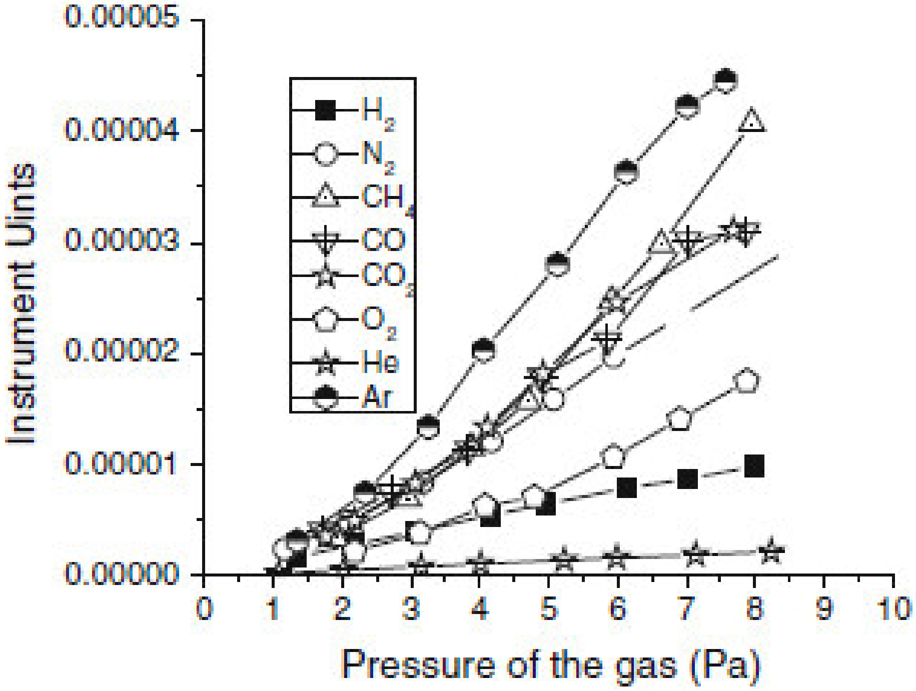

Figure 6.3. Mass intensity versus pressure of gases (parent ion peak intensity for each gas was measured)

Table 6.2 Relative sensitivity and correction factors of various gases with respect to nitrogen

Gas species	**Sensitivity factor (instrument unit/Pa)**	**RSF with respect to Nitrogen**	**Correction factor (1/RSF)**
H_2	$(1.22 \pm 0.02) \times 10^{-6}$	0.32 ± 0.01	3.08 ± 0.09
N_2	$(3.77 \pm 0.09) \times 10^{-6}$	1.00 ± 0.03	1.00 ± 0.03
CO	$(4.85 \pm 0.12) \times 10^{-6}$	1.24 ± 0.08	0.81 ± 0.05
CH_4	$(6.24 \pm 0.41) \times 10^{-6}$	1.65 ± 0.11	0.60 ± 0.04
CO_2	$(4.67 \pm 0.27) \times 10^{-6}$	1.29 ± 0.05	0.78 ± 0.03
O_2	$(2.68 \pm 0.17) \times 10^{-6}$	0.71 ± 0.05	1.41 ± 0.10
Ar	$(7.05 \pm 0.20) \times 10^{-6}$	1.87 ± 0.07	0.53 ± 0.02
He	$(2.71 \pm 0.05) \times 10^{-7}$	0.07 ± 0.01	13.93 ± 0.43

6.5.5. Gas composition calculations

All observed peak intensities of sample (1, 2, 12, 13, 14, 15, 16, 18, 28, 32 and 44) were corrected for respective intensities in blank determinations. It can be seen from the data of Table 6.3that peaks at m/z=15 and 44 are specific only for methane and carbon dioxide respectively. From the peak intensity at m/z =44, the contribution at m/z =12 ($p_{12\,(CO2)}$) and m/z= 28 ($p_{28\,(CO2)}$) due to carbon dioxide were calculated from the fragmentation pattern of CO_2. Similarly, contribution at m/z=12 ($p_{12\,(CH4)}$), m/z=14 ($p_{14\,(CH4)}$) and m/z=16 ($p_{16\,(CH4)}$) due to methane were calculated from the peak intensity at m/z=15. The observed peak intensity $p_{12(obs)}$ was corrected for contribution from CH_4 and CO_2 to get the peak intensity due to CO at m/z=12 ($p_{12(CO)} = p_{12\,(obs)} - p_{12\,(CO2)} - p_{12\,(CH4)}$). From $p_{12(CO)}$ peak intensity, the contribution of carbon monoxide at peak 28 $p_{28(CO)}$ was calculated. Similarly, contribution of methane at m/z=14 was subtracted from the observed peak intensity at m/z=14 to get the contribution of nitrogen at m/z=14. From this, contribution of nitrogen at m/z = 28 ($p_{28\ (N2)}$)was calculated from the fragmentation pattern data of nitrogen.

Fragmentation pattern of gases were calculated by feeding pure gases to HVE-QMS one at a time. The percentage peak intensities of different fragment w.r.t. parent ion were calculated and given in Table 6.3.

Table 6.3 Fragmentation pattern of the gases

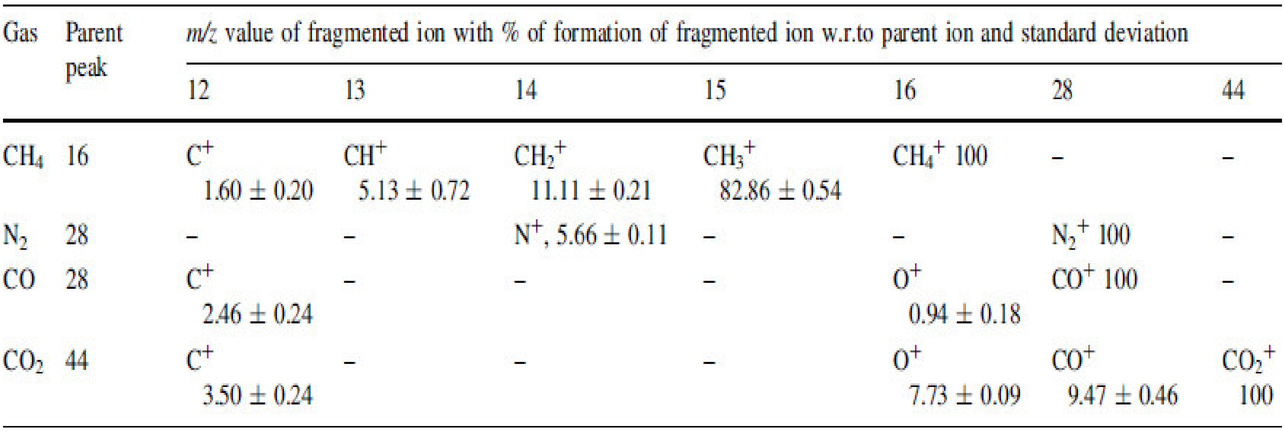

Gas	Parent peak	m/z value of fragmented ion with % of formation of fragmented ion w.r.to parent ion and standard deviation						
		12	13	14	15	16	28	44
CH_4	16	C^+ 1.60 ± 0.20	CH^+ 5.13 ± 0.72	CH_2^+ 11.11 ± 0.21	CH_3^+ 82.86 ± 0.54	CH_4^+ 100	–	–
N_2	28	–	–	N^+, 5.66 ± 0.11	–	–	N_2^+ 100	–
CO	28	C^+ 2.46 ± 0.24	–	–	–	O^+ 0.94 ± 0.18	CO^+ 100	–
CO_2	44	C^+ 3.50 ± 0.24	–	–	–	O^+ 7.73 ± 0.09	CO^+ 9.47 ± 0.46	CO_2^+ 100

Fragmentation pattern of the gases-

For CO_2

Intensity at m/z = 44 was I_{44} (100%).

Intensity at m/z = 12 and m/z = 28 were $I_{12}$and I_{28} respectively.

(I_{12} / I_{44}) x 100 = 3.5

(I_{28} / I_{44}) x 100 = 9.47

For CH_4

Intensity at m/z = 16 was I_{16}(100%)

Intensity at m/z = 12 and m/z = 14 and m/z = 15 were I_{12}, I_{14}andI_{15} respectively

(I_{12} / I_{16}) x 100 = 1.60

(I_{14} / I_{16}) x 100 = 11.11

(I_{15} / I_{16}) x 100 = 82.86

For CO

Intensity at m/z = 28 was I_{28}(100%)

Intensity at m/z = 12 and m/z = 16 were $I_{12}$and I_{16} respectively.
(I_{12} / I_{28}) x 100 = 2.46
(I_{16} / I_{28}) x 100 = 0.94

The peak intensities of the parent peaks of hydrogen (2), methane (16), carbon monoxide (28), nitrogen (28), Oxygen (32) and carbon dioxide (44) were corrected forsensitivity (intensity divided by respective RSF) by considering the RSFs of corresponding gas as mentioned above. Since the sensitivity corrected peak intensity is directly proportional to the partial pressure of the gas and hence its mole fraction, the composition of the species (i) is given as

$$\mathbf{X_i} = \frac{\mathbf{(Peak\ Intensity)_i}}{\sum\mathbf{(Peak\ Intensity)_i}}$$

Where Xi is the mole fraction of the species ‘i'

To validate the methodology for the determination of nitrogen andcarbon monoxide employing their fragmentation pattern, synthetic gas mixtures of N_2 and CO were prepared and the gas composition was determined by QMS (Table 6.4).

Table 6.4 Validation of gas composition measurement

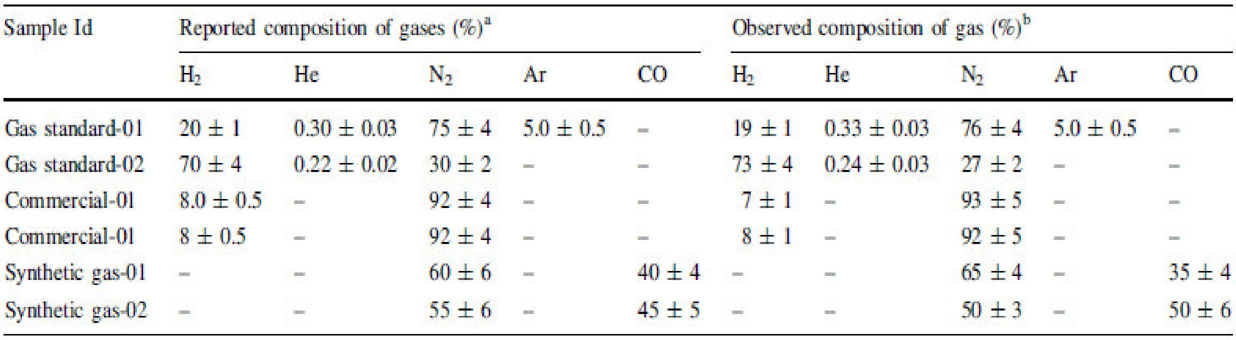

Sample Id	Reported composition of gases (%)[a]					Observed composition of gas (%)[b]				
	H_2	He	N_2	Ar	CO	H_2	He	N_2	Ar	CO
Gas standard-01	20 ± 1	0.30 ± 0.03	75 ± 4	5.0 ± 0.5	–	19 ± 1	0.33 ± 0.03	76 ± 4	5.0 ± 0.5	–
Gas standard-02	70 ± 4	0.22 ± 0.02	30 ± 2	–	–	73 ± 4	0.24 ± 0.03	27 ± 2	–	–
Commercial-01	8.0 ± 0.5	–	92 ± 4	–	–	7 ± 1	–	93 ± 5	–	–
Commercial-01	8 ± 0.5	–	92 ± 4	–	–	8 ± 1	–	92 ± 5	–	–
Synthetic gas-01	–	–	60 ± 6	–	40 ± 4	–	–	65 ± 4	–	35 ± 4
Synthetic gas-02	–	–	55 ± 6	–	45 ± 5	–	–	50 ± 3	–	50 ± 6

[a] reported gas composition was determined by GC-TCD (5 replicate analysis)
[b]mean of five determination with standard deviation

Synthetic gas – 01, (N_2+CO) Analyses

Peak at $I_{12}$was observed.I_{12} peak was due CH_4, CO, CO_2. Blank Intensity was subtracted from sample intensity to obtained corrected peak intensities. After blank correction, peak intensity at m/z = 12 (I_{12}) was only due to CO and its contribution in cracking pattern of CO was 2.46 (as given in Table 6.3). Thus peak intensity of CO (I_{CO}) was -

$(I_{12} / 2.46) \times 100 = I_{CO}$

True peak intensity of CO was $I^1_{CO} = \frac{I_{CO}}{RSFofCO}$

Observed peak intensity at m/z = 28 was I_{28}

$I_{N2} = \frac{I_{28} - I^1_{CO}}{RSFof\,N_2}$

Observed composition of CO was $\frac{I^1_{CO}}{I^1_{CO} + I_{N_2}} \times 100 = 35\ \%$

Observed composition of N_2 was $\frac{I_{N_2}}{I^1_{CO} + I_{N_2}} \times 100 = 65\ \%$ (as shown in Table 6.4).

The composition of this synthetic gas mixture was also determined by GC-TCD method. The results of gas composition determined by both the methods are given in Table 6.4. Results obtained by both the methods agreed well within 10 %.

6.5.6. Validation of methodology

To validate the methodology, Elemental Microanalysis Limited, U.K., make certified hydrogen standards in titanium were analysed by heating at 1,273 K and extracting gases for 30 min. From the data of pressure, volume of collection chamber and mole fraction of hydrogen in released gases, hydrogen content present in the standard was calculated employing ideal gas equation [103]. From the mass of the standard, hydrogen mass fraction was calculated. Results are given in Table 6.5. It can be seen from the Table that there is no significant difference between results obtained in present method and reported values at 95 % confidence level (t test).

Table 6.5. Validation of methodology

Part No	**Reference value [a] (µg/g)**	**Obtained value [b] (µg/g)**
B2601	44 ± 4	50 ± 3
B2603	201 ± 8	198 ± 5
B2602	142 ± 6	144 ± 4

6.5.7. Detection limit of the method

For the estimation of detection limit of the method, ten independent blank measurements were carried out. The mean value of pressure obtained in these blank experiments and its standard deviation were found to be 4.52×10^{-1} and 4.92×10^{-2} Pa respectively.

The values were placed in eq

$$\mathbf{V_T = \frac{P\,V_S\,T_{STP}}{T_R P_{STP}}}$$

Where,

Standard deviation of the pressure obtained in blank experiments, $P = 4.92 \times 10^{-2}$Pa

Volume of the system, $V_S = 19.43$L

Temperature at STP, $T_{STP} = 273$ K

Room Temperature, $T_R = 298$ K

Pressure at STP, $P_{STP} = 101325$ Pa

$$V_T = \frac{4.92 \times 10^{-2} \times 19.43 \times 273}{298 \times 101325} L$$

$$= \frac{26097.6 \times 10^{-2}}{30194850} \text{ L}$$

= 8.6 x 10^{-6}L(at 1σ level of blank)

= 25.8 x10^{-6} L (at 3σ level of blank)

Detection limit of the method for the sample size of 21 g = 25.8 x10^{-6} x 1000 / 21 L/Kg

= 1.22 x 10^{-3} L/Kg

= 0.001 L/Kg

Therefore, detection limit of the method (at 3σ level of blank) was found to be 0.025 x 10^{-3}L(0.001 L/kg at the sample size 21 g). Precision and accuracy of the methodology could not becalculated since standard reference materials for total gas content are not available.

6.5.8. Uncertainty in Total Gas measurement

Uncertainty in the measurement of total gas content was calculated as per ISO guidelines [187] and employing bottom-up approach [188]. Arriving at the overall uncertainty by statistical treatment is explained by applying uncertainty to a typical data obtained by HVE-QMS method in the measurement of Total Gas content.

The total gas content excluding hydrogen was calculated employing gas laws,

$$\mathbf{V_T} = \frac{(\mathbf{P_S - P_B})\mathbf{V_S}\ \mathbf{T_{STP}}}{\mathbf{T_R P_{STP}}\ \mathbf{1000\ W_S}} (\mathbf{1 - X_H}) \text{ ....}\mathbf{(1)}$$

where,

V_T is the volume of total gas excluding hydrogen per unit mass of sample (L/Kg),

P_S is the pressure of the gases released during sample analysis (atm),

P_B is the pressure of the gases released during blank analysis (atm),

V_S is the volume of the collection chamber (19.43 ± 0.27 L),

T_{STP} is the standard temperature (273 K),

T_R is the room temperature(298 K),

P_{STP} is the pressure at STP (1 atm),

W_S is the mass of the sample (g) and

X_H is the mole fraction of hydrogen given by-

$$\mathbf{X_H} = \frac{\mathbf{I_{H2}}}{(\mathbf{I_{H2}} + \mathbf{I_{CH4}} + \mathbf{I_{N2}} + \mathbf{I_{CO}} + \mathbf{I_{CO2}})} \textbf{...(2)}$$

Where,

I_{H2} = Corrected peak intensity of H_2

I_{CH4}= Corrected peak intensity of CH_4

I_{N2} = Corrected peak intensity of N_2

I_{CO} =Corrected peak intensity of CO

Ico_2 = Corrected peak intensity of CO_2

Various steps involved in the analysis of Total Gas content by HVE-QMS technique are: weighing the sample, calculation of volume of system, pressure measurement, temperature, ionic currents measurement, its conversion into partial pressure. Uncertainty of W_S, P, V, T, X_H were determined in the following manner for obtaining the overall uncertainty of Total Gas content measurement.

Weight of sample (B type Uncertainty)

The sample was weighed employing electronic balance which can read up to 0.2 mg. The uncertainty quoted by the manufacturer is 0.2mg over the entire range (10-180 mg). The sample taken is 20.4321 g. Hence the relative standard uncertainty in the weighing was calculated by

$u_w=\frac{0.0002}{20.4321} \times 100\ \%$ = 0.00098 % = 0.001% or <0.01%

Volume of the system (A type uncertainty)

Total Volume of the system was 19.43 L with standard deviation 0.27 L.

Standard uncertainty (standard deviation on mean) = s /$\sqrt{n}$ = 0.27/ $\sqrt{5}$= 0.12 L

where, s = standard deviation

n = number of time the analysis was done

Relative standard uncertainty of volume of the system was calculated as-

$u_V = \frac{0.12}{19.43} \times 100\ \%$

= 0.62 %

Pressure measurement(Blank pressure ⟶ A type uncertainty; Sample pressure ⟶ B type uncertainty)

Pressure of the system was, $P = P_{sample} - P_{blank}$

$= (P_s \pm x_s) - (P_b \pm x_b)$

P_s = 3.58 Pa, pressure of the sample (Average of 5 measurements)

P_b=4.52 x 10^{-1}Pa, pressure of the blank (Average of 5 day's measurements)

x_s = standard deviation of the sample

x_b = 1.099 x 10^{-1} Pa, standard deviation of the blank

Std. uncertainty of blank (z) = std.deviation/$\sqrt{5}$ Pa

= 1.099 x 10^{-1}/$\sqrt{5}$

= 4.91 x 10^{-2} Pa

Pressure was measured by Capacitance manometer with an accuracy of 0.5% of reading.

Standard Uncertainty of the sample (y) =$\frac{0.5 \times 3.58}{100}$

= 1.79 x 10^{-2} Pa

Combined standard uncertainty was, $U_P = \sqrt{y^2 + z^2}$

$$= \sqrt{(1.79 \text{ x } 10^{-2})^2 + (4.91 \text{ x } 10^{-2})^2} = 5.23 \text{ x } 10^{-2} \text{ Pa}$$

Relative standard uncertainty of pressure measurement was calculated as-

$u_P = U_P$ x 100 / (P_s - P_b) %

= 5.23 x 10^{-2} x 100 / (3.58 - 0.452) %

= 1.67 %

Temperature Measurement(B type uncertainty)

Room temperature was 298 K

Standard uncertainty was 1K

Relative standard uncertainty of temperature measurement was found as-

u_T= 1 x 100 / 298 % = 0.34 %

Uncertainty in partial pressure of hydrogen (A type uncertainty)

Values of corrected intensity of H_2, CH_4, N_2 CO, CO_2 as well as their standard uncertainty were calculated similar to the estimation of uncertainty given in Chapter 3. These values were-

- Corrected peak intensity of H_2=1.12 x 10^{-6}

  Standard uncertainty =3.80 x 10^{-8}
- Corrected peak intensity of CH_4=5.49 x 10^{-9}

  Standard uncertainty =3.68 x 10^{-10}
- Corrected peak intensity of N_2=5.98 x 10^{-7}

  Standard uncertainty= 2.15 x 10^{-8}
- Corrected peak intensity of $CH_4$of CO = 2.36 x 10^{-7}

  Standard uncertainty of CO= 2.75 x 10^{-8}
- Corrected peak intensity of CO_2= 2.51 x 10^{-8}

Standard uncertainty =9.65 x 10^{-10}

$$\mathbf{I_{H2} + I_{CH4} + I_{N2} + I_{CO} + I_{CO2} = (1.12 + 0.00549 + 0.598 + 0.236 + 0.0251) \times 10^{-6}}$$

$$\mathbf{= 1.99 \times 10^{-6}}$$

Combined Standard uncertainty,

I_{Total}=

$$\sqrt{[(3.80 \text{ x } 10^{-8})^2 + (3.68 \text{ x } 10^{-10})^2 + (2.15 \text{ x } 10^{-8})^2 + (2.75 \text{ x } 10^{-8})^2 + (9.65 \text{ x } 10^{-10})^2}$$

$$= \sqrt{10^{-16}\,[(3.80)^2 + (0.00037)^2 + (2.15)^2 + (2.75)^2 + (0.00097)^2\,]}$$

$$= \sqrt{10^{-16}\,(14.44 + 1.35 \text{ x } 10^{-7} + 4.62 + 7.56 + 9.31 \text{ x } 10^{-7})}$$

$$= \sqrt{26.62 \text{ x } 10^{-16}} = 5.16 \text{ x } 10^{-8}$$

$$\text{Relative Std. Uncertainty } \left(u_{X_{H_2}}\right) \text{ of } X_{H_2} \text{ or } {}^{I_{H_2}}\!/_{I_{Total}} = \sqrt{(\frac{u_{H_2}}{I_{H_2}})^2 + (\frac{u_{Total}}{I_{Total}})^2}$$

$$= \sqrt{(\frac{3.80 \text{ x } 10^{-8}}{1.12 \text{ x } 10^{-6}})^2 + (\frac{5.16 \times 10^{-8}}{1.99 \text{ x } 10^{-6}})^2}$$

$$= \sqrt{(3.39 \times 10^{-2})^2 + (2.59 \times 10^{-2})^2}$$

$$= \sqrt{11.49 \times 10^{-4} + 6.70 \times 10^{-4}}$$

$$= 4.27 \text{ x } 10^{-2}$$

% Relative Std. Uncertainty $\left(u_{H_2}\right)$ of X_{H_2} = 4.27

Relative combined uncertainty (%) = $\sqrt{u_W{}^2 + u_V{}^2 + u_P{}^2 + u_T{}^2 + u_{X_{H_2}}{}^2}$

$$= \sqrt{(0.01)^2 + (0.62)^2 + (1.67)^2 + (0.34)^2 + (4.27)^2}$$

$$= \sqrt{0.0001 + 0.3844 + 2.7889 + 0.1156 + 18.2329}$$

$$= \sqrt{21.52} = 4.60$$

The relative combined uncertainty in the measurement of total gas content was estimated and it was found to be 4.6 %. Hence, the relative expanded uncertainty (at coverage factor k = 2) in measurement of total gas content is =2 x 4.6 = 9.2%. Details of numerical values of variables, type of uncertainty, standard as well as relative standard uncertainties are also tabulated in Table 6.6.

It may be mentioned that many uncertainty components associated with gas composition calculations are neglected which may be significant. They are-

(i) *Uncertainty associated with the change in gas composition* - Gas composition may change during analysis with QMS while feeding it through micro leak valve.

(ii) *Uncertainty associated with change in sensitivity* - Sensitivity of the gases in QMS was determined in the pressure range of 1Pa - 8 Pa. However, the pressure of some of the gases was less than 1 Pa (e.g. mole fraction of CH_4 is 0.01 so its partial pressure is 0.01 x 3.58 Pa i.e. 0.0358 Pa which is much below 1 Pa).

Table 6.6 Uncertainty in the measurement of Total Gas Content

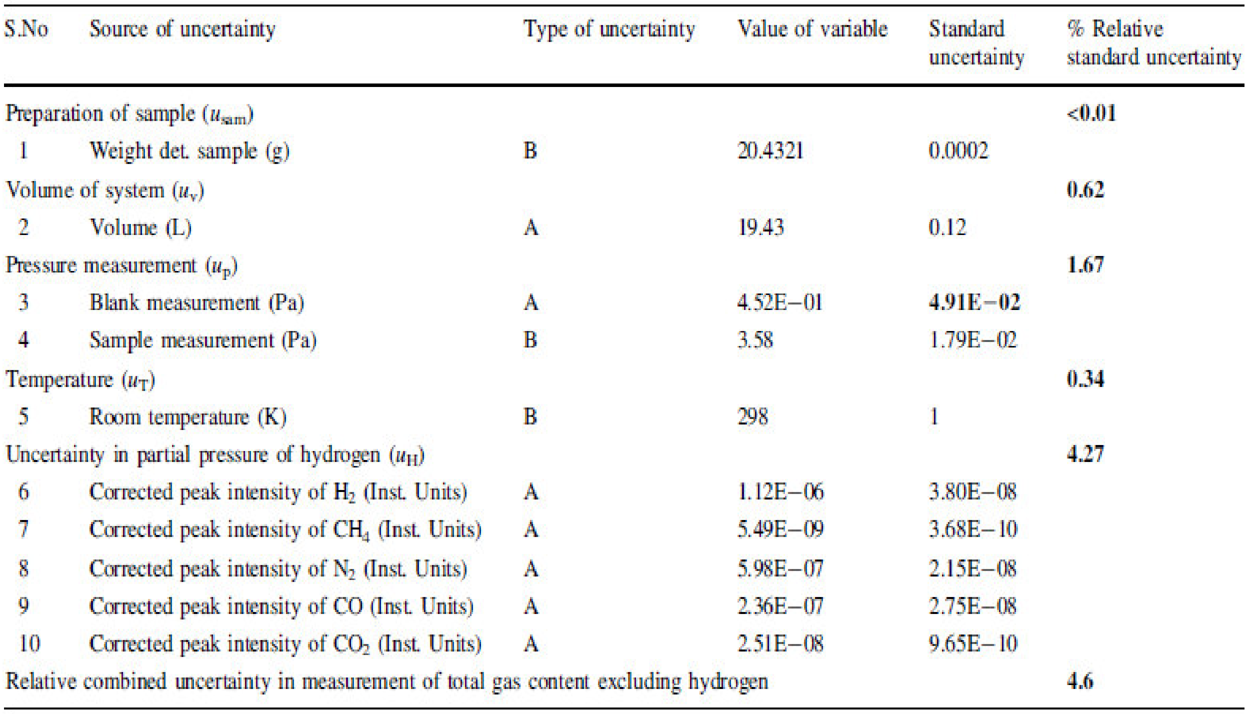

S.No	Source of uncertainty	Type of uncertainty	Value of variable	Standard uncertainty	% Relative standard uncertainty
Preparation of sample (u_{sam})					**<0.01**
1	Weight det. sample (g)	B	20.4321	0.0002	
Volume of system (u_v)					**0.62**
2	Volume (L)	A	19.43	0.12	
Pressure measurement (u_p)					**1.67**
3	Blank measurement (Pa)	A	4.52E−01	**4.91E−02**	
4	Sample measurement (Pa)	B	3.58	1.79E−02	
Temperature (u_T)					**0.34**
5	Room temperature (K)	B	298	1	
Uncertainty in partial pressure of hydrogen (u_H)					**4.27**
6	Corrected peak intensity of H_2 (Inst. Units)	A	1.12E−06	3.80E−08	
7	Corrected peak intensity of CH_4 (Inst. Units)	A	5.49E−09	3.68E−10	
8	Corrected peak intensity of N_2 (Inst. Units)	A	5.98E−07	2.15E−08	
9	Corrected peak intensity of CO (Inst. Units)	A	2.36E−07	2.75E−08	
10	Corrected peak intensity of CO_2 (Inst. Units)	A	2.51E−08	9.65E−10	
Relative combined uncertainty in measurement of total gas content excluding hydrogen					**4.6**

6.5.9. Application of methodology

Employing these optimized conditions, several pellets of DDUO_2 were analysed for total gas content and its composition. A typical mass spectrum obtained from DDUO_2 is shown in Figure 6.4.

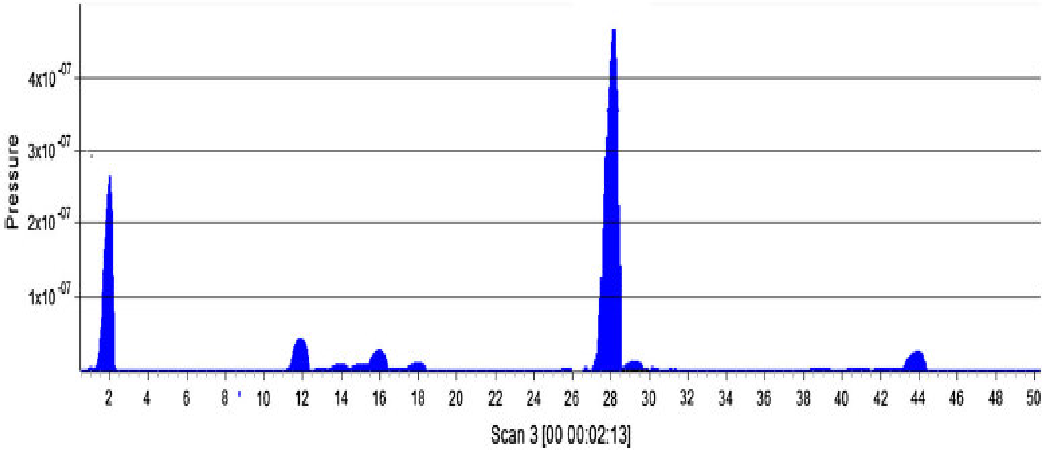

Figure 6.4. Typical mass spectrum of DDUO_2 pellet

Typical results are given in Table 6.7.

Table 6.7 Results of total gas analysis in DDUO_2 pellets along with their expanded uncertainty in measurement (k=2)

Sample ID	**Total Gas Content(L/kg)**	**Total Gas content Excluding hydrogen (L/kg)**	**Composition of the Gases (% i.e.mole fraction ×100)**				
			H_2	CH_4	N_2	CO	CO_2
U-1	0.090 ± 0.003	0.014± 0.001	85.0 ± 6.7	1.0± 0.1	2.0± 0.2	10.0± 2.4	1.0± 0.1
U-2	0.031± 0.001	0.013± 0.001	56.0± 4.5	1.0± 0.1	29.0 ± 2.3	12.0± 2.9	1.0± 0.1
U-3	0.035± 0.001	0.020± 0.002	43.0 ± 3.5	1.0± 0.1	8.0± 0.6	46.0 ± 11.0	2.0 ± 0.2
U-4	0.036± 0.001	0.021± 0.002	43.0± 3.5	1.0± 0.1	9.0± 0.7	45.0± 10.8	1.0± 0.1
U-5	0.039± 0.001	0.016± 0.001	58.0± 4.6	1.0± 0.1	7.0± 0.6	31.0 ± 7.4	2.0± 0.2

For example in Sample ID U-**1**

Total Gas Content (L/kg)

Total gas content was found to be 0.090 L/Kg.

% Relative standard uncertainty for total gas content = $\sqrt{u_V{}^2 + u_P{}^2 + u_T{}^2}$

$$=\sqrt{(0.62)^2 + (1.67)^2 + (0.34)^2}$$

$$= \sqrt{0.38 + 2.79 + 0.12} = 1.81$$

% Relative standard uncertainty in the measurement of Total Gas (K=2) was

1.81x2%=3.62%

Uncertainty in Total Gas content =0.09 x 3.62/100 L/Kg = 0.003 L/Kg

Thus, the total gas content along with expanded uncertainty in measurement (k=2)=(0.090 ± 0.003) L/Kg.

Total Gas content excluding hydrogen (L/kg)

From Table 6.7

Total Gas content = 0.090 L/Kg

Composition of H_2 = 85% =>X_{H2}=0.85

Total gas content excluding hydrogen = 0.090(1- 0.85) = 0.014

% Relative standard uncertainty in Total Gas content measurement (K=2) = 9.2%

Uncertainty in Total Gas (excluding hydrogen)= 0.014 x 9.2/100 =0.001

The total gas content excluding hydrogen along with expanded uncertainty = (0.014 ± 0.001)L/Kg.

Composition of Gases

Mole Fraction of any gas **say** CH_4 (%) = $\frac{I_{CH\,4}}{I_{Total}} \times 100$

where, I_{CH4}= Corrected peak intensity of CH_4

I_{Total} = Sum of the peak intensities of all the gases present

% Mole fraction of H_2 = 85.0

% Mole fraction of CH_4 =1.0

% Mole fraction of N_2 = 2.0

% Mole fraction of CO =10.0

% Mole fraction of CO_2 =1.0

Relative standard uncertainty (given in Table 6.8) of different gas composition was calculated by using following Eq -

$$\text{Relative Std. Uncertainty } (u_{X_a}) \text{ of } X_a \text{ or } {}^{I_a}/_{I_{Total}} \;=\; \sqrt{(\frac{U_a}{I_a})^2 + (\frac{U_{Total}}{I_{Total}})^2}$$

Where, U_a= Standard Uncertainty of gas 'a'

I_a= Intensity of gas 'a'

U_T = Combined std uncertainty

I_T = Total Intensity

Table 6.8 Relative Standard Uncertainty of different gas composition

	Intensity (I)	**StdUncertainty (U)**	**U^2**	**$(U/I)^2$**	**relative Std. Uncertainty • $(U/I)^2+(U_T/I_T)^2$x 100**
H_2	1.12 x 10^{-6}	3.80 x 10^{-8}	1.44 x 10^{-15}	1.15 x 10^{-3}	4.3
CH_4	5.49 x 10^{-9}	3.68 x 10^{-10}	1.35 x 10^{-19}	4.49 x 10^{-3}	7.2
N_2	5.98 x 10^{-7}	2.15 x 10^{-8}	4.62 x 10^{-16}	1.29 x 10^{-3}	4.4
CO	2.36 x 10^{-7}	2.75 x 10^{-8}	7.56 x 10^{-16}	1.36 x 10^{-2}	11.9
CO_2	2.51 x 10^{-8}	9.65 x 10^{-10}	9.31 x 10^{-19}	1.48 x 10^{-3}	4.6
Total Intensity (I_T)	1.98 x 10^{-6}				
Combined std uncertainty (U_T)	$\sqrt{U_{H_2}^2 + U_{CH_4}^2 + U_{N_2}^2 + U_{CO}^2 + U_{CO_2}^2}$ = 5.16 x 10^{-8}				
$(U_T/ I_T)^2$	6.76 x 10^{-4}				

% Relative standard uncertainty in H_2 measurement = $85 \times \frac{4.3}{100}$ = 3.66

Uncertainty in H_2 measurement (K=2) = 3.66 x 2 = 7.3%

% Composition of H_2= (85.0 ± 7.3)

% Relative standard uncertainty in CH_4 measurement = $1 \times \frac{7.2}{100}$ = 0.07

Uncertainty in CH_4measurement (K=2) = 0.07 x 2 = 0.1%

% Composition of CH_4 was (1.0 ± 0.1)

% Relative standard uncertainty in N_2 measurement = $2 \times \frac{4.4}{100}$ = 0.088

Uncertainty in N_2measurement (K=2) = 0.088 x 2 = 0.176% or 0.2%

% Composition of N_2=(2.0 ± 0.2)

% Relative standard uncertainty in CO measurement = $10 \times \frac{11.9}{100}$ = 1.19

Uncertainty in CO measurement (K=2) = 1.19 x 2 = 2.38% or 2.4%

% Composition of CO =(10.0 ± 2.4)

% Relative standard uncertainty in CO_2 measurement = $1 \times \frac{4.6}{100}$ = 0.046

Uncertainty in CO_2 measurement (K=2) =0.046 x 2 = 0.092% or 0.1%

% Composition of CO_2=(1.0 ± 0.1)

The total gas content excluding hydrogen in all the samples was found to be much less than the specification (i.e. 0.1 L/kg) at STP condition.

Chapter – 7

Summary, Conclusions and Future Scope

Summary of the studies carried out in the thesis, conclusions drawn from the studies and the scope for future work are described below:

7.1. Determination of Deuterium pick - up in Zr-Nb alloy

- Due to continuous usage of the pressure tubes inside the reactor, heavy ingress of deuterium into the pressure tubes could occur due to corrosion reactions resulting in hydrogen (or deuterium) embrittlement. Aging management therefore requires quantification of the deuterium pick-up rate for the remedial measures to be taken for the smooth operation of the reactor.

- For this purpose, a hot vacuum extraction-quadrupole mass spectrometry (HVE-QMS) technique has been developed in our laboratory. Experimental conditions like temperature, time of extraction of liberated gases, and measurement methodology were optimized.

- Sensitivity factors ofH_2, HD and D_2were derived for quantification of analytical results. The sensitivity of the gases in quadrupole mass spectrometer is influenced by several factors like electron density, ionization potential of the gas, diffusion through micro-leak valve, differential pumping speed etc.The sensitivity factors of H_2 and D_2 were determined at various pressures from 10^{-1} to 8 Pa. Because of practical difficulty in obtaining pure HD, gas sensitivity factor for HD was calculated as arithmetic mean of sensitivity factors of H_2 and D_2. To validate this, mixture of pure H_2 and D_2 gases was made with different composition. Blank-corrected intensities for H_2, HD, and D_2were calculated and composition of the gas (mole fraction of H_2 and D_2) was determined employing relative sensitive factors. From the results, it was clear that there is no difference between observed and the expected values, confirming the validation of the sensitivity factor measurements.

- Precision of this methodology is10%.

- Studies were carried out on the formation of hydrogen (or deuterium) molecular ion H_3^+ (D_3^+) in QMS as a function of pressure in the measurement system. It was observed that the molecular ion's formation was negligible at system pressures less than 10 Pa. In the analysis of zircaloy samples, the pressure of the gases released was in the range 5 x 10^{-2} Pa to 5 Pa. At these pressures, the molecular ions were not formed. If the pressure is more than 10 Pa, it has to be suitably manipulated and brought down to <5 Pa before feeding it to mass analyser.

- **Conclusion:** The quantification of analytical results required determination of sensitivity factors for hydrogen isotopes. With the hot vacuum extraction coupled with quadrupole mass spectrometer (HVE-QMS), it is possible to get deuterium content in zircaloy coolant channels. This is very useful in nuclear technology in assessing the life expectancy of the coolant channel. The experimental data is useful in validating the theoretical predictions of the life of coolant channels.

7.2. Determination of Diffusion Coefficient of Hydrogen and Deuterium in Zr-2.5%Nb pressure tube material

- The diffusion coefficients of hydrogen and deuterium in Zr–2.5%Nb alloy were measured in the temperature range of 523 to 673K, employing hot vacuum extraction-quadrupole mass spectrometry (HVE-QMS).

- One end of the Zr–2.5%Nb alloy specimens was charged electrolytically with the desired hydrogen isotope. After annealing at different temperatures for a predetermined time, the specimens were cut into thin slices, which were analysed for their H_2/D_2 content using the HVE-QMS technique.

- The depth profile data were fitted into the equation representing the solution of Fick's second law of diffusion. The activation energy of hydrogen/deuterium diffusion was obtained from the Arrhenius relation between the diffusion coefficient and temperature. The temperature dependent diffusion coefficient can be represented as $D_H = 1.41 \times 10^{-7} \exp(-36000/RT)$ and $D_D = 6.16 \times 10^{-8} \exp(-35262/RT)$ for hydrogen and deuterium, respectively.

- The Zr-2.5% Nb tube microstructure consists of elongated α-Zr grains surrounded by thin layer of β-Zr and the diffusivity of hydrogen in β-Zr is about two orders of magnitude higher than in α-Zr. Measured diffusivity values for hydrogen and deuterium at two temperatures were compared with literature and the values were found out to be almost half of the reported values. There are minor differences in the fabrication route of Zr-2.5%Nb pressure tubes used in Indian PHWRs and CANDU reactors. These differences in the fabrication route can vary the micro-structural features of the PTs and this might be the reason for the observed difference in diffusivity values.

- **Conclusion:** The diffusion coefficient of hydrogen and deuterium in Zr–2.5%Nb was determined by electrolytic charging of the specimen at one end, annealing the specimen at different temperatures in the range of 523 to 673 K followed by a determination of the H/D content by the HVE-QMS technique. The activation energies for hydrogen and deuterium are nearly the same (~35 kJ/mol), while the pre-exponential factor is higher for hydrogen (1.41 x $10^{-7}$$m^2$/s)than it is for deuterium (6.16 x 10^{-8} m^2/s). It was observed that the diffusivity of deuterium determined in the present investigation was almost half the value reported by Khatamian, which is probably due to a discontinuous β-phase present in the IndianPHWR pressure tubes.

7.3. Formation of Pd Nanocatalyst on Inorganic host materials for U(VI) reduction by formic acid

- A new synthetic route was developed for anchoring large amount of Pd nanoparticles (NPs) on the surface of inorganic host particles involving grafting of hydrazine on the (3-glycidyloxypropyl)trimethoxysilane coated inorganic particles such as Fe_3O_4 and SiO_2. The hydrazine-grafted inorganic particles reduce Pd^{2+} ions spontaneously at ambient conditions. This results in production of Pd^0seeds, nucleation, and growth of Pd NPs on surface of a host particle itself. The major advantages of this method are: (i) method used for grafting of hydrazine on SiO_2 and Fe_3O_4 particles is simple and applicable to different inorganic host particles, (ii) the Pd NPs are formed by controlled reduction of Pd^{2+} ions by equilibration of hydrazine grafted particles in solution, which prevent loss of precious precursor ions, (iii) controlled formation of spherical nanoparticles in terms of amount and size.

- Formed Pd NPs loaded Fe_3O_4 and SiO_2 particles were characterized by the elemental analyses, microscopy, elemental mappings etc. These studies have shown the formation of $\approx$ 0.3 and 1 nm spherical Pd NPs uniformly on the Fe_3O_4 and

SiO_2particles, respectively. The saturation loading of Pd^0 contents on the Fe_3O_4 and SiO_2 particles were found to be 12 and 20 mg g^{-1}, respectively.

- The formic acid undergoes decomposition in the presence of Pd nanocatalyst and also could be used for the reduction of oxymetal ions such as Cr(VI) and U(VI) ions under similar conditions. H_2 sorption on Pd NPs would affect the reduction of U(VI) to U(IV) by formic acid as formation of PdH_x deteriorates the catalytic activity of Pd NPs. Therefore, the sorptions of H_2 in Fe_3O_4@Pd and SiO_2@Pd were studied at 4 different temperatures (373K, 303K, 273K & 173K) using Sievert apparatus. The H_2 sorption behaviour of SiO_2@Pd was found to be in line with literature. However, H_2 sorption of Fe_3O_4@Pd at 373K was observed to be unusually high. Mössbauer Spectroscopy showed no change in Fe^{3+} and Fe^{2+} ratio before and after hydrogenation. However, the X ray photoelectron spectroscopy (XPS) spectra showed that there may be splitting of Fe-O-Si bond at 373K leading to high sorption of hydrogen.

- The Pd NPs loaded SiO_2 and Fe_3O_4 particles exhibited high catalytic activity in the reduction of Cr(VI) with formic acid. However, U(VI) could be reduced with formic acid in the presence of SiO_2@Pd, but Fe_3O_4@Pd did not show any catalytic activity. This was attributed to the high catalytic activity of 0.1-0.5 nm sized Pd NPs formed on the Fe_3O_4 particles which promoted decomposition of formic acid instead of U(VI) reduction having higher activation barrier and lower redox potential. This seems to suggest that the reduction of such inorganic ions with formic acid requires a balance of catalytic activity of Pd NPs to avoid competing side reaction involving the decomposition of formic acid.

- It was observed from rate profiles of Cr(VI) reduction with formic acid that the best correlation coefficients were obtained from pseudo-first-order (K_1/Pd wt. =0.5146 s^{-1} g^{-1}) and pseudo-second-order (K_2/Pd wt. = 24.6 mol^{-1} cm^3 sec^{-1} g^{-1}) models in the presence of catalyst Fe_3O_4@Pd and SiO_2@Pd, respectively, under identical chemical conditions *i.e.* same Pd amount (1 mg), reactants conc. and 323 K. This seems to suggest that the catalytic activity of Pd NPs influenced the kinetics of reduction. The higher catalytic activity of Pd NPs on Fe_3O_4 particles could be attributed to their lower sizes (0.1-0.5 nm) as compared to that on SiO_2 particles (0.5-2.0 nm). The lower sized Pd NPs would have larger surface area and also higher number of defects that may act as the active sites for catalyzing the reduction.

- **Conclusion:** One-step method developed in the present work for anchoring Pd NPs on the surface of hydrazine-grafted inorganic host particles is simple, similar to egg-shell membrane in terms of reduction and stabilization of NPs, and controlled amount of Pd^0 could be loaded. The sizes of Pd NPs were found to be dependent on the loading of Pd^0. The Pd NPs loaded SiO_2 and Fe_3O_4 particles exhibited a high catalytic activity in the reduction of Cr(VI) with formic acid. However, U(VI) could be reduced with formic acid in the presence of SiO_2@Pd, but Fe_3O_4@Pd did not show any catalytic activity. This was attributed to the high catalytic activity of 0.1-0.5 nm sized Pd NPs formed on the Fe_3O_4 particles which promoted decomposition of formic acid instead of U(VI) reduction having higher activation barrier and lower redox potential. This seems to suggest that the reduction of such inorganic ions with formic acid requires a balance of catalytic activity of Pd NPs to avoid competing side reaction involving the decomposition of formic acid.

7.4.Determination of Total gas content and its composition in DDUUO$_2$ pellets

- Total gas content and its composition are important specifications for sintered nuclear fuel pellets particularly in the case of fast breeder reactor fuels. Most commonly, total gas content and its composition is determined by hot vacuum extraction-quadrupole mass spectrometry (HVE-QMS).

- A number of parameters in this methodology such as temperature, duration of heating for quantitative extraction of evolved gases, total volume of the system, gas analysis conditions etc. needs to be optimized for reliable measurements.

- In addition, sensitivity factors for various gases like H_2, CH_4, N_2, CO, O_2 and CO_2in quadrupole mass spectrometry required for quantification of results were determined and validated employing reference gas mixtures of known composition.

- Employing these optimized conditions total gas content and its composition in blanket pellets (uranium oxide pellets)of Indian prototype fast breeder reactor was determined employing HVE-QMS.

- The relative expanded uncertainty (at a coverage factor k = 2) in the measurement of total gas content excluding hydrogen was estimated as per ISO guidelines and it was found to be 9.2 %.

- **Conclusions:** The total gas content and its composition have been determined in PFBR blanket (DDUO$_2$) pellets employing HVE-QMS. Sensitivity of the various gases in the QMS was determined for computing the gas composition. The correction factors were significantly high for He, H_2 and O_2. Mole fraction of Nitrogen and carbon monoxide in the released gas from the sample was determined by considering their cracking pattern. The detection limit of the methodology is 0.001 L/kg at the sample size of 21 g. The relative expanded uncertainty in measurement is 9.2 % (at a coverage factor of2). The results show that the total gas content observed in these pellets is much less than the specification limit of 0.1 L/kg at STP.

7.5. Future scope

Several features of the present work needs to be studied further like the U(VI) reduction with formic acid using different shape and sized Pd NPs to suppress competitive side reaction involving decomposition of formic acid to form hydrogen. This will also be important for production of hydrogen from formic acid for fuel cell applications. The hydrogen produced by formic acid could be loaded in-situ on Pd NPs. The hydrogen sorption in Fe_3O_4@Pd at 373K has been found to be unusually high. There is possibility of formation of silicon hydride in this case which needs to be investigated further.

The Fe_3O_4 nanoparticles used in the present work as a host could be used as template for forming hollow silica sphere loaded with Pd NPs. After aspirate thick coating of (3-glycidyloxypropyl)trimethoxysilane, the Fe_3O_4 template could be removed by immersing in high concentration HNO_3 or carboxylic acids. Thereafter, the hydrazine grafting and Pd NPs formation would be similar to that reported in the present work. It is reported in literature that hollow sphere could act as a nano-reactor with a high catalytic activity.

The selectivity of competitive sorption of H_2/D_2 in the disc formed by Fe_3O_4@Pd would be interesting to study changes in sorption properties of Pd NPs from bulk Pd metal. This has not been attempted till now.

References

1. India Energy Outlook, International Energy Agency. © OECD/IEA, 2015
2. Integrated Energy Policy, Report of the Expert Committee, Government of India, Planning Commission, New Delhi, August 2006
3. V.K. Sharma, IAEA-TECDOC-1290 (2002).
4. S. K. Sinha, K. Madhusoodanan, B. B. Rupani, R. K. Sinha, Proceedings of the symposium ZIRCONIUM - 2002, BARC, Mumbai, India.
5. R.K. Sinha, S.K. Sinha, K. Madhusoodanan, J. Nucl. Mater., 383 (1–2) (2008) 14.
6. M. Oskarsson, Doctoral thesis, Royal Institute of Technology, Stockholm, Sweden, 2000.
7. The safety of Ontario’s Nuclear Power Reactors, AScientific & Tech. Review, Ontario Hydro submission to the Ontario Nucl. Safety Review, Toronto, Ontario, 29 Feb, 1988.
8. B. K. Dutta, H. S. Kushwaha, V. V. Raj, IAEA TECDOC 1179 (2000).
9. A. B. Cheadle, C. E. Coleman, H. Litcht, Nucl. Tech., 57 (1982) 413.
10. W. Dietz, Structural material: Materials Science & Techno. A Comprehensivetreatment, Eds. R. W. Cahn, P. Haasen and E. J. Kramer, 10B Nuclear Materials, Chapter 8, (1994) 53.
11. C. Lemaignan, A.T. Motta, Zirconium alloys in nuclear applications, ibid 10B chapter 7, (1994) 1.
12. F. H. Froes, T. L. Yau, H. G. Weidinger, Titanium, Zirconium and Hafnium, ibid8 chapter 8, (1996) 399.
13. C. D. Williams, Reactor Technology, 13(2) (1970) 147.
14. E. F. Ibrahim, B. A. Cheadle, Can. Metall. Q., 24(3) (1985)273.
15. R. G. Fleck, V. Perovic, E.T.C Ho, Ontario Hydro Research Review No. 8 (1993) 1.
16. N. R. McDonald, Jl. of Australian Inst. of Metals, 16(4) (1971)179.
17. C. E. Coleman, B.A. Cheadle, C.D. Cann, J.R. Theaker, Zirconium in the nuclear industry : 11th Intl. Symposium, ASTM STP 1295, Eds. E. R. Bradley and G. P. Sabol, (1996) 884.
18. J. R. Theaker, R. Choubey, G. D. Moan, S. A. Aldridge, L. Davis, R. A. Graham, C. E. Coleman, Zirconium in the nuclear industry : 11th Intl. Symposium, Eds. E. R. Bradley and G. P. Sabol ASTM STP 1295 (1996) 221.
19. M. B. Elmoselhi, B. D. Warr, ASTM STP 1245 (1994) 62-77.

20. K. N. Choo, Y. S. Kim, Su-II Pyun, S. I. Pyun, J. Nucl.Mater.,226 (1-2) (1995) 9.

21. A. Ploc Robert, J. Nucl. Mater.,279 (2-3) (2000) 344.

22. Y. P. Lin, J. De Luca, J. Nucl. Mater.,265 (1-2) (1999) 1.

23. R. Kuwae, K. Sato, E. Higashinakagawa, J. Kawashima, S. Nakamura, J. Nucl. Mater., 119 (1983) 229.

24. Y. S. Sayi, P. S. Shankaran, C. S. Yadav, P. S. Ramanjaneyulu, V. Venugopal, K. L. Ramakumar, G. C. Chhapru, R. Prasad, H. C. Jain and D. D. Sood, Bhabha Atomic Research Centre Mumbai, Report No. BARC/2009/E/003.

25. P. Vizcaíno, A. D. Banchik, J. P. Abriata, Metallurgical and Materials Transactions A, 35A (2004) 2343.

26. K. L. Ramakumar, Y. S. Sayi, P. S. Shankaran, G. C. Chhapru, C. S. Yadav, V. Venugopal, Indian J. Chem. Techn., 11 (2004) 865.

27. W. A. Lanford, Nuclear Instruments and Methods in Physics Research, B66 (1992) 65.

28. Z. Qin, W. N. Lennard, C-S. Zhang, K. Griffiths, P. R. Norton, J. Nucl. Mater., 264 (1999) 228.

29. B. L. Cohen, C. L. Fink, J. H. Degnan, Journal of Appl. Phys., 43 (1972) 19.

30. P. W. K. Chu, J. W. Mayer, M. A. Nicolet, Backscattering Spectrometry Academic Press, Ney York, 1983.

31. K. L. Ramakumar, V. A. Raman, V. L. Sant, P. M. Shah, V. D. Kavimandan, H. C. Jain, Analytical Letters, 19 (1986) 2147.

32. R. K. Mc Geary, Zirconium and Zirconium Alloys, ASM, March 23-27, 1953.

33. J. G. Van Raaphorst, A. Kout, Fres. J. Anal. Chem. 291 (1978)324.

34. O. Vega, H. G. Reilla, Rodrigues, J. Nucl Mater., 106 (1982) 121.

35. T. Iwai, I. Takahashi, M. Handa, J Nuclr Sci Technol., 25 (1988) 456.

36. A. Maeda, T. Iwai, T. Ohmichi, M. Handa, IAEA -TECDOC - 466 (1987) 34.

37. R. N. Singh, R. Kishore, S. Mukherjee, S. Roychowdhury, D. Srivastava, T. K. Sinha, P. K. De, S. Banerjee,Bhabha Atomic Research Centre Mumbai, report No. BARC/2003/E/034 .

38. D. O. Northwood, U. Kosasih, International Metals Reviews, 28(2) (1983) 92.

39. A. D. Lepage, W. A. Ferris, G. A. Ledoux, FC-IAEA-03, T1.20.13-CAN-27363-03, (November1998).

40. R. Dutton, Hydrogen embrittlement effects in hydride forming metals, The Metall. Soc. of CIM, 16 (1978).

41. S. Laurent, D. Forge, M. Port, A. Roch, C. Robic, L. V. Elst, R. N. Muller, Chem. Rev., 108 (2008) 2064.

42. L. H. Reddy, J. L. Arias, J. Nicolas, P. Couvreur, Chem. Rev., 112 (2012) 5818.

43. Manoj B. Gawande, Paula S. Brancoa, Rajender S. Varma, Chem. Soc. Rev., 42 (2013) 3371.

44. Ning Yan, Yuan Yuanb, Paul J. Dyson, Dalton Trans., 42 (2013) 13294.

45. Yong Li, Wenjie Shen, Chem. Soc. Rev., 43 (2014) 1543.

46. Brian D. Adams, Aicheng Chen, Materials Today, 14 (2011) 282.

47. Miho Yamauchi, Hiroshi Kitagawa, Synthetic Metals, 153 (2005) 353.

48. Seemita Banerjee, Kinshuk Dasgupta, Asheesh Kumar,Priyanka Ruz, B. Vishwanadh, J. B. Joshi, V. Sudarsan, International journal of hydrogen energy, 40 (2015) 3268.

49. ASTM Standards, American Society for Testing and Materials, C 1008-92, (Standard Specification for Sintered (U,Pu)O_2 Pellets - Fast Reactor Fuel) 12(1) (1995) 431.

50. Y. Sesha Sayi, C. S. Yadav, P. S. Shankaran, G. C. Chhapru, Indian Journal of Chemical Technology, 11 (2004) 648-653.

51. V. Venugopal , K. N. Roy, Ziley Singh, R. Prasad, Dilip Kumar, G. L. Goswami, Seminar On Fast Reactor Fuel Cycle, Igcar, Kalpakkam, Feb 10 - 12, (1986) Paper No. 14.

52. J. Roboz, Introduction to mass spectrometry: Instrumentation and Techniques, Wiley (Interscience), Newyork (1968).

53. B. D. Cullity, S. R. Stock,Elements of X-Ray Diffraction, Prentice Hall: London, (2001).

54. U. Holzwarth, N. Gibson, Nat. Nanotechnol., 6 (2011) 534.

55. R. Kainhofer, One way to get the Scherrer formula for size broadening, TU Vienna, (2000).

56. A. L. Patterson,The Scherrer Formula for X-Ray Particle Size Determination, PRL, 56 (1939) 978.

57. Joseph I. Goldstein, Dale E. Newbury, Patrick Echlin, David C. Joy, Charles E. Lyman, Eric Lifshin, Linda Sawyer, Joseph R. Michael, Scanning Electron Microscopy and X-Ray Microanalysis,Springer, 3rd Ed. (2003).

58. B. C. Dodrill, B. J. Kelley, Measurements with a VSM, Lake Shore Cryotronics, Inc. (1999).
59. B.D. Cullity, Introduction to magnetic materials. Addision - Wesley: New York (1972).
60. Seemita Banerjee, Doctoral thesis, HomiBhabha National Institute, Mumbai (2013).
61. Charles C. Chusuei, D. Wayne Goodman, X- Ray Photoelectron Spectroscopy, Encyclopedia of physical science and Technology, 3rd edition, 17 (2002).
62. P. Gütlich, Y. Garcia, Chemical applications of Mössbauer Spectroscopy, Mössbauer spectroscopy - Tutorials Book (Eds Y. Yoshida, G. Langouche) Springer, 2013, chapter 2, 23-89
63. B. C. Smith, Fundamentals of Fourier Transform Infrared Spectroscopy, CRC Press: Boca Raton (2011).
64. D. O. Northwood, U. Kosasih, International Metallurgical Reviews 28(2) (1983) 92.
65. C. Ganguly, Proceedings of the symposium ZIRCONIUM - 2002, September 11-13 (2002) BARC, Mumbai, India.
66. S. Mishra, K. S. Sivaramakrishnan, M. K. Asundi,J. Nucl. Mater.,45 (1972) 235.
67. I.F. Ibrahim, Technical Report, Canada: Atomic Energy of Canada Limited-8767 (1985).
68. Kundan Kumar, B. B. Rupani, BARC News Letter(2002) Mumbai, India.
69. J. H. Huang, S. P. Huang, Mater. Sci. Eng. A., 161(1993) 247.
70. E. Ramadasan, K. Unnikrishnan, V. D. Alur, V. P. Jathar, K. C. Sahoo, Proceedings of the symposium ZIRCONIUM - 2000, September 11-13 (2002) BARC, Mumbai, India.
71. G. L. Powell, J. B. Condon, Anal. Chem., 45 (1973) 2349.
72. J. G. V. Raaphorst, A. Kout, F. Z. Anal. Chem., 291 (1978) 324.
73. K. Watanabe, M. Ouchi, K. Gunji, F. Z. Anal. Chem., 323 (1986) 225.
74. G. A. Bickel, L. W. Green, M. W. D. James, T. G. Lamarche, P. K. Leeson, H. Michel, J. Nucl. Mater., 306 (2002) 21.
75. Y.S. Sayi, K. L. Ramakumar, R. Prasad, C. S. Yadav, P. S. Shankaran, G. C. Chhapru, H. C. Jain; J. Radioanal. Nucl. Chem., 230 (1998) 5.
76. A. A. Bahurmuz, I. J. Muir, V. F. Urbanic, Proceedings of ASTM 14th International Symposium on Zirconium in Nuclear Industry, ASTM stock number STP1467, (ed. P. Rudling and B. Kammenzid), ASTM, USA. (2004) 547.

77. A. Farkas, Orthohydrogen, Parahydrogen and Heavy Hydrogen. Oxford, UK: Cambridge University Press (1935).
78. J. W. Pyper, E. M. Kelley, J. G. Megisted, R. T. Tsugava, P. E. Roberts, P. C. Souers, Lawrence Livermore Laboratory, UCRL-52391. USA: University of California Press (1978).
79. R.E. Taylor, Anal. Chim. Acta.,21 (1959)549.
80. T. Jayaprakash, M. S. Krishnan, Proceedings of the Seminar on Mass Spectrometry, Applications and Current Trends, (ed. C. K. Mathews), Mumbai, India (1978) 88.
81. EURACHEM / CITAC Guide CG4, Quantifying Uncertainty in Analytical Measurement Second Edition (2000).
82. E.A. Gulbransen, K.F. Andrew, J.Electrochemical Society, 101 (1954) 560.
83. A. Sawatzky, C. E. Ells, Zirconium in the Nuclear Industry: 12th International Symposium ASTM, STP 1354(2000) 32.
84. D. Srivastava, G. K. Dey, S. Banerjee, Metall. Trans., 26A (1995) 270.
85. R.N. Singh, S. Mukherjee, R. Kishore, B.P. Kashyap, J.Nucl. Mater.,345(2005) 146.
86. A. Sawatzky, J. Nucl. Mater.,2 (1960) 62.
87. A. Sawatzky; J. Nucl. Mater.,2 (1960) 321.
88. A. Sawatzky, B. J. S. Wilkins, J. Nucl. Mater.,22(1967) 304.
89. J. J. Kearns, J. Nucl. Mater.,22 (1967) 292.
90. J. J. Kearns; J.Nucl. Mater.,43 (1972) 330.
91. D. Khatamian, V. C. Ling, J. Alloys Compd., 253 (1997) 162.
92. H. Wipf, B. Kappesser, R. Werner, J. Alloys Compd., 310 (2000) 190.
93. T. Laursen, M. Leger, J. L. Whitton, J. Nucl. Mater.,158 (1988) 49.
94. T. Laursen, M. Leger, Xin-Pei Ma, J. D. Mac Arther, G. R. Palmer, J. L. Whitton, J. Nucl. Mater., 165 (1989) 156.
95. D. Khatamian, J. Alloys and Compd., 253-254 (1997) 471.
96. L. W. Green, G. A. Bickel, P. K. Lessen, M. W. D. James, T. G. Lamarche, H. Michel, Atomic Energy of Canada Limited 11342 (1996).
97. D. Khatamian, J. Alloys Compd., 580 (2013) 558.
98. C. M. Schwartz, M. W. Mallett, Trans. Amer. Soc. Metals, 46 (1954) 640.
99. M. W. Mallett, W. M. Albrecht, J.Electrochem. Soc., 104 (1957) 142.
100. D. K. Rodgers, C. E. Coleman, M. Griffiths, G. A. Bickel, J. R. Theaker, I. Muir, A. A. Bahurmuz, S. St. Lawrence, M. Resta Levi, J. Nucl. Mater., 383 (2008) 22.

101. A. D. Lepage, W.A. Ferris, G. A. Ledoux, FC-IAEA-03, T1.20.13-CAN-27363-03, November 1998.

102. D. Khatamian, A. Shaddick , V. F. Urbanic, Atomic Energy of Canada Limited - 11951 (1998).

103. Komal Chandra, P.S. Ramanjaneyulu, C.S. Yadav, A. S. Kulkarni, Y. S. Sayi, K.L.Ramakumar, Analytical Letters, 45 (2012) 2136.

104. Pan, I. G. Ritchie, M. P. Puls, J. Nucl. Mater., 228 (1996) 227.

105. G. F. Slattery, J. Inst. Met., 95 (1967) 43.

106. D. Srivastava, S. Neogi, G. K. Dey, S. Banerjee, E. Ramadasan, S. Anantharaman, Bhabha Atomic Research Centre Mumbai, report No. BARC/E/2011/007.

107. D. Khatamian, J.Alloys and Compd., 356–357 (2003) 22.

108. B. Cox, Y.M. Wong, J. Nucl. Mater.,270 (1999) 134.

109. H.L. Li, Q. Wen, J. Szpunar; Defect and Diffusion Forum, 263 (2007) 117.

110. Chen, C. Ostrom, Chem. Rev., 115 (2015) 11999.

111. S. Cheong, J. D. Watt, R. D. Tilley, Nanoscale, 2 (2010) 2045.

112. W. P. Zhou, A. Lewera, R. Larsen, R. I. Masel, P. S. Bagus, A. Wieckowski, J. Phys. Chem. B, 110 (2006) 13393.

113. M. Shao, J. Power Sources, 196 (2011) 2433.

114. C . Bianchini, P. K. Shen, Chem. Rev., 109 (2009) 4183.

115. X. Yu, P. G. Pickup, J. Power Sources, 182 (2008) 124.

116. H. Miyake, T. Okada, G. Samjeské, M. Osawa, Phys. Chem. Chem. Phys., 10 (2008) 3662.

117. K. Mori, M. Dojo, H. Yamashita, ACS Catal., 3 (2013) 1114.

118. A. Bej, K. Ghosh, A. Sarkar, D.W. Knight, RSC Adv., 6 (2016) 11446.

119. F. Wei, C. Cao, Y. Sun, S. Yang, P. Huang, W. Song, Chem. Cat. Chem., 7 (2015) 2475.

120. R. Zhang, D. Shuai, K. A. Guy, J. R. Shapley, T .J. Strathmann , C.J. Werth, Chem. Cat. Chem, 5 (2013) 313.

121. W. Sun, W. Yang, Z. Xu, Q. Li, J. K. Shang, ACS Appl. Mater. Interfaces, 8 (2016) 2035.

122. T. Toraishi, T. Kimura, M. Arisaka, Chem. Commun., (2007) 240.

123. M. Yu. Boltoeva, A.V. Trefilova, A.V. AnaDev, Radiochemistry, 50 (2008) 38.

124. Y. Huang, H. Ma, S. Wang, M. Shen, R. Guo, X. Cao, M. Zhu, X. Shi, ACS Appl. Mater. Interfaces, 4 (2012) 3054.
125. M. A. Omole, I. O. K'Owino, O. A. Sadik, Appl. Cat. B: Environ., 76 (2007) 158.
126. I. O. K'Owino, M. A. Omole, O. A. Sadik, J. Environ. Monit., 9 (2007) 657.
127. H. Zhang, M. Jin, Y. Xiong, B. Lim, Y. Xia, Acc. Chem. Res., 46 (2013) 1783.
128. I. Hussain, N. B. Singh, A. Singh, H. Singh, S. C. Singh, Biotechnol.Lett., 38 (2016) 545.
129. S. Guo, E. Wang, Nano Today, 6 (2011) 240.
130. H. Xu, B.W. Zeiger, K. S. Suslick, Chem. Soc. Rev., 42 (2013) 2555.
131. C. Dispenza, N. Grimaldi, M. A. Sabatino, I. L. Soroka, M. Jonsson, J. Nanosci. Nanotechnol., 15 (2015) 3445.
132. K. L. Mc Gilvray, J. Granger, M. Correia, J. T. Banks, J. C. Scaiano, Phys. Chem. Chem. Phys., 13 (2011) 11914.
133. Y. Xiong, Y. Xia, Adv. Mater., 19 (2007) 3385.
134. G. Agostini, A. Piovano, L. Bertinetti, R. Pellegrini, G. Leofanti, E. Groppo, C. Lamberti, J. Phys. Chem. C, 118 (2014) 4085.
135. C. Zhu, J. Zeng, P. Lu, J. Liu, Z. Gu, Y. Xia, Chem. - Eur. J., 19 (2013) 5127.
136. W. Niu, L. Zhang, G. Xu, ACS Nano., 4 (2010) 1987.
137. H. P. Choo, K. Y. Liew, H. Liu, J. Mater. Chem., 12 (2002) 934.
138. Y. Wang, S. Xie, J. Liu, J. Park, C. Z. Huang, Y. Xia, Nano Lett., 13 (2013) 2276.
139. H. Zhang, M. Jin, Y. Xiong, B. Lim, Y. Xia, Acc. Chem. Res., 46 (2013) 1783.
140. M. A. Mahmoud, R. Narayanan, M. A. El-Sayed, Acc. Chem. Res., 46 (2013) 1795.
141. H. Zhang, M. Jin, Y. Xia, Chem. Soc. Rev., 41 (2012) 8035.
142. C. H. Liu, R. H. Liu, Q. J. Sun, J. B. Chang, X. Gao, Y. Liu, S. T. Lee, Z. H. Kang, S. D. Wang, Nanoscale, 7 (2015) 6356.
143. D. S. Su, S. Perathoner, G. Centi, Chem. Rev., 113 (2013) 5782.
144. H. Chang, H. Wu, Energy Environ. Sci., 6 (2013) 3483.
145. L. Ren, F. Yang, C. Wang, Y. Li, H. Liu, Z. Tu, L. Zhang, Z. Liu, J. Gao, C. Xu, RSC Adv., 4 (2014) 63048.
146. B. Zhang, L. Shao, W. Zhang, X. Sun, X. Pan, D. S. Su, Chem. Cat. Chem., 6 (2014) 2607.
147. R. Ricciardi, J. Huskens, W. Verboom, Chem. Sus. Chem., 8 (2015) 2586.
148. M. B. Gawande, P. S. Branco, R. S. Varma, Chem. Soc. Rev., 42 (2013) 3371.

149. X. Pan, Y. J. Xu, ACS Appl. Mater. Interfaces, 6 (2014) 1879.

150. R. Li, P. Zhang, Y. Huang, C. Chen, Q. Chen, ACS Appl. Mater. Interfaces, 5 (2013) 12695.

151. C. Deraedt, D. Wang, L. Salmon, L. Etienne, C. Labrugère, J. Ruiz, D. Astruc, Chem. Cat. Chem., 7 (2015) 303.

152. R. Haag, S. Roller, Topics in Current Chemistry, Ed. A. Kirschning, Springer-Verlag, Berlin Heidelberg, 242 (2004) 1-42.

153. Y. Y. N. Bonggotgetsakul, R.W. Cattrall, S. D. Kolev, React. Funct.Polym., 97 (2015) 30.

154. M. Zeng, X. Yuan, Z. Yang, C. Qi, Int. J. Biol. Macromol., 68 (2014) 189.

155. K. Soukup, P. Topka, V. Hejtmánek, D. Petráš, V. Valeš, O. Šolcová, Catal. Today, 236 (2014) 3..

156. E. Hariprasad, T. P. Radhakrishnan, ACS Catal., 2 (2012) 1179.

157. V. W. Faria, D. G. M. Oliveira, M. H. S. Kurz, F. F. Gonçalves, C.W. Scheeren, G. R. Rosa, RSC Adv., 4 (2014) 13446.

158. R. Mallampati, S. Valiyaveettil, ACS Sustainable Chem. Eng., 2 (2014) 855.

159. M. Liang, R. Su, W. Qi, Y. Zhang, R. Huang, Y. Yu, L. Wang, Z. He, Ind. Eng. Chem. Res., 53 (2014) 13635.

160. M. Opanasenko, P. ` t•pni•ka, J. • ejka, RSC Adv., 4 (2014) 65137.

161. A. J. Forman, J. N. Park, W. Tang, Y. S. Hu, G. D. Stucky, E. W. McFarland, Chem. Cat. Chem., 2 (2010) 1318.

162. B. Li, W. Z. Weng, Q. Zhang, Z.-W. Wang, H. L. Wan, Chem. Cat. Chem., 3 (2011) 1277.

163. Z. Zhang, Y. Yu, P. Wang, ACS Appl. Mater. Interfaces, 4 (2012) 990.

164. S. Chappa, R. N. Shinde, A. K. Pandey, Green Chem., 17 (2015) 4157.

165. D. V. Goia, E. Matijevi•, New J. Chem., (1998) 1203.

166. W. Liu, D. Wang, Y. Duan, Y. Zhang, F. Bian, Tetrahedron Lett.,56 (2015) 1784.

167. M. Yadav, Q. Xu, Chem. Commun., 49 (2013) 3327.

168. W. Tu, K. Li, X. Shu, W. W. Yu, J. Nanopart. Res., 15 (2013) 1593.

169. X. Zhou, Y. Huang, W. Xing, C. Liu, J. Liao, T. Lu, Chem. Commun., (2008) 3540.

170. Y. Wang, S. I. Choi, X. Zhao, S. Xie, H. C. Peng, M. Chi, C. Z. Huang, Y. Xia, Adv. Funct. Mater., 24 (2014) 131.

171. V. Mazumder, S. Sun, J. Am. Chem. Soc., 131 (2009) 4588.

172. S. Patra, A. K. Pandey, S. K. Sarkar, A. Goswami, RSC Adv., 4 (2014) 33366.

173. S. Lagergren, Handlingar, 24(1898) 1.

174. S. J. Azizian, Colloid Interface Sci., 276 (2004) 47.

175. S. Das, A. K. Pandey, A. A. Athawale, V. K. Manchanda, J. Phys. Chem. B, 113 (2009) 6329.

176. A. Dandapat, D. Jana, G. De, Appl. Catal. A: General, 396 (2011) 34.

177. Miho Yamauchi, Ryuichi Ikeda, Hiroshi Kitagawa, Masaki Takata, J. Phys. Chem. C, 112 (2008)3294.

178. Tong Liu, Lei Xie, Yaoqi Li, Xingguo Li, Shujie Pang, Tao Zhang, Journal of Power Sources 237 (2013) 74.

179. F. Albert Cotton, Geoffrey Wilkinson, Advanced Inorganic Chemistry, fifth edition (1988) John Wiley & Sons.

180. T. Hiyama, S. Sugaya, J. Yamamoto, K. Kamimura, J. Nucl. Mater.,217 (1994)1.

181. O. Vega, H. G. Riella, C. Rodrigues, J. Nucl. Mater., 106 (1982) 121.

182. J. A. Basford, M. D. Boeckmann, R. E. Ellefson, A. R. Fillppelli, D. H. Holkeboer, L. Lieszkovszky, C.M. Stupak, J Vac Sci. Technol A, 11 (1993) A22.

183. T. Tisarky, V. Nikolajenko, Vacuum, 47 (1996) 173.

184. Y. S. Sayi , J. Radhakrishna, C. S. Yadav, P. S. Shankaran, G. C. Chhapru, Anal Lett, 23 (1990) 2049.

185. B. Zajec, R. Rozman, V. Nemanic, Vacuum, 101 (2014) 445.

186. D. J. Santeler, J Vac Sci Technol A, 5 (1987) 129.

187. ISO (2008) Uncertainty of measurement-Guide to the expression of uncertainty in measurement, 98-3, Part-3, (GUM-1995). ISO/ IEC Guide, Geneva.

188. P. S. Ramanjaneyulu, K.L. Ramakumar, Y. S. Sayi, J Accredit Qual Assur., 15 (2010) 665.